Of Sounds, Photons and Maps:

In Vivo Optical Characterisation of the Auditory Thalamocortical System

Sebastian A. Vásquez-López

St Hugh's College

University of Oxford

A thesis submitted for the degree of

Doctor of Philosophy

Trinity Term, 2017

Consuelo Arroyave (1932 – 2017)

Sebastian A. Vásquez-López

Of Sounds, Photons and Maps:

In Vivo Optical Characterisation of the Auditory Thalamocortical System

Supervisors: Prof Andrew King, Dr Johannes Dahmen and Prof Nigel Emptage

Reviewers: Prof Jennifer Linden and Dr Tommas Ellender

University of Oxford

St Hugh's College

Oxford, UK

Acknowledgement

If it was possible to chronicle the many small and large gestures of guidance and support that one is bestowed with over the course of a doctoral project, the length of this thesis would increase manyfold. Yet, the help that I received from some was so significant and ever-present that, even if only in these short pages, I ought to express my gratitude.

Firstly, I must thank my supervisors, Dr Johannes Dahmen, Professor Andrew King and Professor Nigel Emptage. You offered me both the freedom to follow my own ideas and the guidance to develop my academic skills.

I must also thank the Clarendon Fund and St Hugh's College, for financial support during my DPhil, as well as the Colfuturo foundation, who funded my MSc and brought me to Oxford in the first place.

Many thanks to all the members of the Auditory Neuroscience Group (ANG) and the Emptage lab. Here, I must give special mentions to all the "mouse people" of the ANG, with whom I shared, not only an interest in a small and whiskered model organism, but also friendships, stimulating scientific discussions, hours of work as well as leisure, and, with some of them, even an office. What is more, all of them contributed significantly to the development of research methods in our lab, from which this project ultimately benefited. Therefore, many thanks to Yves Weissenberger, Michael Lohse, Peter Keating and Samuel Picard. I must also give special thanks to Zahid Padamsey, from the Emptage lab, for his valuable advice at key moments of my time as a DPhil student and all his help with the *in vitro* aspects of this project.

To my collaborators from Dundee University, Dr Tomas Cizmar and Dr Martin Ploschner (who is now in Sydney), I must thank for allowing me to visit their lab a couple of times for the development of the fibre-based system. On this note, I must also acknowledge the work of Vadim Koren, who has been part of the fibre-imaging project too and has equally contributed to the acquisition of some of the first *in vivo* images we captured with it.

I must thank all the helpful staff in the Sherrington Building, the Pharmacology Department and Veterinary Services, as well as Dan, our lab manager. Without their contribution most of the research taking place in our labs, including the one presented in this thesis, would have never come to fruition.

Next, my family, in particular my parents, who supported me to be able to come to the UK in the first place. To you, I am immensely thankful and forever in debt.

I would have also liked to mention here, name by name, every single one of my friends—those with whom I lived, studied, travelled, ate, partied, and so on—but I am not going to. I will just say that I owe them many of the best memories I have of my time as a student in Oxford. Thanks a million for that.

Finally, I would like to thank Ines. Here, I fall short of words to express how much her love and support helped me get through the last stages of experiments and the writing of this thesis. She was there for me, on the late nights and the non-very-early mornings. Much of the emotional strain of finishing my doctorate was lightened by her. As hard as things were, sometimes, I believe I could go through the same again, as long as I have her by my side. Yet, I know for certain, she would rather have me going through the writing of a thesis, just this once.

Contents

Nomenclature

2PLSM: Two-photon laser scanning microscope.

A1: Primary auditory cortex.

A2: Secondary auditory field.

AAF: Anterior auditory field.

aCSF: Artificial cerebrospinal fluid.

ANOVA: Analysis of variance.

AOD: Acousto-optic deflectors.

BF: Best frequency.

C-type: Core-type.

CB: Calbindin.

CB+: Calbindin-positive.

CCD: Charge-coupled device.

cm: Centimetre.

CR: Calretinin.

CR-: Calretinin-negative.

CR+: Calretinin-positive.

CT: Corticothalamic.

DA: Dorsoanterior field.

dB: Decibel SPL.

DIV: Days in vitro.

DM: Dorsomedial field.

DP: Dorsoposterior field.

eGFP: Enhanced green fluorescent protein.

EPSP: Excitatory post-synaptic potential.

FM: Frequency-modulated.

FO: First order.

FRA: Frequency response area.

fs: Femtosecond.

FWHM: Full width at half maximum.

g: Gram.

GABA: Gamma-aminobutyric acid.

GECI: Genetically-encoded calcium indicator.

GFP: Green fluorescent protein.

GPU: Graphics processing unit.

GRIN: Graded index.

h: Hour.

HO: Higher order.

HOG: Histograms of oriented gradients.

HSD: Honest significance difference.

Hz: Hertz.

IAF: Insular auditory field.

IC: Inferior colliculus.

ICcn: Inferior colliculus central nucleus.

ICdc: Inferior colliculus dorsal cortex.

ICec: Inferior colliculus external nucleus.

IL-type: Intralaminar-type.

IRES: Internal ribosome entry site.

Kg: Kilogram.

L: Litre.

L1: Neocortical layer 1.

L2/3: Neocortical layers 2 and 3.

L3: Neocortical layer 3.

L3b/4: Neocortical layers 3b and 4.

L4: Neocortical layer 4.

L5: Neocortical layer 5.

L6: Neocortical layer 6.

LFP: Local field potentials.

LGN: Lateral geniculate nucleus.

M-type: Matrix-type.

M1: Primary motor cortex.

mg: Milligram.

MGB: Medial geniculate body.

MGBd: Dorsal division of the medial geniculate body.

MGBm: Medial division of the medial geniculate body.

MGBv: Ventral division of the medial geniculate body.

min: Minute.

ml: Millilitre.

mm: Millimetres.

mM: Millimolar.

MUA: Multi-unit activity.

MMF: Multimode optical fibres.

ms: Millisecond.

n: Number/sample size.

NA: Numerical aperture.

NIR: Near-infrared radiation.

PBS: Phosphate-buffered saline.

PIN: Posterior intralaminar nucleus.

PMF: Polarisation maintaining fibre.

PMT: Photo-multiplier tube.

Pol: Posterior thalamic nucleus.

PP: Peripeduncular thalamic nucleus.

PV: Parvalbumin.

PV+: Parvalbumin-positive.

ROI: Regions of interest.

RTN: Reticular nucleus.

s: Seconds.

s.d.: Standard deviation.

S1: Primary somatosensory cortex.

SG: Suprageniculate thalamic nucleus.

SLM: Spatial light modulator.

SMF: Single-mode fibre.

SOM: Somatostatin.

SOM+: Somatostatin-positive.

SPL: Sound pressure level.

TC: Thalamocortical.

TCSPC: Time-correlated single-photon counting.

TM: Transmission matrix.

TRN: Thalamic reticular nucleus.

UF: Ultrasonic field.

μm: Micrometre.

μg: Microgram.

V1: Primary visual cortex.

VIP: Vasoactive intestinal peptide.

VIP+: Vasoactive intestinal peptide-positive.

VL: Ventral lateral thalamic nucleus.

VP: Ventroposterior thalamic nucleus.

VSD: Voltage-sensitive dyes.

W: Watts.

List of Figures

Abstract

As information ascends up the sensory streams, the maps of receptor surface might be faithfully relayed from one brain structure to another, degraded or lost altogether. Such transformations can inform about the type of circuit computation carried out in each region. *In vivo* high-resolution imaging methods, like two-photon microscopy, are useful for characterising the functional architecture of neuronal circuits down to the micro-scale. To better understand the rules governing thalamocortical connectivity and the origin of cortical maps, I used *in vivo* two-photon calcium imaging to characterise the properties of thalamic axons innervating different layers and subfields of mouse auditory cortex. Although topographically organised at a global level, I found the frequency selectivity of individual thalamocortical axons to be surprisingly heterogeneous, even in the middle layers (L3b/4) of the primary cortical areas where the thalamic input is dominated by the lemniscal projection. Subsequently, I employed a dual-colour imaging approach to explore the spectral transformations taking place between the thalamocortical projection and granular and supragranular layers of auditory cortex. Some differences in local spectral properties between neurons in L4 and L2/3 were observed in awake, passively listening mice, confirming previous observations on the anaesthetised preparation. Finally, I present a demonstration of a novel fibre-based high-resolution fluorescence imaging method to optically investigate neuronal circuits in deep brain regions, with minimal invasiveness. In short, my work provides some new insights on the functional micro-organisation of the auditory thalamocortical system and constitutes a classical example of the power of optical methods for the study of neuronal circuits *in vivo*.

1 Introduction

> *The thalamus is like the Flying Dutchman: many have heard of it, some believe in it, but few have actually seen it.*
>
> **— Attributed to J. E. Rose**

1.1 A tale of thalamus and cortex

Tightly folded, directly underneath the skull, lies the most recent addition to the 500-million-year evolution of brains, from cephalochordates to mammals. The presence of this structure, the neocortex, is seen as the defying characteristic of the mammalian brain (Nieuwenhuys et al., 1998). Of land-dwelling mammals, primates and in particular humans have the largest brains in proportion to body size. Much of their large neuronal mass comes from the neocortex, which in humans accounts for as much as 80 percent of brain volume (Passingham, 1982). It is this large neocortex which is thought to be the seat of most of our higher cognitive functions, including conscious perception, goal-directed action, abstract thinking, language, numeracy, introspection and imagination (Fuster, 2005). Thus, considerable effort has been put on the study of cortical circuits and their functions (Harris, 2015; Douglas and Martin, 2004; Winer and Schreiner, 2010; Passingham et al., 2002). In comparison, another brain region has received considerably less attention, despite its function being so noticeably interdependent with that of the neocortex as to be deemed the 'deepest of cortical layers' (Sherman et al., 2006). This region is the thalamus, and

unlike the superficial neocortical sheet, its location is much more inaccessible to direct experimental interrogation. It can be found anywhere between 2.5 mm from the brain surface in the mouse to 6 cm in humans. Yet, despite being topographically separated from each other, the thalamus provides the main source of ascending inputs to cortex, whilst the feedback projections from cortex, in turn, constitute the main form of input to thalamus[1].

In anatomy, the word cortex (derived from the Latin word for bark) describes the outermost layer of an organ. What is commonly referred to as the cerebral cortex can be further subdivided into the phylogenetically older allocortex and the more recent neocortex (Nieuwenhuys et al., 1998). The allocortex, in turn, includes a hippocampal portion, the archicortex, and an olfactory portion or paleocortex. Only the brain of mammals is known to feature a neocortex, whereas allocortical structures can be found in many non-mammalian vertebrate species. Histologically, the neocortex has at least six distinct cellular layers, whereas allocortices are characterised by having just three or four layers. Because the neocortex takes up a much larger area of the cortex, the word cortex is generally equated to neocortex. Thus, when the words cortex and cortical are used in this report, they can be assumed to refer to the neocortex, unless stated otherwise. Likewise, the term thalamus (derived from the Greek word for chamber) is broadly used in reference to the two largest portions of the mammalian diencephalon (Jones, 2007). The dorsal thalamus is by far the largest subdivision and all of its nuclei project to one or more areas of the neocortex. A second, smaller subdivision, the ventral thalamus, sends no axons to the cortex. Its main portion, the thalamic reticular nucleus (TRN), is placed in the course of the axons that are going from the dorsal thalamus to the neocortex and it is mostly inhibitory. Thus, it is the dorsal thalamus which has the most direct functional relationship to the neocortex and when the words thalamus and thalamic are used here, they can be assumed to refer to the dorsal thalamus.

[1] Corticothalamic feedback projections outnumber almost 10 to 1, the thalamic afferents from the periphery (Jones, 2007).

The thalamus provides the main source of inputs to the neocortex (Jones, 2007; Sherman et al., 2006). Virtually all sensory information arrives to the neocortex via the thalamus[2], as well as information from other brain regions such as the cerebellum and the mamillary bodies (**Fig. 1.1**). What is more, not only does the thalamus sends projections to sensory cortices, but also to every higher association and motor area (**Fig. 1.2**). These observations alone strongly suggest that, in order to understand the functional organization of cortical circuits, it is essential to uncover the rules of thalamocortical (TC) connectivity.

1.2 On cortical and thalamic maps

Structure and function in neuronal circuits are inherently linked. Properties of sensory systems organisation such as retinotopy, somatotopy and tonotopy, which are present from the receptor surface up to the cortex, are examples of topographic maps. In these, a particular stimulus feature is continuously represented on a brain structure. Topography is also present beyond sensory systems, as in the case of the somatotopic organization of the motor cortex and its projections (Penfield and Rasmussen, 1950) . Topographic maps have been best characterised in the cortex, owing to the tangential representation of mapped features over the cortical sheet, which greatly facilitates the study of functional topography. In the thalamus, grey matter can be subdivided into cytoarchitectonically and functionally-defined nuclei, which receive ascending inputs from specific pre-thalamic pathways. For example, inputs carrying auditory information are largely confined to the medial geniculate body (MGB), information from skin mechanoreceptors goes to the ventroposterior

[2] Olfactory information is often quoted an exception to the rule of TC relay. This comes from the ambiguous use of the word cortex to describe both the six-layered neocortex and the three-layer and phylogenetically older paleocortex, which includes the pyriform cortex. The olfactory pathways reach the pyriform cortex without passing through the thalamus but from there, they relay through the medial dorsal nucleus in their way to association areas in the neocortex (Kuroda et al., 1992).

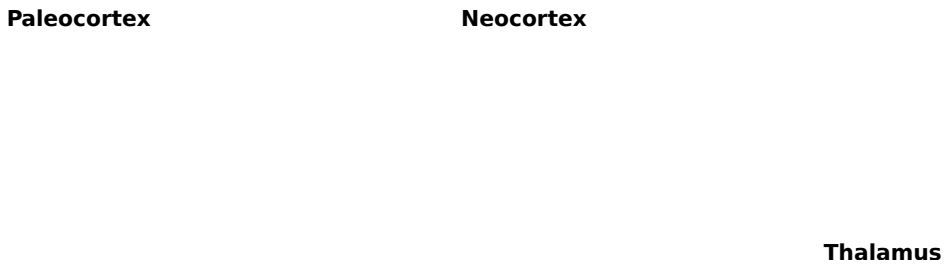

Figure adapted from copyrighted material. Not available in the Online dissemination version of this thesis.

Fig. 1.1: Sources of ascending inputs to sensory cortical areas. All ascending sensory inputs to the six-layered neocortex must relay on one thalamic nucleus. The phylogenetically older paleocortex receives olfactory inputs directly. Adapted from Swanson (2012). *a,b*, spinothalamic tract and medial lemniscus, respectively; *bp*, retinal bipolar cell; *CN*, cochlear nuclei; *DCN*, dorsal column nuclei; *DRG*, dorsal root ganglion; *IX,X ganglia*, glossopharyngeal and vagal ganglia; *gc*, retinal ganglion cell; *IC*, inferior colliculus; *GV*, trigeminal ganglion; *IX, X ganglia*, glossopharyngeal and vagal ganglia; *LGN*, lateral geniculate nucleus; *LP/PULV*, lateral posterior nucleus /pulvinar; *MGN*, medial geniculate nucleus; *NTSc, r*, nucleus of the solitary tract, caudal, rostral parts; *PBl, m*, parabrachial nucleus, lateral, medial divisions; *PSV*, principal trigeminal sensory nucleus; *SC*, superior colliculus; *SP*, spinal cord; *SPV*, spinal trigeminal nucleus; *VII, IX, Xg*, geniculate, petrosal, and nodose ganglia.; *VIIIgang.*, vestibulocochlear ganglion; *VP*, ventral posterior nucleus; *VPLpc*, ventral posterolateral nucleus, parvicellular part; *VPMpc*, ventral posteromedial nucleus, parvicellular part.

(VP) nucleus, whereas retinal input targets neurons in the lateral geniculate nucleus (LGN). Generally speaking, thalamic nuclei which receive topographically ordered sensory input relay information to cortex also in an ordered manner. This makes the organisation of cortical maps inherently linked to that of maps in the thalamus.

Origins of maps in thalamus and cortex

During the evolution of mammals, the expansion and differentiation of the neocortex allowed for ever more precise neuronal representations of perceptual information, a process which is reflected in the organisation of cortical maps (Kaas, 1995; Schnei-

Figure adapted from copyrighted material. Not available in the Online dissemination version of this thesis.

Fig. 1.2: Every neocortical area receives input from one major nucleus of the thalamus. The human cerebral hemisphere, medial and lateral view (top), and the primate thalamus (bottom), colour-coded to indicate the thalamic cell groups and their major projection areas in the cortex. Reprinted from Schneider (2014). *A*, anterior nuclei; *ac*, anterior commissure; *Aud*, primary auditory cortex; *CC*, corpus callosum; *IC*, inferior colliculus; *LD*, lateral dorsal nucleus; *LG*, lateral geniculate body; *LP*, lateral posterior nucleus; *ot*, optic tract; *MD*, mediodorsal nucleus; *MG*, medial geniculate body; *ped*, cerebral peduncle; *Pulv*, pulvinar nucleus; *SC*, superior colliculus; *sm*, stria medullaris; *splen*, splenium; *VA*, ventral anterior nucleus; *VB*, ventrobasal nucleus (ventral posterior nuclei); *VL*, ventral lateral nucleus.

der, 2014). Primary cortical sensory areas in the visual (Essen and Zeki, 1978), auditory (Woolsey, 1964), somatosensory (Penfield and Rasmussen, 1950) and even gustatory systems (Chen et al., 2011a) have been found to contain topographic maps representing the complete sensory surface. The nature and general layout of these maps has been found to be relatively well preserved across different mammalian lineages. It has been suggested that the appearance of specialised cortical areas and the expansion of existing ones was accompanied by an increasing specialization of the thalamic cell groups that provided cortex with ascending inputs (Butler, 1994; Butler, 2009) (**Fig. 1.3**). Similarly, TC inputs appear to be instrumental for the appropriate formation of primary cortical sensory areas and sensory maps. This is

supported the observation that interventions altering the connectivity in thalamus during development often result in alteration on the formation of functional cortical areas (Pouchelon et al., 2014).

Figure adapted from copyrighted material. Not available in the Online dissemination version of this thesis.

Fig. 1.3: Parcellation of thalamic cell groups in the dorsal thalamus during the evolution of major vertebrate groups. Dendrogram and schematic representation of evolutionary thalamic parcellations based on cladistic analysis. Colours indicate nuclei from different developmental origins: the lemnothalamic nuclei (blue) receive predominantly lemniscal sensory input and the collothalamic nuclei (red) receive mostly input from midbrain structures. Reprinted from Schneider (2014). Based on Butler (1994).

Mapping circuit microarchitecture can inform about circuit function

As information ascends up the sensory streams, the maps of receptor surface might be faithfully relayed from one brain structure to another, degraded or lost altogether. Such transformations can inform about the type of circuit computation carried out in each region. This is because all maps can be seen as the product of the particular functional microarchitecture within a brain area, and this microarchitecture underlies how networks of neurons process information. Because wiring between neurons is metabolically costly, there is a strong pressure for neuronal circuits to be organised in such a way as to have connected neurons as close to each other as possible, whilst maintaining circuit function (Chklovskii and Koulakov, 2004; Chklovskii et al., 2002; Chen et al., 2006). So, for example, in cortical maps were the representation of sensory stimuli remains smooth down to the micro-scale, the local circuit computation might rely on precise stimulus selectivity. On the other hand, a heterogeneous functional organization suggests forms of processing requiring networks of neurons with different selectivities, which together might be able to

encode more complex features than a homogeneous circuit. Evolutionary constrains are likely to play a significant role in shaping circuit microarchitecture too. It has been argued, for example, that small brains might not support or even require the homogeneous organisation of sensory maps observed in larger brains, explaining observations of local heterogeneity in orientation and frequency tuning in the visual (Bonin et al., 2011) and auditory (Bandyopadhyay et al., 2010; Rothschild et al., 2010) cortices of rodents, respectively.

Fine-scale maps derive from the spatial organisation of individual neurons sorted by their receptive field properties. These properties are typically measured through the neurons' spiking activity. However, in mechanistic terms, they are actually the summed product of the neurons' synaptic inputs, which, for most cortical neurons, arrive on synapses located on extensive dendritic arbours (London and Häusser, 2005). Through its dendritic arbour, a neuron might have access to a functionally heterogeneous range of inputs—and there is evidence that cortical neurons do (Chen et al., 2011b; Jia et al., 2010)—, but still exhibit sharp stimulus selectivity when measured by firing rate. This could be the result of biased sampling, differences in synaptic weights, dendritic non-linearities, differences between subthreshold tuning and tuning based on firing (Harris and Mrsic-Flogel, 2013), and even the particular experimental conditions in which the receptive field is characterised. Thus, a proper understanding of functional circuit microarchitecture might necessitate the recording signals beyond the neuronal soma and include subcellular structures such as dendrites and presynaptic axonal terminals, in particular when the latter ones originate in separate brain regions where the somatic activity cannot be measured directly.

Thalamocortical functional microarchitecture

There are three major types of neuronal constituents common to most micro-circuits of the brain: *intrinsic* or *local neurons* (and their dendritic and axonal processes), concerned only with local processing; *principal* or *projection neurons*, which send out long axons carrying signals to other regions; and the *input fibers* carrying signals

arriving from projection cells of other micro-circuits (Shepherd, 2004). Within these three major types of neuronal components, a much larger functional variety exists, and considerable effort has been put on classifying the different classes of interneurons, projection neurons and efferent fibers. Nowhere in the brain such variety is more evidently than in the neocortical circuit (Harris and Shepherd, 2015). Subpopulations of neurons with common structural and functional characteristics are organised radially to form six cytoarchitectonically distinguishable layers that make up the cortical column (Mountcastle, 1997). Many neuronal subtypes can be found within each layer, with inhibitory interneurons contributing to most of the diversity, whilst excitatory neurons are the most numerous (estimated at 70% –80% of the total population). Neurons from each layer have specific afferent and efferent connections with other neurons in other layers of the same column, with cortical regions and with subcortical structures.

As previously mentioned, most subcortical afferents in cortex originate from the thalamus. TC inputs are densest in layers 3 and 4, but are also prominent in layers 1 and 6. In primary sensory areas, the topographic organisation of TC inputs on the tangential (horizontal) plane is the main factor contributing to the formation of the cortical maps observed within each modality. Inputs from the LGN to V1, the ventral MGB to A1, the VP nucleus to S1 and the VL nucleus to M1 are among the ones exhibiting the ordered topography (Brandner and Redies, 1990; Essen and Zeki, 1978). However, inputs of most of the other thalamic nuclei do not follow a strict point to point organisation. What is more, there are a number of additional factors, which together with the topographic arrangement of inputs, play a role in determining how faithfully a thalamic map is inherited to cortex.

1. *Physiology of thalamic projection neurons:*

The response properties of thalamic projection neurons to physiological stimuli determine the neurons' receptive fields. It is those receptive fields which ultimately dictate the nature of the map that is inherited and transformed through the TC relay. A neuron's receptive field is the combined product of the summed inputs a neuron

receives, its synaptic chemistry and its electrophysiological properties. In primary thalamic nuclei, relay neurons receive glutamatergic input from ascending pathways (retina, inferior colliculus, spinal cord, etc.), which in itself is topographically ordered. Despite being outnumbered by corticothalamic (CT) projections, ascending inputs have a dominant, driving effect on thalamic activity thanks to the innervation of single thalamic neurons by many synapses from a small number of ascending axons (Richardson et al., 2009; Bruno and Sakmann, 2006). This causes synchronised glutamatergic release, precise temporal summation and large excitatory post-synaptic potentials (EPSPs). The result is, as electrophysiological studies in many species have shown, a faithful preservation of sensory maps in primary thalamic nuclei (Rothschild and Mizrahi, 2015; Schreiner and Winer, 2007).

2. *Axonal topology of thalamic projection neurons:*

Even when functional topography is preserved within the TC radiation, the local distribution, density, and extent of the terminal axonal arborisations in cortex might vary significantly. The arbors of individual thalamic afferents may extend over several millimetres of the cortical surface, so any given point on the cortex might be covered by the arbors of at hundreds of different thalamic neurons (Shepherd, 2004). Axonal branching can result in considerable divergence of TC projections, and single axon labelling studies have revealed that many thalamic neurons project to two or more non-contiguous cortical areas, which can result in the duplication of cortical maps (Winer and Lee, 2007) and the cortical convergence of terminals from primary and higher-order thalamus. Axonal topology also determines the laminar distributions of the terminals in cortex, which in turn dictates what post-synaptic targets the terminal boutons have access to. So, for example, inputs from primary thalamic nuclei are generally thought to arrive mainly to layers 3 and 4, where they synapse onto spiny stellate excitatory neurons (Lübke et al., 2000; Kratz and Manis, 2015; Schoonover et al., 2014). However, most of what is known about the laminar distribution of TC inputs comes from studies using bulk tracer injections, which inevitably obscured the extent and topological complexity that single axons can exhibit. Only recently, the combination of single-axon labelling and serial volumetric

tomography has started to provide new insights in the structural diversity of TC projection systems (Clascá et al., 2016).

3. *Physiology of cortical target neurons:*

TC inputs to every cortical layer can directly activate excitatory and inhibitory neurons (Harris and Shepherd, 2015; Ji et al., 2015). However, thalamic inputs constitute only a small fraction of the excitatory input that any cortical neuron receives. Instead, most inputs are of cortical origin, either from neurons within the column or from other cortical areas. So, for example, layer 2/3 (L2/3) excitatory neurons receive strong input from layer 4 (L4) and from other L2/3 neurons. Layer 5 (L5) neurons receive input from its neighbours and from all layers above it, as well as feedback input from higher order cortex (Harris and Mrsic-Flogel, 2013). Only neurons in L4 of primary cortices appear to have little intracolumnar input, although L4 of higher order cortex receives strong ascending input from L5 neurons in lower order areas. In sensory cortices, this strong intracortical connectivity, which appears to be stronger between cells with similar receptive fields (Cossell et al., 2015), is thought to play an important role in the amplification of TC signals[3] (Li et al., 2013b). This excitatory amplification, however, is strongly counteracted by the feedforward inhibition from GABAergic interneurons found in every cortical layer (particularly PV-positive), which are activated by both TC terminals and non-specific connections from local excitatory cells (Ji et al., 2015). Receptive field properties and thus feature mapping are thought to be strongly influenced by the interplay between excitation and inhibition in local cortical circuits (Liu et al., 2007; Wu et al., 2008b; Zhou et al., 2014).

4. *Dendritic topology of cortical target neurons:*

Most synaptic connections, and in particular excitatory ones, occur on the dendrites of neurons. Cortical neurons have complex and extensive dendritic arbours that vary across cell types, laminar locations and cortical areas (Stuart et al., 2017; Petreanu

[3] It has also been suggested that TC input alone can drive cortex, owing to the numerous and synchronous nature of primary TC inputs (Bruno and Sakmann, 2006).

et al., 2009). The tangential spread of a neuron's dendritic arbour determines the range of focal inputs it can sample from. So for example, stellate cells in L4, as well as many inhibitory interneurons, have a dendritic arbors as a spherical radiation that allow them to selectively or sparsely sample axonal inputs that congregate locally within the neuropil of their laminar domain (Kratz and Manis, 2015). On the other hand, the radial span of a dendritic tree determines the set of laminar inputs a neuron has access to. This is most evident with the dendrites of pyramidal neurons, which have two distinct functional domains, one at the apex and one at the base of the soma. The apical domain can be located at a considerable distance from the cell body, as in the case of L5 pyramidal cells, which have extensive dendritic arborisations in L1 (Larkum et al., 2009; Larkum, 2012). Dendrites of pyramidal neurons can generate local spikes and thus act as non-linear integrators of synaptic inputs (Jia et al., 2011; Cichon and Gan, 2015). Thus, cortical neurons can and generally receive inputs from thalamic axons terminating on layers other than where their soma is located. This is an important consideration when examining laminar transformations within a cortical column.

On the classification of thalamocortical projection systems

Thus far, this discussion has only hinted at some of the functional and structural diversity observed across TC projection neurons. A number of classification systems has been proposed to account for this diversity. Their proponents have made use of anatomical, cytochemical, electrophysiological and synaptic criteria to categorise thalamic neurons, often within a pair of classes.

Relay, non-specific and association nuclei:

One of the earliest classifications of TC projection systems, separated thalamic nuclei in relay, association and non-specific. The classification was largely based on axonal degeneration and bulk tracing studies (discussed in Guillery, 1995). Relay nuclei receive ordered pre-thalamic inputs, and projected in similarly ordered manner to primary sensory cortices. Non-specific nuclei, most of which belong to the intralaminar group, project diffusely to many cortical areas and also to striatum

(Jones and Leavitt, 1974). Association nuclei are those that receive comparatively little pre-thalamic input and project to higher-order cortical areas. The use of the term "association" to describe these nuclei has been discouraged, as it seemed to have originated from the erroneous belief that they formed associative connections with other thalamic nuclei (Guillery, 1995; Jones, 2007).

Specific and non-specific projections:

Jones (2007) grouped together all nuclei that project specifically to any cortical area —irrespectively of whether the projection is ordered— into the "specific" category. He distinguishes these from nuclei with diffuse projections (primarily intralaminar nuclei), which he called "non-specific". This distinction actually goes back to early work by Rafael Lorente de No (1938), who used Golgi stains in postnatal mice cortex to label axons, which he presumed to be of thalamic origin. He observed the same specific and non-specific patterns, in addition to a laminar distribution of specific arbours to middle layers, and non-specific to superficial layers.

Core and matrix projections:

The core and matrix theory is effectively a refinement of the specific and non-specific classification (Jones, 1998). The main addition to the theory is the identification of groups of neurons with diffuse projections to cortex outside of the intralaminar nuclei (**Fig. 1.4**). This was brought about by the use of molecular markers, in specific calcium-binding proteins, which revealed that most neurons with diffuse projections to L1 were calbindin-positive and could be found throughout the dorsal thalamus, unconstrained by nuclear borders (hence the label "matrix"). In contrast, core neurons, which project to middle layers, were only found in some nuclei, particularly primary sensory and motor. They were shown to express parvalbumin (PV) in primate thalamus, although it was later found not to be case for rodents (Cruikshank et al., 2001). In functional terms, core-type projections are thought to be the principal conduits of information whilst matrix-type projections would have a role in large-scale TC synchrony.

Figure adapted from copyrighted material. Not available in the Online dissemination version of this thesis.

Fig. 1.4: Core and matrix thalamocortical projections to sensory cortices. Diffuse (matrix) and focused (core) thalamic projections from the matrix and core compartments of (**A**) the ventral nucleus, (**B**), the medial geniculate body, and (**C**) the lateral geniculate body of the macaque monkey, also showing patterns of laminar projections. *AI*, primary auditory field; *A-I*, anterolateral field; *A-m*, anteromedial field; *D*, dorsal nuclei *M*, medial field; *mc*, magnocellular nucleus; *P-I*, posterolateral field; *P-m*, posteromedial field; *R*, rostral field; *V*; ventral nucleus; *VMb*, basal ventral medial nucleus; *VPI*, ventral posterior inferior nucleus; *VPL*, ventral posterior lateral nucleus; *VPM*, ventral posterior medial nucleus. Reprinted from Jones (2001).

Lemniscal, paralemniscal and non-lemniscal pathways:

Ascending projections in the auditory and somatosensory systems are often classified as belonging to the lemniscal pathway or not. In the auditory system, the tonotopically organised bundle of primary sensory fibres that carry ascending inputs to the central nucleus of the inferior colliculus is called the lateral lemniscus[4]. All other ascending auditory projections, which primarily target portions of the inferior colliculus other than the central nucleus, are referred to as non-lemniscal (Lee, 2015). In the somatosensory system the classification is similar, with the bundle of ascending lemniscal projections in the brain stem receiving the name of medial lemniscus. They carry somatotopic information to the ventral posterior medial nucleus of the thalamus (Mo et al., 2017). Ascending somatosensory projections outside of this pathway are referred to as paralemniscal and primarily target the thalamic posterior medial nucleus. The later parts of the auditory and somatosensory pathways, including their thalamocortical projections, keep the name of lemniscal and non-/para- lemniscal, reflecting the parallel organisation of the processing streams. This classification, however, derives primarily from the anatomical features that are present in these two modalities, but it does not apply to the visual pathway. As such,

[4] Lemniscus is the Greek word for ribbon or band.

the classification of core/matrix might be more appropriate, as it captures all the features of the lemniscal classification but also applied to the visual modality (Jones, 2001).

First and higher-order nuclei:

Sherman and Guillery (Sherman et al., 2006; Sherman and Guillery, 2013) championed the classification of thalamic nuclei in two categories: first order (FO) and higher order (HO) (**Fig. 1.5**). FO nuclei receive direct, mostly topographically ordered inputs from pre-thalamic sources like the retina, the inferior colliculus (IC), spinal cord and cerebellum. In contrast, HO nuclei receive most of their inputs in the form of CT projections. They emphasise the role of HO nuclei as a transthalamic route for corticocortical communication. This model is heavily based around the distinction between driver or class 1, and modulator or class 2 inputs (discussed below). It suggests that information carried through class 1 projections from FO thalamic nuclei, arrives to L4 of primary cortical areas where it is transformed and passed on to HO thalamic nuclei through L5 CT projections, which are also class 1. Importantly, according to this model, HO thalamic nuclei projects to middle layers of secondary cortical areas, also through class 1 projections. This classification effectively returns to the old separation between relay and association nuclei, emphasising the fact that the latter receives less pre-thalamic input. It also leaves out intralaminar nuclei and multimodal nuclei like the medial division of the medial geniculate body (MGBm), which project sparsely to many different cortical areas, as well as amygdala and striatum.

Drivers and modulators:

Sherman and Guillery (Sherman et al., 2006; Sherman and Guillery, 2013) also proposed a functional classification for excitatory projections, which applies not only to thalamocortical, but also to tectothalamic, corticothalamic and corticocortical glutamatergic pathways. Driver pathways are suggested to be the main route for information flow, while modulator pathways modify how driver inputs are processed. The distinction between class 1 inputs or "drivers" and class 2 inputs or

Figure adapted from copyrighted material. Not available in the Online dissemination version of this thesis.

Fig. 1.5: First- and higher-order nuclei of the thalamus. (**A**) Coronal sections through the thalamus of a monkey (numbered 1 through 5) showing the major thalamic nuclei. The nuclei that are filled by diagonal hatching are described as first order nuclei. AD, anterior dorsal nucleus; AM, anterior medial nucleus; AV, anterior ventral nucleus; CM, center median nucleus; CN, caudate nucleus (not a part of the thalamus); H, habenular nucleus (part of the epithalamus); IL, intralaminar (and midline) nuclei; LD, lateral dorsal nucleus; LGN, lateral geniculate nucleus; LP, lateral posterior nucleus; MD, medial dorsal nucleus; MGN, medial geniculate nucleus; PO, posterior nucleus; PU, pulvinar; TRN, thalamic reticular nucleus; VA, ventral anterior nucleus; VL, ventral lateral nucleus; VPI, VPL, and VPM, inferior, lateral, and medial parts of the ventral posterior nucleus. Reprinted from Sherman et al. (2006). (**B**) Schematic of first order (FO) and higher order (HO) thalamic relays. The first order relay receives driving afferents from ascending pathways, whereas the higher order relay receives driving afferents from cortex. Both of these driving afferents send branches to subcortical motor or premotor centers. Reprinted from Sherman et al. (2006).

"modulators" is based on criteria such as the type of glutamate-receptor the inputs act on (ionotropic or metabotropic), the synaptic release probability (high or low), the size of their evoked EPSP (large or small), the calibre of the axons (thick or thin) and the morphology of the axonal terminal arbour (dense or sparse). Most of what is known about drivers and modulators comes from studying ascending inputs to FO nuclei (driver), and CT inputs from layers 5 (driver) and 6 (modulator). There is some evidence on the existence of class 1 and class 2 TC projections, which suggests differences on what cortical neurons they target (**Fig. 1.6**). However, it is unclear how drivers and modulators differ anatomically —both in terms of thalamic nuclei distribution and cortical laminar patterns—, as well as cytochemically. Moreover, little is known about the relationship between the functional classification of driver/modulator and the core/matrix model proposed by Jones (2007).

Figure adapted from copyrighted material. Not available in the Online dissemination version of this thesis.

Fig. 1.6: Driver and modulator thalamic inputs to the different layers of somatosensory and auditory cortices. Schematic representation of projections from (**A**) the ventral posterior medial nucleus (VPM, first order) and the posterior medial nucleus (POm, higher order) to the primary somatosensory cortex, and from (**B**) the ventral medial geniculate nucleus (MGNv, first order) to the auditory cortex. The line thickness of the projections represent the percentage of cells receiving either class 1 (driver) or class 2 (modulator) inputs. Reprinted from Sherman and Guillery (2013).

Axonal morphotypes:

The complex architectures of TC projections could not be appreciated through early bulk tracing studies and only began to be described with the advent of single-axon labelling (**Fig. 1.7**). Clascá and colleagues (2012) have identified at least four major classes of morphologically distinct TC projection neurons: core-type (C-type), matrix-type (M-type) specific, matrix-type non-specific and intralaminar-type (IL-type). Their classification criteria include, besides axonal morphology, the type of calcium-binding proteins the neurons express (**Fig. 1.8**). All neuronal classes are found in most thalamic nuclei, but significantly varying proportions, and any given nucleus can be defined by the prevalence of one class. The use of viral vectors to drive the expression of fluorescent proteins in genetically identified neurons promises to enlighten our understanding of the relationship between the morphological, biochemical and synaptic properties of TC projection neurons. This would also minimise concerns about incomplete labelling when neurons are loaded with synthetic dyes.

Figure adapted from copyrighted material. Not available in the Online dissemination version of this thesis.

Fig. 1.7: Schematic of the general thalamic axonal morphotypes, represented on an idealized mammalian forebrain. The thalamic nuclei containing each cell type are indicated in abbreviations. Italicised nuclei do not have direct evidence from single-cell labeling studies, only bulk anterograde tracing data. Within each group of nuclei, identified by a particular colour, some nuclei are underlined using a second colour to indicate that their neurons consistently extend an additional collateral to a particular subcortical target structure (indicated using second colour in the diagram). Numbers indicate cortical layers. Four idealized cerebral cortex areas, labeled *a*–*d* are shown. Yellow case letters indicate selective expression of calbinin (cb) or calretinin (Cr) in some neuron types. Reprinted from Clascá et al. (2016). AM, amygdala; AV, anteroventral nucleus; Calb, calbindin; CeL, central lateral nucleus ; CeM, central medial nucleus; CM–Pf, center median–parafascicular nucleus; CMc (primate), core region of center median nucleus; DCla, dorsal claustrum; DLG (w), dorsal lateral geniculate, W or equivalent cells; DLG (x,y), dorsal lateral geniculate; X and Y cells, or equivalent cells in other species; IAM, interanteromedial nucleus; LD, laterodorsal nucleus; LPL, lateral posterolateral nucleus; LPm, lateral posteromedial nucleus; MD, mediodorsal nucleus; MGD, medial geniculate nucleus, dorsal division; MGM, medial geniculate nucleus, medial division; MGV, medial geniculate nucleus, ventral division; Pc, paracentral nucleus; Po, posterior nucleus, rostral part; PoT, posterior nucleus, triangular part; Pt, paratenial nucleus; Pu, pulvinar complex (primates); PVA, anterior paraventricular nucleus; Re, reuniens nucleus; RPtN, reticular prethalamic nucleus; Sg, supragenicular nucleus; Spf, subparafascicularnucleus; Str, striatum; VA, ventral anterior nucleus; VL, ventral lateral nucleus; VM, ventromedial nucleus; VPM, ventroposterior medial nucleus; VPL, ventroposterior lateral nucleus.

Which classification system to use? Whilst there is a large amount of overlap across classification systems, an overarching theory that accounts for anatomical, biochemi-

cal, synaptic and hodological (connectivity-based) differences is still missing. Most theories present an oversimplistic bimodal categorisation, which appears at odds with the diversity revealed by single-axon labelling. This is undoubtedly due to the methodological difficulties for acquiring both anatomical and functional information about TC projections. What is more, most of the functional evidence for these theories comes from *in vitro* studies, and much is unclear about their functional relevance *in vivo*. The existence of so many classification systems for thalamocortical projections can often lead to confusion, particularly when trying to establish equivalence between classes. The anatomical classifications of core/matrix (Jones, 2007) and first-order/second-order (Sherman et al., 2006; Sherman and Guillery, 2013) are useful when considering one-to-one projections from specific thalamic subnuclei to specific cortical subfields. However, as recent anatomical studies suggest (Clascá et al., 2016), thalamic neurons in all nuclei often exhibit branching axons that can have different projection patterns depending on the area they target. As such, it might be necessary to classify projections not only based on their thalamic origin, but accounting for their postsynaptic targets too, even if this requires categorising branches rather than whole projections. Ultimately, the value of any classification system is its explanatory power. Thus, the inclusion of functional criteria, on top of anatomical and cytochemical ones, is not only desirable but essential. Of all the existing classification systems, the driver and modulator model is the one that emphasises most the functional properties of the different projection types. Additionally, it provides clear and testable hypotheses that can be explored both *in vivo* and *in vitro*, as well as a theoretical framework to describe functional pathways beyond the thalamocortical projection system (Guillery, 2017).

Figure adapted from copyrighted material. Not available in the Online dissemination version of this thesis.

Fig. 1.8: Schematic neuronal distribution of TC cell types throughout the thalamus. General cell-type prevalence is represented by colour dots on six coronal section diagrams of the rat thalamus. Reprinted from Clascá et al. (2012). AD, anterodorsal thalamic nucleus; AM, anteromedial thalamic nucleus; AV, anteroventral thalamic nucleus; CL, central lateral thalamic nucleus; CM, central medial thalamic nucleus; DLG, Dorsal Lateral Geniculate thalamic nucleus; IAM, interanteromedial thalamic nucleus; LD, lateral dorsal thalamic nucleus; LDDM, lateral dorsal thalamic nucleus, dorsomedial division; LDVL, lateral dorsal thalamic nucleus, ventrolateral division; LPLC, lateral posterior thalamic nucleus, caudal division; LPMC, lateral posteromedial thalamic nucleus, caudal division; LPMR, lateral posterior thalamic nucleus, rostral division; MD, mediodorsal thalamic nucleus; MGD, medial geniculate nucleus thalamic nucleus, dorsal division; MGM, medial geniculate thalamic nucleus, medial division; MGMZ, medial geniculate thalamic nucleus, marginal zone; MGV, medial geniculate thalamic nucleus, ventral division; PC, paracentral thalamic nucleus; Po, posterior thalamic nucleus; PoT, posterior thalamic nucleus, triangular division; PT, paratenial thalamic nucleus; PvA, Anterio paraventricular thalamic nucleus; Re, reuniens thalamic nucleus; Rt, reticular (pre)thalamic nucleus; SG, suprageniculate thalamic nucleus; SPFPC, Subparascicular thalamic nucleud, parvocellular part; Sub, submedius thalamic nucleus; VA, ventral anterior thalamic nucleus; VL, ventral lateral thalamic nucleus; VM, ventromedial thalamic nucleus; VPL, ventroposterior lateral thalamic nucleus; VPM, ventroposterior medial thalamic nucleus; VPPC, parvocelular ventroposterior medial nucleus.

1.3 Auditory thalamocortical relations

Studying thalamocortical circuits in the auditory system

Many functional and structural features of TC circuits have been shown to be common to all studied pathways and preserved across species. This has given rise to the idea of a canonical microcircuit underlying a general computational strategy for processing multiple types of information in cortex and thalamus (Harris and Shepherd, 2015; Sherman and Guillery, 2013). Primary sensory pathways have been preferentially chosen for the study of TC transformations, owing in part to

their mapped representation of stimulus features. By studying how the sensory map changes through the various stages of the pathway, it is possible to make some inferences about the functional organisation of the circuit. Such inferences might apply to TC organisation in general, to primary sensory areas only, or the selected modality in particular. In the least desirable case, the observation might reflect an evolutionary variation which is present only in the particular model organism studied. Thus, it is critical to take into account known differences across species and cortical areas, not only for interpreting experimental findings but also for choosing a suitable model for the experimental question being researched.

Even when only primary sensory areas are considered, there is a considerable degree of variability in the functional microarchitecture of TC circuits. In the chapters that follow, I explore a number of questions about the functional distribution of TC inputs from the medial geniculate body (MGB) to the auditory cortex, using the mouse as a model organism. Naturally, the conclusions drawn from this research will be, foremost, indicative of TC relations in the auditory system. Thus, it is important to briefly discuss the suitability of the mouse as a model organism for the study of TC organisation in the auditory pathway. Here, the availability of genetic tools is often presented as a good reason to use mice in neuronal circuit research. Whilst this is an undeniable advantage, it could, if nothing else is considered, lead to the fallacy of choosing an experimental question based on the availability of a method more than on its scientific value. Thus, I would like to briefly discuss some additional reasons that make the mouse auditory modality, a good choice to study TC interactions.

The merits of hearing

There is no known vertebrate species which lacks the sense hearing (Fay, 1989). Various species of moles and other rodents living underground, as well as fish living in turbid waters, are totally or nearly totally blind. Somatosensation varies widely across the mammalian lineage, for example, in the presence of highly specialised structures such as vibrissae, found in most mammals but absent in primates. Many

animals, including humans, have a very limited sense of smell. Yet, there is no such a thing as a naturally deaf vertebrate.

In mammals, all species studied to this day have been found to have an ascending neuronal pathway from the cochlea to the neocortex in which the cochleotopic representation of sound frequencies is topographically preserved through all stages of processing up to A1 (Kaas, 2011). The organisation of the MGB and its subdivisions is relatively constant across different mammalian lineages (Butler, 2009). Whilst much species variability exists in the organisation of secondary auditory cortical areas (Kaas, 2011), the overall size of auditory cortex relative to total cortical area is more constant than for the visual and somatosensory modalities[5] **(Fig. 1.9)** (Krubitzer, 2007). In contrast, the organisation of the visual thalamus and in particular its higher-order nuclei such as the pulvinar, as well as the visual cortical areas, have become dramatically more complex and numerous throughout mammalian evolution, particularly in carnivores and primates (Kaas, 1995; Butler, 2009). Likewise, the somatosensensory thalamus and cortex exhibit great diversity across mammalian taxa, owing to variations in the distribution of somatosensensory receptors and the presence of specialised structures, such as whiskers or electroreceptors (Kaas, 2009).

Gross anatomical comparisons, however, do not necessarily imply a similar degree of conservation at the circuit level. In rodents, the organisation of cortical maps appears to be highly heterogeneous at the small scale, including in primary visual, auditory and somatosensory cortices. Orientation columns in V1 for example, which in carnivores and primates show a very smooth organisation, are completely absent in rodents where a scattered "salt and pepper" organisation is present instead. Evidently, this complicates the use of orientation features to study TC transformations in rodents. In contrast, the mouse has been shown to have variable degrees of tonotopic organisation in primary auditory fields (Kanold et al., 2014), depending on the layer being studied (Winkowski and Kanold, 2013). Such differences are useful, for example, to study intracolumnar transformations (Linden and Schreiner, 2003) and

[5] A prominent exception to is the order Chiroptera (bats) in which auditory areas constitute a significant proportion of the cortical surface (Kaas, 2011).

the differences in coding strategies of subpopulations of cortical neurons (Harris, 2015).

Figure adapted from copyrighted material. Not available in the Online dissemination version of this thesis.

Fig. 1.9: Evolution of common cortical sensory areas across major groups of mammals. Evolutionary tree of the brains of various mammalian species based on cladistic analysis, showing the relative change on brain size and the size of cortical sensory areas. Reprinted from Krubitzer (2007).

Besides its potential suitability for understanding TC relations in general, studying auditory TC micro-architecture in the mouse can provide valuable insights towards our understanding of auditory cortical function. As it will be discussed in detail next, ascending TC projections are essential contributors to spectral integration by auditory cortical neurons. Their topographic distribution underlies the formation of tonotopic maps in primary auditory fields, whilst in non-tonotopic fields, it suggests the existence of maps of more complex stimulus features, still to be characterised (Schreiner and Winer, 2007). Indeed, there is much to be said about the functional and anatomical organisation of auditory TC circuits. However, just before discussing the functional micro-architecture of auditory cortex and thalamus it would be useful

to provide a short description of the stages of auditory processing that precede the thalamocortical projection.

The ascending auditory pathway of mammals

Acoustic information is carried by pressure variations in the air (sound waves) which reach the peripheral auditory system. Whilst travelling through the outer, middle and inner ear the nature of these signals remains the same: mechanical vibrations of the molecules that make up the media (air, cartilaginous tissue, bones, liquid). It is only until these vibrations reach the *cochlea* in the inner ear that they are transduced into the neural signals that will travel up the auditory pathway. Thus, this brief journey through the auditory system stars here, in the cochlea.

The cochlea:

The cochlea is a coiled, tube-like structure that is found deep within each temporal bone. It contains a sensory epithelium, the basilar membrane, composed of specialised cells, the hair cells, which can convert vibrations travelling through the cochlear fluid into electrochemical signals. Whilst much is known about the mechanisms of auditory transduction in the cochlea, one aspect of this process is of particular relevance for the work described in the following chapters. The basilar membrane can separate out the frequency components of a sound thanks to gradual variations on its width and thickness along its longitudinal axes. This results on different portions of the membrane exhibiting different resonant frequencies, with the base of the membrane being more responsive to high frequencies and the apex to low frequencies. Thus, hair cells at a particular location along the basilar membrane will also exhibit frequency selectivity resulting on a tonotopically ordered cochlear output. The spatial relationship of these frequency selectivities is preserved in the cochlear nerve and throughout the tonotopically organised streams of the auditory pathway.

The auditory nerve and cochlear nucleus:

Hair cells form synapses with auditory nerve fibres in the cochlea. The auditory nerve, sometimes called cochlear nerve, is composed of the projections of sensory bipolar neurons whose cell bodies are located in the spiral ganglion within the cochlea. The auditory nerve axons bifurcate and project to neurons in the dorsal and ventral cochlear nucleus (DCN and VCN). The DCN projects to the inferior colliculus via the lateral lemniscus, while the VCN projects to the superior olivary complex.

The superior olivary complex:

Neurons in the superior olivary complex (SOC) receive inputs from neurons of the cochlear nucleus of both sides of the brain stem. This allows SOC neurons to compute the spatial location of sounds. For this computation, one portion of the SOC uses time differences in the arrival of inputs from the two ears. The other portion uses differences in the sound levels detected by the two ears, delivered in the form of differences in firing rates.

The nuclei of the lateral lemniscus:

Whilst most ascending fibres from the cochlear nucleus and the superior olivary complex directly target the inferior colliculus, some fibres synapse onto neurons located halfway between these two stages, in the nuclei of the lateral lemniscus. The ventral nucleus of the lateral lemniscus is part of the sound identification stream whilst the dorsal nucleus is part of the stream for sound localisation. The nuclei of the lateral lemniscus form inhibitory connections with the ipsilateral and contralateral inferior colliculus.

The inferior colliculus:

The inferior colliculus is a central hub for ascending auditory information and the last stage of processing before the thalamus. Information on sound identity and sound localisation from ipsilateral and contralateral brain stem nuclei converge here. Neurons in the central nucleus of the inferior colliculus show a layered tonotopic arrangement. Nerve fibres from different preceding nuclei, but with the same

frequency selectivity, converge to the same isofrequency layer of this structure. A detailed description of the projections from the inferior colliculus to the medial geniculate body of the thalamus will be given in later sections.

Now we shall turn our attention to the main focus of this thesis: the auditory thalamus and cortex and the functional organisation of the projections between the two.

Early studies

The earliest studies of auditory TC connectivity made use of retrograde degeneration after lesions of the temporal lobe in cats (Monakow, 1895), monkeys (Poliak, 1932; Walker, 1937) and rats (Waller, 1934). They showed neuronal degeneration in the MGB which, by then, had already been shown to be the main target of auditory ascending projections from the brain stem (Ferrier and Turner, 1894). With more refined lesions, Waller (1934) also showed that degeneration in what we now know as the ventral MGB resulted from damage of the most granular (sensory-like) portion of the auditory cortex—what we now call A1. When the lesion was done more ventrally, the degeneration was observed mainly in what we know call the dorsal and medial divisions of MGB. This represent perhaps the first evidence of the parcellations of the auditory TC projection into lemniscal and non-lemniscal pathways.

The first anatomical studies however, provided very limited information about the functional organisation of the pathway. The seminal description of auditory cortical functional organisation came from the body of work of Rose and Woolsey in the cat (Woolsey and Walzl, 1942; Woolsey, 1964). Their studies included *in vivo* recordings from various auditory cortical subfields of potentials evoked by electrical stimulation in different parts of the MGB and the cochlea (Woolsey, 1964). This showed, for the first time, a direct functional connection between MGBv and A1 that was also tonotopically organised. Further anatomical (Andersen et al., 1980) and electrophysiological (Calford, 1983) studies in the cat, provided the

first comprehensive description of the functional parcellation of the MGB and its projections to auditory cortex.

Functional divisions of the medial geniculate body and the geniculo-cortical projection

Building on the work in the cat, and as better anterograde and retrograde tracers became available, detailed anatomical descriptions of MGB projections to auditory cortex were obtained in a other species including ferret (Pallas et al., 1990), macaque (Hackett et al., 1998), marmoset (Mothe et al., 2006), gerbil (Budinger et al., 2000), guinea pig (Redies et al., 1989), rabbit (Velenovsky et al., 2003), rat (Smith et al., 2012; Donishi et al., 2006; Kimura et al., 2003) and mouse (Hackett et al., 2011). Three main divisions, present in all other species studied, exist in the MGB: the ventral (MGBv), dorsal (MGBd) and medial (MGBm) divisions (**Fig. 1.10**). Each has distinct anatomical, histochemical and physiological response properties (reviewed in Banks and Smith, 2011), as well as specific regional and laminar projection patterns to cortex (**Fig. 1.11**). There are other auditory thalamic nuclei apart from the MGB (Jones, 2007). These include the lateral part of the posterior thalamic nucleus (Pol), which is known to be tonotopically organised and similar to MGBv in its responses (Imig and Morel, 1985a; Anderson and Linden, 2011), and the auditory portion of the reticular nucleus, which is not part of the dorsal thalamus and thus not projecting to cortex. Both fall outside of the scope of this thesis and will not be discussed further.

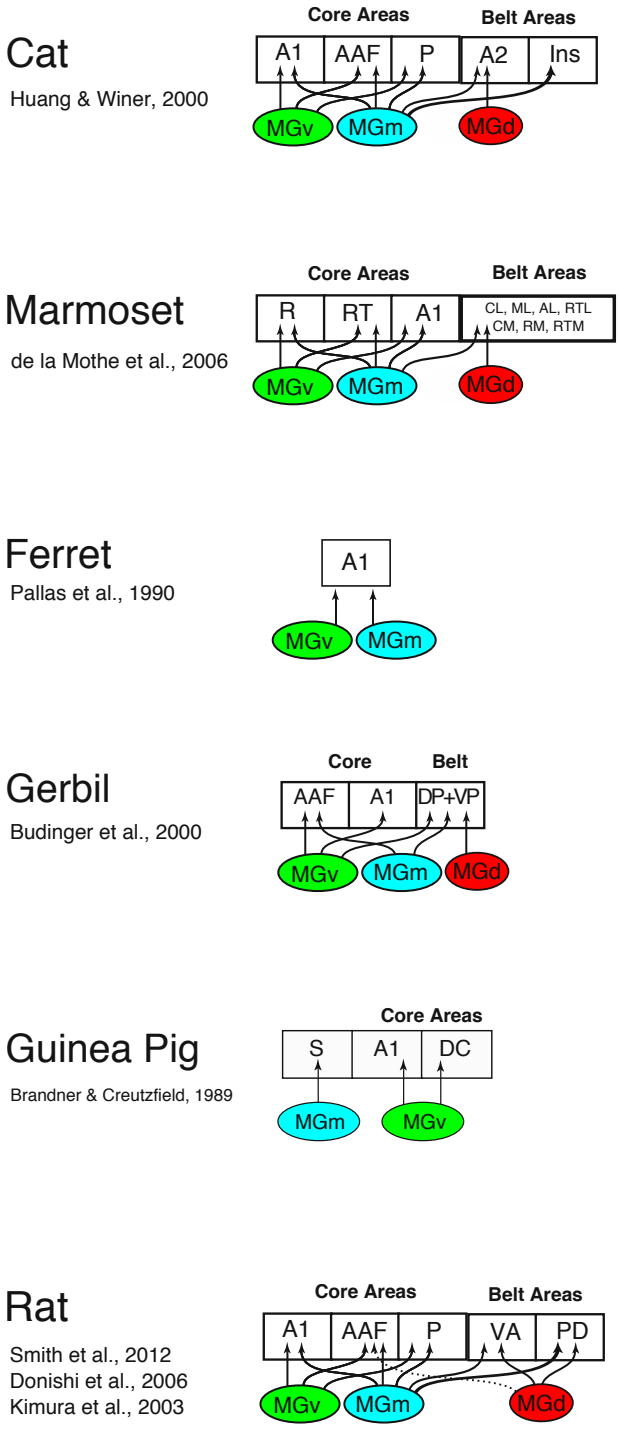

Part of the figure adapted from copyrighted material. Not available in the Online dissemination version of this thesis.

Fig. 1.10: Parallel thalamocortical projection systems from the medial geniculate body to the auditory cortex. Summary of characteristic projection patterns from the ventral, dorsal and medial division of the medial geniculate body to core and belt auditory cortical areas, in a number of mammalian species (Mothe et al., 2006; Pallas et al., 1990; Budinger et al., 2000; Brandner and Redies, 1990; Smith et al., 2012; Donishi et al., 2006; Kimura et al., 2003). Left, cortical map diagrams depicting the organisation of auditory cortex in the same species. Cortical maps (left) taken from Kaas (2011).

Ventral MGB: The ventral MGB (MGBv) is part of the tonotopically organised lemniscal pathway that projects to core auditory fields. Ascending input to MGBv comes from the tonotopically organized central nucleus of the inferior colliculus (IC) (Andersen et al., 1980; Calford, 1983). The vast majority of ascending inputs to MGBv, as well as its projections to auditory cortex can be classified as class 1 or driver, based on bouton morphology and synaptic properties (large EPSPs evoked through ionotropic glutamate receptors). MGBv also receives descending, class 2 input from from layer 6 (L6) corticothalamic projection neurons in primery auditory cortex. MGBv neurons exhibit greater fidelity in response timing and sharper frequency tuning than neurons in the non-tonotopic dorsal MGB (Anderson et al., 2007; Calford, 1983; Redies et al., 1989; Imig and Morel, 1985b). In primates, relay neurons in MGBv are immunoreactive for the calcium-binding protein parvalbumin (PV) whilst very few express calbindin (CB) or calretinin (CR). In rodents, however, virtually no cell in the MGBv expresses PV (although CB and CR are still absent), whereas in carnivores, PV is expressed only in intrinsic interneurons. TC projections from MGBv have a focal cortical distribution and are densest in L3/4 with some branches on L6. Some studies have also reported labelling in L1 after bulk tracer injections in MGBv, but single-axonal tracing studies are lacking (Clascá et al., 2016).

Dorsal MGB: The dorsal MGB (MGBd) is part of the non-lemniscal auditory pathway, which studies have been found to lack tonotopic organisation. MGBd neurons project to the belt auditory areas, i.e. those surrounding the primary auditory fields (Smith et al., 2012; Huang and Winer, 2000), with many collaterals to the amygdala (Doron and LeDoux 2000). Neurons in this nucleus are broadly tuned to frequencies, many with multi-peaked and complex receptive fields (Winer et al., 2005). Most MGBd neurons express CB and/or CR, but not PV. Ascending input to MGBd comes from the IC external nucleus (ICec) and dorsal cortex (ICdc) (Calford, 1983) and, in the mouse, it has been shown to receive non-reciprocal CT inputs from L5 of A1. Despite the lack of tonotopic organisation in the MGBd and its cortical target areas, TC projections from this nucleus are highly topographic, just as much as the projections from MGBv to the tonotopic core fields of the auditory cortex (Lee and Winer, 2005;

Schreiner and Winer, 2007), and they target most densely L3/4 and send branching collaterals to L6 and L1.

Medial MGB: The medial MGB (MGBm), like the MGBd, also lacks tonotopic organisation. For this reason, it has previously been regarded as part of the non-lemniscal pathway. However, examination of its neurons' projection patterns and response properties have revealed major differences with MGBd neurons. Thus, MGBm has been more appropriately categorised as a 'multi-sensory' projection, functionally separate from the non-lemniscal. MGBm is the smallest of the three divisions, yet the most heterogeneous in its micro-architecture (Banks and Smith, 2011). MGBm neurons can be multi-sensory, responding to both auditory, somatosensory or visual stimuli (Bordi and LeDoux, 1994). Ascending inputs to MGBm come from the IC external nucleus (ICec) and dorsal cortex (ICdc) which also contain non-tonotopic and multi-sensory responsive neurons (Wenstrup, 2005). In contrast with the ventral and dorsal divisions, MGBm neurons project widely across L1 of all auditory cortical areas (Huang and Winer, 2000; Jones, 2007). The expression of calcium binding proteins in MGBm is similar to that of MGBd. The posterior interlaminar (PI), suprageniculate (SG), and peripeduncular (PP) subnuclei all belong to the MGBm (Winer, 1984; Banks and Smith, 2011).

Figure adapted from copyrighted material. Not available in the Online dissemination version of this thesis.

Fig. 1.11: Laminar distribution of MGB thalamocortical boutons. Tracer injections in the ventral and dorsal divisions result in labelling that is concentrated in layer 3b/4 of cortex. Medial division deposits had a bi-laminar pattern on layers 1 and 5/6. Summary of the findings by Huang and Winer (2000) using bulk deposits of biotinylated dextran amines. Adapted from Winer and Lee (2007).

Synaptic organisation of thalamic inputs to auditory cortex

Few studies have gone beyond examining the laminar distributions of TC afferents in auditory cortex, to actually examine the functional connectivity of these terminals with cortical neurons. The reverse is also true: most studies that have assessed functional connectivity have done so using whole-cell patch recordings which provide little information about the laminar distribution of the inputs. This information is particularly necessary for cortical pyramidal neurons which can receive inputs anywhere on their extensive dendritic trees and integrate them differently. L4 and lower L3 of auditory cortex contain mostly small pyramidal neurons which are the main thalamorecipient subtype (Smith and Populin, 2001). This is unlike other sensory modalities where spiny stellate cells, with shorter dendrites, are predominant in L4. Incidentally, one study employed *in vitro* calcium imaging to characterise the spatial distribution of excitatory inputs onto L4 pyramidal neurons in mouse auditory cortex. Whereas intracortical inputs would target any location of the dendritic tree, MGBv inputs preferentially cluster on basal dendrites of layers 3 and 4 (Richardson et al., 2009) where they could generate larger EPSPs than inputs to more distal synapses.

Whereas TC input to both primary and secondary auditory cortex targets most densely L4, excitatory neurons in all layers have been shown to receive direct inputs from MGB (**Fig. 1.12**), a feature which has also been observed in other sensory cortices (Viaene et al., 2011a; Viaene et al., 2011b; Viaene et al., 2011c; Constantinople and Bruno, 2013; Sun et al., 2016). In primary auditory cortex of the mouse, PV-positive inhibitory interneurons in all cortical layers were shown to also be targeted by TC afferent. What is more, PV-interneurons in L4 were driven more strongly by the *in vitro* stimulation TC axons than excitatory neurons in the same layer. Also in L4, somatostatin (SOM)- and vasoactive intestinal peptide (VIP)-positive interneurons have direct innervation by thalamus. Finally, in layer 1, a large portion of a population of inhibitory interneurons, not positive for PV, SOM or VIP, was also shown to receive strong inputs from the ventral division of MGB (Ji et al., 2015).

Figure adapted from copyrighted material. Not available in the Online dissemination version of this thesis.

Fig. 1.12: Summary of known synaptic targets of thalamocortical projections. Many connections on principal neurons in the scheme are derived from work on rodent barrel and motor cortex reviewed by Harris (2015). Connections on inhibitory interneurons are derived from work on visual and auditory cortex performed by Ji et al. (2015). Figures adapted from Harris (2015) and Ji et al. (2015). CT, corticothalamic neuron; L1, layer 1 interneuron; L2 IT, layer 2 intratelencephalic neuron; L3 IT, layer 3 intratelencephalic neuron; L4 IT, layer 4 intratelencephalic neuron; L5A/B IT, layer 5A/5B intratelencephalic neuron; L6 IT, layer 6 intratelencephalic neuron; PT, pyramidal tract neuron; PV, parvalbumin-expressing interneuron; SOM, somatostatin-expressing interneuron; VIP, vasoactive intestinal peptide-expressing interneuron.

Tonotopy in the geniculo-cortical projection

Second only to the laminar cytoarchitecture common to all cortical areas, the gradual change in the preferred frequency of neurons across the cortical surface is a quintessential feature of cortical organisation in primary auditory cortex. This tonotopic map has been observed in everyone of the more than 20 mammalian species where auditory cortex has been mapped for frequency tuning. Tonotopy is the product of the spatial filtering of sound frequencies performed by the cochlea, and it is preserved through the several stages of the auditory lemniscal pathway.

Whilst there is little doubt of a tonotopically organised projection from MGB to A1, how topographically precise the inputs are relayed it is still not clear. In A1, TC projections from MGBv target isofrequency regions where they strongly drive neurons in layer 4 and lower layer 3. Electrophysiological experiments *in vivo* report an approximate point-to-point convergence of tuning preference from MGBv to A1 within one-third of an octave (Hackett et al., 2011; Imig and Morel, 1984; Winer et al., 1999). On the other hand, *in vitro* studies using an auditory TC slice preparation show that focal stimulation of MGBv causes widespread activation of the cortex over several hundred micrometers (Hackett et al., 2011; Kaur et al., 2005). Whilst modern single-axon tracing studies with fluorescent proteins have revealed

the complexity of TC axonal arbourisation patterns in cortex, they have not been carried out yet in MGB neurons (Clascá et al., 2016).

Most studies of cortical tonotopy to date have used electrophysiological methods which sparsely sample neuronal activity. This has, to a certain extent, limited our understanding of sensory representations at the fine-scale and their relationship to circuit micro-architecture. It was only until the first high-resolution imaging studies, using two-photon microscopy to map A1 of the mouse, that tonotopy could be assessed at the fine-scale (Bandyopadhyay et al., 2010; Rothschild et al., 2010). They revealed a heterogeneous functional micro-organization in frequency tuning embedded in the macroscale tonotopic map. Pairs of neurons located less than 150 μm apart on the same cortical plane would often differ in tuning preference by as much as 2-3 octaves. If this level of heterogeneity was missed for local neurons, which generate a comparatively strong electrophysiological signal, could we expect something similar of the micro-organisation of TC afferents? This question will serve as preamble for the series of experiments presented in chapters 4 of this thesis.

1.4 High-resolution imaging of thalamocortical circuits

The functional study of TC projections *in vivo* poses particular challenges for traditional neurophysiological methods. On one hand, the small size of the structures studied—thalamic axons are 1.0 μm in diameter in average and can form a synaptic bouton every 20 μm within the cortex (Braitenberg et al., 1998)—makes it necessary to have high spatial resolution, which most electrophysiological methods lack. On the other hand, the electric potentials originating from individual axons are so small and the axons so close together that electrophysiological methods must rely on

averaging the activity from hundreds of axons, as done with measuring local field potentials (LFPs) or in voltage sensitive dye imaging.

Even when neuronal activity is being recorded directly, electrophysiological recordings typically sample only a small subset of neurons (Rothschild et al., 2010). This was clearly demonstrated by the numerous findings of heterogeneous micro-organisation, revealed by two-photon microscopy, inside the macroscale cortical maps acquired through electrode recordings. Incidentally, it is this same high-resolution imaging method, two-photon calcium imaging, which offers the ideal combination of spatial and temporal resolution for the study of micro-organisation of thalamic afferents in auditory cortex. Therefore, I will briefly discuss now the principles and advantages of imaging methods to study neuronal function *in vivo*, with a focus on two-photon calcium imaging. This introductory chapter will finish by presenting the potential advantages of implementing adaptive optics methods to the study of neuronal circuit, in particular those located in deep brain regions like the thalamus. The implementation of one of such methods will be the focus of chapter 6.

Imaging neuronal activity *in vivo*

Imaging of intrinsic signals aside, using microscopy to investigate neuronal activity requires the use of reporters: molecules that converts membrane potential or its ionic correlates into an optical signal. Once such reporters are delivered to the target cells, the use of light to probe neuronal activity avoids the need for direct physical contact with the tissue. In contrast to electrophysiology, light offers exceptional spatial resolution, with some optical systems being able to resolve signals in even the smallest neuronal structures (Wilt et al., 2009; Ji et al., 2008). What is more, imaging allows the simultaneous measurement of signals from a wide range of spatial locations.

The last couple of decades brought about a surge of advances in *in vivo* imaging methods. Of all of these, two-photon laser scanning microscopy (2PLSM) has undoubtedly had the most impact on the study of neuronal circuits of the mammalian brain (**Fig.**

1.13). It allowed for high-resolution fluorescence imaging in the highly scattering brain tissue, with penetration depths of up to several hundreds of micrometers. Advances in optics were paralled by advances in chemistry and molecular biology, which propelled the development of activity reporters that were more sensitive and biologically compatible. A major breakthrough was the creation of genetically encoded calcium indicators (GECIs), protein-based reporters which are delivered as genetic constructs and expressed by the neuronal population of interest.

In recent years, two-photon calcium imaging has been extensively used to probe neural circuits *in vivo*, in a wide range of species and brain areas, including various parts of the auditory system. Notably, it has also been used to record the activity of corticocortical and thalamocortical axonal terminals in a number of cortical areas. By simultaneously recording the signals from hundreds of individual axons, one is effectively studying the activity of populations of projection neurons which might be located in brain regions inaccessible to direct observation.

Figure adapted from copyrighted material. Not available in the Online dissemination version of this thesis.

Fig. 1.13: Two-photon calcium imaging of genetically-labelled neurons A two-photon laser scanning microscope (2PLSM) can be used to monitor the activity of large populations of neurons or neuronal compartments in the living brain. Genetically-encoded calcium indicators can be used to stably label specific subpolulations of neurons. Adapted from Sadakane et al. (2015).

Reaching deeper

The main application of two-photon microscopy in neuroscience has been in the study of cortical circuits. Its average penetration depth allows for the imaging of neuronal structures down to the granular layer of the mouse cortex. Based on the same optical principles, the recently developed three-photon microscopy provides penetration depths of just over 1 mm. Nevertheless, this still limits the optical access to most subcortical structures including all thalamic nuclei.

Gaining optical access to the thalamus would bring about all the advantages that imaging methods and GECIs have already given to the study of cortical circuits. TC projections are part of a large network consisting of reciprocal projections between groups of thalamic nuclei and neocortical areas. Single thalamic divisions can project to several cortical areas, which in turn project back to multiple thalamic targets (Sherman et al., 2006). Thalamic nuclei also form bidirectional connections with the TRN, primarily in the form of colateral projections that branch from TC axons. Whilst it would be ideal to be able to study this large functional network as a whole, and to probe the micro-architecture of thalamic structures *in vivo*, the position of the thalamus makes it challenging.

Attempts to gain access to deep brain regions has precipitated the use of invasive strategies, including the macroscopic removal of overlying structures (cortex) (Dombeck et al., 2010), the insertion of fibre bundles (Szabo et al., 2014) and graded index (GRIN) lenses (Barretto et al., 2011; Resendez et al., 2016). However, where these techniques become problematic is the extent to which they damage the brain (Bocarsly et al., 2015). Under such broad impact into sensitive tissues, whether the damage is consequential for the normal behaviour of the organism and the physiology of the network remains ambiguous (Xu et al., 2007; Moshayedi et al., 2014). Nonetheless, it is an inescapable reality that were it possible to cause little or no damage then such approach would be wholly desirable as a route to new insight into intact nervous system.

Holographic optics and fibre-based microscopy

Optical aberrations grow progressively larger the deeper one attempts to image into a scattering media, such as the brain. Some adaptive optical techniques seek to correct these aberrations by applying the reverse transformation of what is being done to the light wavefront as it travels through the turbid sample. Adaptive optical relies on the principle of iterative manipulation of the wavefront: if one knows how a particular sample is supposed to look like, then one may deduce the type of deformations it has undergone after travelling trough complex media (Popoff et al., 2010). If one can reverse the transformation done to the known sample, then one can reverse the transformations done to any other sample, as long as the properties of the media do not change (**Fig. 1.14**). A range of holographic methods can be used to iteratively correct for optical aberrations (Ji, 2017), but the real difficulty lies on deducing what are the wavefront deformations occurring within individual volumes of brain without having a known sample inside it.

An alternative is to use a complex media which lacks the inhomogeneities of neuronal tissue, and that can be thoroughly analysed to achieve deterministic light propagation. Then this propagation media can be brought in close proximity to the region of interest in the brain and used as a guide for optical imaging. Multimode optical fibres (MMF) are an example of such optically complex media. Light wavefront manipulation can be used to turn these fibres, commonly used only as light guides, into imaging forming devices of their own right (Čižmár and Dholakia, 2011; Cižmár and Dholakia, 2012; Plöschner and Čižmár, 2015). The resulting MMF probes are many fold thinner than other types of microendoscopes.

To exploit this technology in the field of neuroscience and, in particular, for the optical investigation of neuronal circuits in the thalamus, I have contributed to the development of a compact and highly optimised imaging system for minimally invasive *in vivo* applications. The system uses holographic control of light propagation to perform scanning fluorescence microscopy through a single $50\,\mu$m-core multimode fibre. In the last chapter of this thesis, I present the first demonstration of this

technique applied *in vivo*, which I performed by acquiring fluorescent images and functional signals from neuronal structures located deep in the living rodent brain.

Figure adapted from copyrighted material. Not available in the Online dissemination version of this thesis.

Fig. 1.14: Holographic manipulation of light wavefront for scanning fluorescence imaging. Light travelling through scattering media can undergo aberrations. Holographic technologies, such as spatial-light modulators (SLMs), can correct for such aberrations by manipulating the incoming source of light. Adapted from Horstmeyer et al. (2015).

1.5 Thesis structure

The present work constitutes an investigation on the relationship between spectral receptive field properties of auditory TC terminals and their topographic distributions throughout the cortical surface and its layers. It is also an account of the development of a novel imaging method for the study of neuronal circuits of the thalamus (and other deep brain structures) *in vivo* and with minimal invasiveness. There will be a number of specific questions being address in this thesis, which are related to each other, but which I have divided in chapters in order to give a coherent and progressive narrative. The topics and objectives of the following chapters are as follows:

Chapter 2

A detailed description of the materials and methods used in the experiments described in the other chapters.

Chapter 3

The account of anatomical and functional imaging experiments attempting to characterise the projection patterns and spectral properties of the various thalamocortical projection channels in the mouse auditory system.

Chapter 4

This chapter pertains to the study of the tonotopic and laminar micro-organisation of thalamocortical boutons in primary auditory cortex of the mouse, mostly through axonal calcium imaging experiments.

Chapter 5

The description of experiments aimed at studying the transformations that spectral receptive fields and the tonotopic map undergo as they are transferred from the thalamocortical projection to the granular and supragranular layers of the auditory column.

Chapter 6

The description, characterisation and pilot demonstration of a novel fibre-based optical method for studying the microarchitecture of neuronal circuits in the intact brain, with particular applicability to deep brain regions.

Chapter 7

General discussion and conclusions of the thesis.

2 Materials and Methods

2.1 Two-photon calcium imaging

All experiments were approved by the local ethical review committee at the University of Oxford and licensed by the UK Home Office. The data presented in this thesis derives from fifteen female C57BL/6 (Harlan Laboratories) mice, five female C57BL/6NTac.Cdh23$^{753A>G}$ (MRC Harwell Institute, UK) mice and two female as well as one male B6(Cg)-Calb2$^{tm1(cre)Zjh}$/J ('CR-IRES-cre', Jackson Laboratories, Stock No: 010774) which were used for calcium imaging. Four female C57BL/6 (Envigo, UK) mice and one female B6(Cg)-Calb2$^{tm1(cre)Zjh}$/J were used for anatomical experiments. A further thirty-one C57BL/6 (Harlan Laboratories) mice were used during the pilot stages of the experiments.

Virus transfection

As described before (Barnstedt et al., 2015) animals aged 4–6 weeks were premedicated with intraperitoneal injections of dexamethasone (Dexadreson, 4 μmg), atropine (Atrocare, 1 μmg) and carprofen (Rimadyl, 0.15 μmg). General anesthesia was induced by an intraperitoneal injection of fentanyl (Sublimaze, 0.05 mg/kg), midazolam (Hypnovel, 5 mg/kg), and medetomidine (Domitor, 0.5 mg/kg). Mice were then placed in a stereotaxic frame (Model 900LS, David Kopf Instruments) equipped with mouth and ear bars, and located in a sterile procedure area. Depth of anaesthesia was monitored by pinching the rear foot and by observation of the respiratory pattern. Body temperature was closely monitored throughout the procedure, and kept constant at 37°C by the use of a heating mat and a DC temperature controller in conjunction with a rectal temperature probe (FHC). The skin over the injection site was shaved and an incision was made, after which a small hole of 0.5

mm diameter was drilled (Foredom K.1070, Blackstone Industries, CT, USA) into the skull with a 0.4 mm drill bit. Viral injections were done using a pulled glass pipette and a custom-made pressure injection system.

For purely axonal calcium imaging experiments, C57BL/6 and C57BL/6NTac.Cdh23$^{753A>G}$ mice were injected with approx. 200 nl of AAV1.Syn.GCaMP6m.WPRE.SV40 (Penn Vector Core), diluted 1:2 in PBS, and B6(Cg)-Calb2$^{tm1(cre)Zjh}$/J mice were injected with approx. 200 nl of AAV1.Syn.Flex.GCaMP6m.WPRE.SV40 (Penn Vector Core), diluted 1:2 in PBS, into the right auditory thalamus. For anatomical experiments, one B6(Cg)-Calb2tm1(cre)Zjh/J mouse was injected with a approx. 200 nl 1:1 mixture of AAV1.Syn.GCaMP6m.WPRE.SV40 and AAV1.CAG.Flex.tdTomato.WPRE.bGH (Penn Vector Core). The thalamic stereotaxic coordinates were 2.9 mm posterior to bregma, 2.05 mm to the right of the midline and 3.0 mm from the cortical surface.

Further anatomical experiments were carried out in C57BL/6 mice injected with very small amounts (<5 nl) of a 1:1 mixture of highly diluted (1:50000-100000 in PBS) AAV1.hSyn.Cre.WPRE.hGH (Penn Vector Core) and AAV1.CAG.Flex.eGFP.WPRE.bGH (Penn Vector Core). For these experiments the stereotaxic coordinates were altered slightly from experiment to experiment in order to selectively target different subdivisions of the auditory thalamus.

After the above-mentioned injections, the skin was then sutured and general anesthesia was reversed with an intraperitoneal injection of naloxone (1.2 mg/kg), flumazenil (Anexate, 0.5 mg/kg), and atipamezol (Antisedan, 2.5 mg/kg). Buprenorphine (Vetergesic, 1 ml/kg) and enrofloxacine (Baytril, 2 ml/kg) were injected postoperatively and again 24h later.

For dual-imaging experiments, C57BL/6 mice were first injected with approx. 200 nl of AAV1.Syn.GCaMP6m.WPRE.SV40 (Penn Vector Core), diluted 1:2 in PBS, into the right thalamus, and then with 600 nl of AAV1.Syn.NES.jRGECO1a.WPRE.SV40 (Penn Vector Core) spread across three sites on the right auditory cortex. Dual-labelling injections were carried out together with the window surgery (see below), and the location of the cortical injection sites was chosen relative to the cranial window.

Histology

In order to verify the successful transfection of neurons throughout the entire auditory thalamus and supragranular layers of primary auditory cortex, each mouse was killed at the end of the experiments and perfused transcardially, first with PBS and then with 4% paraformaldehyde in PBS. Mice used in anatomical experiments were euthanized and perfused three weeks after the virus injections. The relevant parts of the fixed brains were sectioned in the coronal plane at a thickness of 100 or 150 μm and images were taken with a Leica DMR upright fluorescence microscope or an Olympus FV1000 confocal microscope. Images were processed offline using ImageJ (NIH). Axonal reconstructions were carried out using a Leica DMR upright fluorescence microscope and Neurolucida (Microbrightfield) software.

Window surgeries

For acute terminal imaging experiments mice were premedicated with dexamethasone (4 mg/kg) and atropine (0.5 ml/kg), and general anesthesia was induced with ketamine (100 mg/kg, Vetalar) and medetomidine (140 μmg/kg). Ketamine (50 mg/kg/h) and medetomidine (0.07 mg/kg/h) were regularly topped up at 30 min intervals to maintain a stable level of anaesthesia throughout the experiment. The mouse was placed in a stereotaxic frame and body temperature was kept constant at 37°C. Both eyes were covered with eye ointment (Maxitrol, Alcon) to prevent corneal desiccation during anesthesia. A 2 cm flap of skin was cut to expose the parietal and temporal bones on the right hemisphere. The right temporalis muscle was separated from the temporal bone with a scalpel and pushed ventrally. A 4.0 mm diameter region was marked on the right hemisphere, with its center approx. 2.5 mm posterior to bregma and approx. 4.5 mm to the right of the midline. Cyanoacrylate glue (Pattex Classic, Henkel, Germany) was applied to the surrounding skull, muscle, and wound margins to prevent further bleeding. A drill fitted with a 0.4 mm bit was used to thin the marked skull region and the central island of bone was removed to expose the underlying cortex. Saline was applied continuously for a few minutes to wash away any blood from the dura that could obscure imaging. Once all the bleeding

stopped, a glass coverslip, 4.0 mm in diameter, was placed in direct contact with the surface of the cortex and attached to the edges of the skull with cyanoacrylate glue (Pattex Ultra Gel, Henkel, Germany). A small metal bar was attached to the skull over the left hemisphere with dental cement (Unifast Trad, GC Europe), which was also used to cover all exposed areas of skull. The mouse was then placed on a custom-made stage, its head fixed to the stage using the steel bar.

To implant the cranial window and head bar in preparation for chronic, awake imaging experiments, anaesthesia was induced with an intraperitoneal injection of fentanyl (Sublimaze, 0.05 mg/kg), midazolam (Hypnovel, 5 mg/kg) and medetomidine (Domitor, 0.5 mg/kg) and afterwards reversed with an intraperitoneal injection of naloxone (1.2 mg/kg), flumazenil (Anexate, 0.5 mg/kg), and atipamezol (Antisedan, 2.5 mg/kg). Buprenorphine (Vetergesic, 1 ml/kg) and enrofloxacine (Baytril, 2 ml/kg) were injected postoperatively and again 24 h later. The head bar used for these experiments had a different shape, was larger, placed nearer the window and attached to the skull using Super-Bond C&B dental acrylic. Mice were allowed to recover for at least one week before the first imaging session.

Imaging

The imaging experiments were performed 3–6 weeks after making the virus injection. For anaesthetised imaging, ketamine (50 mg/kg/h) and medetomidine (0.07 mg/kg/h) were regularly topped up at 30 min intervals to maintain a stable level of anesthesia throughout the experiment. For awake imaging, mice were placed inside a plexiglass body tube on a custom-made stage (Guo et al., 2014). All imaging took place inside a sound-attenuated chamber. A thin silicone tube coupled to an electrostatic loudspeaker (EC1, Tucker-Davis Technologies) was placed near the entrance of the mouse's left ear canal to deliver sounds during the experiment. The position of the tube was kept consistent across imaging session. The drivers were calibrated using a GRAS 40DP microphone coupled to the tube to ensure a flat ($\pm$3 dB) response at all presented frequencies (1.25 to 80 kHz). Ambient noise was kept low by keeping the laser's power supply in a separate room. Sound generated by

the resonant scanner was <40 dB SPL near the mouse's head. Stimuli were generated with an RZ6 processor (Tucker-Davis Technologies) and controlled through custom-written MATLAB (MathWorks) code.

To measure neuronal sound frequency sensitivity, I presented pure tones of 200 ms duration (with 5 ms raised cosine onset and offset ramps), which were varied randomly in frequency (from 1.25 to 80 kHz in 1/4 octave steps for purely axonal imaging; from 2.5 to 40 kHz in 1/4 octave steps for dual-colour dense imaging) and level (in 20 dB steps from 20 to 80 dB SPL for purely axonal imaging; in 20 dB steps from 40 to 80 dB SPL for purely axonal imaging; based on measurements taken at the entrance to the ear canal in a mouse cadaver). They were presented at a rate of approx. 0.66 Hz (1 every 45 frames). This rate was similar to or slower than that used in previous, comparable, in vivo two-photon imaging studies (Issa et al., 2014; Roth et al., 2016; Rothschild et al., 2010), and was chosen because the calcium signal had usually fully decayed by the onset of the next stimulus. Using an even slower rate of approx. 0.5 Hz did not change the tuning quality (data not shown). Each frequency-level combination was presented nine to ten times. These 900-1000 stimuli were presented in blocks of 300 allowing for the correction, between blocks, of any small drift in our imaging fields. Imaging was performed using a commercial two-photon laser-scanning microscope (B-Scope, ThorLabs). Excitation light (930 nm) came from a SpectraPhysics Mai-Tai eHP laser fitted with a DeepSee prechirp unit (70 fs pulse width, 80 MHz repetition rate). The beam was directed into a Conoptics modulator (laser power, as measured under the objective, varied from 10 to 50 mW) and scanned onto the brain with an 8 kHz resonant scanner (X) and a galvanometric scan mirror (Y). The resonant scanner was used in bidirectional mode, enabling the acquisition of 512 × 512 pixel frames at a rate of approx. 30 Hz. Emitted photons were guided through a 525/50 filter onto GaAsP photomultipliers (Hamamatsu). ScanImage (http://scanimage.org) was used to control the microscope. Imaging was performed with a 40×/0.80 NIR Apo immersion objective (Nikon). A motorised XYZ stage with a digital controller (ThorLabs) was used to record the coordinates of the imaged regions. Pictures of

the vasculature were taken with a CCD camera (Lumenera) attached to the B-Scope and used, together with low-zoom two-photon images, for careful re-alignment of the window coordinates across imaging sessions. Reconstructed vasculature maps of the whole window were used for alignment of the electrophysiological recordings with the imaging sites.

Electrophysiological recordings

After the final imaging session, extracellular electrophysiological cortical mapping experiments were carried out under anaesthesia (ketamine 50 mg/kg/h + medetomidine 0.07 mg/kg/h) in each of the C57BL/6NTac.Cdh23$^{753A>G}$ mice to help with the identification of primary auditory cortical areas. After removal of the glass coverslip, 64 channel (8 x 8) probes (Neuronexus) were inserted to record from the middle layers of auditory cortex. Electrophysiological data were acquired on a RZ2 BioAmp processor (Tucker-Davis Technologies), and collected and saved using Benware (https://github.com/beniamino38/benware). Stimuli were generated using a RX6 Multifunction Processor (Tucker-Davis Technologies), amplified by a TDT SA1 Stereo Amplifier (Tucker-Davis Technologies), and delivered via a modified ultrasonic dynamic loudspeaker (Vifa, Avisoft Bioacoustics) coupled to a tube that was positioned near the entrance of the mouse's left ear canal. They consisted of 200 ms pure tones spaced in one-third octave steps from 2 – 64 kHz at 40, 60 and 80 dB SPL.

Data analysis

Data analysis was performed in MATLAB. Image stacks were registered to a 50-frame average using efficient subpixel registration methods (Guizar-Sicairos et al., 2008) to correct for x–y motion. Bouton regions of interest (ROIs) were automatically extracted using a custom-written script implemented in MATLAB. Initially, each 512 × 512 pixel imaging area was parcellated into overlapping 8 × 8 pixel image patches. Next, a set of descriptors was calculated for each image patch. The descriptors used, "Histograms of Oriented Gradients" (HOG; Dalal and Triggs, 2005), were extracted

separately from each of the image patches and used as features for subsequent classification. After pre-training using manually annotated data, a support vector machine then used the HOG features of each image patch to determine whether it contained a bouton. The subset without boutons was discarded, whereas those classified as containing boutons were processed further. To draw the ROI masks for each image patch containing a bouton, a region-growing algorithm (Nixon and Aguado, 2012) was applied to each patch individually. The seed pixel for the region-growing algorithm was selected using a two-step procedure. First, a "circular Hough transform" ("imfindcircles" MATLAB function) was applied to each image patch containing a bouton and a circle was drawn around the bouton. The brightest pixel within the circle was then used as a seed. After region growing, morphological erosion (Nixon and Aguado, 2012) was applied to each image patch, enhancing separation of overlapping bouton ROI masks. Finally, image patches were recombined into a single image containing all ROI masks. ROI of neuronal somata were manually drawn using a custom-made graphic user interface in Matlab. Once defined, all pixels within each ROI were averaged to give a single time course (dF/F). For each somatic ROI, a doughnut-like region around the cell body, double the diameter of the internal ROI, was automatically drawn and all its pixels averaged to give a single time course of neuropil activity. This trace was scaled by a factor of 0.75 and substracted from the somatic ROIs fluorescence. The resulting signal was high-pass filtered at a cutoff frequency of 0.03 Hz to remove slow fluctuations in fluorescence.

The first 15 frames (approx. 500 ms) following stimulus onset were defined as the response window and a single-trial response was defined as the average dF/F within that window. ROIs were included for analysis only if they exhibited a statistically significant difference in response among the 100 frequency-level combinations (one-way ANOVA, $P < 0.001$). For each ROI, a matrix of the averaged responses to different frequency-level combinations was constructed, with different levels arranged in rows and different frequencies arranged in columns. This matrix was then smoothed across frequencies using a three point wide running average. Best

frequency (BF) was defined as the sound frequency associated with the highest response averaged across all sound levels. This measure of frequency preference is considered to produce the most orderly tonotopic maps (Hackett et al., 2011; Guo et al., 2012). In order to assess the tuning quality I fitted Gaussians to the level-averaged tuning curves. Bandwidths were the full width at half maximum (FWHM) of the level-averaged tuning curve. Co-tuning was defined as the standard deviation of a given BF distribution. The pairwise BF difference was defined as the difference in BF in octaves between two boutons in the same imaged region. To determine whether the boutons' BFs varied along a particular axis over the surface of the brain, I correlated the BFs with their position on a series of axes spanning 360° at 1° intervals. The axis associated with the strongest positive correlation was taken as the direction of the tonotopic gradient. Signal correlations were the correlation coefficients of the linearised FRA matrices for pairs of tuned ROIs within the same imaged field. FRA similarity coefficients were as signal correlations, but for pairs of ROIs within the same and across different imaged regions. For noise correlations a noise residual vector was first obtained for each ROI by subtracting its mean response to each stimuli from the corresponding single-trial responses. The noise correlations were the correlation coefficients between the vectors of pairs of ROIs. The tuning of multi-unit clusters was analyzed in a similar fashion to that of axonal boutons. The first 50 ms after stimulus onset were defined as the response window. Clusters were included for analysis only if they exhibited a statistically significant difference in response among the frequency-level combinations tested (one-way ANOVA, $P < 0.001$). The BF was defined as the sound frequency associated with the highest spike count averaged across all sound levels. Coefficients of thalamic overlap and cortical coverage for pairs of bouton ROI and neuron ROI were calculated based on the bandwidth of the main excitatory peak in the level-averaged tuning curves. Cortical coverage was the proportion of the cortical receptive field peak covered by that of the thalamic input. Thalamic overlap was the proportion of the thalamic receptive field peak overlapping that of the cortical neuron.

Statistics

Decisions on sample sizes were made on the basis of group sizes reported in published literature (e.g. Roth et al., 2016; Vasquez-Lopez et al., 2017). Depending on the normality of distributions (Shapiro–Wilk test), parametric or non-parametric tests were used. All tests used are two-sided. Data are reported as median ± interquartile range unless stated otherwise. Effect size r is defined as $r = z/(\sqrt{N})$, where z corresponds to the statistical z value and N is the sample size (Fritz et al., 2012).

2.2 Fibre-based imaging

Extensive descriptions of the fibre-based imaging setup assembled and used as part of this project are included in chapter 6.

All animal work was carried out in accordance with the Animals (Scientific Procedures) Act, 1986 (UK), and under project and personal licenses approved by the Home Office (UK). Eleven C57BL/6 (Harlan Laboratories) and eight Thy1-eGFP-M (Jackson Laboratories) mice, of both sexes, were used during the development of the *in vivo* fibre-based imaging system described in this thesis.

In vitro experiments

Cultured organotypic hippocampal brain slices ($350\,\mu\mathrm{m}$) were prepared from male Wistar rats (postnatal day 7). Slices were plated on Millicell inserts (Millipore) and incubated at 34°C and 5% CO_2 for 7-14 days prior to use. Slices were maintained in 1 mL of culture medium (50% Minimum Essential Media, 25% heat-inactivated horse serum, 23% Earl's Balanced Salt Solution, and 2% B-27 with 6.5 g/L added glucose; ThermoFisher Scientific), which was replaced every 2-3 days. Slices were imaged at room temperature in 1 mL of physiological Tyrode's solution (in mM: 120 NaCl, 2.5 KCl, 30 glucose, 2 $CaCl_2$, 1 $MgCl_2$, and 25 HEPES, with 2 ascorbic

acid and 1 Trolox added to minimize photodynamic damage; Sigma Aldrich; pH = 7.2-7.4). For structural imaging, some slices were prepared from male Wistar rats (P7) and biollistically transfected with a DsRed-expressing plasmid, closely following the protocol described by O'Brien and Lummis (2006).

For proof-of-principle dynamic imaging experiments, dentate granule neurons were loaded with fluorescent dye using whole-cell patch electrophysiology. Briefly, glass electrodes (4-8 MΩ resistance) were filled with standard internal solution (in mM: 135 K Gluconate, 10 KCl, 10 HEPES, 2 $MgCl_2$, 2 Na_2ATP and 0.4 Na_3GTP; pH = 7.2-7.4) containing 1 mM of the Ca2+ sensitive dye, Oregon Green BAPTA-1 (ThermoFisher Scientific). Cells were patched for 5-10 minutes to give adequate time for dye diffusion, after which the patch electrode was slowly retracted, enabling the plasma membrane to reseal. Structural and functional images were obtained through an optic fibre. During functional imaging, $500\,\mu$l of a high potassium Tyrode's solution (in mM: 32.5 NaCl, 90 KCl, 30 glucose, 2 $CaCl_2$, 1 $MgCl_2$, and 25 HEPES, with 2 ascorbic acid and 1 Trolox added to minimize photodynamic damage; pH = 7.2-7.4) was added to the bath to drive spontaneous neuronal activity.

In vivo imaging

Transgenic Thy1-GFP-M mice (line 007788, Jackson Laboratories) that express EGFP in sparse subsets of neurons were used for *in vivo* imaging of dendritic spines. Animals aged 4–6 weeks were premedicated with intraperitoneal injections of dexamethasone (Dexadreson, $4\,\mu$g), atropine (Atrocare, $1\,\mu$g) and carprofen (Rimadyl, $0.15\,\mu$g). General anesthesia was induced by an intraperitoneal injection of fentanyl (Sublimaze, 0.05 mg/kg), midazolam (Hypnovel, 5 mg/kg), and medetomidine (Domitor, 0.5 mg/kg). Mice were then placed in a stereotaxic frame equipped with mouth and ear bars. Depth of anesthesia was monitored by pinching the rear foot and by observation of the respiratory pattern. Body temperature was closely monitored throughout the procedure, and kept constant at 37°C by the use of a heating mat and a temperature controller in conjunction with a rectal temperature probe. Both eyes were covered with eye ointment (Maxitrol, Alcon) to prevent corneal

desiccation during the experiment. The skin over the craniotomy site was shaved and an incision was made to expose the skull, after which a small hole of 0.5 mm diameter was drilled (Foredom K.1070, Blackstone Industries, CT, USA) into the skull with a 0.4 mm drill bit. The craniotomy was centred at 1.3 mm anterior and 1.0 mm lateral to bregma. Cyanoacrylate glue (Pattex Classic, Henkel, Germany) was applied to the surrounding skull, muscle, and wound margins to prevent further bleeding. A small metal bar was attached to the skull over the left hemisphere with dental cement, which was also used to cover all exposed areas of skull.The mouse was then placed on a custom-made stage, its head fixed to the stage using the steel bar, for imaging. Subsequently, the multimode optic fibre (MMF, diameter $125\,\mu\mathrm{m}$) was gradually lowered up to $1.8\,\mathrm{mm}$ into the brain tissue targeting the dorsal striatum. At the end of the imaging session, the mouse was given an overdose of sodium pentobarbital (240 mg/kg) prior to transcardial perfusion with phosphate buffered saline (PBS) and then 4 % paraformaldehyde. The fixed brain was then extracted and section to confirm the location of the fibre tract.

For dynamic imaging, C57BL/6 mice were injected with very small amounts (<5 nl) of a 1:1 mixture of highly diluted (1:50000-100000 in PBS) AAV1.hSyn.Cre.WPRE.hGH (Penn Vector Core) and AAV1.CAG.Flex.GCaMP6m.WPRE.bGH (Penn Vector Core) into the right medial geniculate body of the thalamus. For these experiments the stereotaxic coordinates were the same as for the injections described in section 2.1. Fibre-imaging was performed 3-4 weeks after GCaMP6m viral injections. The pre-imaging surgery was like described above, but with a different anaesthetic regime: general anesthesia was induced with ketamine (100 mg/kg, Vetalar) and medetomidine (140 μmg/kg), and ketamine (50 mg/kg/h) and medetomidine (0.07 mg/kg/h) were regularly topped up at 30 min intervals to maintain a stable level of anaesthesia throughout the experiment. Sound presentation was as described in section 2.1. Stimuli were single 16 kHz pure tones of 100 milliseconds duration.

3 Auditory Thalamocortical Projection Channels in the Mouse

3.1 Auditory thalamocortical organisation: here, there and the gap in between

Our understanding of auditory thalamocortical relations has been greatly aided by advancements in anatomical and electrophysiological methods. Following the early axonal degeneration studies (Monakow, 1895; Poliak, 1932; Walker, 1937; Waller, 1934) and as better anterograde and retrograde tracers were developed, detailed anatomical descriptions started to appear. The patterns of TC input to the various subfields and laminae of auditory cortex were obtained in various primate, feline and rodent species (Huang et al., 2010; Hackett et al., 2011; Smith et al., 2012; Mothe et al., 2006; Hackett et al., 1998). The use of immunocytochemical and histochemical markers led to the identification of functional pathways, such as the core and matrix projections (Jones and Leavitt, 1974), that are spatially intermingled and thus not discernible through gross anatomical methods. On the other hand, functional studies moved from early measurements of surface evoked-potentials to recording stimulus-evoked single- and multi-unit activity in awake and anaesthetised animals. This allowed for the investigation of circuit properties that go beyond the mere topography. Gradually, the characterisation of response properties of individual cortical neurons or small groups of them led to the identification of maps of tonotopy and other acoustic features across cortical areas (Schreiner and Winer, 2007; Winer and Schreiner, 2010).

The last 20 years has brought about nothing short of a revolution in the study of neuronal circuits, thanks to the implementation of methods from genetics and molecular biology (Luo et al., 2008; Huang and Zeng, 2013). The identification of genetic markers for functionally and anatomically distinct subpopulations of neurons has allowed unprecedented precision in the monitoring and manipulation of neuronal activity and function. In turn, the house mouse *Mus musculus*, being the species for which most genetic tools are available, has quickly become a favourite model in systems neuroscience. Auditory neuroscience is no exception and a great deal of attention has been given to questions regarding the basic organisation of the mouse auditory circuits (Bandyopadhyay et al., 2010; Rothschild et al., 2010; Anderson and Linden, 2011; Hackett et al., 2011; Guo et al., 2012; Rothschild and Mizrahi, 2015; Barnstedt et al., 2015; Tsukano et al., 2017b).

Here: cortical auditory subfields in the mouse

Despite the great diversity in the organisation of auditory cortical subfields in mammals, there are a number of features that seem to be common to all species studied (Kaas, 2011). All mammals appear to have one or more tonotopically organised cortical subfield, which receives core-type thalamic inputs from the ventral division of the medial geniculate body (MGB). In the mouse, the first description of auditory cortex organisation was provided by Stiebler et al. (1997), who identified five subfields based on the topographic distribution of neuronal frequency tuning: two tonotopic regions, the anterior auditory field (**AAF**) and primary auditory cortex (**A1**); and three non-tonotopic regions, the secondary auditory field (**A2**), ultrasonic field (**UF**), and dorsoposterior field (**DP**). More recent studies, using optical imaging, proposed the existence of additional tonotopic gradients (**Fig 3.1**), including a gradient dorsal to A1 (encompassing Steblier's UF) named the dorsomedial (**DM**) field (Tsukano et al., 2015; Tsukano et al., 2017a; Tsukano et al., 2017b), a tonotopic gradient in A2 (Issa et al., 2014), and a gradient in a novel auditory subfield, isolated from the primary ones, which was named the insular auditory field (**IAF**) (Sawatari et al., 2011). An additional non-tonotopic subfield has also been proposed dorsal to AAF and named dorsoanterior (**DA**) field (Tsukano et al., 2016), although its

existence is not clearly supported by electrode mapping (Guo et al., 2012; Stiebler et al., 1997; Joachimsthaler et al., 2014).

Apart from the presence or absence of tonotopy, a few other functional differences have been reported across the various auditory subfields of the mouse. Mapping with dense electrode arrays revealed that frequency selectivity is comparable across most fields and only slightly higher in AAF (Linden et al., 2003), whilst onset latency is shortest in AAF and considerably higher in A2 (Guo et al., 2012; Joachimsthaler et al., 2014). Optical imaging studies suggest that DA exhibits characteristic responses to slow frequency-modulated (FM) sounds (Honma et al., 2013; Tsukano et al., 2015). Cytochemically, A1 and AAF show strong immunoreactivity for the calcium binding protein parvalbumin (PV), which is absent in A2. Calbindin shows the opposite distribution, with the strongest immunoreactivity in infragranular layers of A2 (Cruikshank et al., 2001). Nevertheless, the pattern of inputs from anatomically identifiable subdivisions of the MGB is arguably, alongside with tonotopy, the most defining characteristic for distinguishing auditory cortical subfields. The physiological and anatomical characterisation of such projections in the mouse is the focus of the experiments presented in this chapter.

There: thalamic auditory subnuclei in the mouse

As in all mammalian species, the MGB is the main thalamic centre for auditory information in the mouse[1]. It can be classified into three main subdivisions: the lemniscal *ventral MGB* (MGBv), which is the largest subnucleus and receives tonotopic inputs from the central nucleus of the inferior colliculus (ICcn) (Wenstrup, 2005; Lee and Sherman, 2010); the non-lemniscal *dorsal MGB* (MGBd), which receives non-tonotopic inputs from the IC external nucleus (ICec) and dorsal cortex (ICdc); and the *medial MGB* (MGBm), which receives multi-sensory inputs from the IC and is frequently grouped together with the other para-laminar nuclei, the

[1] The lateral part of the posterior thalamic nucleus (Pol) and the auditory portion of the reticular nucleus (RTN) are also auditory thalamic nuclei (Jones, 2007), separate from the MGB. They both fall outside of the scope of this thesis and will not be discussed at any length here.

Mouse

Llano & Sherman, 2008
Hacket et al., 2011
Ji et al., 2015
Tsukano et al., 2017

Fig. 3.1: Thalamocortical pathways to the auditory cortical subfields in the mouse. Projections from the mouse MGBv target the tonotopically ordered subfields A1 and AAF. Projections from MGBd target subfields DP and A2. Sparse projections from MGBm target all cortical subfields. Schematic of cortex adapted from Guo et al. (2012). The insular auditory field (IAF), which is separated from the auditory cortex proper, is not depicted, nor are subfields DM and DA (Tsukano et al., 2016), whose existence is unsupported by electrode mappings (Stiebler et al., 1997; Hackett et al., 2011). *AAF*, anterior auditory field; *DP*, dorsoposterior auditory field; *MGd*, dorsal division of the medial geniculate body; *MGm*, medial division of the medial geniculate body; *MGv*, ventral division of the medial geniculate body.

posterior intralaminar nucleus (PIN), the suprageniculate nucleus (SG) and the peripeduncular nucleus (PP).

Electrophysiological studies in the mouse have revealed at least one tonotopic gradient in the MGBv which was mirrored by a similar reversed gradient in MGBm (Hackett et al., 2011). In terms of neuronal response properties, Anderson and Linden (2011) found MGBv to have the highest spontaneous firing rate, MGBd the longest response latencies and the greatest proportion of broadly tuned neurons, and MGBm the highest response probability, which was closely matched by that of

MGBv. Hackett et al. (2011) also reported a broader FRA bandwidth in MGBm than in MGBv, although no difference was observed by Anderson and Linden (2011).

Like the auditory cortex, the MGB subdivisions of the mouse have been shown to differ in the expression of calcium binding proteins (Cruikshank et al., 2001; Lu et al., 2009). Calretinin and calbindin are both expressed throughout the MGBd and MGBm but are virtually absent in MGBv. Calretinin appears to be more common in MGBm, whilst calbindin is more common in MGBd. However, a significant proportion of neurons in both divisions express both proteins (Lu et al., 2009). These cytochemical differences, together with more detailed anatomical and electrophysiological characterisations of single neurons in the MGB of rats (Bartlett and Smith, 1999; Smith et al., 2006), have informed recently proposed classification systems for rodent TC projections (**Fig. 3.2**; Clascá et al., 2012; Clascá et al., 2016). There is, however, a lack of detailed anatomical data of TC projections in the mouse. Thus, one of the aims of the experiments presented in this chapter is to provide insights on the diversity of TC projections of the mouse MGB.

The gap in between: auditory geniculo-cortical projection pathways

The aforementioned mouse studies have, for the most part, described the organisation of the MGB subnuclei and the auditory cortical subfields separately. As discussed in chapter 1, every cortical area is a target of and projects to one or more nuclei of the thalamus (**Fig. 1.2**). Most of what is known about the organisation of the thalamic inputs to the individual auditory subfields of the mouse comes from studies aimed at characterising their topographic distribution. The topography of projections from MGBv to A1 and AAF was studied in great detail by Hackett et al. (2011), using a combination of *in vivo* electrophysiology and *in vitro* bulk imaging with voltage-sensitive dyes (VSD). Tracing studies showed that A1 and AAF receive input primarily from MGBv (Llano and Sherman, 2008), possibly from separate tonotopic compartments (Horie et al., 2013). In contrast, A2 and DP receive input primarily from MGBd (Llano and Sherman, 2008). A further two distinct tonotopic compartments have been suggested in MGBv, one projecting to IAF (Takemoto et al.,

Fig. 3.2: Thalamocortical projection types in the rodent MGB. Schematic of the distribution of TC projection neuron types in the rodent medial geniculate body and their typical axon morphology, as proposed by Clascá et al. (2012). *ACx*, auditory cortex; *CB+*, calbindin positive; *CR+*, calretinin positive; *MGBd*, dorsal division of the medial geniculate body; *MGBm*, medial division of the medial geniculate body; *MGBv*, ventral division of the medial geniculate body; *TRN*, thalamic reticular nucleus.

2014) and one to DM (Tsukano et al., 2017a). Anatomical tracing in the mouse by Hackett et al. (2011) did not show topographically ordered inputs from MGBm to cortex, although the same study reported a tonotopic gradient within MGBm that mirrors that of MGBv.

Single axon-labelling studies—also discussed in chapter 1 (**Fig. 1.7**)—have revealed a considerable amount of diversity in the cortical projection patterns of individual neurons from various nuclei of the rodent and primate thalamus (Clascá et al., 2012; Clascá et al., 2016). Such studies, however, have not been carried out in the mouse MGB. Thus, all of what we know about the auditory TC projection patterns of this species comes from bulk tracer studies, which cannot resolve the complexity of the axonal arbours. What is more, reports of the bulk laminar distribution of TC inputs

in the mouse have only been done for projections originating in MGBv and MGBd (Llano and Sherman, 2008; Ji et al., 2015). Axonal complexity also complicates the interpretation of the few studies which have attempted to directly measure the response properties of TC afferents by low resolution methods like VSD imaging (Hackett et al., 2011) or local-field potential (LFP) recordings (Intskirveli et al., 2016).

In this chapter, I present the results from a series of experiments designed to unveil, through high-resolution imaging methods, the anatomical and functional differences in the medial geniculo-cortical projection pathways of the mouse. I use a combination of sparse fluorescent labelling of MGB projection neurons for anatomical tracing and two-photon calcium imaging of thalamic axons in cortex for the characterisation of response properties of TC inputs *in vivo*.

3.2 Anatomical characterisation of MGB projections in the mouse

Projections labelled through non-lemniscal markers target mostly secondary auditory fields

To better understand the contributions of the lemniscal, non-lemniscal and paralaminar subnuclei to the thalamocortical projection of the mouse, I carried out a number of mostly anatomical experiments. As discussed previously, calretinin (CR) has been identified as a useful marker for distinguishing between different parts of the thalamus in the mouse. Among the MGB subdivisions, only neurons in the MGBd, MGBm and the para-laminar nuclei SG, PIN and PP, but not in the MGBv, contain CR (Lu et al., 2009). With this in mind, I injected a mixture of viruses driving the cre-dependent expression of a red fluorescent protein and the non-cre dependent expression of a green fluorescent protein into the auditory thalamus of CR-IRES-cre mice (Taniguchi et al., 2011), which express *cre* recombinase only in CR+ neurons. While green labelled neurons were found throughout the auditory thalamus, red labelled neurons were found exclusively outside of the MGBv (**Fig. 3.3**), which confirmed that the CR-IRES-cre line is suitable for targeting the non-lemniscal and para-laminar nuclei of the auditory thalamus. Input to the cortex from the neurons in these nuclei is restricted mostly to secondary auditory subfields, particularly the ventrally located subfield A2 (**Fig. 3.4**).

Closer examination of laminar labelling patterns revealed that the very few CR-positive axons in primary auditory cortical subfields were restricted mostly to layer 1 and that the even fewer axons in the middle layers were located primarily below the main thalamic input, which was CR-negative (**Fig. 3.5**). Projections to regions outside the auditory cortex were found mostly in the amygdala and striatum.

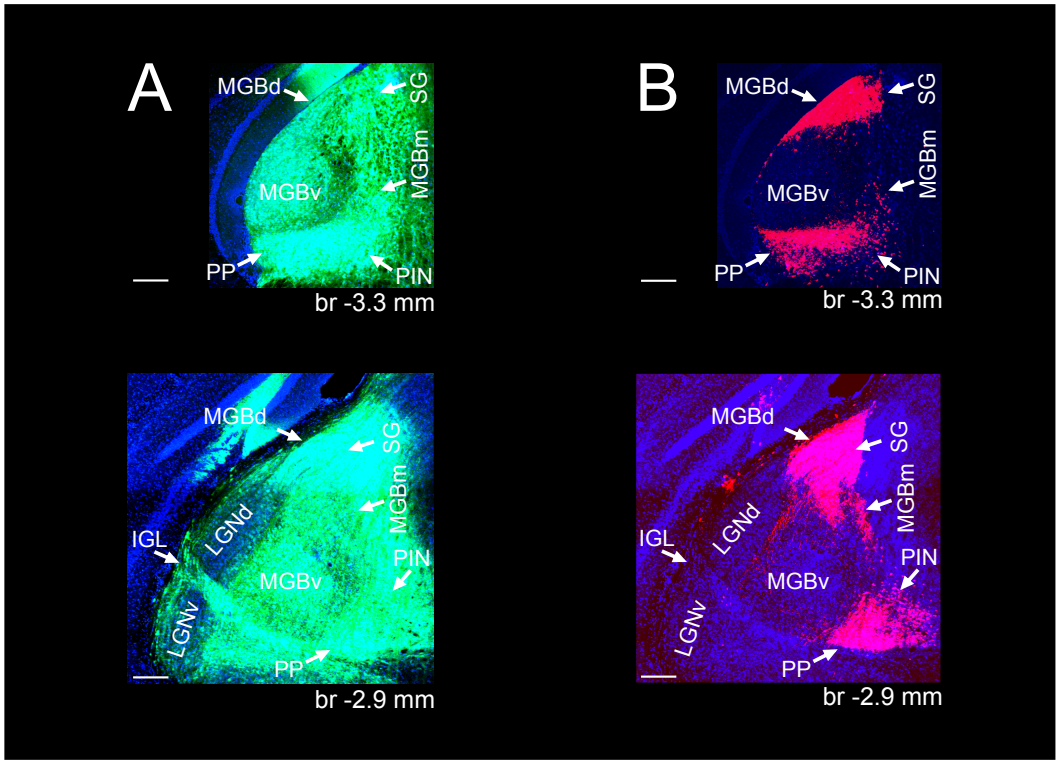

Fig. 3.3: Selective labelling of non-lemniscal and para-laminar nuclei of the mouse MGB. Coronal sections of the medial geniculate body of a CR-IRES-cre mouse injected with AAV1.Syn.GCaMP6m.WPRE.SV40 and AAV1.CAG.Flex.tdTomato.WPRE.bGH. Left panels show GCaMP6m labelled neurons throughout the whole auditory thalamus. Right panel shows tdTomato labelled neurons exclusively in non-lemniscal and paralaminar nuclei. Scale bars: 200 μm. Locations of thalamic subdivisions adopted from Lu et al. (2009). *MGBd*, dorsal division of medial geniculate body; *MGBm*, medial division of medial geniculate body; *MGBv*, ventral division of medial geniculate body; *SG*, suprageniculate nucleus; *PIN*, posterior intralaminar nucleus; *PP*, peripeduncular nucleus; *LGNd*, dorsal division of lateral geniculate nucleus; *LGNv*, ventral division of lateral geniculate nucleus; *IGL*, intergeniculate leaf; *br*, distance from bregma; *CR+*, calretinin-positive.

Sparse labelling of MGB projection neurons

To better resolve the organization of thalamic axons in the auditory cortex, I performed minute injections of a mixture of highly diluted cre-expressing and cre-dependent eGFP-expressing viruses in different parts of the auditory thalamus of C57BL/6 mice. This approach (Chen et al., 2013; Xu and Sudhof, 2013) results in the transfection of small and sparse numbers of neurons (12-53) and allowed me to obtain a clearer view of the projection patterns from individual MGB subnuclei.

Projections from the MGBv to primary auditory cortical areas are several orders of magnitudes more extensive than the projections from other thalamic nuclei, both in

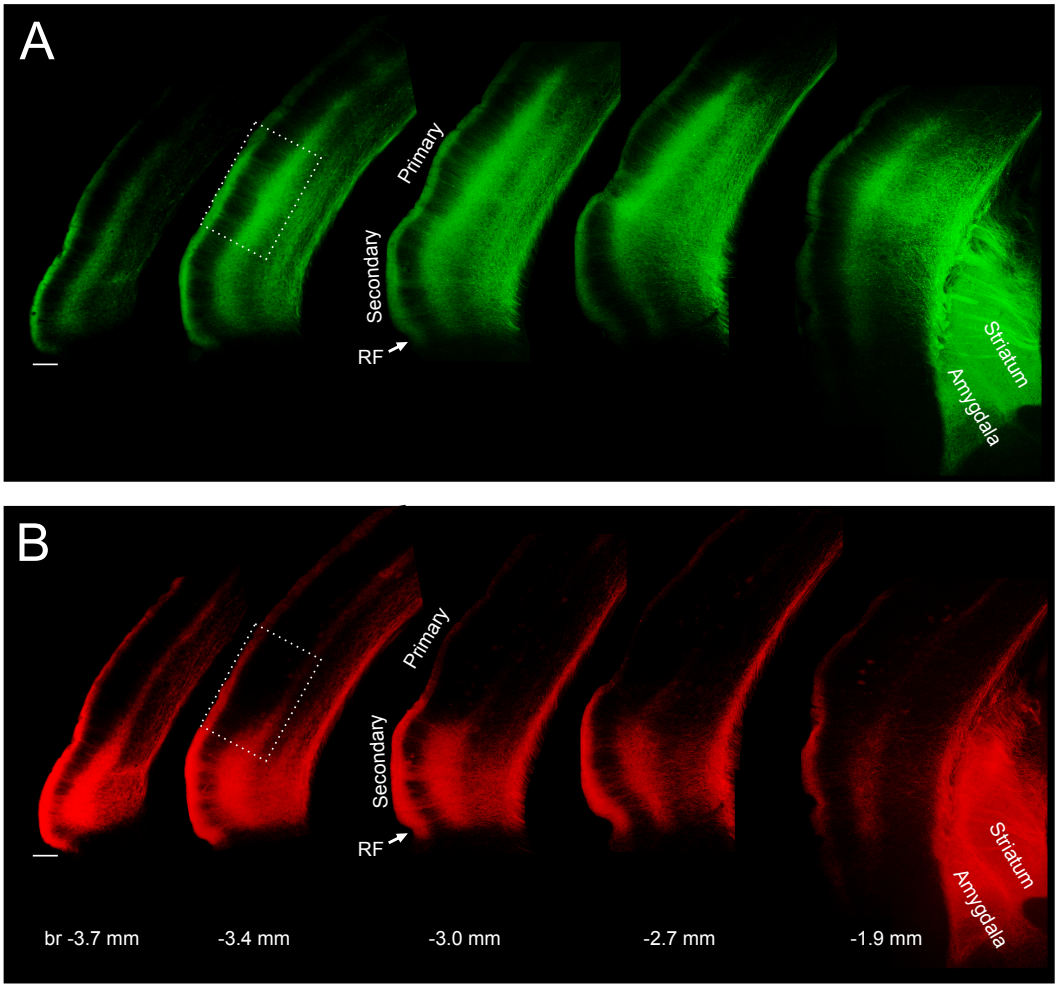

Fig. 3.4: Projection patterns of lemniscal, non-lemniscal and para-laminar nuclei of the mouse MGB. Coronal sections showing thalamic projection patterns in auditory cortex, striatum and amygdala in a CR-IRES-cre mouse injected with AAV1.Syn.GCaMP6m.WPRE.SV40 and AAV1.CAG.Flex.tdTomato in the medial geniculate body.WPRE.bGH (same as **Fig. 3.3**). Top, sections showing GCaMP6m (green) labelled thalamic axons (from all MGB nuclei) in auditory cortex, amygdala and striatum. Bottom, sections showing tdTomato (red) labelled thalamic axons almost exclusively in secondary auditory cortex, amygdala and striatum. Scale bars: 200 μm. Locations of auditory cortical regions adopted from Tsukano et al. (2016). *br*, distance from bregma; *RF*, rhinal fissure.

L1 and in the middle layers (**Fig. 3.6**). Closer inspection of the MGBv axons also revealed that they tend to travel from the middle layers to L1 in a columnar fashion, that is, in an almost straight line (**Fig. 3.6**, inset).

From the nuclei in the medial part of the auditory thalamus, which can be classified as polysensory (Anderson et al., 2009), MGBm and PIN provide only extremely sparse input to auditory cortex (**Fig. 3.7**). This input primarily terminates in L1, and otherwise is located below the middle layer(s) where input from the MGBv

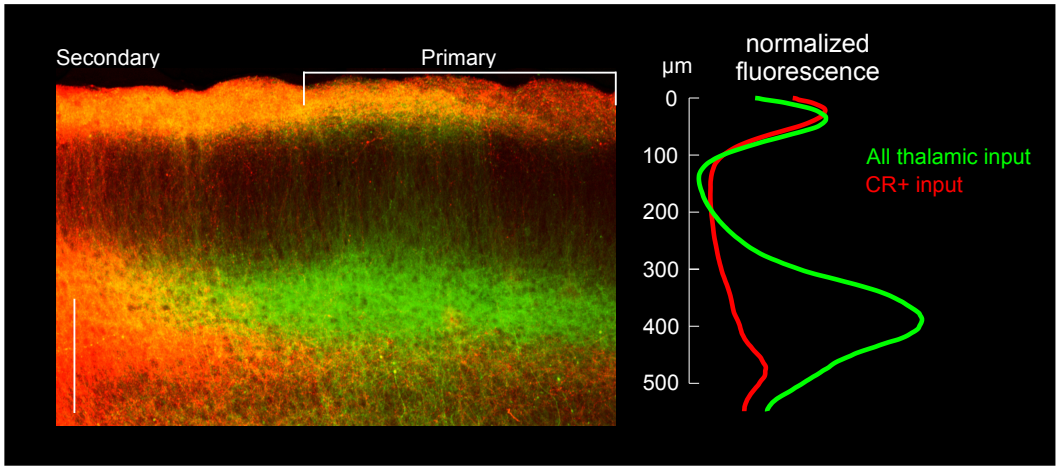

Fig. 3.5: Laminar distribution of projections from lemniscal, non-lemniscal and paralaminar MGB nuclei in the auditory cortex of the mouse Left, overlay of GCaMP6m (all thalamic input) and tdTomato (CR+ input) labelled axons in transition area from secondary to primary auditory cortex indicated by white rectangle in **Fig. 3.4**. Right, cortical depth profile of labelling from non-lemniscal thalamic axons (red, CR+) versus all thalamic axons (green) within primary auditory cortex. Profiles are the average of the fluorescence signal in the zone delineated by white horizontal bracket in right panel (N = 1). The red and green lines were normalized to have same peak height in layer 1. Scale bar: 200 μm. *CR+*, calretinin-positive.

is densest. Whilst the number of labelled neurons by the injection in MGBm and PIN (Fig. 3.7) was smaller than in the MGBv injection described above (Fig. 3.6), even sparser MGBv injections (e.g. Fig. 4.12) resulted in more labelling in primary primary auditory cortical areas, particularly in middle layers, than that seen in Fig. 3.7. Projections from the PP were found not to enter the auditory cortex and instead remain subcortical where they target amygdala, striatum and midbrain (**Fig. 3.8**). Whether these axons also send collaterals to cortical areas other than the auditory cortex, as M-type projections often do (Clascá et al., 2016), was not examined.

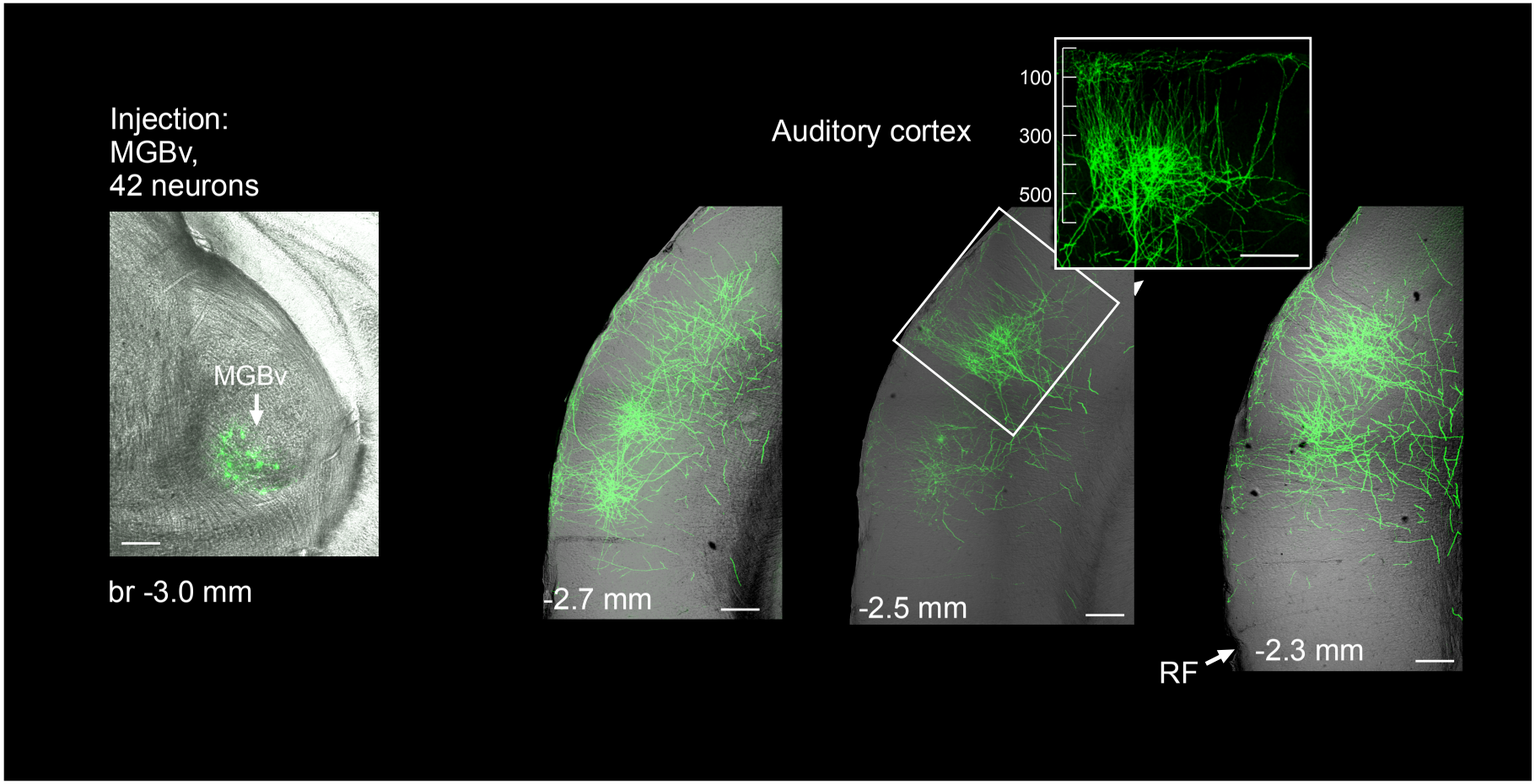

Fig. 3.6: The ventral MGB provides the most substantial thalamic input to primary auditory cortex of the mouse. eGFP labelled neurons following an injection of AAV1.CAG.Flex.eGFP.WPRE.bGH and highly diluted AAV1.hSyn.Cre.WPRE.hGH in MGBv. Inset shows projections travelling from the middle layers to L1 in columnar fashion. Scale bar: 200 μm. *br*, distance from bregma; *MGBv*, ventral division of the medial geniculate body; *RF*, rhinal fissure.

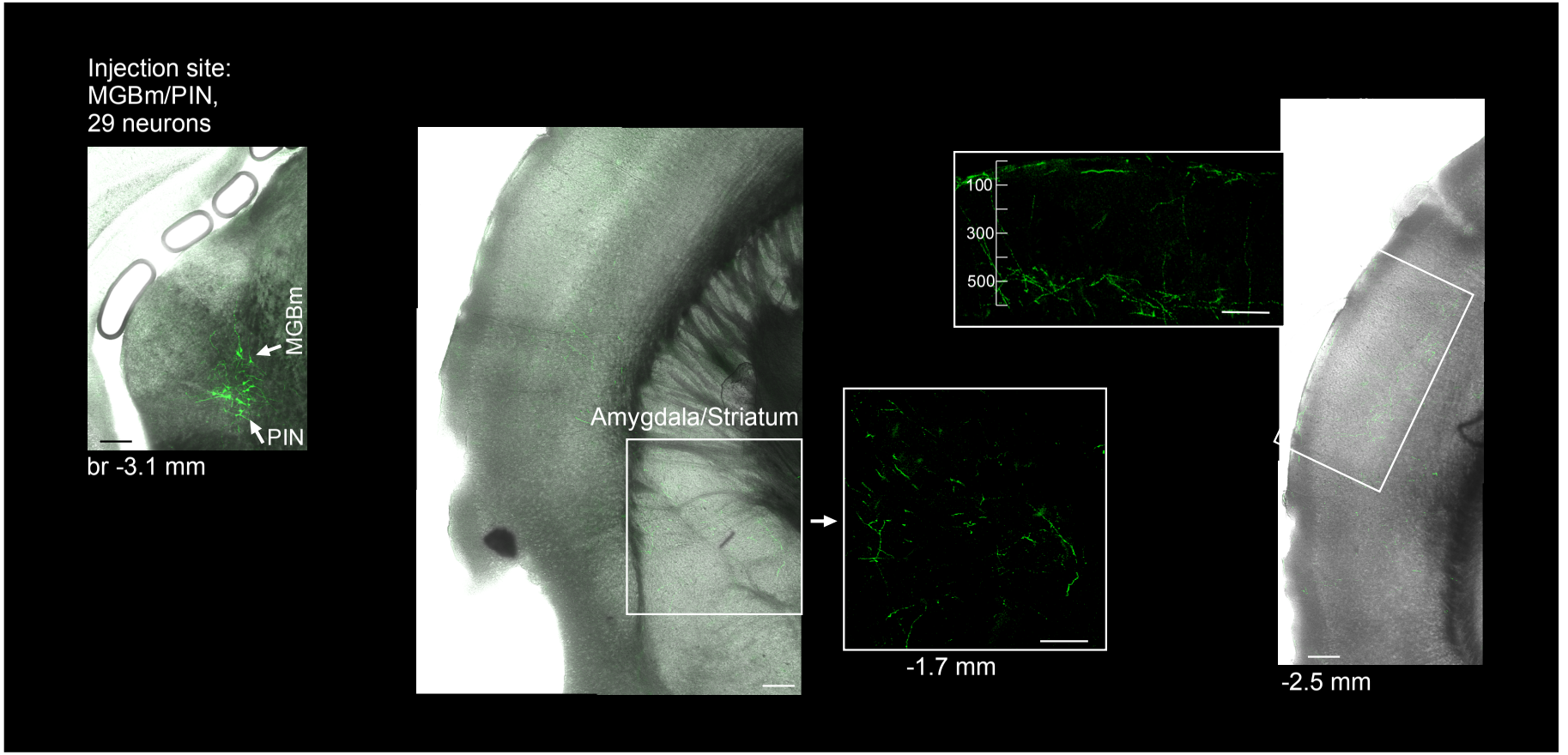

Fig. 3.7: MGBm provides very sparse input to auditory cortex concentrated in L1 and subgranular layers. eGFP labelled neurons following an injection of AAV1.CAG.Flex.eGFP.WPRE.bGH and highly diluted AAV1.hSyn.Cre.WPRE.hGH in MGBm and PIN (both para-laminar polysensory nuclei). Projections were found sparsely in L1 and L5-6 of cortex and in the striatum and amygdala. Scale bar: 200 μm. *br*, distance from bregma; *MGBm*, medial division of the medial geniculate body; *PIN*, posterior intralaminar nucleus.

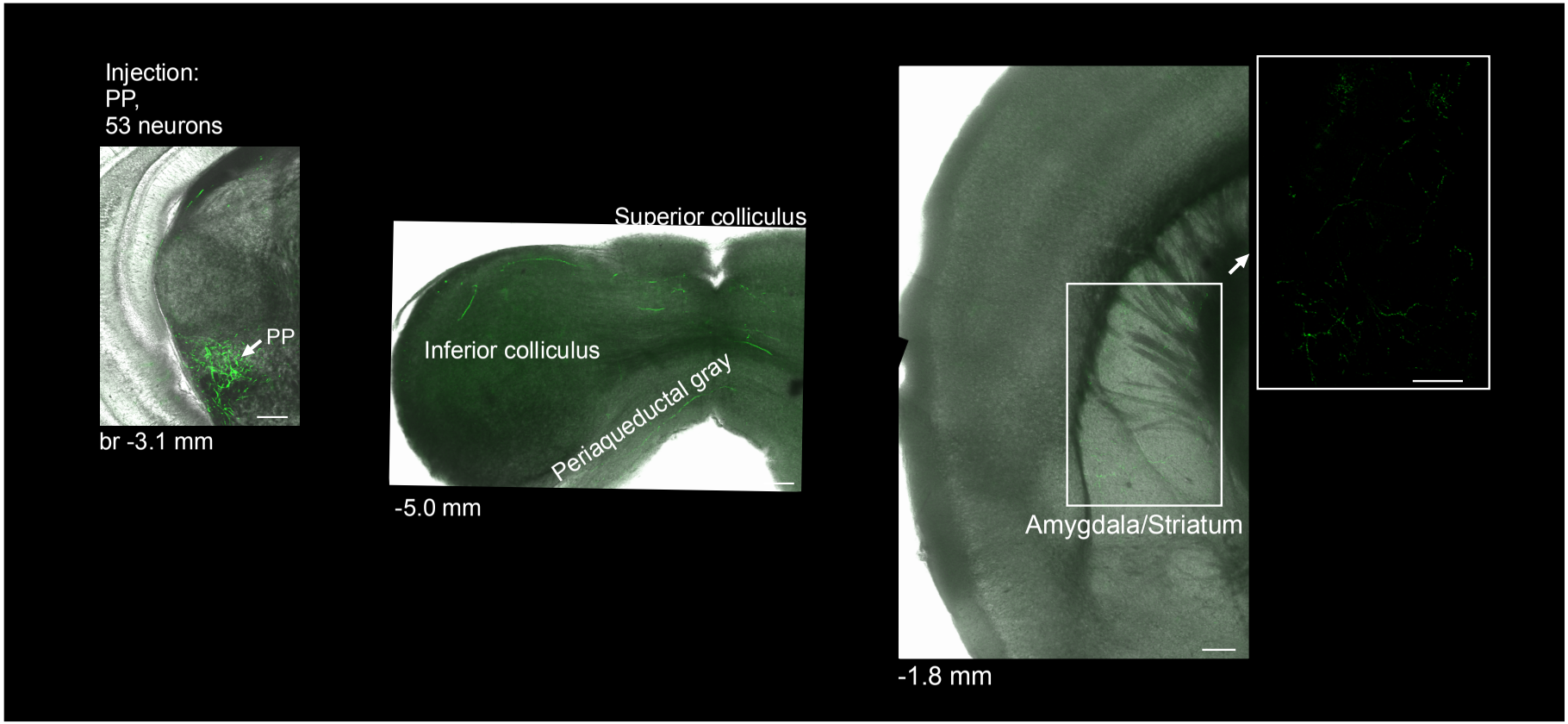

Fig. 3.8: The para-laminar peripeduncular nucleus does not send projections to auditory cortex in the mouse. eGFP labelled neurons after an injection in the peripeduncular nucleus (PP). Projections were absent from auditory cortex and found mostly in amygdala, striatum and midbrain. Scale bar: 200 μm. *br*, distance from bregma; *PP*, peripeduncular nucleus.

3.3 Physiological characterisation of MGB projections in the mouse

Labelling MGB projections to auditory cortex for functional imaging

I used *in vivo* two-photon (Denk et al., 1990) axonal calcium imaging (Petreanu et al., 2012; Glickfeld et al., 2013; Roth et al., 2016) to characterise the response properties of MGB projections to the various subfields of the mouse auditory cortex. The experiments described here were performed primarily on the C57BL/6NTac.Cdh23$^{753A>G}$ mouse line (n = 5 mice), and on a few CR-IRES-cre (Taniguchi et al., 2011) mice (n = 3). In C57BL/6NTac.Cdh23$^{753A>G}$ mice, the Cdh23^{ahl} allele that otherwise predisposes this strain to age-related high frequency hearing loss has been corrected (Mianné et al., 2016). Some differences between this corrected line and the common C57BL/6J line will be discussed in chapter 4.

In order to image the activity of thalamic afferents in auditory cortex, I labelled thalamic projection neurons with the genetically calcium indicator GCaMP6m (Chen et al., 2013) by means of a viral injection in the MGB (**Fig. 3.9-A**) and implanted a chronic cranial window over the right auditory cortex. The experiments were designed to characterize the full extent of the auditory thalamic input available to auditory cortex, so large viral injections were made in the MGB to label all its divisions (**Fig. 3.9-B**). Most of the thalamic axons were found in the middle cortical layers, L3b/4, although substantial input was also observed in L1 (**Fig. 3.9-C**).

Imaging started 3-4 weeks after the viral injections, which allowed for appropriate GCaMP6 expression in TC axons (**Fig. 3.10-A**). In awake, head-fixed mice, I measured calcium transients, which correlate with somatic spiking activity (Petreanu et al., 2012), in individual putative synaptic boutons of thalamocortical axons during the presentation of pure tones (**Fig. 3.10-B-D**). This allowed me to characterise their frequency sensitivity and frequency response area (**Fig. 3.10-E-F**). For each cortical location imaged, an attempt was made to always image from at least two

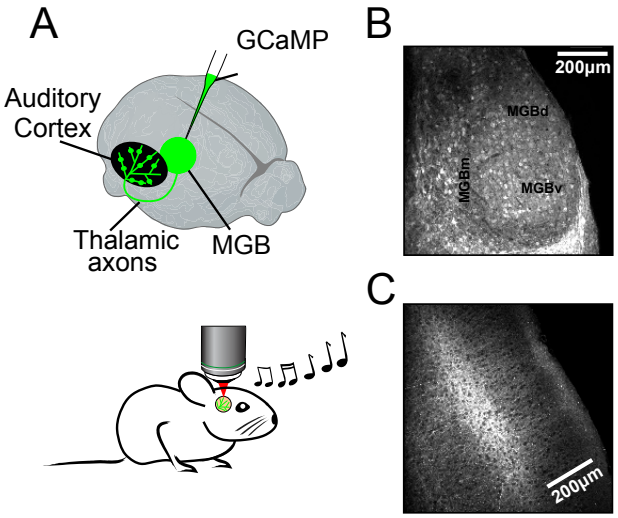

Fig. 3.9: Labelling of MGB projection neurons for *in vivo* calcium imaging of thalamocortical afferents in auditory cortex. (**A**) Experimental schematic. Responses of thalamocortical axons in auditory cortex to pure tones were imaged using two-photon microscopy in awake, head-fixed mice expressing the calcium indicator GCaMP6m in the MGB. (**B**) Histological coronal section showing neurons transfected with GCaMP6m throughout the MGB. (**C**) Histological coronal section through the auditory cortex showing GCaMP6m-labelled thalamic axons.

cortical planes corresponding to L1 and L3b/4 of cortex, where the peaks of axonal labelling occurred (**Fig. 3.9-C**).

Matching inputs to specific auditory cortical subfields

Through several sessions of imaging, it was often possible to image regions over a large enough span of cortex for the caudo-rostral, low-to-high and high-to-low tonotopic gradients that are respectively indicative of A1 and AAF to emerge. Nevertheless, the last imaging session of each C57BL/6NTac.Cdh23$^{753A>G}$ mouse was followed by anaesthetised microelectrode recordings to obtain cortical multi-unit frequency maps. In this way, individual imaging regions could be confidently assigned to specific auditory cortical subfields, even in those cases when the thalamic input frequency maps were inconclusive (**Fig. 3.11**). Based on these maps and the maps of mouse auditory cortex described in the literature (Tsukano et al., 2016; Issa et al., 2014; Guo et al., 2012), imaging regions were sorted as belonging to A1 or AAF, if they fell on one of the tonotopic gradients, or to DP/DA, if they were outside and dorsal to A1/AAF (**Fig. 3.11**, white arrows). In order to image exclusively

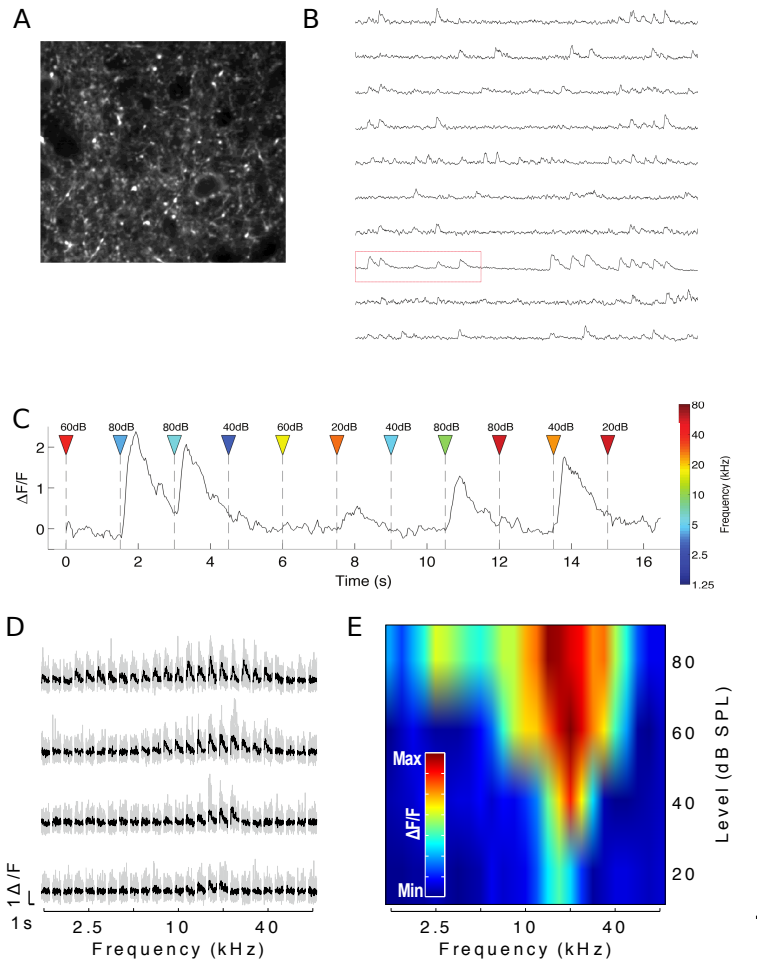

Fig. 3.10: *In vivo* calcium imaging of CGaMP6m-labelled MGB afferents in auditory cortex. (**A**) *In vivo* two-photon image of thalamic axons and axonal boutons in auditory cortex. Scale bar = 200 μm. (**B**) Example fluorescence traces from ten different ROIs segmented from putative axonal boutons in A during 30 seconds of stimulus presentation and a sampling rate of 30 Hz. (**C**) Inset of B depicting the frequency and level of the randomized pure tones presented every 1.5 seconds. (**D**) Example of traces of one bouton in response to 9 repetitions of a set of 25 pure tones at 4 levels, shown here ordered according to sound frequency and level. Gray traces indicate responses to individual repetitions. Black traces indicate mean responses. (**E**) Frequency response area corresponding to traces in D.

non-lemniscal thalamic inputs, I used a cre-dependent virus in the CR-IRES-cre mice to express GCaMP6m exclusively in neurons outside the MGBv. In these experiments, I identified A2 by its ventral location and the particularly dense thalamocortical axon labelling. Areas slightly dorsal of A2 were deemed to be in primary auditory fields

and were also imaged, for comparison, despite having comparatively fewer labelled boutons.

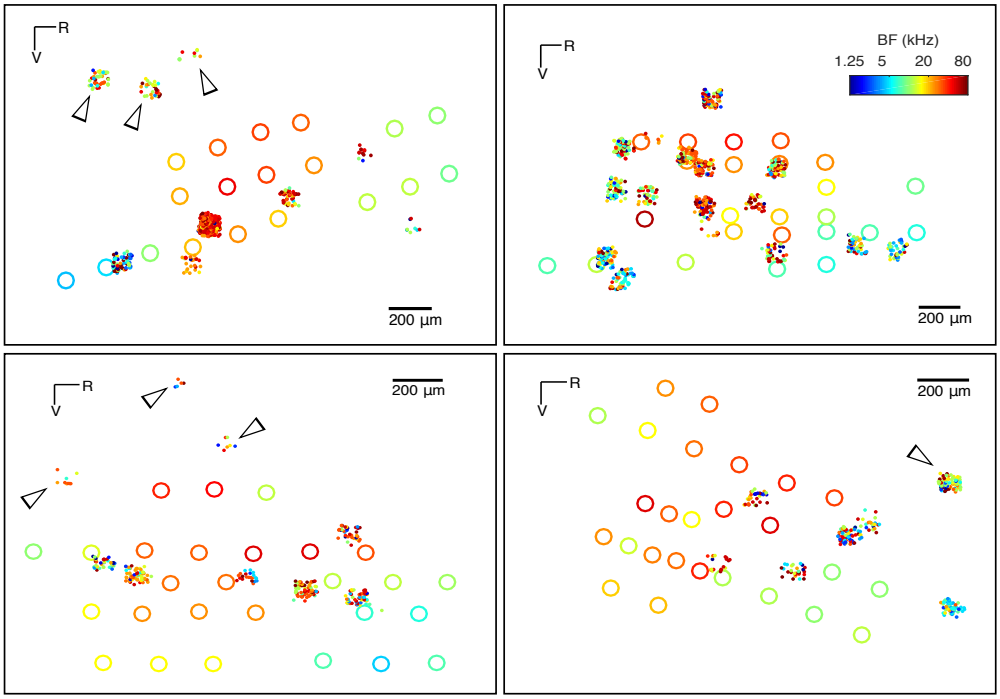

Fig. 3.11: Functional imaging of thalamocortical projections was followed by mapping through electrophysiological MUA-recordings. Location of thalamic boutons (small dots) and multi-unit recordings (large circles) from four animals, colour-coded by BF and collapsed onto the same horizontal plane. The colour of the large circles indicates the mean BF of all tone-responsive multi-units recorded under anaesthesia with multi-electrode arrays at the same site following completion of awake imaging. The tonotopic gradients from the bouton and MU maps were used to sort imaged regions as belonging to the primary subfields (A1 or AFF) or to the dorsal non-primary subfields DP/DA (white arrows), if falling outside and dorsal to them.

Frequency tuning is significantly more prevalent in inputs to primary fields

Each imaged 90 x 100 μm region of auditory cortex contained hundreds of GCaMP6 labelled thalamic boutons that were imaged. Outside of A2, CR-IRES-cre mice had significantly fewer (CR+) labelled boutons. The number of labelled boutons (**Fig. 3.12-A**) per imaged region was comparable across all other auditory cortical subfields (A1: 234 $\pm$ 179 (median $\pm$ interquartile range) ROIs, n = 40; AAF: 242 $\pm$ 225 ROIs, n = 18; DP/DA: 213 $\pm$ 160 ROIs, n = 28; A2-CR+: 242 $\pm$ 260 ROIs, n = 9; non-A2-CR+: 65 $\pm$ 49 ROIs, n = 6; p = 0.008, one-way ANOVA followed

by Tukey's HSD) and also when grouped as primary (A1 + AAF) and non-primary (DP/DA + A2) areas (primary: 236 ± 192 ROIs, n = 58; non-primary: 198 ± 193 ROIs, n = 43; p = 0.08, Wilcoxon rank-sum test).

Of all imaged boutons, only those that exhibited a statistically significant difference (one-way ANOVA, $P < 0.001$) in response among the 100 frequency-level combinations were considered tuned and used for further analysis. The proportion of tuned boutons (**Fig. 3.12-B**) was highest in A1, and overall, significantly higher in primary subfields than in secondary ones (A1: 16.8 ± 11.9 %, n = 40; AAF: 8.8 ± 6.2 %, n = 18; DP/DA: 5.7 ± 4.9 %, n = 28; A2-CR+: 0.9 ± 1.4 %, n = 9; non-A2-CR+: 0.35 %, n = 6; $p = 5.0\ e^{-12}$, Kruskal–Wallis test followed by Tukey's HSD. Primary: 14.3 ± 9.6 %, n = 58; non-primary: 4.0 ± 5.7 %, n = 43; $p = 4.6\ e^{-11}$, Wilcoxon rank-sum test). In the CR-IRES-cre line, CR+ boutons typically responded very poorly to acoustic stimulation and, consequently, only very few FRAs were obtained that passed the inclusion criterion. Five out of six imaged areas in primary auditory areas produced no FRAs at all, and one produced three FRAs. Even in A2, where the labelling was typically very dense (**Fig. 3.13**), these numbers were very low. Here, the median number of FRAs obtained per imaged area was 1 ± 3.5 (range: 0-9, n = 9 areas). Thus, axonal boutons with clearly defined FRAs are predominantly a feature of the projection from MGBv to the primary auditory cortical areas.

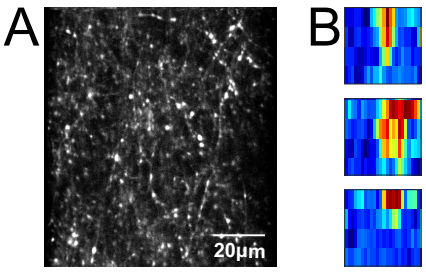

Fig. 3.13: CR+ axons are abundant in A2 but few are tuned. Amount of labelled CR+ axons in A2 is comparable to labelled axons in other areas, but the prevalence of tuning is considerably lower. (**A**) *In vivo* two-photon image of CR+ thalamic axons in middle layers of A2 of a CR-IRES-cre mouse injected with AAV1.Syn.Flex.GCaMP6m.WPRE.SV40. (**B**) Example FRAs.

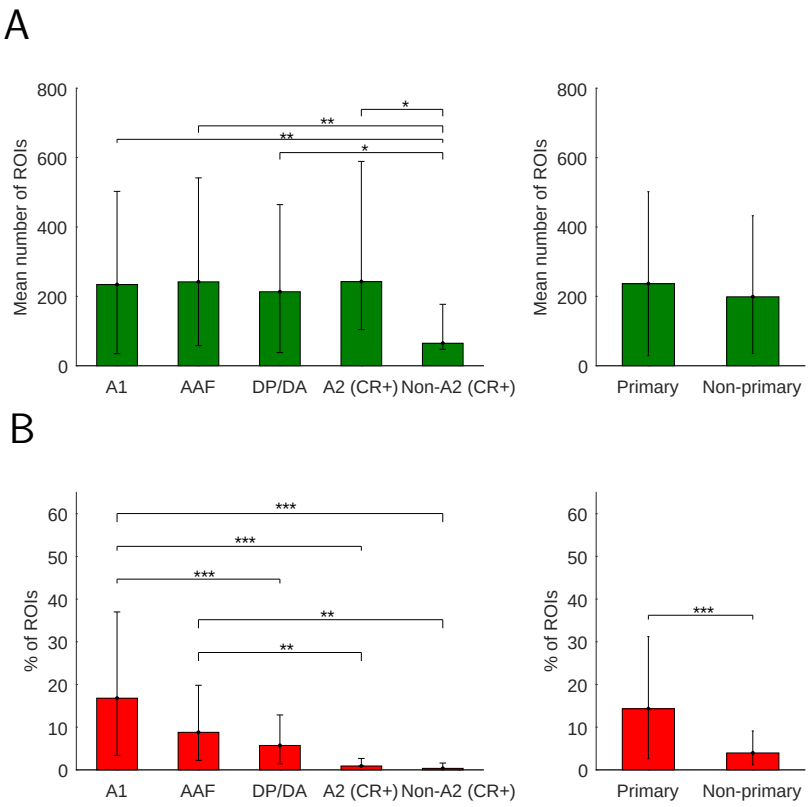

Fig. 3.12: Number of GCaMP6-labelled boutons and prevalence of tuning across auditory cortical subfields. (**A**) Comparisons of mean number of segmented bouton ROIs per imaged area across auditory cortical subfields (left) and between primary (A1, AAF) and non-primary (DP/DA, A2-CR+) ones (right). (**B**) Comparisons of the proportion of frequency-tuned bouton ROIs per imaged area across auditory cortical subfields (left) and between primary and non-primary ones (right). Data on A1, AAF and DP/DA comes from C57BL/6NTac.Cdh23$^{753A>G}$ mice where the imaging locations were confirmed electrophysiologically. Data on A2 (CR+) and non-A2 (CR+) comes from CR-IRES-cre mice injected with cre-dependent GCaMP6 virus. Error bars are 95% confidence intervals. One asterisk (*) indicates $p < 0.05$, otherwise m asterisks indicate $p < 10^{-m}$. See text for details on statistical tests.

The co-tuning of TC inputs is comparable across all auditory subfields

In order to quantify the variation in frequency selectivity among a population of nearby thalamocortical boutons, I determined each bouton's best frequency (BF), defined as the frequency at which the strongest response occurred in the level-averaged tuning curve (Guo et al., 2012). This measure of frequency preference is considered to produce the most orderly tonotopic maps (Hackett et al., 2011). I then measured the co-tuning (the standard deviation of the BF distribution) for each imaged region containing tuned boutons, and compared regions across auditory cortical subfields (**Fig. 3.14**). Co-tuning was surprisingly weak across all auditory subfields (A1: 1.2 ± 0.6 octaves, n = 40; AAF: 1.2 ± 0.4 octaves, n = 18; DP/DA: 1.4

$\pm$ 0.8 octaves, n = 27; A2-CR+: 0.6 $\pm$ 1.2 octaves, n = 6; p = 0.107, Kruskal–Wallis test followed by Tukey's HSD) and, at least within the size of imaging fields used (90 x 100 μm), similar between primary and non-primary auditory cortex (primary: 1.2 $\pm$ 0.6 octaves, n = 58; non-primary: 1.3 $\pm$ 0.8 octaves, n = 34; p = 0.800, unpaired t-test). Even in small patches of primary auditory cortex, neighbouring boutons could be tuned to frequencies several octaves apart (**Fig. 3.15**). Such a high variability in bouton tuning preferences within individual imaged regions was a very unexpected but highly consistent finding, at all cortical depths imaged. In chapter 4, I will explore extensively this local heterogeneity and its implications for the tonotopic organisation of projections to primary auditory fields.

Whilst there appear to be some differences in the BF distributions across subfields (**Fig. 3.14-A**), with, for example, an over-representation of high frequencies in AAF, no definitive conclusion should be drawn from this, because my imaging experiments did not attempt to evenly sample across all frequency bands.

FRA quality and bandwidth are higher in AAF

In order to get a measure of the frequency selectivity of the boutons, I calculated the receptive field bandwidths from the level-averaged tuning curves. Because only 4 different levels were used in my stimulus set, an accurate measure of the bouton's threshold cannot be obtained. Thus, rather than measuring the bandwidth at a particular level above threshold, I used the value corresponding to the full width at half maximum (FWHM) of the level-averaged tuning curve (Bandyopadhyay et al., 2010; Issa et al., 2014). The mean bandwidth was comparable across most auditory subfields, although significantly higher in AAF than in A1 (**Fig. 3.16**; A1: 2.22 $\pm$ 1.79 octaves, n = 1383; AAF: 2.48 $\pm$ 2.17 octaves, n = 430; DP/DA: 2.25 $\pm$ 1.88 octaves, n = 344; A2-CR+: 2.47 $\pm$ 1.82 octaves, n = 22; p = 0.004, Kruskal–Wallis test followed by Tukey's HSD. Primary: 2.28 $\pm$ 1.87 octaves, n = 1813; non-primary: 2.27 $\pm$ 1.87 octaves, n = 369; p = 0.881, Wilcoxon rank-sum test). The FWHM measure for bandwidth can be affected by edge effects in which the tuning curve cannot be reliably measured when it extends past the edges of

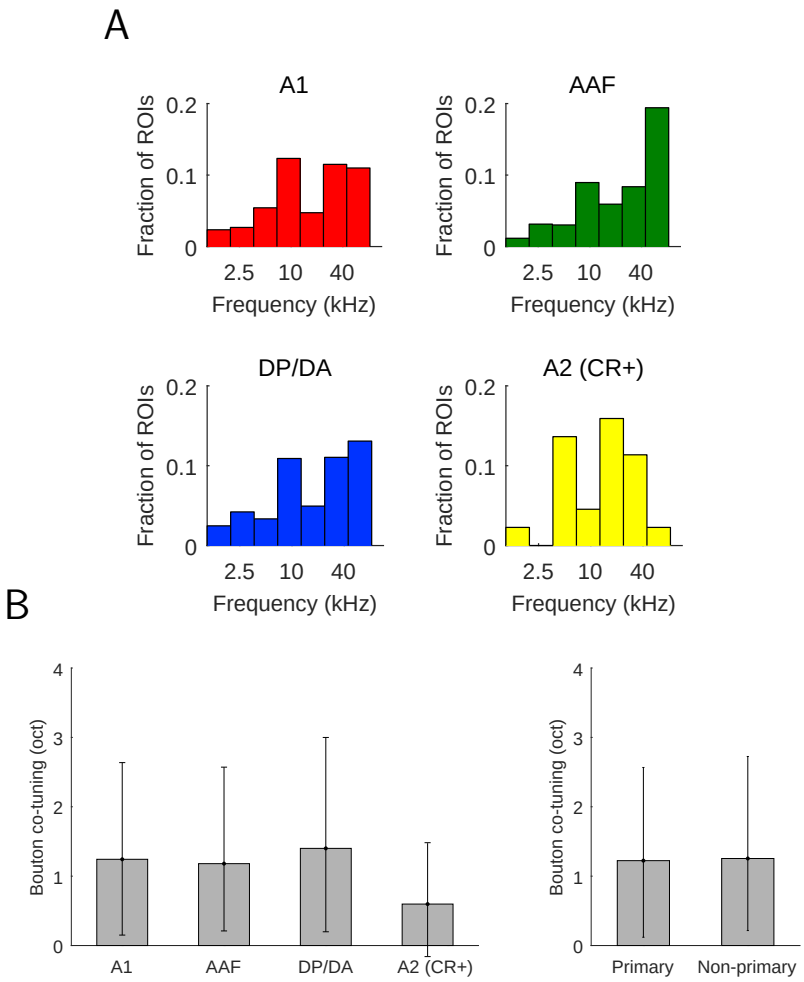

Fig. 3.14: Local bouton co-tuning across auditory cortical subfields. (**A**) Distributions of co-tuning measures within all the 90 x 100 μm imaged regions across auditory cortical subfields. (**B**) Comparisons of mean local bouton co-tuning across auditory cortical subfields (left) and between primary (A1, AAF) and non-primary (DP/DA, A2-CR+) ones (right). Data on A1, AAF and DP/DA comes from C57BL/6NTac.Cdh23$^{753A>G}$ mice where the imaging locations were confirmed electrophysiologically. Data on A2 (CR+) comes from CR-IRES-cre mice injected with cre-dependent GCaMP6 virus. Error bars are 95% confidence intervals. One asterisk (*) indicates $p < 0.05$, otherwise m asterisks indicate $p < 10^{-m}$. See text for details on statistical tests.

the frequency range measured before reaching half-height. This is unlikely to be an issue for the measurements presented here, as the range of frequencies used spans most of the mouse hearing range. Accordingly, the same differences in mean subfield bandwidth (with AAF being significantly higher) was observed in an analysis that excluded any bouton with bandwidth greater than 5 octaves (A1: 2.14 $\pm$ 1.74 octaves, n = 1349; AAF: 2.39 $\pm$ 2.13 octaves, n = 416; DP/DA: 2.21 $\pm$ 1.86 octaves, n = 340; A2-CR+: 2.47 $\pm$ 1.82 octaves, n = 22; p = 0.009, Kruskal–Wallis test followed by Tukey's HSD).

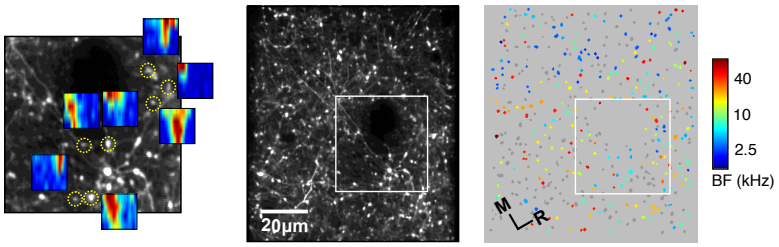

Fig. 3.15: Example area with typical local heterogeneity in the tuning of thalamocortical boutons. Middle: *in vivo* two-photon image of thalamic axons and boutons in a small patch of auditory cortex. Left: FRAs are shown for several example boutons (locations indicated by yellow circles) within the inset region delineated by the white square in the middle panel. Right: ROIs corresponding to putative thalamocortical boutons from the same patch of cortex colour-coded according to each bouton's BF. Non-responsive ROIs are shown in dark gray. White rectangle corresponds to area shown in the left panel.

Electrophysiological recordings in the mouse have revealed differences in the tuning quality of neurons across the auditory subfields (Guo et al., 2012). Thus, I assessed the tuning quality of the boutons by fitting Gaussians to the level-averaged tuning curves and comparing the R^2 values of the fits. Higher R^2 values come from more primary-like FRAs, whilst lower values likely to be multi-peaked (**Fig. 3.17-A**). The distributions and average R^2 values were comparable across most auditory subfields although significantly higher in AAF than in A1 (**Fig. 3.17-B-C**; A1: $R^2 = 0.42 \pm 0.38$, $n = 1383$; AAF: $R^2 = 0.49 \pm 0.43$, $n = 430$; DP/DA: $R^2 = 0.45 \pm 0.42$, $n = 344$; A2-CR+: $R^2 = 0.4 \pm 0.47$, $n = 22$; $p = 0.00025457$, Kruskal–Wallis test followed by Tukey's HSD. Primary: $R^2 = 0.44 \pm 0.39$, $n = 1813$; non-primary: $R^2 = 0.45 \pm 0.42$, $n = 369$; $p = 0.480$, Wilcoxon rank-sum test).

Whilst the assumption that tuning quality can be measured by fitting a Gaussian to the level-averaged tuning curve is well supported by previous studies (Guo et al., 2012), it is possible that such a measure would obscure the presence of level-tuned receptive fields. Therefore, I also fitted Gaussians to the tuning curves at 60 dB and found the R^2 values to be significantly correlated to those obtained from the fitting to level-averages (**Fig. 3.18**; $R = 0.528$, $P < 0.0001$, $n = 1383$, Pearson correlation). Moreover, the observations of differences in the tuning quality between A1 and AAF were still present when using the tuning curve at 60 dB (A1: R^2 at 60dB $= 0.18 \pm 0.22$, $n = 1383$; AAF: R^2 at 60dB $= 0.22 \pm 0.30$, $n = 430$; DP/DA: R^2 at 60dB =

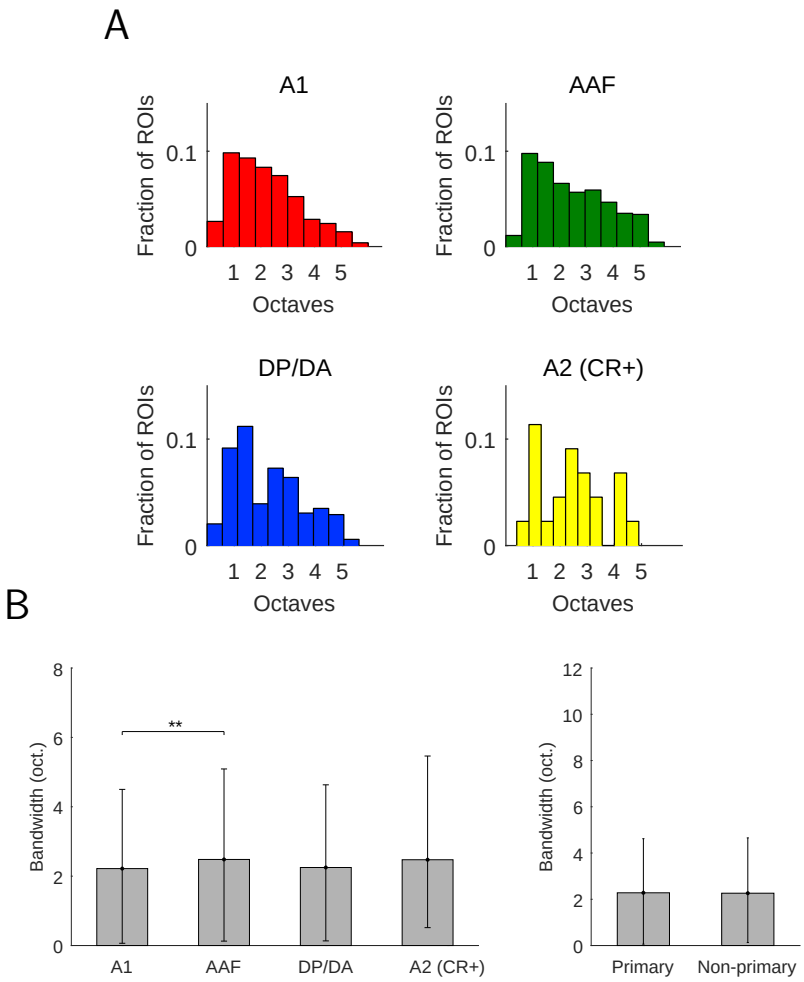

Fig. 3.16: Receptive field bandwidth of boutons across auditory cortical subfields. (**A**) Distributions of bandwidth measures of all boutons across auditory cortical subfields. (**B**) Comparisons of mean bouton bandwidth across auditory cortical subfields (left) and between primary (A1, AAF) and non-primary (DP/DA, A2-CR+) ones (right). Data on A1, AAF and DP/DA comes from C57BL/6NTac.Cdh23$^{753A>G}$ mice where the imaging locations were confirmed electrophysiologically. Data on A2 (CR+) comes from CR-IRES-cre mice injected with cre-dependent GCaMP6 virus. Error bars are 95% confidence intervals. One asterisk (*) indicates $p < 0.05$, otherwise m asterisks indicate $p < 10^{-m}$. See text for details on statistical tests.

0.22 ± 0.27, n = 344; A2-CR+: R^2 at 60dB = 0.15 ± 0.20, n = 22; p = 0.0163, Kruskal–Wallis test followed by Tukey's HSD. Primary: R^2 at 60dB = 0.19 ± 0.24, n = 1813; non-primary: R^2 at 60dB = 0.21 ± 0.27, n = 369; p = 0.2418, Wilcoxon rank-sum test).

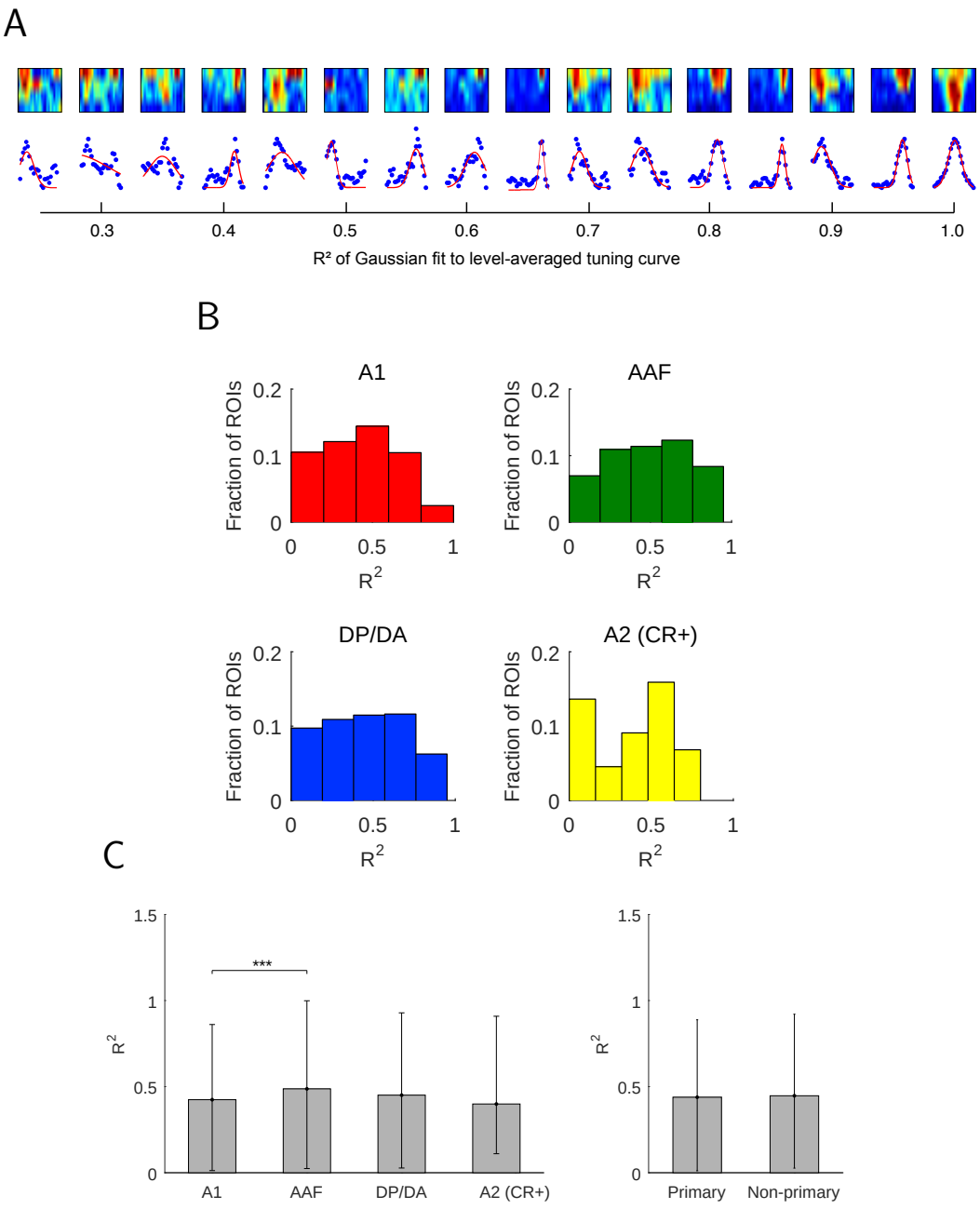

Fig. 3.17: Tuning quality of boutons across auditory cortical subfields. (**A**) Top, example frequency response areas (FRAs) of individual boutons. Bottom, level-averaged frequency tuning curves (blue dots). In order to assess the quality of frequency tuning, the level-averaged tuning curves were fitted with Gaussians (red). The R^2 values given below indicate the quality of the fits. (**B**) Distributions of tuning quality, measured by the R^2 value of a Gaussian fit, of all boutons across auditory cortical subfields. (**C**) Comparisons of mean tuning quality across auditory cortical subfields (left) and between primary (A1, AAF) and non-primary (DP/DA, A2-CR+) ones (right). Data on A1, AAF and DP/DA comes from C57BL/6NTac.Cdh23$^{753A>G}$ mice where the imaging locations were confirmed electrophysiologically. Data on A2 (CR+) comes from CR-IRES-cre mice injected with cre-dependent GCaMP6 virus. Error bars are 95% confidence intervals. One asterisk (*) indicates $p < 0.05$, otherwise m asterisks indicate $p < 10^{-m}$. See text for details on statistical tests.

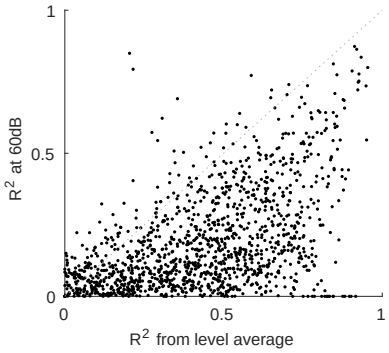

Fig. 3.18: Measurements of tuning quality with level-averaged tuning curve correlates with tuning quality at a single level. In order to assess the measurement of tuning quality based on the level-averaged tuning curve or the tuning curve at a single level (60 dB), both curves for each bouton were fitted with Gaussians. The R^2 values of the fits for each bouton were positively correlated.

Signal and noise correlations suggest diverse thalamic origin of imaged boutons

Correlations in the responses of neurons to stimuli (signal correlations) and in the variability of such responses (noise correlations) can provide important information about the functional connectivity of neuronal networks (Averbeck et al., 2006; Cohen and Kohn, 2011). Pairs of sensory cortical neurons with high signal correlation (i.e. very similar receptive fields) have been found to have a higher probability of being interconnected (Ko et al., 2011). High noise correlations are generally indicative of common synaptic inputs (Cohen and Kohn, 2011). In the case of axonal boutons, one might expect both very high signal and noise correlations between pairs of boutons belonging to the same axon. Thus, measuring these correlations can indicate to what extent the population of boutons sampled represents a varied population of thalamic neurons.

The signal and noise correlations of pairs of tuned boutons within the same imaged region were calculated for all regions. Signal correlations were the correlation between the boutons' FRAs. This measure includes both stimulus-dependent and stimulus-independent variability, but because of noise correlations being at least an order of magnitude smaller than signal correlations, this measure was taken as being predominately stimulus-derived. AAF and A1 exhibited significantly higher signal

correlations between its boutons than DP/DA, and they were also higher in AAF than in A1 (**Fig. 3.19-A**; A1: 0.23 ± 0.29, n = 31093 pairs; AAF: 0.28 ± 0.42, n = 7820 pairs; DP/DA: 0.22 ± 0.38, n = 3103 pairs; A2-CR+: 0.26 ± 0.5, n = 65 pairs; p = 3.0 e^{-37}, Kruskal–Wallis test followed by Tukey's HSD). Signal correlations were also significantly higher in the combined primary subfields (A1 and AAF) than in non-primary ones (DP/DA and A2) (**Fig. 3.19-C**; primary: 0.24 ± 0.31 pairs, n = 38913; non-primary: 0.23 ± 0.39, n = 3168 pairs; p = 7.4 e^{-15}, Wilcoxon rank-sum test). Whereas the long tails of the signal correlation distributions indicate that a fraction of boutons likely belonged to the same axon, the vast majority of pairs had much lower correlations.

For noise correlations, the fluctuations of single trial responses of pairs of boutons around their mean response were correlated (Rothschild et al., 2010). A noise residual vector was first obtained for each bouton by subtracting its mean response to each stimulus from the corresponding single-trial responses. The noise correlations were the correlation coefficients between the vectors of pairs of boutons. Noise correlations were also significantly higher in AAF than in both A1 and DP/DA (**Fig. 3.19-B**; A1: 0.05 ± 0.03, n = 31093 pairs; AAF: 0.06 ± 0.05, n = 7820 pairs; DP/DA: 0.06 ± 0.04, n = 3103 pairs; A2-CR+: 0.06 ± 0.05, n = 65 pairs; p = 1.9 e^{-47}, Kruskal–Wallis test followed by Tukey's HSD). However, no significant difference was observed between the combined primary and non-primary subfields (**Fig. 3.19-D**; primary: 0.05 ± 0.04, n = 38913 pairs; non-primary: 0.06 ± 0.04, n = 3168 pairs; p = 0.13735, Wilcoxon rank-sum test).

Finally, I compared the signal and noise correlations of each pair of boutons (**Fig. 3.19-E-F**). This can test if boutons with similar FRAs also tended to respond in the same trials. There was a significant positive correlation between the signal correlation and the noise correlation of pairs of boutons (R = 0.578, P < 10 e^{-10}, Pearson correlation). Pairs of boutons from the same axon tend to be found towards the top right corner of the graph. There was indeed a fraction of boutons that showed this trend (**Fig. 3.19-E**). However, a density map shows that these are actually a very small fraction of all pairs (**Fig. 3.19-F**) and that most of the boutons

show correlations that resembled those from pairs of mouse A1 neurons recorded with two-photon calcium imaging (Rothschild et al., 2010; Winkowski and Kanold, 2013). The observed differences in signal correlation, with AAF displaying the highest measures, could nonetheless be related to the higher mean bandwidths in the same subfield (Fig. 3.16). Boutons with larger bandwidth are likely to have larger signal correlations because they are activated by shared ascending inputs covering a wider range of sound frequencies.

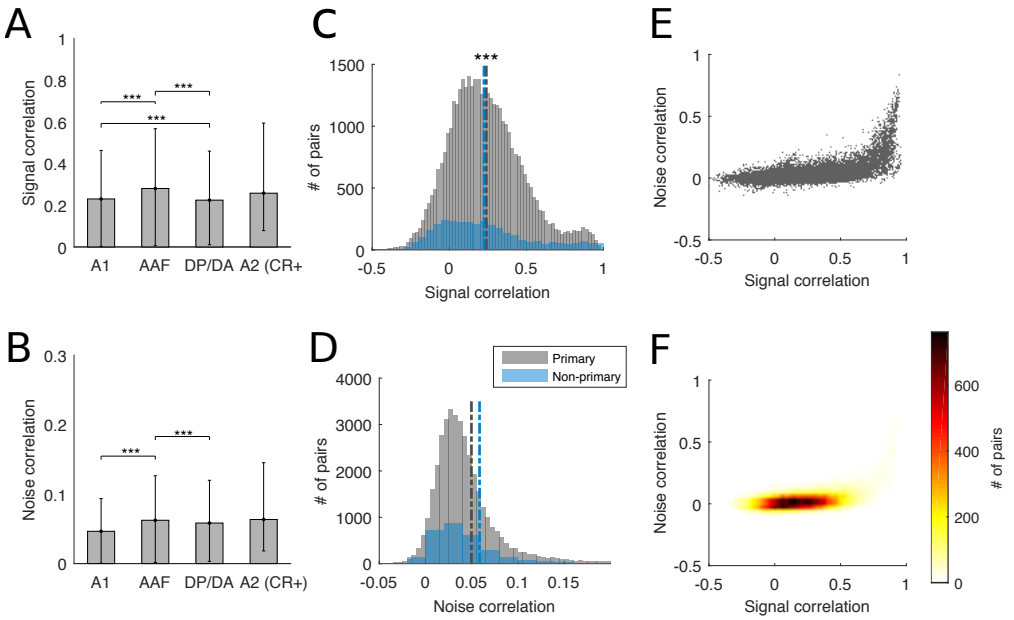

Fig. 3.19: Signal and noise correlations of local pairs of boutons across auditory cortical subfields. (**A**) Comparisons of mean signal correlations between pairs of boutons within the same imaged region, across auditory cortical subfields. (**B**) Same as A for noise correlations. (**C**) Signal correlation distributions for primary (A1, AAF) and non-primary (DP/DA, A2-CR+) fields. (**D**) Same as C for noise correlations. (**E**) Noise correlation as a function of signal correlation for all pairs of boutons across all imaged regions. (**F**) Density map for E. Data on A1, AAF and DP/DA comes from C57BL/6NTac.Cdh23$^{753A>G}$ mice where the imaging locations were confirmed electrophysiologically. Data on A2 (CR+) comes from CR-IRES-cre mice injected with cre-dependent GCaMP6 virus. Error bars are 95% confidence intervals. One asterisk (*) indicates $p < 0.05$, otherwise m asterisks indicate $p < 10^{-m}$. See text for details on statistical tests.

3.4 Discussion

In order to better understand the projection pathways from the medial geniculate (MGB) to the auditory cortex of the mouse, I carried out a number of anatomical and functional imaging experiments. Sparse and localised labelling of MGB neurons and selective labelling of calretinin-positive (CR+) projections, revealed the patterns of thalamic input to the various subfields of mouse auditory cortex and to subcortical structures. Two-photon calcium imaging of MGB afferents in auditory cortex allowed for the characterisation of individual response properties of thalamic boutons across the various auditory subfields. The findings provide some valuable insights into the functional differences among thalamocortical projection channels of the auditory modality.

A general finding throughout all imaged areas was that only a small proportion of boutons (10-20%) exhibited frequency tuning. This could be partly due to the strict inclusion criteria used: $P < 0.001$ for the null hypothesis of no preference for any of the 100 frequency-level combinations. Auditory neurons rarely respond to all sound frequencies over the wide range used here (Pickles, 2012). However, it is possible that the use of different auditory stimuli such as broadband noise and frequency modulated (FM) sweeps would reveal a greater number of acoustically responsive boutons. Nonetheless, the low prevalence of tuning among boutons is not unlike what has been observed in the visual thalamocortical projection (Roth et al., 2016) as well as in the auditory corticocollicular projection (Barnstedt et al., 2015). Imaging in behaving animals might provide some cues about what type of signals are being imparted by these non-tuned inputs (Guo et al., 2017a; Krakauer et al., 2017).

Input to the cortex from CR+ neurons, which were only present in the MGBd and MGBm, was restricted mostly to secondary auditory subfields, particularly A2. In comparison to calretinin-negative terminals in other subfields, a significantly smaller proportion of CR+ thalamic terminals in A2 were frequency tuned. Whilst the

discrepancies between electrophysiological (Stiebler et al., 1997; Guo et al., 2012) and optical imaging studies (Issa et al., 2014; Tsukano et al., 2017b) about the tonotopic organisation of A2 could be due to awake vs anaesthetised differences, my data show no indication of a tonotopic gradient in the thalamic projection to A2 in the awake mouse. If a tonotopic gradient does exist in A2, as the optical imaging experiments have suggested (Issa et al., 2014; Tsukano et al., 2017b), it is unlikely to be imparted by the thalamus. Instead, the topographic cortico-cortical projections from the core to the belt subfields (Lee and Winer, 2005; Hackett et al., 1998) might contribute to the tonotopic gradient observed in A2. This possibility might be best explored through two-photon axonal calcium imaging.

Given that in other sensory systems (Roth et al., 2016), input from higher-order thalamic nuclei has been shown to carry more motor and contextual sensory signals than the input from the first order nucleus, and that the thalamocortical projection from MGBd is as topographically ordered as that from MGBv (Lee and Winer, 2005), it is likely that recordings in behaving animals will reveal more about what stimulus features are being represented in these non-lemniscal projections (Schreiner and Winer, 2007). In particular, two-photon axonal calcium imaging would offer the possibility to explore what stimulus features are being represented in these non-lemniscal projections (Schreiner and Winer, 2007), particularly if it is combined with yet-to-be-identified markers for more specific labelling of the various thalamic subdivisions.

It is important to mention that although the use of the CR-IRES-cre line allowed me to selectively target MGB neurons from subnuclei other than the MGBv, calretinin-positive neurons constitute only a subset—albeit a substantial one (Lu et al., 2009)—of non-lemniscal and paralaminar MGB projecting neurons. Half to a third of MGB neurons outside of the ventral division express calbindin, some alongside calretinin, some on its own. Whether there is a functional difference between thalamic neurons expressing either of these two markers is not known. Thus, further studies aimed at the identification of more specific markers for the various thalamic subdivisions

will pave the way for the precise functional characterisation of thalamic inputs from higher order nuclei.

Another important finding from my experiments concerns the laminar distribution of thalamic afferents in auditory cortex. The sparse labelling of MGBv neurons revealed that many lemniscal thalamic axons travel from the middle layers up to L1 in a columnar fashion. Traditionally, thalamic inputs to L1 and L3b/4 have been classified as belonging to orthogonal channels, with L1 inputs described as matrix-type and L3b/4 input as core-type (Clascá et al., 2012; Harnett et al., 2012; Jones, 2001). Yet, studies with small anterograde tracer injections in MGBv of rats (Romanski and LeDoux, 1993; Kimura et al., 2003), monkeys (Hashikawa et al., 1995) and rabbits (McMullen and Venecia, 1993), as well as single thalamic axon reconstructions in primary auditory cortex of rabbits (Cetas et al., 1999) and monkeys (Hashikawa et al., 1995) have described thalamic projections that form dense plexuses in L4 and project collaterals to L1. Such observations have also been made in the projections from other first-order thalamic nuclei to primary motor (Kuramoto et al., 2009) and somatosensory cortices (Oda et al., 2004). These and our current findings suggest that the laminar separation of matrix- and core-type inputs based on laminar segregation requires some revisions.

The maps obtained from multi-unit electrode recordings did not allow me to confidently assign any imaged region to a dorsomedial (DM) auditory subfield (Tsukano et al., 2017a). There was also no dorsal gradient that could be deduced from inputs alone. However, this is not to say that thalamic input to DM was not present. Rather, my imaging experiments focused mostly on the ventral half of the cranial window where the gradient reversal characteristic of A1 and AAF was consistently found. It is possible that some of the imaged regions found dorsal to the A1-AAF gradients and assigned to DP/DA subfields might have belonged to DM. However, the comparably low prevalence of tuning in DP/DA and A2 afferents suggests this was not the case, since both DP and A2 receive inputs from MGBd (Llano and Sherman, 2008) whilst inputs to DM come from MGBv (Tsukano et al., 2017a) and thus, might be expected to be more similar to A1/AAF.

Besides the relative prevalence of tuning, which was considerably higher in A1 and AAF, the receptive field properties of the tuned boutons were very similar across all cortical subfields. The most significant differences were observed between AAF and A1. Boutons in AAF had wider bandwidth (**Fig. 3.16**) and clearer tuning (**Fig. 3.17**) than boutons in A1. The same differences between these two fields were previously reported by Guo et al. (2012) and Hackett et al. (2011) in the anaesthetised preparation. All this, together with the higher noise and signal correlations in AAF (**Fig. 3.19**), points towards some important functional distinctions between MGBv neurons projecting to A1 or AAF, which go beyond their thalamic compartmentalisation (Horie et al., 2013).

The mean signal correlation for pairs of boutons in A1 or AAF was similar to that of pairs of A1 neurons imaged in L4 (0.25) (Winkowski and Kanold, 2013). Because local signal correlations have been shown to be similar in A1 and MGB (Chechik et al., 2006), it seems likely that most of the boutons within each of the regions I imaged belonged to different thalamic neurons. The boutons' noise correlations also support this, with an average of 0.05 which falls on the lower range of what has been reported for the mouse cortex (0.05 – 0.20) (Rothschild et al., 2010; Winkowski and Kanold, 2013; Bathellier et al., 2012; Bonin et al., 2011; Ko et al., 2011).

Arguably, the most surprising finding from these experiments was the great degree of local heterogeneity in the tuning preference of thalamic boutons in cortex. Even in primary auditory fields, which were independently identified by multi-unit recordings, the co-tuning of boutons within 90 x 100 μm patches of cortex was, on average, over 1 octave. This means that over a seventh of the frequencies spanned by the hearing range of the mouse are found in an area only a thirtieth of the whole auditory cortex[2]. Such a weak co-tuning in local inputs has major implications for our understanding of tonotopic maps (chapter 4) and spectral integration (chapter 5) in the primary auditory cortex.

[2] The auditory cortex of the mouse is approximately 4 mm^2 in size (Stiebler et al., 1997), and its hearing range is between 1 and 100 kHz (Willott, 2001).

4 Functional Micro-Architecture of Thalamocortical Projections to Primary Auditory Cortex

4.1 Tonotopic organisation in the auditory cortex: a question of depth and scale

Most of the brain's auditory neurons, including those in the medial geniculate body (MGB) of the thalamus, are tuned to sound frequency and their spatial arrangement reflects the tonotopic organization established by the biomechanical properties of the cochlea. Tonotopy is preserved across species and at every lemniscal stage of the ascending auditory pathway up to the cortex (Kaas, 2011; Schreiner and Winer, 2007; Woolsey and Walzl, 1942). Like the receptor surface maps that are also hallmarks of the visual and somatosensory pathways, the presence of sound frequency gradients within each of these brain regions is therefore the most well characterized feature of the auditory system.

While the existence of cortical tonotopy is universally accepted, how precise this organization really is has recently been debated (Guo et al., 2012; Kanold et al., 2014; Rothschild and Mizrahi, 2015). In particular, the opportunity to image the activity of large populations of neurons at single-cell resolution in the mouse auditory cortex (Bandyopadhyay et al., 2010; Rothschild et al., 2010; Winkowski and Kanold, 2013; Issa et al., 2014) has questioned the smooth tonotopic organization revealed with microelectrode recordings (Guo et al., 2012; Hackett et al., 2011; Stiebler et al., 1997) or low-resolution imaging methods (Horie et al., 2013; Moczulska

et al., 2013; Tsukano et al., 2016). The current view holds that neurons in the main thalamorecipient layers 4 and 3b, which tend to be most commonly sampled by microelectrode recordings, exhibit precise tonotopy that transitions into a coarse and more heterogeneous frequency organization in the supragranular layers (Kanold et al., 2014).

One implication of this arrangement is that the homogeneous tonotopy of the middle cortical layers is inherited from thalamic input which is itself precisely tonotopically ordered. However, it is unclear how tightly organized this projection actually is. Although retrograde tracing of thalamocortical inputs (Brandner and Redies, 1990; Hackett et al., 2011) suggests strict topography, anterograde tracing (Huang and Winer, 2000) and reconstruction of single thalamic axons (Cetas et al., 1999) indicate considerable divergence in the auditory thalamocortical pathway. Indeed the frequency tuning of thalamic inputs that converge onto individual auditory cortical neurons can span several octaves (Liu et al., 2007), suggesting a need for integration across differently tuned afferent terminals. Furthermore, while most thalamocortical projections target the middle cortical layers, axons from the MGB can also be found in other layers (Frost and Caviness, 1980; Huang and Winer, 2000; Ji et al., 2015; Kimura et al., 2003; Llano and Sherman, 2008), but nothing is currently known about the relative specificity or precision of these inputs.

As discussed in previous chapters, our current understanding of the functional micro-organization of the auditory thalamocortical pathway has been limited by the relatively poor spatial resolution of the methods that have so far been used to investigate it. The imaging experiments described in chapter 3 constitute the first ever measurement of frequency selectivity of individual axonal boutons of the auditory geniculo-cortical projection. The particular finding of weak local co-tuning of axonal boutons from MGBv in primary auditory cortex have great implications for tonotopy. In this chapter, I set out to investigate the micro-organisation of these inputs to cortex, with a particular emphasis on their topographic and laminar profile. I explore these questions in the awake and anaesthetised states and in different strains of mice, using the same high-resolution *in vivo* two-photon (Denk et al.,

1990) axonal calcium imaging (Petreanu et al., 2012; Glickfeld et al., 2013; Roth et al., 2016) method introduced in chapter 3.

4.2 Laminar differences in the organisation of auditory thalamocortical inputs

Tuned thalamic inputs to auditory cortex concentrate in layers 3b/4 and 1

I first explored the micro-organisation of MGB axonal boutons in primary auditory cortex and, in particular, the topographic distribution of frequency preference, using C57BL/6 mice anaesthetised with a ketamine-medetomidine mixture. Not only is this the state in which measurements of tonotopy have been found to be sharpest (Hackett et al., 2011; Rothschild and Mizrahi, 2015), but this preparation also reduces the effects of motion artifacts on the quality of the FRAs obtained through imaging. Subsequently, this would also allowed me to compare the findings from awake and anaesthetised imaging experiments (section 4.4).

As described in section 3.3, I labelled thalamic projection neurons with the genetically calcium indicator GCaMP6m (Chen et al., 2013) by means of a viral injection in the MGB (**Fig. 3.9 A**). Most of the thalamic axons were found in the middle cortical layers, L3b/4, although substantial input was also observed in L1 (**Fig. 4.1**, left). In order to characterise the micro-organisation of these laminar inputs, I imaged from pairs of regions that had the same location on the cortical surface (i.e. the same x-y coordinates) but depths corresponding to L1 ($55 \pm 39\ \mu\mathrm{m}$, (median $\pm$ interquartile range)) and L3b/4 ($311 \pm 43.5\ \mu\mathrm{m}$) (**Fig. 4.1**, right).

For each 90 x 100 $\pm$ region of primary auditory cortex imaged, the number of labelled boutons (**Fig. 4.2-A**) was higher (i.e. the labelling was densest) at the level of L1 than L3b/4 (L3b/4: 154 ± 118 ROIs, L1: 314 ± 109 ROIs, n = 36 pairs of

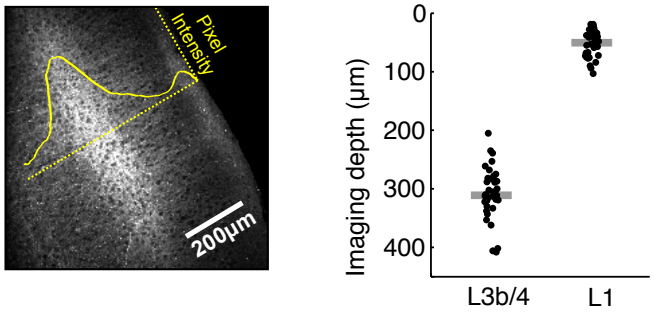

Fig. 4.1: Laminar labelling patterns of thalamocortical terminals guided the choice of imaging depths. Left, histological coronal section through the auditory cortex showing GCaMP6m-labelled thalamic axons. Graph shows intensity of labeling as function of depth. Right, depth of all regions imaged in L1 and L3b/4. Thick gray lines indicate medians.

imaged regions; $p = 3.9\ e^{-14}$, paired t-test). This is very likely due to the tangential arrangement of axonal terminals on layer 1 (Rubio-Garrido et al., 2009). Each imaged region was found to contain dozens to hundreds of tone-responsive (L1: 90.5 ± 64, L3b/4: 87 ± 84, $n = 36$) and mostly well-tuned boutons (**Fig. 4.2-C-D**). The proportion of tuned boutons was comparable between both layers (**Fig. 4.2-B**; L3b/4: 10 ± 12.0 %, L1: 8 ± 7.0 %; $p = 0.13788$, Sign-rank test).

Local tuning of thalamic inputs is highly heterogeneous and slightly more so in L1

Given that the auditory cortex is tonotopically organized and that this organisation must be inherited from the thalamus, the cortex's sole source of ascending auditory information, it is expected that thalamic input would be tightly tonotopically ordered. Consequently, when sampling from a small patch of cortex, the boutons found therein ought to be tuned to similar frequencies. In order to quantify the variation in frequency selectivity among a population of nearby thalamocortical boutons, I determined each bouton's best frequency (BF), defined as the frequency at which the strongest response occurred in the level-averaged tuning curve (Guo et al., 2012), measured the co-tuning (the standard deviation of the BF distribution) for each imaged region and compared pairs of regions recorded at L1 and L3b/4 (**Fig. 4.3**). While the average co-tuning of thalamic boutons in a 90 x 100 $\pm$ region of

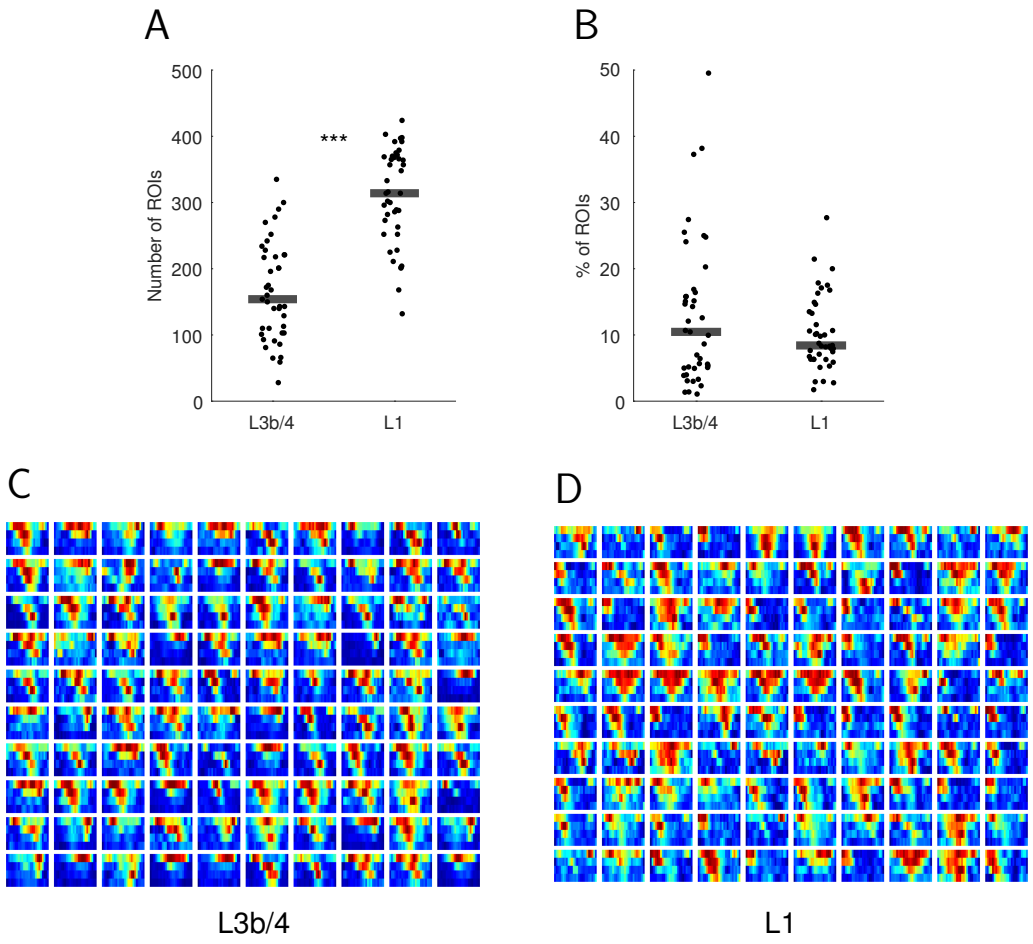

Fig. 4.2: Laminar prevalence in frequency tuning of thalamocortical boutons in layers 3b/4 and 1 of auditory cortex. (**A**) Total number of GCaMP6-labelled thalamic boutons imaged within each region in L3b/4 and L1. (**B**) Fraction of GCaMP6-labelled thalamic boutons exhibiting frequency tuning within each imaged region in L3b/4 and L1. (**C**) Examples of frequency response areas (FRAs) from individual boutons within a single imaged area in layer 3b/4. (**D**) Same as **C** but for boutons in layer 1.

auditory cortex was about one octave, there was a slight, but statistically significant, difference between the inputs to the different layers. Input to L3b/4 shows stronger co-tuning (0.93 ± 0.25 octaves) and is, thus, more homogeneous than the input to L1 (1.15 ± 0.37 octaves, $p < 0.001$, effect size: $r = 0.43$, $n = 36$, Wilcoxon signed-rank test). Within L3b/4 there was no relationship between depth and co-tuning ($R = 0.14$, $P = 0.41$, $n = 36$, Spearman's correlation), which suggests that layer 4 is no more homogeneous than lower layer 3 (**Fig. 4.4**).

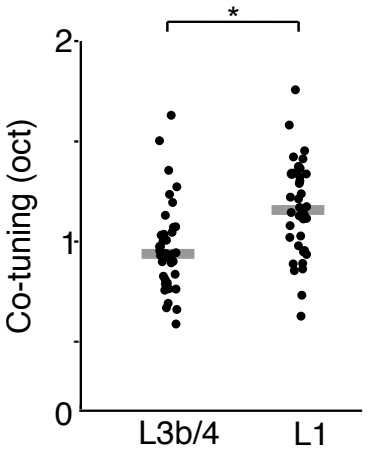

Fig. 4.3: Local heterogeneity of thalamic input is higher in layer 1. Co-tuning (standard deviation of BF distribution) within individual regions imaged in L1 (n = 36) and L3b/4 (n = 36). Thick gray lines indicate medians.

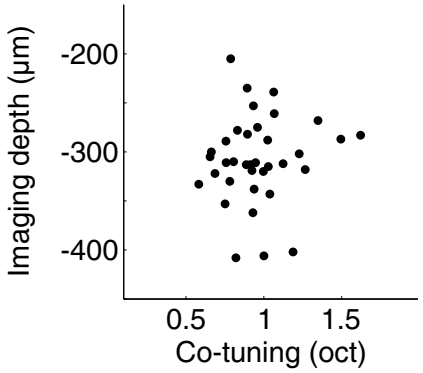

Fig. 4.4: Layer 4 is no more homogeneous than lower layer 3. No relationship was observed between imaging depth within L3b/4 and co-tuning.

Every imaged region consistently showed that neighbouring boutons could be tuned to frequencies several octaves apart, both in L1 and L3b/4 (**Fig. 4.5 A-D**). Given the size of the imaged regions relative to the size of the auditory cortex and its subfields, the variation in frequency tuning appeared unexpectedly large so, for comparison, I pooled all boutons across all imaged regions and animals to obtain overall BF distributions for L1 and L3b/4. Mice are sensitive to frequencies between about 1 and 100kHz (Willott, 2001), but their brains do not represent all frequencies within that range equally. Most auditory nerve fibers (Ehret, 1979) and most neurons in the inferior colliculus (Stiebler and Ehret, 1985) and thalamus (Anderson and Linden, 2011) are tuned to frequencies in the middle one to two octaves of the mouse's hearing range. Consistent with the frequency distributions reported in the inferior colliculus and thalamus, I found that the overall BF distribution of thalamocortical inputs, both in L3b/4 and L1, had a pronounced bias towards frequencies near the centre of the mouse's hearing range (**Fig. 4.5 E-F**).

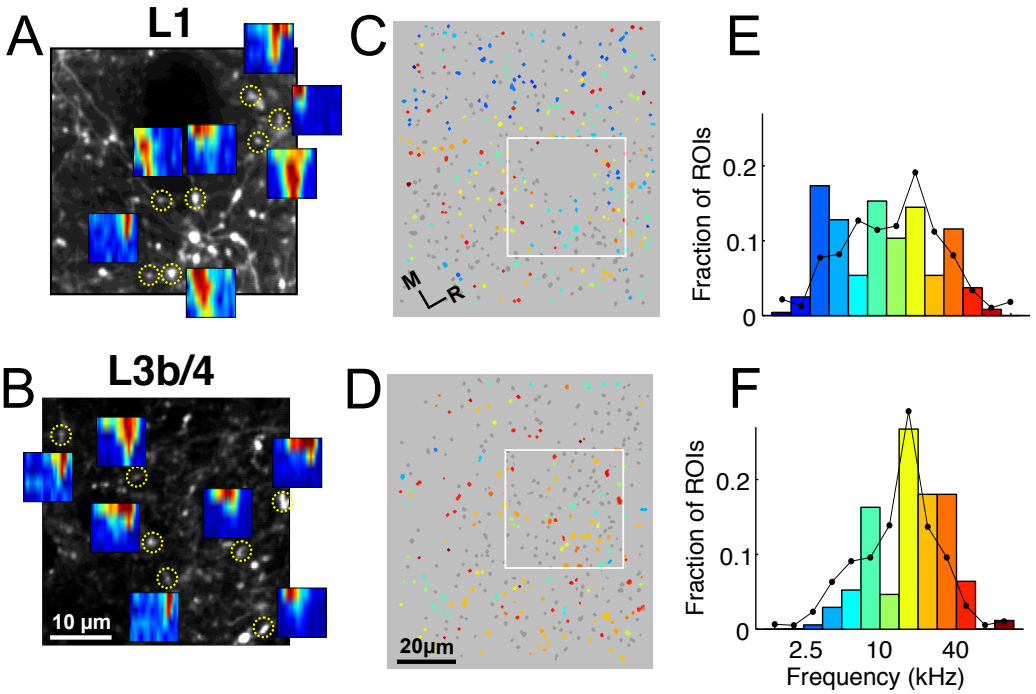

Fig. 4.5: Example of local heterogeneity in a representative pair of imaged regions. (**A**) In vivo two-photon image of thalamic axons and boutons in a small patch of L1 of the auditory cortex. FRAs are shown for several example boutons (locations indicated by yellow circles). (**B**) Same as A for L3b/4. (**C**) ROIs corresponding to putative L1 thalamocortical boutons from a single optical plane color-coded according to each bouton's BF. Non-responsive ROIs are shown in dark gray. White rectangle corresponds to area shown in (A). (**D**) Same as C for region imaged in L3b/4. (**E**) Distribution of BFs from the L1 region shown in C. Line shows overall BF distribution of all L1 boutons pooled from all imaged regions and animals. (**F**) Same as E for L3b/4.

Could the high local heterogeneity in tuning preferences be due to the presence of poorly tuned boutons? As described in section 3.3, it is possible to assess the tuning quality of the boutons by fitting Gaussians to their level-averaged tuning curves (**Fig. 3.17-A**). Selecting only boutons with various degrees of good tuning (R^2 values higher than 0.5 and 0.7), does not significantly affect the distribution of BFs within single regions (**Fig. 4.6**, top), particularly in L3b/4. Even when only V-shaped boutons are used ($R^2 > 0.7$), the co-tuning across imaged regions is still weak, and slightly more so in L1 than in L3b/4 (**Fig. 4.6**, bottom). No significant difference in the average quality of tuning was observed between L1 and L3b/4 (**Fig. 4.7**; L3b/4: $R^2 = 0.46 \pm 0.16$, L1: $R^2 = 0.45 \pm 0.11$; $p = 0.69551$, paired t-test).

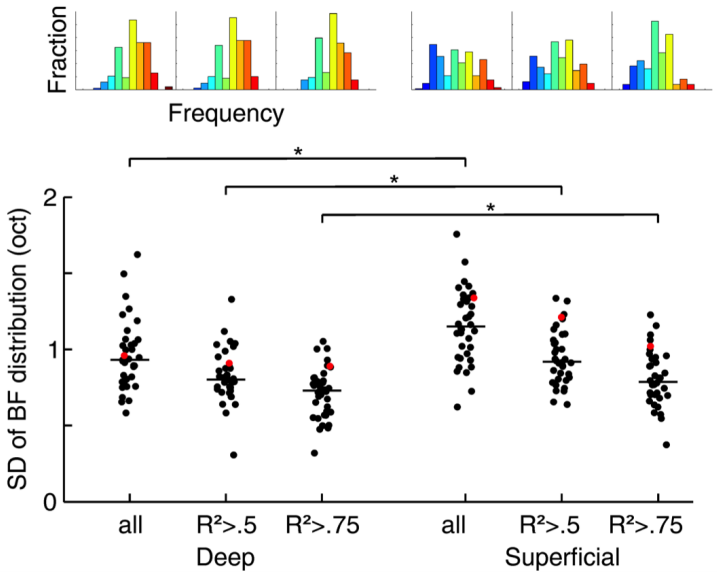

Fig. 4.6: Effects of tuning quality on measures of local heterogeneity. Top, changes in the distribution of BFs within a pair of regions in L3b/4 and L1 (same as shown in Fig. 4.5) when only boutons with an R^2 value (from Gaussian fitting to the level-averaged tuning curve) higher than a certain threshold are included. Bottom, co-tuning remains weak and slightly more so in L1, even after removing poorly tuned boutons. Red dots also correspond to the areas in in Fig. 4.5.

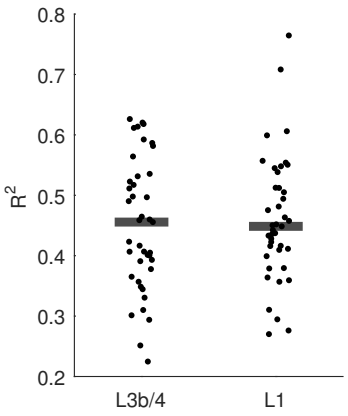

Fig. 4.7: No difference in the tuning quality of boutons in L3b/4 and L1. The mean tuning quality of boutons within an imaged area, is comparable between L3b/4 and L1 pairs. Tuning quality is measured as the R^2 value from Gaussian fitting to the level-averaged tuning curve.

Laminar differences in neuronal correlations

Besides tuning preferences, I decided to investigate other properties of the TC inputs, particularly in the form of signal and noise correlations. As in chapter 3, signal correlations were the correlation coefficients of the linearised FRA matrices for pairs of tuned bouton within the same imaged field. For noise correlations a noise vector was first obtained for each ROI by subtracting its mean response to each stimuli from

the corresponding single-trial responses. The noise correlations were the correlation coefficients between the vectors of pairs of boutons. The mean signal correlations between pairs of inputs in the same imaged area was similar for L1 and L3b/4 (**Fig. 4.8 A**; L3b/4: 0.22 ± 0.11, L1: 0.22 ± 0.14; p = 0.936, Wilcoxon Sign-rank test). However, noise correlations between the same pairs of boutons were significantly higher for pairs in L1 than in L3b/4 (**Fig. 4.8 B**; L3b/4: 0.04 ± 0.02, L1: 0.05 ± 0.02; p = 0.0004, Wilcoxon Sign-rank test). This could be partly attributed to the imaging of boutons from the same axons, which, because of its tangential arrangement in projections, would be expected to be more common in L1.

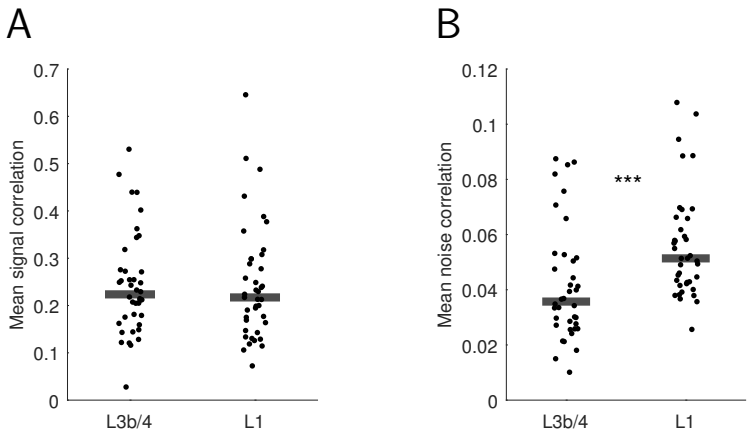

Fig. 4.8: Laminar differences in signal and noise correlation between pairs of thalamocortical boutons. (**A**) Mean signal correlations within individual regions imaged in L1 (n = 36) and L3b/4 (n = 36). (**B**) Mean noise correlations within individual regions imaged in L1 (n = 36) and L3b/4 (n = 36). Thick gray lines indicate medians.

4.3 Tonotopy in the auditory thalamocortical inputs

How can the large scale tonotopic organisation of the lemniscal projection, confirmed in the mouse through anatomical and *in vitro* voltage imaging experiments (Hackett et al., 2011), arise from such locally heterogeneous distributions? There are a number of indications, even within the small imaged patches of cortex, of tonotopic

order at the larger scale. First of all, the data revealed a close correspondence between the mean BF of a region imaged in L3b/4 and the mean BF of one imaged in L1 immediately above (**Fig. 4.9 A**; R = 0.59, P = 0.0002, n = 36, Pearson correlation). The fact that the inputs to L1 and L3b/4 are in register implies the existence of an overall BF that prevails at any x-y location of auditory cortex. It also means that, if there is a frequency gradient, the two input channels are tonotopically matched.

If the thalamic input exhibits a tight tonotopic organisation, the BF distributions of individual imaged regions should be much more narrow, i.e. they should show stronger co-tuning, than the overall BF distribution. If there is no relationship between spatial position and frequency, the BF distributions of individual regions (**Fig. 4.9 C-D**, bars) should resemble the overall BF distribution (**Fig. 4.9 C-D**, lines). I found that the overall BF distributions for L1 (1.29 octaves) and L3b/4 (1.05 octaves) exhibited slightly but significantly weaker co-tuning than individual imaged regions (L1: P = 0.003, effect size: r = 0.50, n = 36; L3b/4: P = 0.014, effect size: r = 0.42, n =36, Wilcoxon signed-rank test), indicating some selectivity in the BFs represented within imaged regions. Furthermore, the difference in co-tuning between pairs of individual L1 and L3b/4 regions (**Fig. 4.9 B**) could be accounted for by the difference between the overall BF distributions for L1 and L3b/4 (co-tuning of boutons within imaged regions / co-tuning of overall BF distribution: for L1 = 89.4 $\pm$ 29.1 %; for L3b/4 = 88.9 $\pm$ 24.3 %, P = 0.56, n = 36, Wilcoxon signed-rank test).

If the difference in co-tuning between individual regions and the overall BF distribution is the result of tonotopic organisation, then neighbouring boutons—even within a small patch of cortex—should be more similar in their tuning than topographically distant ones. Indeed, I observed a relationship between topographic distance and the difference in BF (**Fig. 4.10**). Interestingly, this very small but statistically significant correlation was present not only in the main thalamic input to L3b/4 (**Fig. 4.9-A**; R = 0.034, P < 10^{-45}, for all possible pairs of boutons, n = 167521, Spearman's correlation), but also in L1 (R = 0.035, P < 10^{-63}, n =

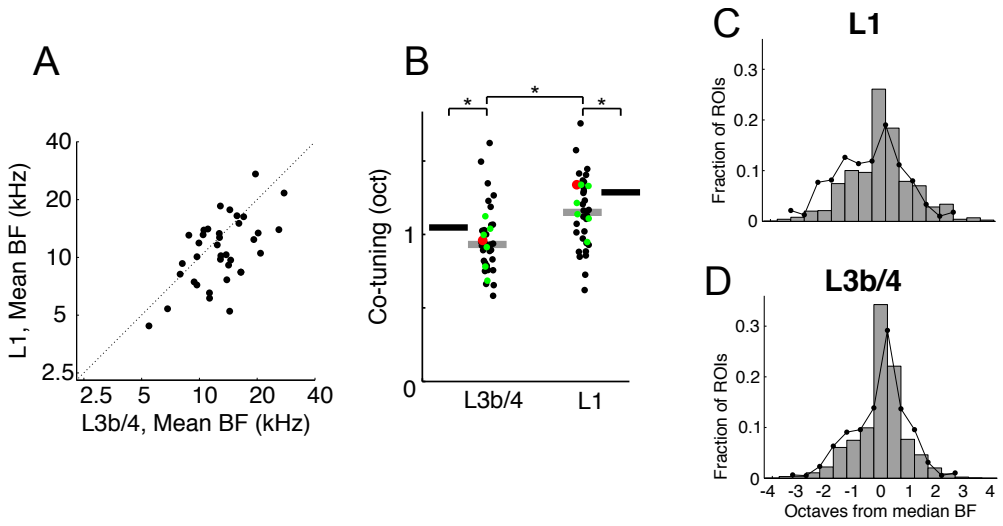

Fig. 4.9: Local indications of larger scale tonotopic organisation of inputs. (**A**) Mean BF of individual imaged regions in L1 versus mean BF of regions in L3b/4. (**B**) Co-tuning (standard deviation of BF distribution) within individual regions imaged in L1 (n = 36) and L3b/4 (n = 36). Thick gray lines indicate medians. Thick black lines indicate co-tuning for overall BF distributions (black lines in C,D). Red dots indicate co-tuning of regions shown in Fig. 4.5. Green dots indicate co-tuning of regions shown in Fig. 4.11. (**C**) Bar graph shows the average of the normalised BF distributions for L1. In order to produce this average distribution the BF distributions of individual regions (such as the one in Fig. 4.5) were normalised by setting the median BF to zero before averaging. Line plots the overall BF distribution of all pooled L1 boutons (also shown in Fig. 4.5). (**D**) Same as C for L3b/4.

237107, Spearman's correlation), suggesting that input to L1 has a similar degree of topographic order. The relationship between distance and frequency selectivity was not simply the result of a topographic clustering of boutons from the same axon because the correlation remained even when pairs with the same BF were excluded from the analysis (L3b/4: $R = 0.027$, $P < 10^{-24}$, $n = 142108$; L1: $R = 0.024$, $P < 10^{-28}$, $n = 210001$, Spearman's correlation).

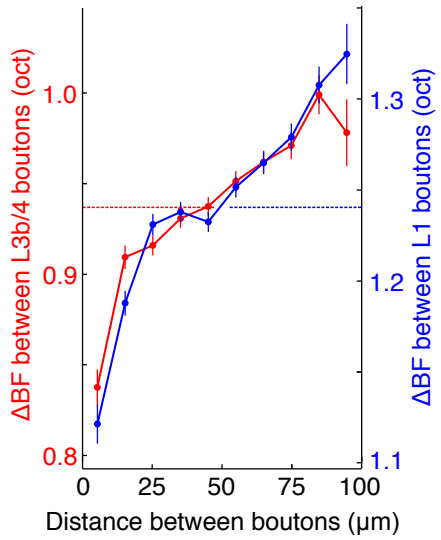

Fig. 4.10: BF difference increases as a function of physical distance between boutons. Pairwise difference in BF (delta BF) between boutons as a function of topographic distance in L1 (blue) and L3b/4 (red) for all possible bouton pairs. Number of pairs per 10 μm wide bin is between 2330 and 36725. Horizontal lines indicate average delta BF across all bouton pairs for L1 (blue) and L3b/4 (red).

Finally, I examined whether, on a more global scale spanning several hundred micrometers of cortex and several imaged regions, tonotopic gradients might become apparent. Figure 4.11 illustrates the results from an experiment in which gaps in the vasculature allowed for the imaging of several regions close together. The caudo-rostral low-to-high tonotopic gradient indicative of mouse A1 now emerged both in the inputs to L3b/4 and the inputs to L1.

As the anatomical experiments in chapter 3 revealed (section 3.2), projections from the MGBv to primary auditory cortical areas are several orders of magnitudes more extensive than the projections from any other MGB subnuclei, both in L1 and in the middle layers (**Figures 3.4 to 3.8**). The sparse labelling experiments revealed that MGBv axons tend to travel from the middle layers to L1 in columnar fashion, that is, in an almost straight line (**Fig. 3.6**, inset). This arrangement provides an anatomical substrate for the finding that L1 and L3b/4 thalamic input are in register tonotopically and exhibit a very similar organisation. Furthermore, by partially reconstructing the axon from one MGBv neuron, I was able to confirm previous work in the rabbit (Cetas et al., 1999) and monkey (Hashikawa et al., 1995) showing how extraordinarily wide the arbors of MGBv axons tend to be, and that the same MGBv neurons provide input to different layers of the auditory cortex (**Fig. 4.12**).

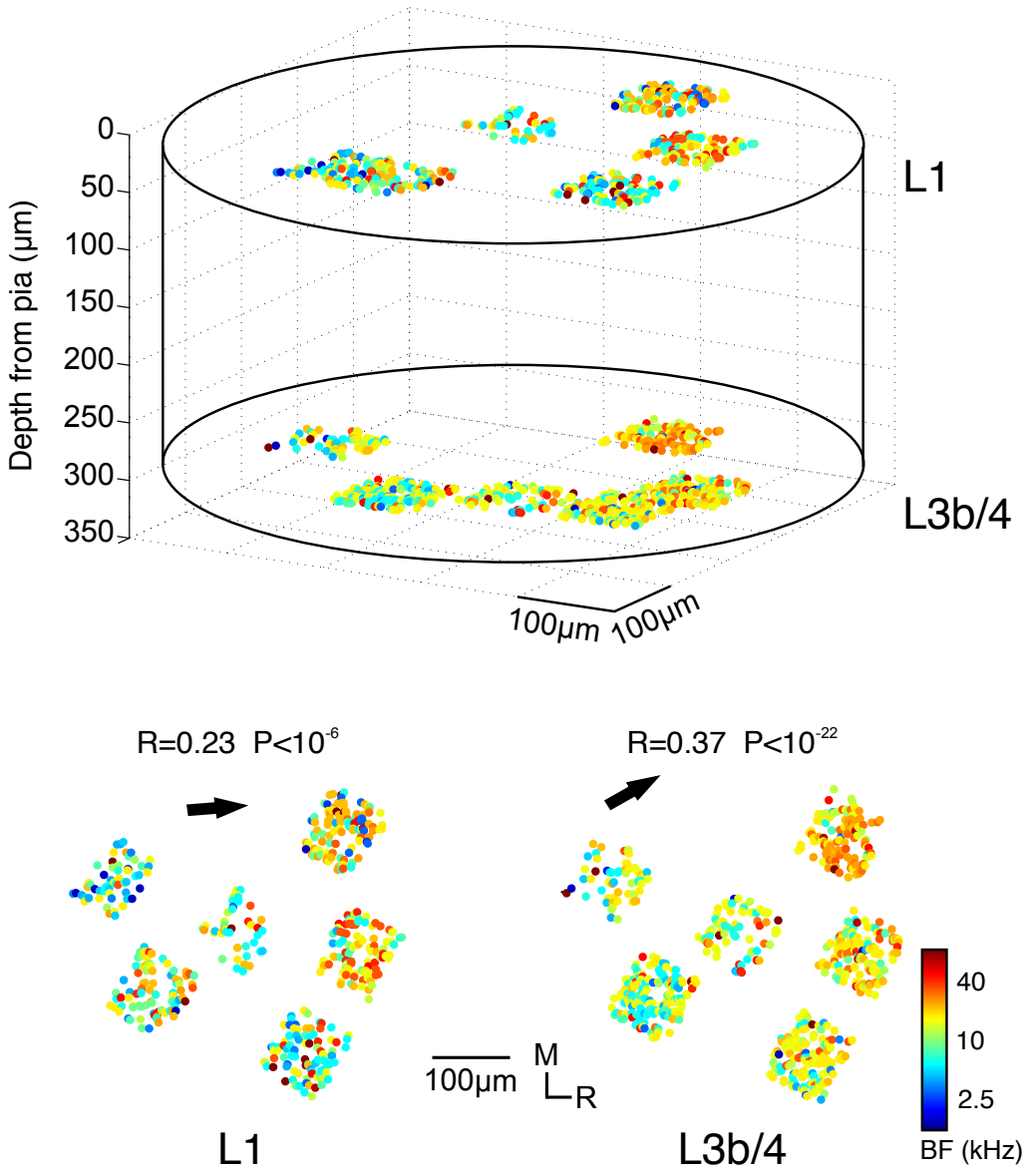

Fig. 4.11: Matching large scale tonotopic gradients in inputs to L3b/4 and L1. Top panel: relative spatial locations of tone-responsive boutons from several regions in L1 and L3b/4 of the same animal reconstructed in 3D space and color-coded according to each bouton's BF. Bottom panel: top view of the boutons shown in C separated into L1 (left) and L3b/4 (right). Arrows indicate direction of tonotopic axis in L1 and L3b/4.

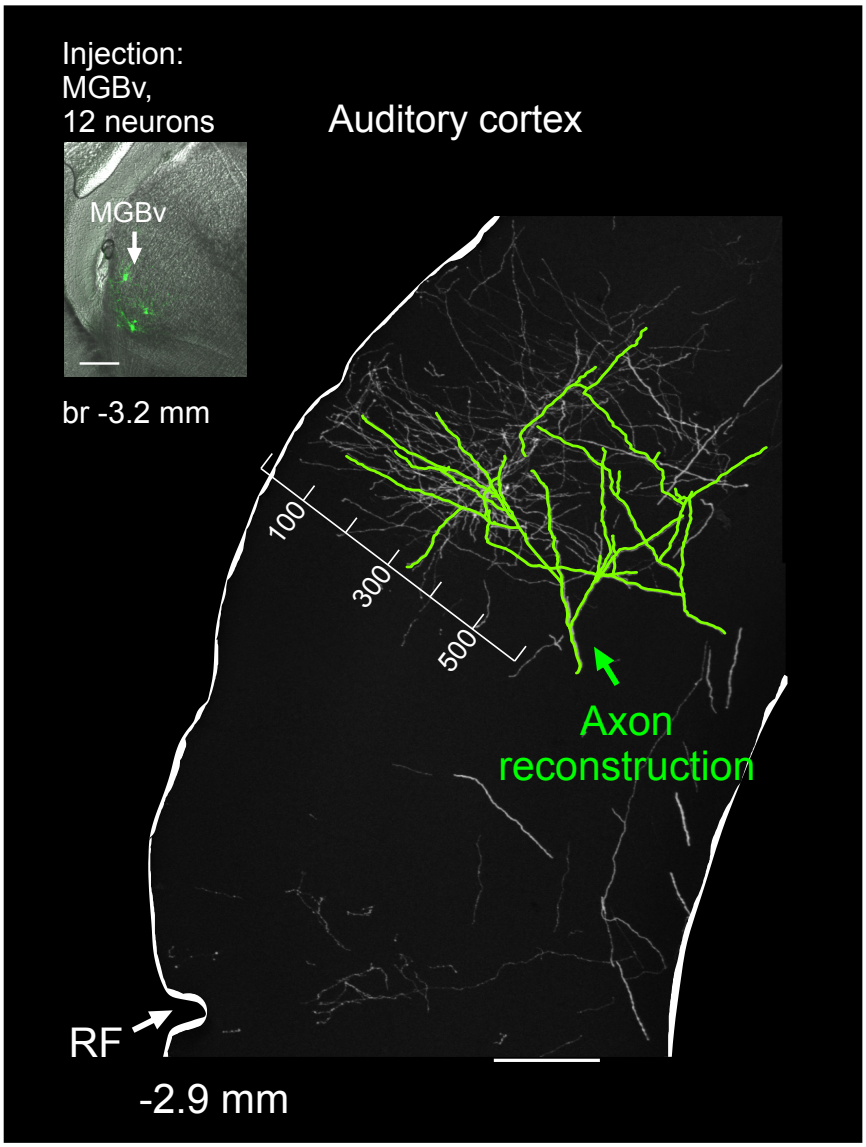

Fig. 4.12: Extensive arborisation patterns of single MGBv axons in auditory cortex. Partial reconstruction of a single MGBv axon within a 100 μm thick section of auditory cortex. Numbers indicate distance from cortical surface in μm. Top left, eGFP labelled neurons in MGBv. Scale bars, 200 μm.

Tonotopic maps of thalamic inputs and cortical neurons

One question to ask is how the tonotopy of the thalamic afferents compares with the tonotopic maps obtained from recording cortical neuron responses? Thus, I

mapped the tuning of L4 cortical neurons in a transgenic mouse line expressing GCaMP6f in most cortical excitatory neurons, using two-photon calcium imaging, and compared it with the axonal tonotopy. I found that the span and steepness of the axonal tonotopic gradient in A1 strongly resembles those of the neuronal tonotopic map (**Fig. 4.13**). A more direct observation, however, comes from those imaging experiments that were followed by anaesthetised microelectrode recordings to obtain cortical multi-unit frequency maps (**Fig. 3.11**). These show how the maps of boutons BFs at the large scale approximate generally well the BF maps from multi-unit activity in the same animal.

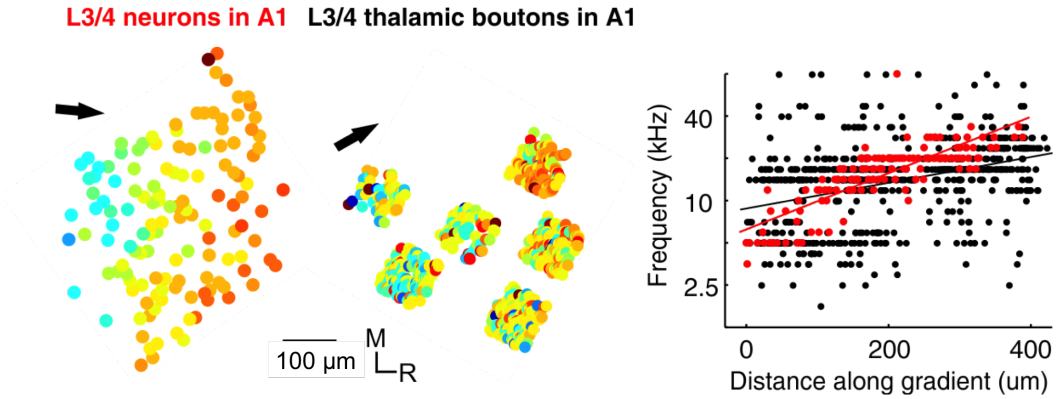

Fig. 4.13: Resemblance between tonotopic maps obtained from imaging TC boutons and cortical neurons. Left panel: tonotopic maps from two different mice, one expressing GCaMP6 in thalamocortical boutons (Same as in Fig. 4.11) and the other expressing GCaMP6 in excitatory cortical neurons. Arrows indicate direction of tonotopic axis. Right panel: Frequency gradients of both maps on the left panel, as a function of distance alongside the gradient.

Definite confirmation for the large scale tonotopicity of the lemniscal geniculo-cortical projection comes from the experiments where it was possible to image regions over a large enough span of cortex, for the caudo-rostral, low-to-high and high-to-low tonotopic gradients—that are respectively indicative of A1 and AAF—to emerge. This was particularly the case in the awake imaging experiments where a more comprehensive mapping could be carried out over several imaging sessions (**Fig. 4.14**).

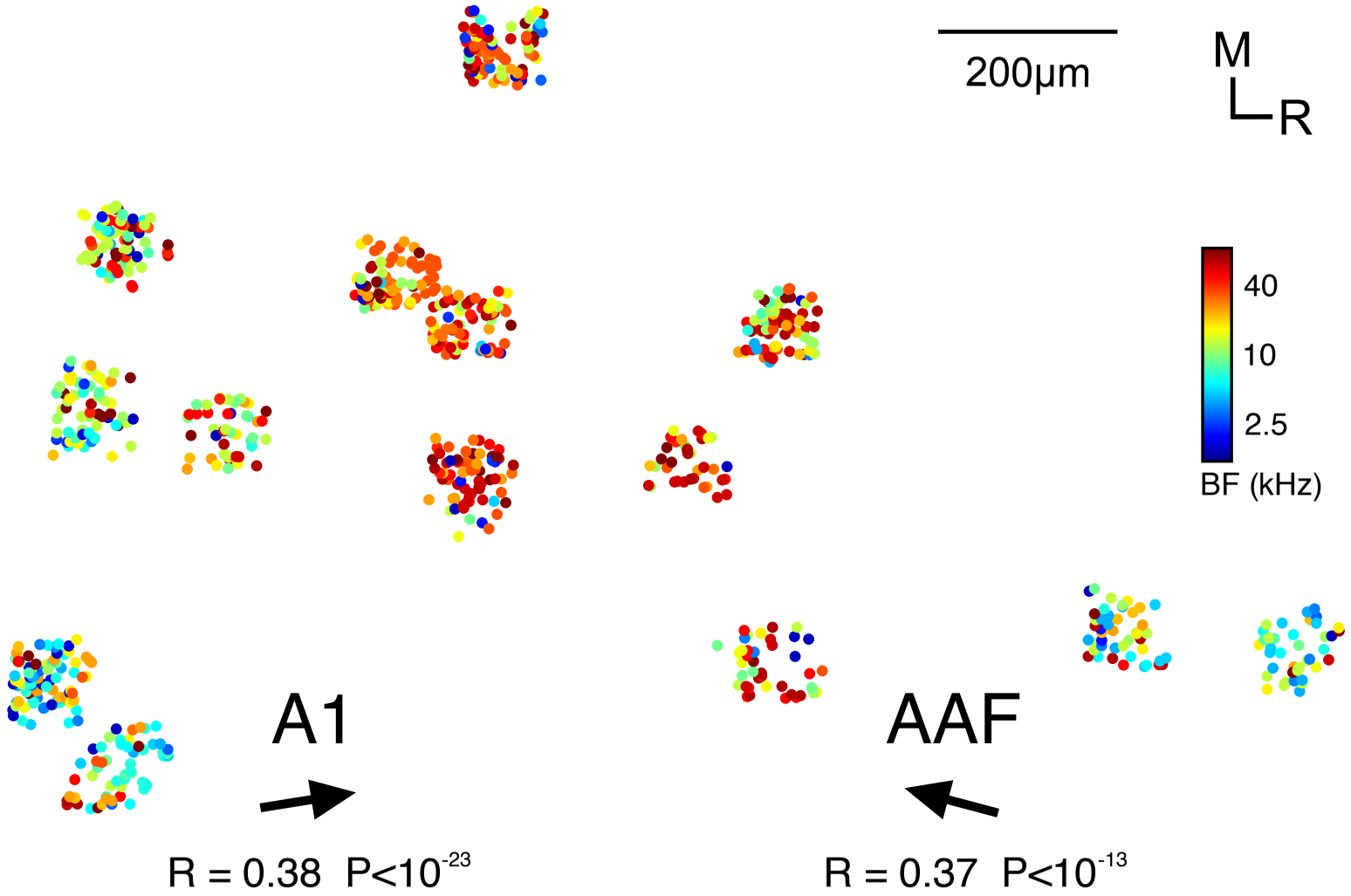
200µm
M
L
R
40
10
2.5
BF (kHz)
A1
AAF
R = 0.38 P<10-23
R = 0.37 P<10-13

(previous page)

Fig. 4.14: Tonotopic map with gradient reversal from thalamocortical boutons imaged in an awake mouse. Locations of thalamic boutons from one mouse, imaged awake, colour-coded by BF and collapsed onto the same horizontal plane. Arrows indicate direction of tonotopic axis of boutons deemed to be in A1 (left) and AAF (right).

4.4 Methodological considerations

Physiological state

The main findings from the anaesthetised imaging experiments could be all replicated in awake, head-fixed, passively listening mice (**Fig. 4.15**). In the latter, the average co-tuning per imaged region of auditory cortex was just above one octave both near the cortical surface and in the middle layers (**Fig. 4.15-A-B**) with slightly stronger co-tuning in L3b/4 (1.21 $\pm$ 0.64 octaves) than in L1 (1.42 $\pm$ 0.50 octaves, P = 0.011, effect size: r = 0.40, n = 20, Wilcoxon signed-rank test, Figure 3D). Moreover, as in the preceding experiments, the inputs to L1 and L3b/4 were matched tonotopically (**Fig. 4.15-C**; R = 0.67, P = 0.0013, n = 20, Pearson correlation) and, as seen in figures 4.14 and 3.11, tonotopic gradients were also observed in the bouton maps at the large scale.

The imaging in awake mice revealed an even weaker co-tuning of inputs within imaged regions of the same size as the anaesthetised condition (**Fig. 4.16-A**; awake: 1.25 $\pm$ 0.34 octaves, anaesthetised: 1.06 $\pm$ 0.34; p = 0.001, unpaired t-test). This difference might be to a great extent caused by the overall lower tuning quality of boutons in the awake condition as compared to the anaesthetised imaging (**Fig. 4.16-A**; awake: 0.45 $\pm$ 0.32, anaesthetised: 0.65 $\pm$ 0.32; 4 e^{-234}, Wilcoxon rank-sum test).

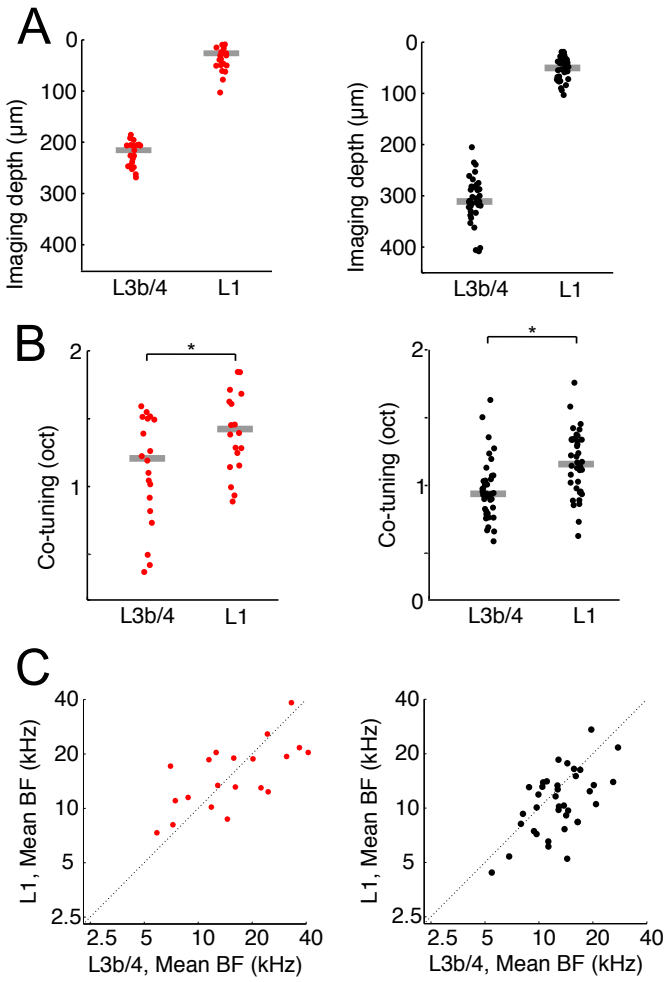

Fig. 4.15: Replication of main findings using awake C57BL/6NTac mice. (**A**) Depth of all imaged regions in awake C57BL/6NTac.Cdh23$^{753A>G}$ (left) and anaesthetised C57BL/6 (right) mice (same as Fig. 4.1). (**B**) Co-tuning (standard deviation of BF distribution) within individual regions imaged in L1 (n = 20) and L3b/4 (n = 20) in awake C57BL/6NTac.Cdh23$^{753A>G}$ (left) and anaesthetised C57BL/6 (right) mice (same as Fig. 4.3). (**C**) Mean BF of individual imaged regions in L1 versus mean BF of regions in L3b/4 in awake C57BL/6NTac.Cdh23$^{753A>G}$ (left) and anaesthetised C57BL/6 (right) mice (same as Fig. 4.9 A).

Mouse strain

The anaesthetised imaging experiments reported in this chapter were performed on C57BL/6 mice and later replicated in awake mice of the related line C57BL/6NTac. Cdh23$^{753A>G}$. The C57BL/6 strain is the most popular laboratory mouse strain, and is used as genetic background for the overwhelming majority of genetically modified mouse strains. This strain has been reported to undergo high-frequency hearing loss by 3–6 months of age which progresses to profound impairment by 15 months

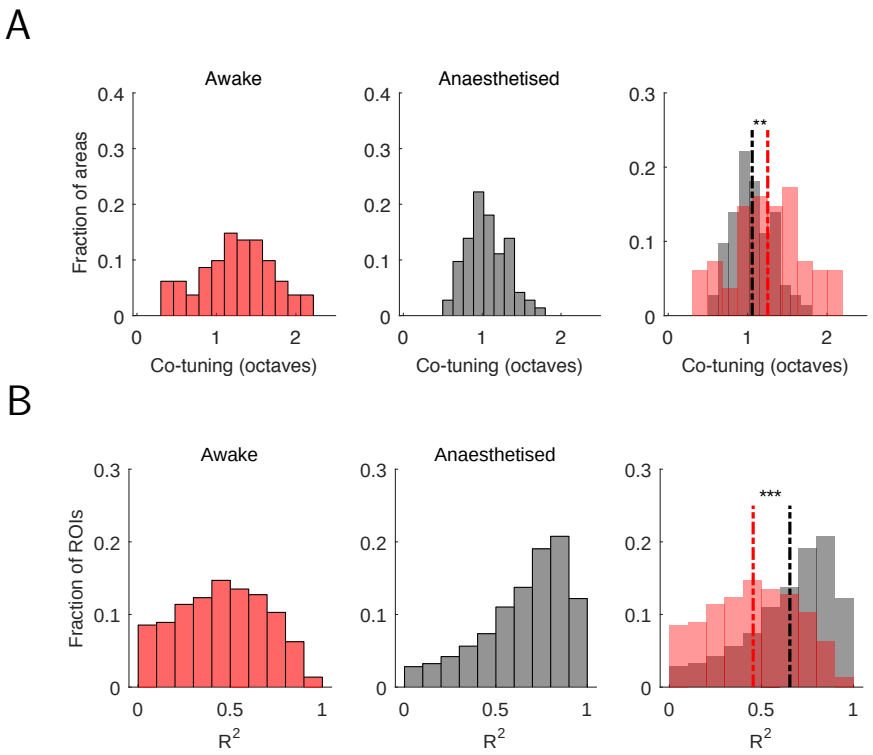

Fig. 4.16: Awake-anaesthetised differences in tuning quality and local co-tuning of thalamocortical boutons. (**A**) Distributions of co-tuning measures for all areas imaged in the awake and anaesthetised experiments. (**B**) Distributions of tuning quality for all bouton ROIs imaged in the awake and anaesthetised experiments. Tuning quality is measured as the R^2 value from Gaussian fitting to the level-averaged tuning curve.

(Henry and Chole, 1980). While C57BL/6 mice are not normally considered to suffer from impaired hearing at the age used here (Ison et al., 2007), there have been some reports that a decline in the number of neurons tuned to high frequencies can be detected as early as 1-2 months after birth, especially at higher levels of the auditory pathway such as the cortex (Willott et al., 1993). This was the motivation to use the C57BL/6NTac.Cdh23$^{753A>G}$ line, in which the Cdh23ahl allele that otherwise predisposes this strain to age-related high-frequency hearing loss has been corrected (Mianné et al., 2016).

While the C57BL/6NTac.Cdh23$^{753A>G}$ mice also showed a bias for frequencies near the middle of their hearing range, the proportion of high frequency BFs was greater than in the C57BL/6 mice and the overall BF distribution, thus, broader (**Fig. 4.17**). Overall, the median number of tone-responsive boutons obtained per imaging region was lower (29.5 $\pm$ 23), which could be partly due to the effects of anaesthesia vs

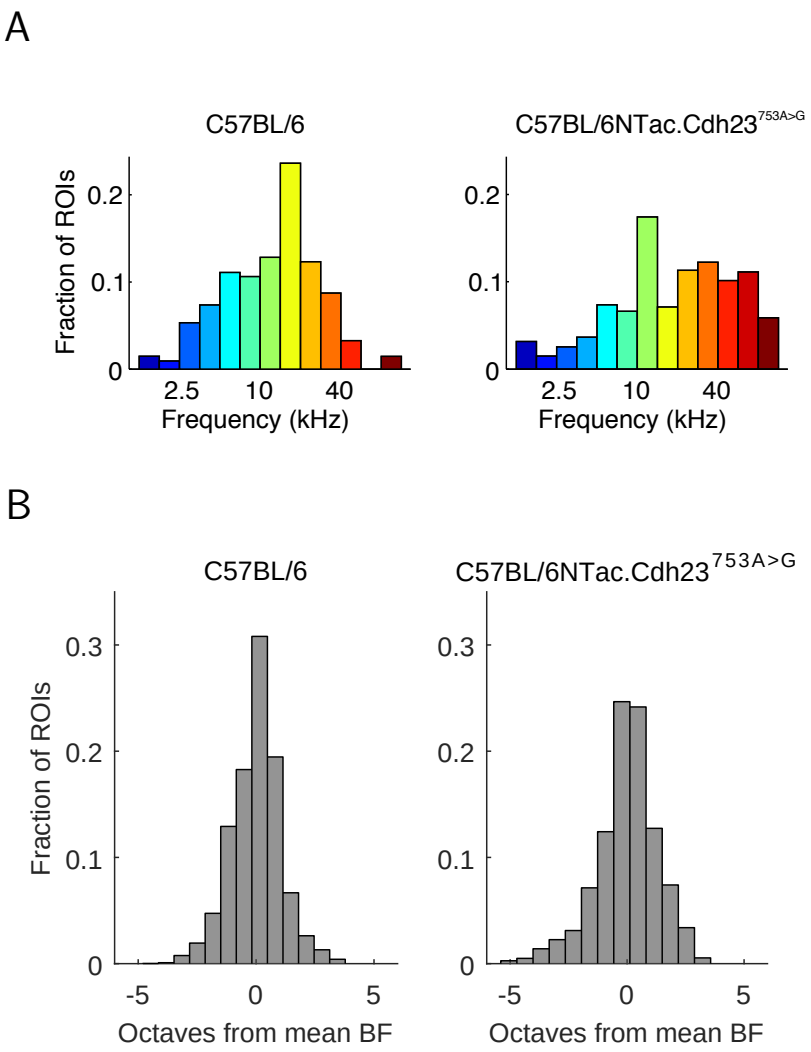

Fig. 4.17: Over-representation of higher frequencies in experiments using awake C57BL/6NTac.Cdh23$^{753A>G}$ mice. (**A**) Left: overall BF distribution of all boutons from C57BL/6 mice. Right: overall BF distribution of all boutons from C57BL/6NTac.Cdh23$^{753A>G}$ mice. (**B**) Bar graphs show the average of the normalised BF distributions for all imaged areas. In order to produce this average distribution the BF distributions of individual regions were normalised by setting the median BF to zero before averaging. Left: distribution for C57BL/6 mice. Right: distribution for C57BL/6NTac.Cdh23$^{753A>G}$ mice.

wakefulness (Zurita et al., 1994). However, this might also reflect strain differences or other differences in methodology, such as the fact that I tended to image these animals slightly sooner after the virus injections (3-4 weeks) but over several days rather than in a single session immediately after the window implantation. Otherwise, as described above, the results were remarkably similar.

4.5 Discussion

That the thalamocortical projection is topographically arranged has been known for a long time (Le Gros Clark, 1936; Walker, 1937). Until recently, however, it has not been possible to characterize the receptive fields of individual thalamic boutons (Roth, 2003), preventing any physiological assessment of how precisely organised this projection is. Very similar patterns of results were observed across two strains of C57BL/6 mice, one of which had the $Cdh23^{ahl}$ allele that otherwise predisposes this strain to age-related high frequency hearing loss corrected, and across both anaesthetised and awake animals. The proportion of neurons with high BFs was greater in the C57BL/6NTac.$Cdh23^{753A>G}$ mice, potentially indicative of the beginning of high-frequency loss in the other animals. It is important to note, nonetheless, that my experiments did not attempt to evenly sample from every frequency band of auditory cortex. Thus, it is possible that the differences in BF distributions between C57BL/6 and C57BL/6NTac.$Cdh23^{753A>G}$ might in reality be more or less pronounced than described here. While the study was designed to capture the full extent of the thalamic input available to the auditory cortex, my own anatomical data together with the work of others (Hackett et al., 2011; Llano and Sherman, 2008), show that the organisation I describe here reflects almost exclusively the properties of the lemniscal thalamocortical projection from the MGBv to the primary cortical areas.

The presence of a well-defined tonotopic organization in the main thalamorecipient middle layers of auditory cortex (Guo et al., 2012; Hackett et al., 2011; Winkowski and Kanold, 2013) implies that the thalamic input should also be precisely arranged. Although the diffuse organization observed with axon bouton imaging contrasts with that expectation, it does provide an explanation for other findings. For instance, the observation that focal electrical stimulation of the MGB causes widespread activation of the cortex over several hundred micrometers (Hackett et al., 2011; Kaur et al., 2005) is easier to reconcile with a diffuse thalamocortical connectivity pattern in which similarly tuned thalamic axons, or even the same axon (Cetas et al.,

1999), can connect with neurons located far apart in the auditory cortex. Similarly, the demonstration that thalamic inputs determine the bandwidth of the broadly tuned excitatory synaptic FRAs of auditory cortical neurons (Liu et al., 2007) can be explained more readily by my finding that most auditory cortical neurons have, within the boundaries of their dendritic trees (Richardson et al., 2009), access to thalamic terminals tuned to frequencies that collectively span several octaves.

My results show that the cortical frequency map is built from a thalamic input map which is itself poorly organised. Thalamic projections synapse preferentially on spines within 100 μm of the soma of L3 and L4 neurons (Richardson et al., 2009) but how exactly these neurons integrate the available thalamic input to produce a more precisely ordered cortical frequency representation is unclear. Several mechanisms could contribute to this transformation. First, recent work in the visual cortex has shown that dendritic nonlinearities can affect the tuning of neurons (Wilson et al., 2016). Second, recurrent connections between cortical neurons, comprising over half of their inputs (Lübke et al., 2000), can amplify (Happel et al., 2010; Li et al., 2013a) and may potentially homogenise (Liu et al., 2007) local tuning, especially if they are biased (Cossell et al., 2015). Finally, auditory cortical neurons may sample their thalamic inputs in a biased manner, similar to what has been proposed in the visual system (Clay Reid and Alonso, 1995). However, given the broad synaptic tuning reported for thalamic inputs onto individual auditory cortical neurons —in rats the range of frequencies covered by the thalamic inputs onto a single L4 neuron lies between 3 and 5 octaves (Liu et al., 2007)— such biased connectivity seems less likely in the auditory thalamocortical system.

I found that L1 and L3b/4 inputs are fairly well matched tonotopically and show only minor differences in the degree of BF heterogeneity. This is consistent with two other studies which also found only minor differences between the responses to oriented gratings of thalamic axons in L1 and L4 of visual cortex (Kondo and Ohki, 2016; Sun et al., 2016). Furthermore, my anatomical work revealed that many lemniscal thalamic axons travel from the middle layers up to L1 in a columnar fashion, a feature that helps explain why the properties of the thalamic input to L1

and to the middle layers are so similar. Traditionally, thalamic inputs to L1 and L3b/4 have been classified as belonging to orthogonal channels, with L1 inputs described as matrix-type and L3b/4 input as core-type (Clascá et al., 2012; Harris, 2015; Jones, 2001). Yet, a number of single axon tracing studies in various species and cortical regions have described thalamic axons that form dense plexuses in L4 and project collaterals to L1 (Cetas et al., 1999; Hashikawa et al., 1995; Kuramoto et al., 2009; Oda et al., 2004). These and my current findings suggest that the laminar separation of matrix- and core-type inputs might require some revisions (**Fig. 4.18**).

Although thalamic inputs primarily target the middle cortical layers, they innervate all cortical layers and particularly L1 (Huang and Winer, 2000; Kimura et al., 2003; Kondo and Ohki, 2016; Roth et al., 2016; Rubio-Garrido et al., 2009; Sun et al., 2016). Thalamic axons in L1 have different neuronal targets, mostly L1 inhibitory neurons (Cruikshank et al., 2007; Ji et al., 2015) and the apical dendrites of supra- and infragranular excitatory neurons (Harris, 2015; Petreanu et al., 2009), from those terminating in the middle layers, but whether the content of the information transmitted to different cortical layers also differs is not well understood. In other sensory systems (Roth et al., 2016), input from higher-order thalamic nuclei has been shown to carry more motor and contextual sensory signals. Nevertheless, L1 does receive a larger proportion of input from higher-order thalamic nuclei than L3b/4 (Frost and Caviness, 1980; Linke, 1999; Linke and Schwegler, 2000; Llano and Sherman, 2008; Ryugo and Killackey, 1974; Smith and Häusser, 2010). Given that, in other sensory systems (Roth et al., 2016), input from higher-order thalamic nuclei has been shown to carry more motor and contextual sensory signals than the input from the first order nucleus, and that I observed generally poor responses to tone stimulation in higher-order thalamic axons, it is likely that recordings in behaving animals will reveal more pronounced differences between L1 and L3b/4 input.

A key question arising from my findings is why auditory thalamocortical projections are so imprecise. Precisely-organized tonotopic maps have been identified subcortically in the lemniscal part of the mouse inferior colliculus (Barnstedt et al., 2015;

Portfors et al., 2011; Stiebler and Ehret, 1985), and anatomical and electrophysiological data indicate that the lemniscal thalamus is likely to be similarly organised (Hackett et al., 2011; Lee and Sherman, 2010; Wenstrup, 2005). Input from the dorsolateral geniculate nucleus to the visual cortex tends to be highly retinotopically ordered (Roth et al., 2016), so the mouse brain is capable of establishing and maintaining very precise connections between thalamus and cortex. This suggests that the diffuse topographic arrangement I observed in the auditory system may be functionally relevant. Broad spectral integration enables auditory cortical neurons to form representations of behaviorally-relevant sound sources (Bar-Yosef et al., 2002; Las et al., 2005). Furthermore, studies in different species have shown that auditory cortical frequency representations are highly plastic over multiple timescales (Dahmen and King, 2007), and individual neurons can rapidly change their stimulus selectivity with the behavioral context (Fritz et al., 2003). Such dynamic modulation of sound frequency processing can only be possible if cortical neurons have access to spectrally broad inputs (Chen et al., 2011b; Intskirveli et al., 2016; Metherate et al., 2005; Miller et al., 2001; Winer et al., 2005). The organization of the thalamocortical projection revealed here is likely to be one part of the neural architecture underpinning this rapid plasticity and the cognitive flexibility it enables.

Fig. 4.18: Revised model of thalamocortical projections types in the mouse MGB. Updated schematic of the distribution of TC projection neuron types in the mouse medial geniculate body (MGB) and their typical axon morphology, based on the results from the experiments in this chapter. Adapted from Fig. 3.2 and Clascá et al. (2012). *ACx*, auditory cortex; *CB+*, calbindin positive; *CR+*, calretinin positive;*MGBd*, dorsal division of the medial geniculate body; *MGBm*, medial division of the medial geniculate body; *MGBv*, ventral division of the medial geniculate body; *TRN*, thalamic reticular nucleus.

5 Auditory Thalamocortical and Columnar Transformations

5.1 The auditory cortical column

Having obtained an understanding about the topographic micro-organisation of TC afferents in cortex, the next question to ask is how cortical neurons sample this map of inputs and transform it through subsequent intracortical columnar processing. As discussed earlier, such transformations in cortical maps can inform about micro-circuit function. Observations of degradation or sharpening of tonotopy have been frequently been used in attempting to infer the function and computations performed within and across auditory cortical fields (Linden and Schreiner, 2003; Schreiner and Winer, 2007). In the case of auditory columnar transformations, there has been little consensus across electrophysiological studies attempting to assess how auditory receptive fields are transformed through the layers of the cortical column (reviewed in Linden and Schreiner, 2003).

Although the term *cortical column* is used here, a column in the strictest sense of distinguishable functional unit may not be a canonical organisational principle in auditory cortex, as their variable presence in some species and cortical areas suggests (Horton and Adams, 2005). However, the existence of a laminar organisation with specific patterns of vertical connectivity, and well characterised layer differences in terms of inputs and outputs is a well documented feature of auditory cortex (Winer and Schreiner, 2010).

More recently, high-resolution imaging through two-photon microscopy was again able to shed some light on the matter. Winkowski and Kanold (2013) revealed

that neurons in L4 show a more homogeneous spatial organisation of frequency tuning and higher signal and noise correlations than neurons in L2/3. This particular transformation of spectral representations between layers of the auditory cortex could generate progressively more complex analysis of sound features. However, it is not clear how this transformation comes about. Whilst cortico-cortical inputs are likely to play a role, one important consideration is that neurons, both excitatory and inhibitory, throughout all cortical layers receive direct TC input, albeit with different synaptic strengths (Ji et al., 2015; Harris, 2015; Constantinople and Bruno, 2013). The way in which these direct thalamic inputs interact with lateral and vertical intracortical inputs to shape an auditory neuron's receptive fields is not well understood.

In this chapter, I will present the results of a series of experiments using dual-colour two-photon calcium imaging of thalamic axons and cortical neurons in the auditory cortex of awake, passively listening mice. The attempt is to evaluate the contribution of thalamocortical inputs to spectral integration in auditory cortex, as well as to explore the transformations in spectral receptive fields taking place between thalamus and cortex and within the granular and supragranular layers of the cortical column. By studying laminar differences in response properties of cortical neurons and, in this case, of nearby thalamic inputs, I hope to provide some insights into the type of local transformations taking place within primary auditory cortex.

5.2 Experimental strategy

There are on the order of 10^5 neurons in a cubic millimetre of cortex (Braitenberg et al., 1998). This makes comprehensive measurement of cortical neural activity with traditional electrophysiological methods challenging. As previously mentioned, two-photon calcium imaging has been successfully used to study laminar differences

in response properties of neurons in the mouse auditory cortex (Winkowski and Kanold, 2013). The same method has also been used to produce a cellular resolution map of barrel cortex activity during tactile behaviour in mice (Peron et al., 2015a; Peron et al., 2015b). Such experiments involved the imaging of multiple cortical planes in the supragranular layers of barrel cortex and revealed a heterogeneous representation of multiple tactile features throughout the column. The following is a demonstration that a similar approach can be used to study the laminar distribution of spectral properties of both auditory cortical neurons and thalamic afferents.

In order to acquire a comprehensive map of tone-evoked activity in a cortical volume, I made combined use of two-photon calcium imaging and genetically-encoded calcium indicators. This time, I took advantage of the recent improvements in red-shifted indicators (Akerboom et al., 2013; Dana et al., 2016) that have given them comparable sensitivity to GCaMP indicators. Of these red indicators, I found jRGECO1a (Dana et al., 2016) to provide the best levels of expression, sensitivity and, most importantly, spectral separation with GCaMP6m. By virally transfecting neurons in primary auditory cortex of the mouse with jRGECO1a, and MGB neurons with GCaMP6m, I was able to distinguish the activity of TC axon terminals and local neurons within the same volume of tissue.

Thalamic viral injections were done in the same way as for the tonotopy mapping experiments in chapter 4. Injections were large enough to ensure that all divisions of the medial geniculate body (MGB) were labelled with GCaMP6m (**Fig. 5.1**). For labelling neurons in primary auditory cortex with jRGECO1a, I performed cortical viral injections at the same time as the cranial window surgery. As with all the imaging experiments discussed previously, stereotaxic coordinates and skull landmarks were used for keeping the location of window placement relatively constant. As a consequence, A1 and AAF were always located in the same quadrants of the cranial window. This was used to guide the location of the jRGECO1a viral injections. Moreover, injections were made at 3 to 4 sites along the rostro-caudal axis to allow for the initial determination of tonotopic gradients in the first imaging session. After the final round of imaging, I confirmed histologically the extent of

MGB labelling and the location of cortical labelling using existing stereotaxic fine-scale atlases of the mouse brain (Tsukano et al., 2017b; Paxinos and Franklin, 2013). Detailed descriptions of the viral injection and craniotomy surgeries can be found in the Materials and Methods chapter.

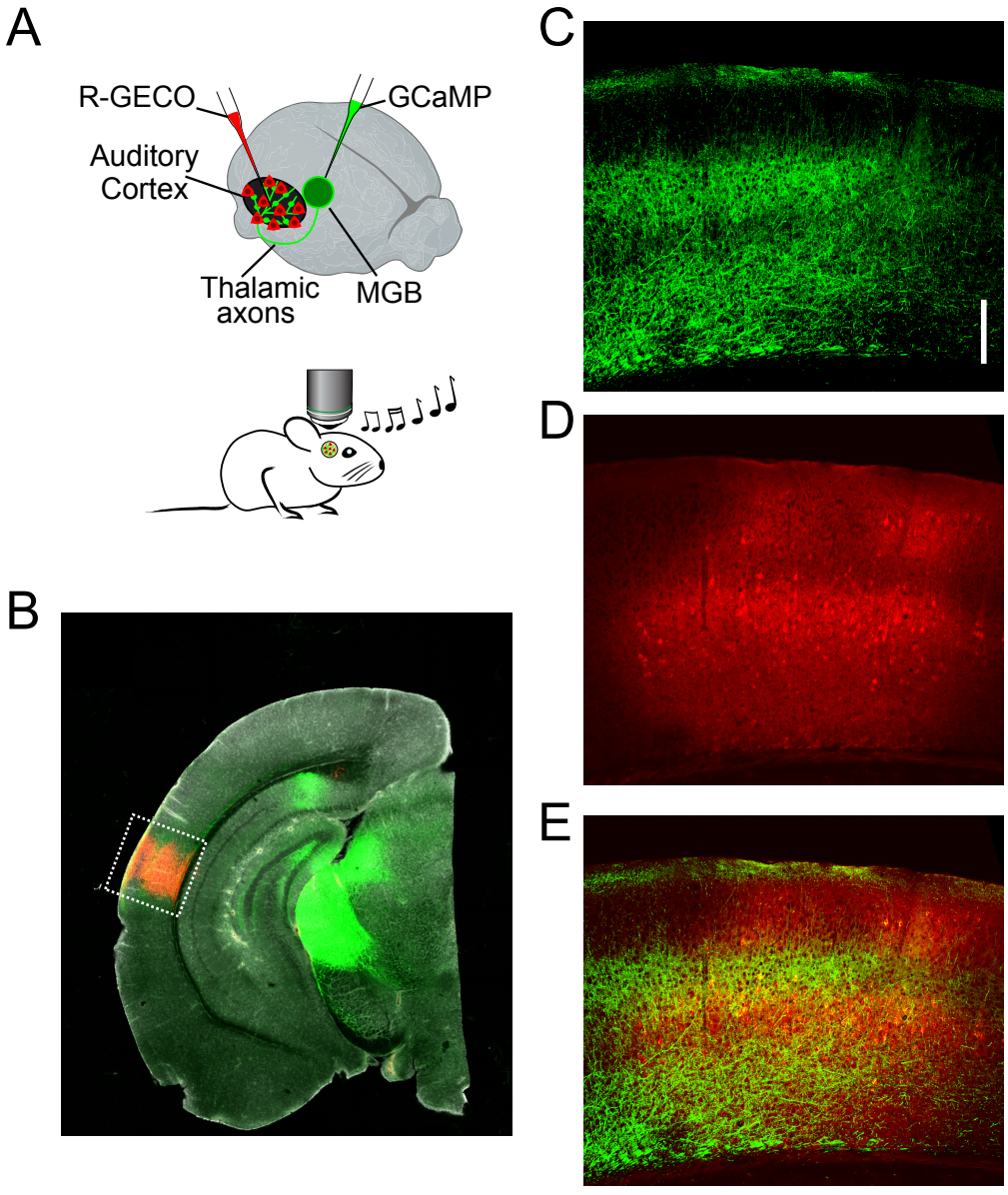

Fig. 5.1: Functional characterization of auditory thalamocortical transformations through dual-color calcium imaging. (**A**) Experimental schematic. Responses to pure tones of thalamocortical terminals and cortical neurons in auditory cortex were imaged using two-photon microscopy in awake, head-fixed mice expressing the green calcium indicator GCaMP6m in the MGB and the red calcium indicator jRGECO1a in auditory cortex. (**B**) Coronal section showing labelling of MGB with GCaMP6m and auditory cortex with jRGECO1a. (**C**-**E**) Closer view of labelling in auditory cortex (dashed box in B) showing GCaMP6m-labelled thalamic terminals (**C**), jRGECO1a-labelled cortical neurons (**D**), and merge (**E**). Size bar = 200 μm.

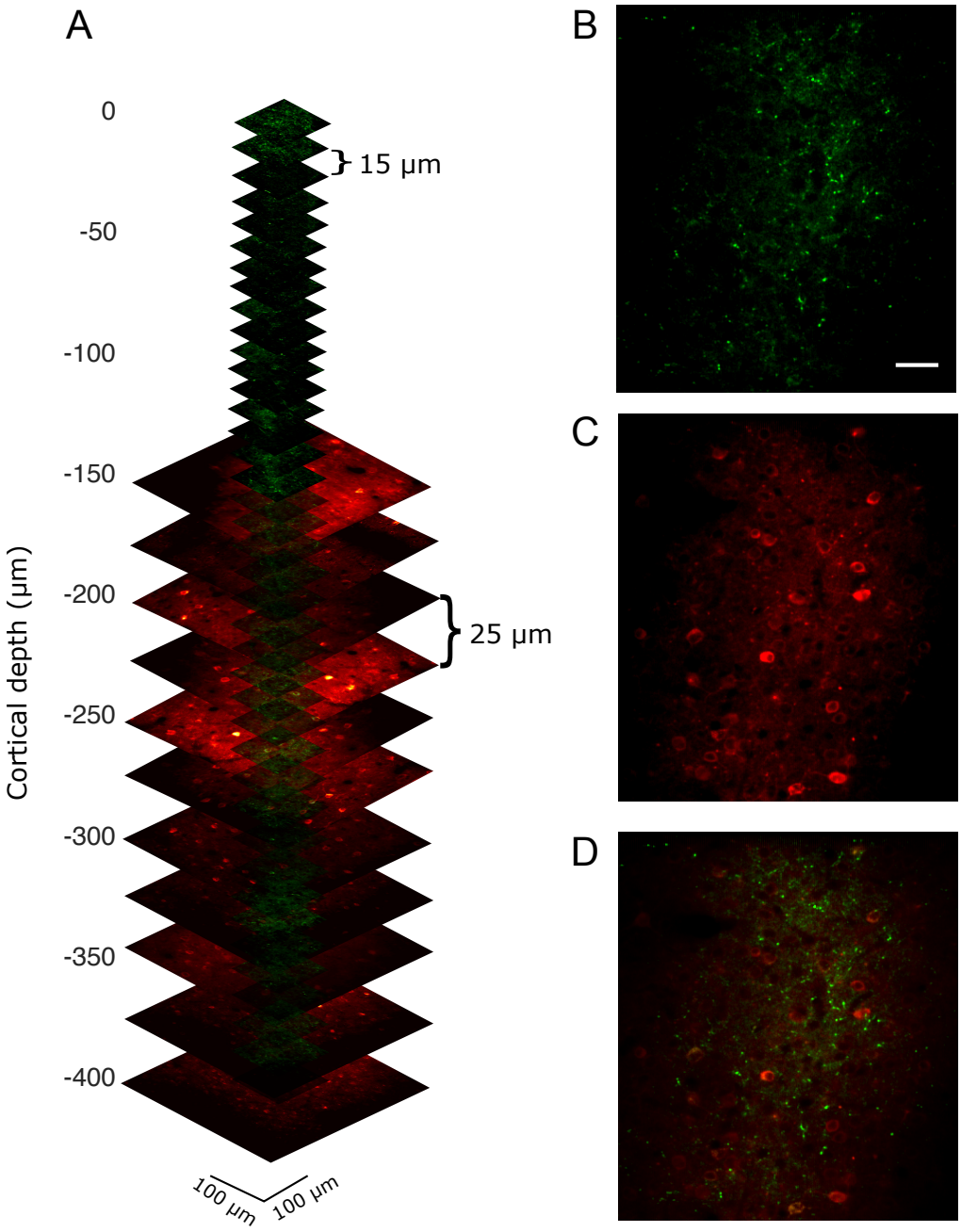

Fig. 5.2: Volume imaging of auditory cortex in awake, head-fixed mice. (**A**) Stacked reconstruction of an jRGECO1a volume and a GCaMP6 subvolume. Red fluorescence indicates cortical neurons labelled with jRGECO1a; green fluorescence indicates thalamic axonal terminals labelled with GCaMP6m. Imaging volumes and subvolumes consist of a series of imaging planes imaged consecutively, every 15 μm and 25 μm respectively, and at zoom levels and laser settings optimal for the structures and calcium indicator being monitored. Within these neuronal imaging volumes, a subvolume of thalamic axons was imaged. Two to three pairs of volume-subvolume were imaged per animal, each at different X-Y coordinates on the auditory cortex. (**B**-**D**) Example of one imaging plane (100 μm x 100 μm for GCaMP6m, 330 μm x 330 μm for jRGECO1a, 512 x 512 pixels) showing the expression of GCaMP6m in thalamic axons (green) (**B**), RGECO in cortical neurons (red) (**C**), and merge (**D**). Dashed box shows the size of the axonal imaging plane. Axonal and neuronal planes within the same volume do not always overlap. Scale bar = 200 μm.

Imaging sessions in awake, head-fixed mice were started three weeks after viral injections. Because of differences in the absorption spectra of jRGECO1a and GCaMP6m, the laser wavelength had to be adjusted for appropriate excitation of each indicator, thus, cortical neurons and thalamic axons were imaged in separate trials. In order to determine the spectral receptive fields of a large proportion of neurons within volumes of primary auditory cortex, I imaged the same cortical locations at different z-planes (330 μm x 330 μm field of views; 512 x 512 pixels), each 25 μm apart, from a depth of 150 μm to 400 μm from the cortical surface (**Fig. 5.2**). The average volume of cortex sampled for neuronal imaging was 0.044 mm^3 $\pm$ 0.006 (s.d.) (mean number of imaged planes per volume: 11 $\pm$ 2.1). Within each of these large cortical volumes, I imaged subvolumes (100 μm x 100 μm field of views; 512 x 512 pixels), with planes 15 μm apart and from a depth of 15 μm to 400 μm, in order to characterise the receptive fields of labelled TC terminals found therein. The average subvolume of axonal imaging was 0.0040 mm^3 $\pm$ 0.0016 (s.d.) (mean number of imaged planes per volume: 23 $\pm$ 10.8), or a tenth of the average volume sampled with neuronal imaging.

5.3 Laminar differences in spectral tuning

During imaging, a large number of labelled neurons was observed throughout layers 2, 3 and 4. The mean number of segmented neurons per volume was 935 $\pm$ 576 (s.d.), whilst boutons per subvolume were 5592 $\pm$ 2991 (s.d.). The average number of labelled neurons visible per image plane was relatively constant from 100 μm to 200 μm in depth, after which it decreased as a function of depth (**Fig. 5.3 A**). Since the histology revealed RGECO labelling through all cortical layers, this was possibly due to the limitations of our optical system. The average number of putative synaptic boutons was highest in L1, where the density of TC terminals is also highest. It then decreased slightly and did not increase again in middle layers, as would be

expected from the histology, again suggesting that the optical limits of our setup were being reached. The maximum depth of imaged planes was 400 μm, after which the fluorescent signal was too low to be detected.

The quality of tuning is comparable in cortical neurons and thalamic boutons

For each imaged area, I presented randomised blocks of pure tones at three different levels, in order to determine the spectral receptive fields of cortical neurons and TC boutons. A smaller stimulus set than in the previous experiments (although with the same number of repetitions) was used here, which allowed me to image more areas in the available imaging sessions and to achieve an appropriately dense sampling of the cortical volumes. For each volume of auditory cortex sampled, I recorded from dozens of cortical neurons and hundreds of thalamic boutons that were tone-responsive and mostly well-tuned (**Fig. 5.3B-D**) (tuned neurons: 73 $\pm$ 46 (s.d.), n = 12 volumes; tuned boutons: 337 $\pm$ 296 (s.d.), n = 12 subvolumes). For cortical neurons, tuning was most prevalent in layer 3b/4 (250 - 400 μm, 12.5% $\pm$ 3.2 of neurons). For TC boutons, tuning was also most prevalent in layer 3b/4 (14.2% $\pm$ 4.1 of putative boutons) and in layer 1 (11.3% $\pm$ 3.0). The quality of tuning was comparable between neurons and boutons as assessed by fitting the level-averaged tuning curves with a Gaussian (**Fig. 5.4**, R^2 for boutons: 0.58 $\pm$ 0.37 (median $\pm$ interquartile range), R^2 for neurons: 0.59 $\pm$ 0.37; p = 0.08, Wilcoxon rank-sum test).

Laminar differences in spectral tuning variability

This dense mapping confirmed the observations from the experiments in chapter 4, of high local heterogeneity in the tuning of TC boutons (**Fig. 5.5**), although the degree of co-tuning (0.78 $\pm$ 0.28 octaves) was slightly stronger than what was recorded in chapter 3 and 4. This is very likely due to the fact that the range of frequencies used here for receptive field mapping was narrower (2.5 – 40 kHz) than the one used before (1.25 – 80 kHz). The experiments also revealed a high degree of local

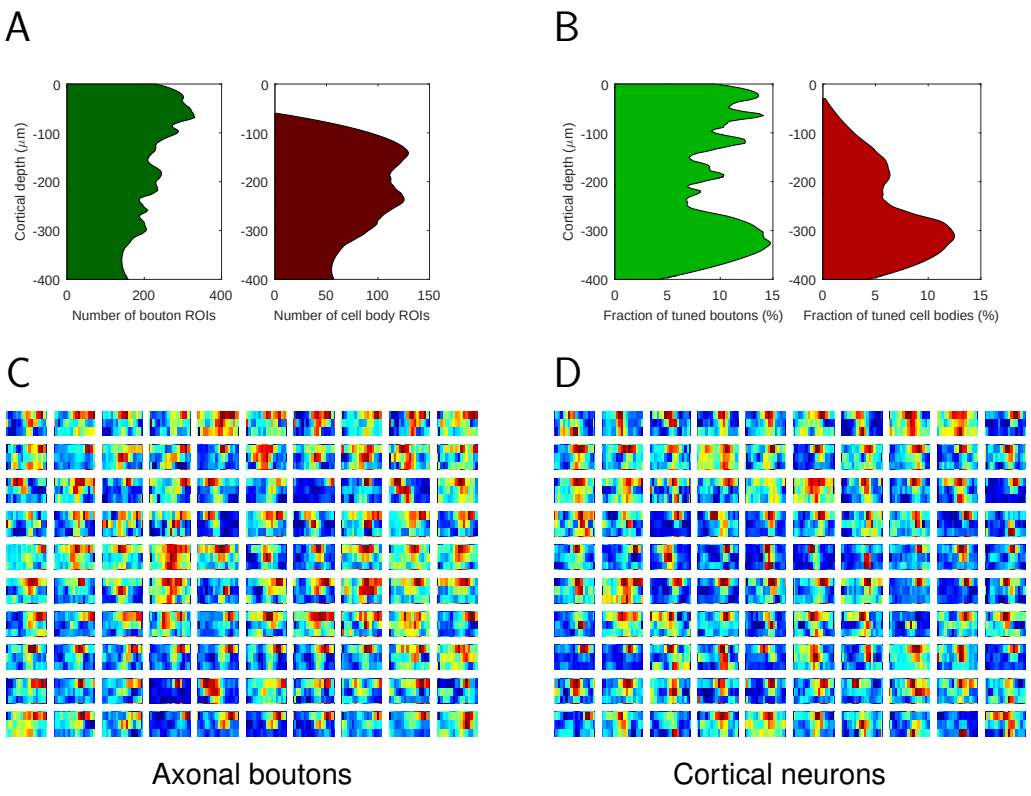

Fig. 5.3: Prevalence of frequency tuning in thalamocortical boutons and cortical neurons within middle to superficial layers of auditory cortex. (**A**) Average distribution of GCaMP6-labelled thalamic boutons (left) and RGECO1-labelled cortical neurons (right) through all the volumes of cortex imaged (n = 12 volumes). Distributions were obtained by pooling all imaged areas in bins of 50 μm and applying a kernel smoothing function. (**B**) Fraction of GCaMP6-labelled thalamic boutons (left) and RGECO1-labelled cortical neurons (right) exhibiting frequency tuning. Distributions obtained as in **A**. (**C**) Examples of frequency response areas (FRAs) from individual boutons within a single cortical volume. (**D**) Same as **C** but for neurons within the same cortical volume.

variability in the best frequencies of cortical neurons (**Fig. 5.6**). This is in agreement with what was first revealed by the earliest two-photon calcium imaging studies of auditory cortex which employed calcium-sensitive dyes (Bandyopadhyay et al., 2010; Rothschild et al., 2010). A significant correlation between co-tuning an cortical depth was observed (**Fig. 5.6 A,C**; R = 0.306, P = 0.0030156, Pearson correlation, n = 94), although when the co-tuning measures for all areas imaged in L2/3 were compared with those from L4, no significant difference was observed within single volumes or between the overall distributions (**Fig. 5.6 B,D**). Winkowski and Kanold (2013) reported a strong difference in the overall heterogeneity of tuning of neurons in L2/3 and L4, when comparing single pairs of areas a good distance apart. My

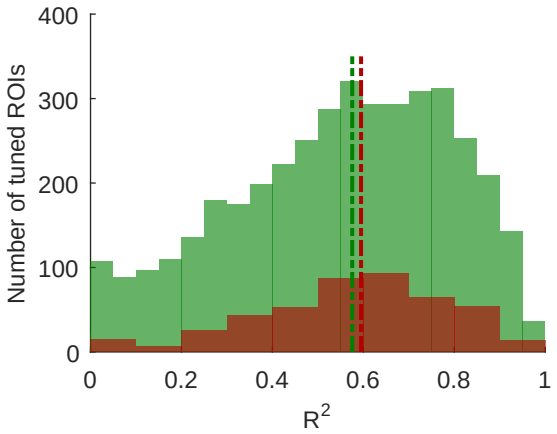

Fig. 5.4: Quality of tuning for thalamic boutons and cortical neurons. In order to assess the quality of frequency tuning, level-averaged tuning curves were fitted with Gaussians. Distribution of R^2 values from the fittings indicate that the tuning curves could generally be well approximated by a Gaussian, both for boutons (green) and neurons (red). Lines indicate means.

results suggest that rather than a sudden change in co-tuning from L4 to L2/3, there is a smooth gradient in which co-tuning weakens as cortical depth decreases.

In order to compare the differences in co-tuning between TC boutons and cortical neurons, I selected the subset of neurons found within the same subvolume where axonal terminals were imaged. The overall BF distribution for boutons was broader than for neurons, and for each cortical volume imaged the co-tuning of boutons (0.78 ± 0.28 octaves) was significantly weaker than that of nearby neurons (0.54 ± 0.2 octaves; $p = 0.0048$, paired Student's t-test; **Fig. 5.7**). What is more, within a subvolume, the mean BF of the boutons correlate well with the mean BF of cortical neurons in L4 (**Fig. 5.8 A**; $R = 0.675$, $P = 0.0460$, Pearson correlation, $n = 9$) but not with the BF of L2/3 neurons (**Fig. 5.8 B**; $R = 0.506$, $P = 0.1641$, Pearson correlation, $n = 9$).

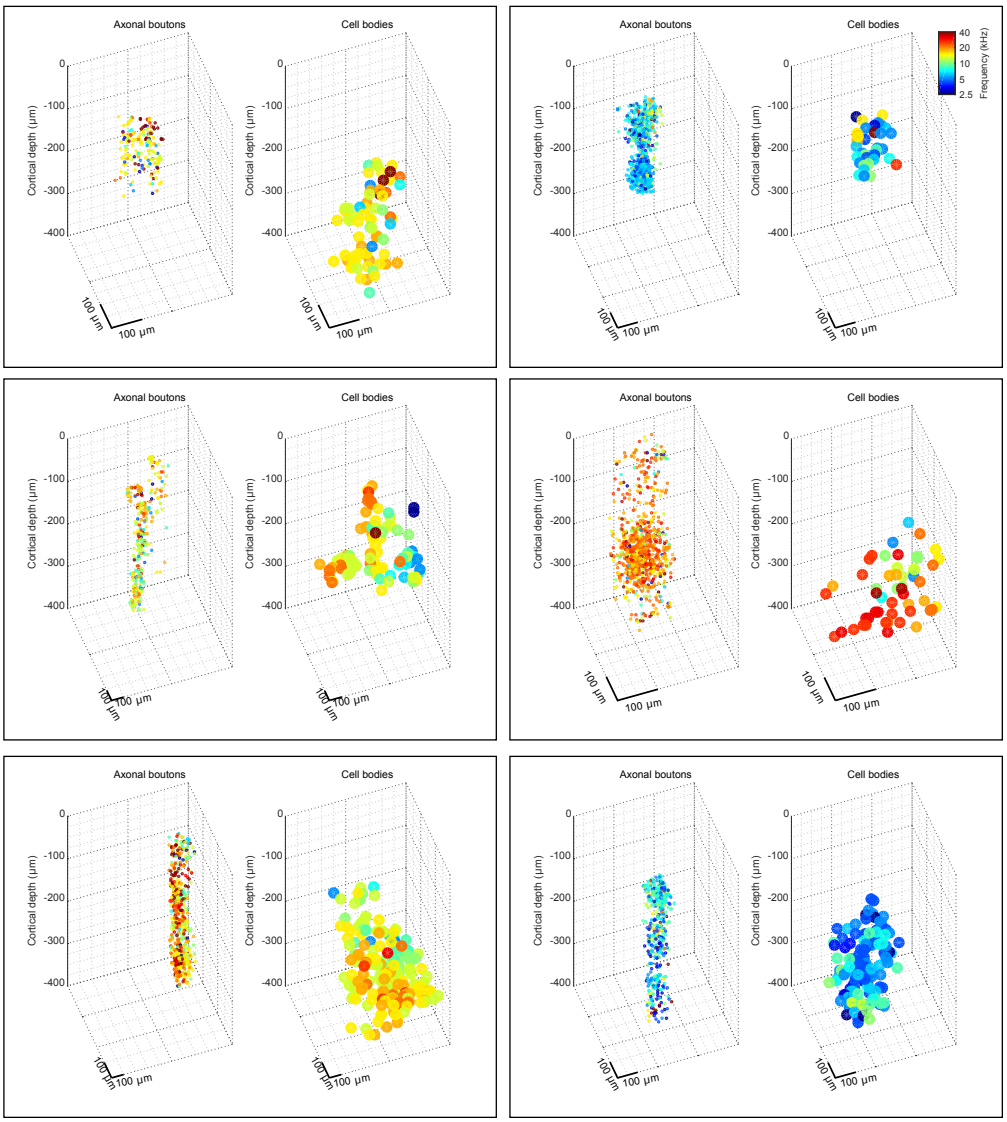

Fig. 5.5: Examples of imaged cortical volumes with tuned thalamic boutons and cortical neurons. Six example imaged volumes showing tuned cortical neurons and tuned thalamic boutons colour-coded by their best frequency.

5.4 Laminar differences in neuronal correlations

Laminar differences in signal correlations

Signal and noise correlations can provide important information about the functional connectivity of neuronal networks (Averbeck et al., 2006; Cohen and Kohn, 2011). In mouse V1, pairs of cortical neurons with high signal correlation have been found

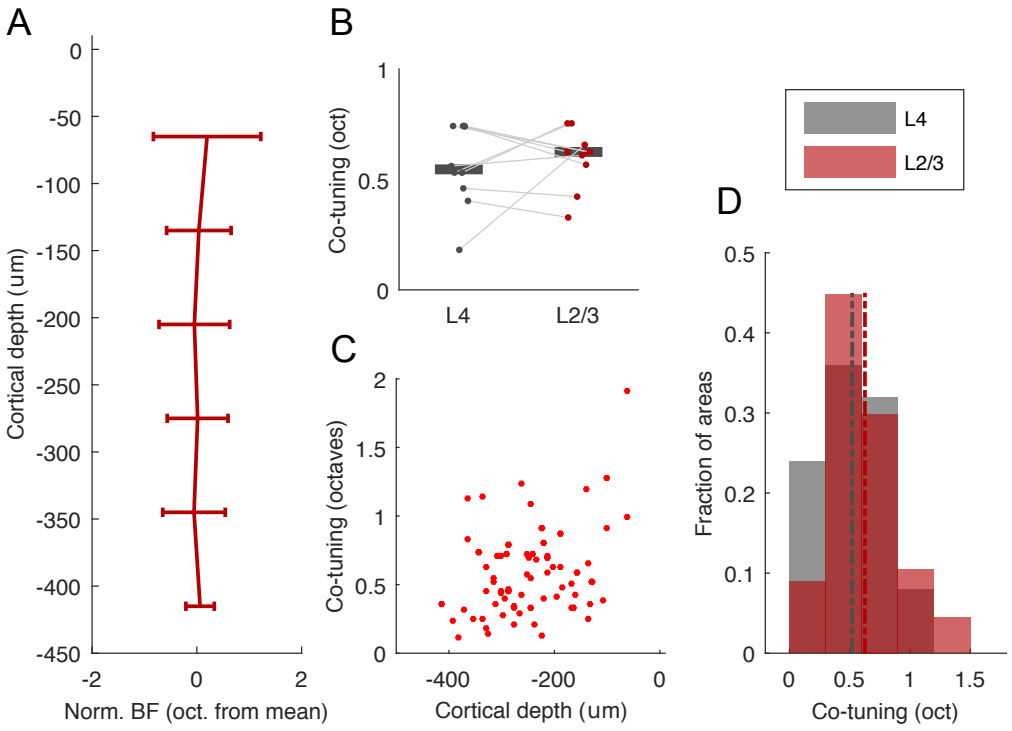

Fig. 5.6: Laminar distribution of neuronal best frequencies. (**A**) Variation in the best frequencies (BFs) of cortical neurons in layers 2-4 across all imaged volumes (n = 12). The BF of each neuron was normalised to the mean BF in its imaging plane. Number of neurons per 75 μm wide bin is between 137 and 378. Error bars are the standard deviation of BFs (co-tuning). (**B**) Co-tuning (standard deviation of BF distributions) of all neurons imaged in layer 2/3 (depth $<$ 300 μm) and layer 4 (depth $\geqslant$ 300 μm). Only volumes containing imaging planes in both L2/3 and L4 are included (n = 7). Thick grey lines indicate medians (L2/3: 0.61 octaves; L4: 0.53 octaves). L2/3 had in average greater variation in BFs than L4, although the difference was not statistically significant (p = 0.29, Paired Student's t-test). (**C**) Correlation between imaging depth and co-tuning for all imaged areas (R = 0.306, P = 0.0030156, Pearson correlation, n = 94). (**D**) Distribution of co-tuning within individual areas imaged in L2/3 (red) and L4 (grey) showed no significant difference between the two (p = 0.16, Wilcoxon rank-sum test). Dashed lines indicate means (L2/3: 0.62 octaves, n = 69; L4: 0.52 octaves, n = 25).

to have a higher probability of being synaptically interconnected (Ko et al., 2011). In the anaesthetised auditory cortex of the mouse, signal correlations have been found to be higher in L4 than in L2/3 (Winkowski and Kanold, 2013). Here, I set out to evaluate the variations in signal correlations of auditory cortical neurons and thalamic axons as a function of cortical depth. In agreement with the reports by Winkowski and Kanold (2013) in anaesthetised mice, the mean signal correlation between pairs of neurons in the same imaged area was slightly but significantly higher in L4 than in L2/3 in the overall population (**Fig. 5.9 D**; L2/3: 0.290, n = 3112 pairs; L4: 0.320, n = 2385 pairs; p $<$ 0.0001, Wilcoxon rank-sum test). Whilst

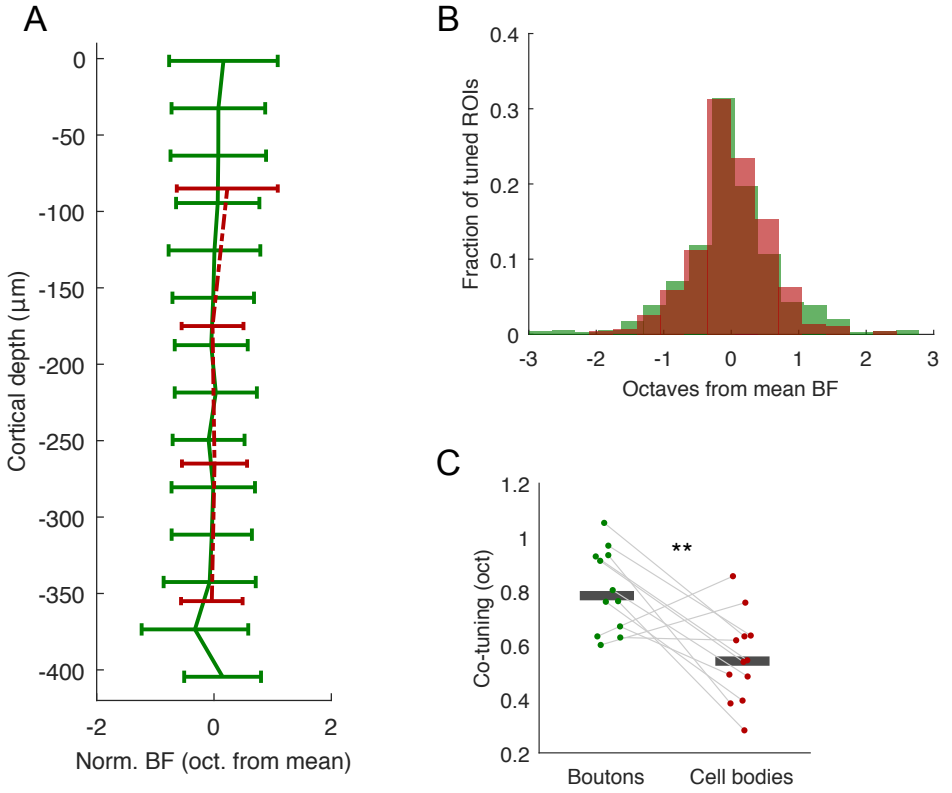

Fig. 5.7: Laminar distribution of neuronal and axonal best frequencies. (**A**) Variation in the best frequencies (BFs) of thalamic axonal boutons (green) and nearby cortical neurons (red) in layers 1-4 across all imaged subvolumes (n = 12). Only neurons found inside the subvolume imaged for thalamic axons are included. The BF of each neuron and bouton was normalised to the mean BF in its imaging plane. Number of neurons per 90 μm wide bin is between 25 and 205. Number of boutons per 30 μm wide bin is between 17 and 648. Error bars are the standard deviation of BFs (co-tuning). (**B**) BF distributions of all boutons (green) and neurons (red) from all imaged subvolumes. All BFs were normalised to the mean BF in its imaging plane. The distribution of boutons' BFs is wider than that of neurons. (**C**) Co-tuning (standard deviation of BF distributions) of all tuned boutons and neurons found inside the same cortical subvolumes (n = 12). Thick grey lines indicate medians (boutons: 0.76 octaves; neurons: 0.54 octaves). The distributions of bouton BFs by cortical subvolume were significantly wider than for neurons.

a difference was also present within imaged volumes (**Fig. 5.11 B**; L2/3: 0.201; L4: 0.307; p = 0.4707, n = 10, Wilcoxon signed-rank test), more observations might be required to obtain statistical significance. Only a weak negative correlation was observed between signal correlation and cortical depth (**Fig. 5.9 C**; R = -0.219, P = 0.0382, Pearson correlation).

In order to compare the signal correlations between pairs of TC boutons and pairs of cortical neurons, I first selected the subset of neurons found within the same

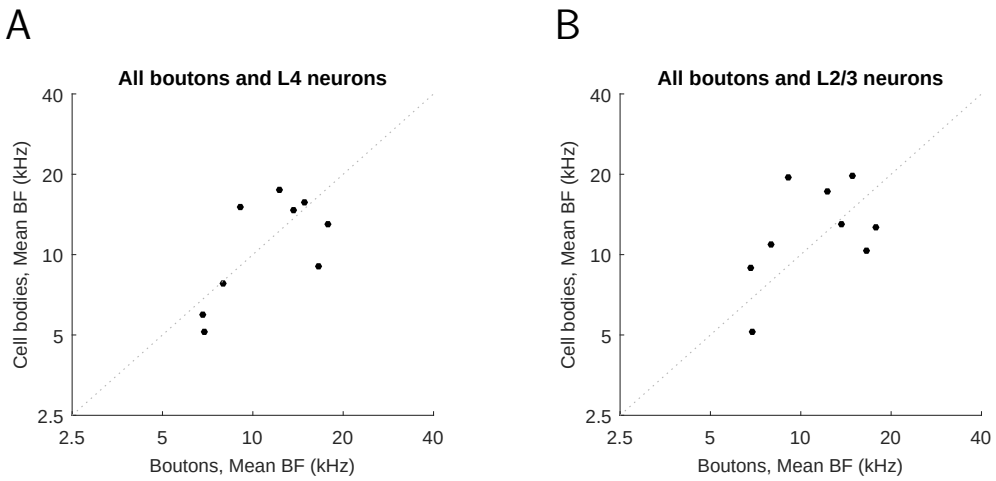

Fig. 5.8: Correlation between the mean best frequency of thalamic boutons and cortical neurons in the same cortical column. The mean BF of thalamic boutons inside a subvolume of cortex matches the mean BF of neurons found inside the same subvolume (n = 9).

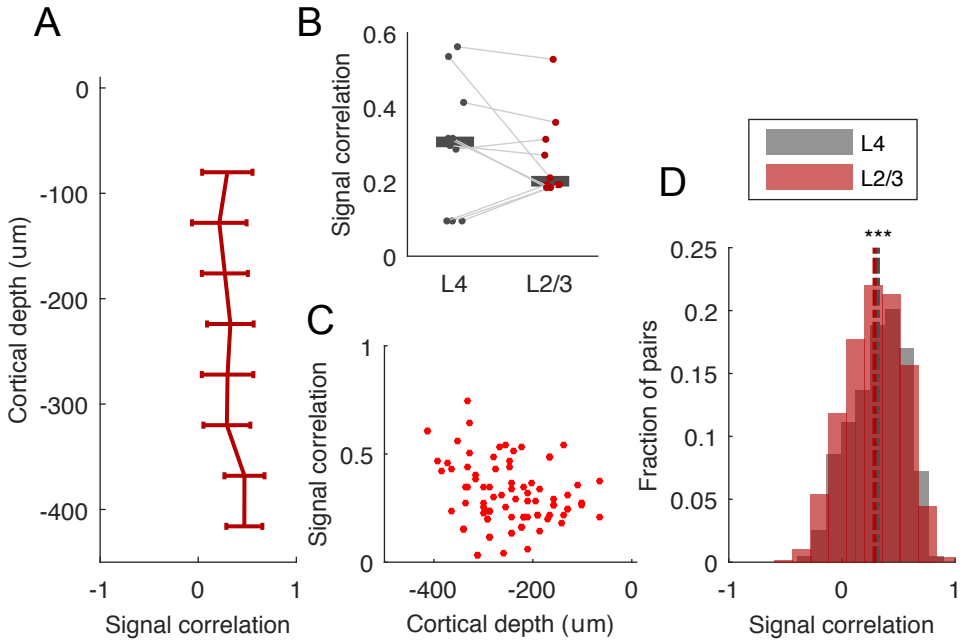

Fig. 5.9: Laminar distribution of neuronal signal correlations. (**A**) Mean signal correlation of pairs of cortical neurons in layers 2-4 across all imaged volumes (n = 12). The mean signal correlation decreases from granular to supragranular layers. Signal correlations were calculated between pairs of neurons belonging to the same imaging field. Number of pairs per 50 μm wide bin is between 92 and 1479. Error bars are the standard error of the mean (**B**) Mean signal correlation of all neuron pairs imaged in layer 2/3 (depth $<$ 300 μm) and layer 4 (depth $\geqslant$ 300 μm). Only volumes containing imaging planes in both L2/3 and L4 are included . Thick grey lines indicate medians. (**C**) Correlation between imaging depth and signal correlation for all imaged areas (n = 94). (**D**) Distribution of noise correlations from pairs of neurons pooled from all areas imaged in L2/3 (red) and L4 (grey). Dashed lines indicate means.

subvolume where axonal terminals were imaged, and then randomly drew the same number of pairs from the distribution of bouton pairs as there were neuron pairs in each volume (**Fig. 5.10 A**). This prevents the overall distribution being biased by areas with a greater number of bouton pairs. This comparison revealed that the signal correlation of pairs of boutons was not significantly different from that of pairs of neurons (**Fig. 5.10 B**; boutons: 0.21; neurons: 0.27; p = 0.35, Paired Student's t-test).

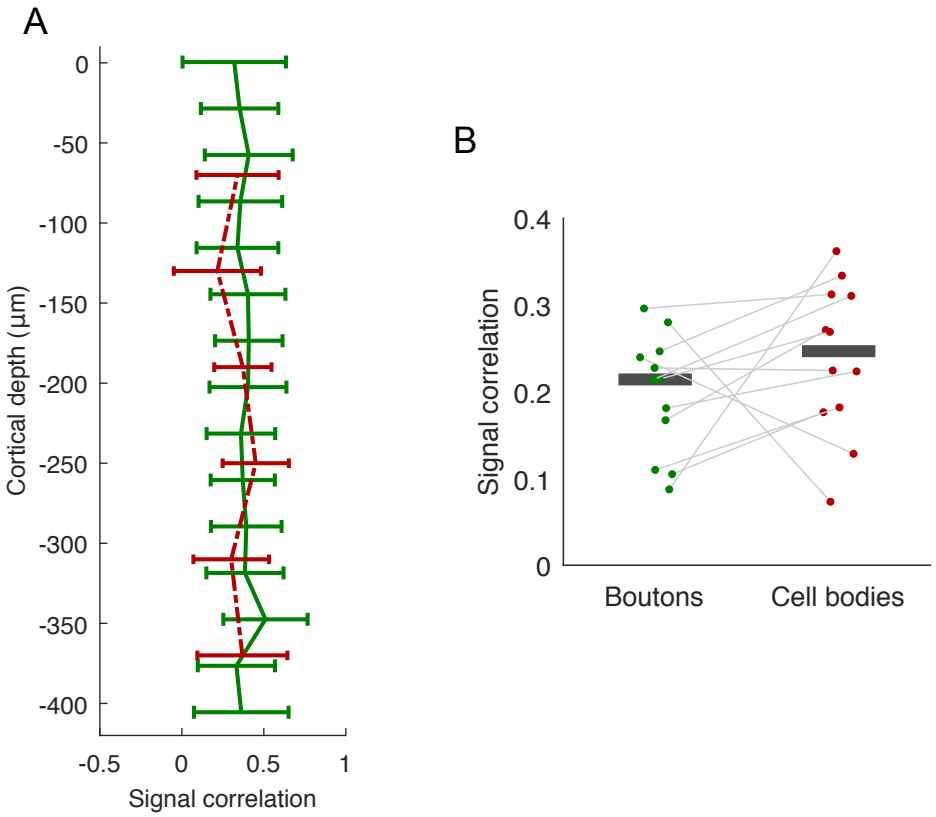

Fig. 5.10: Laminar distribution of neuronal and axonal signal correlations. (**A**) Mean signal correlation of pairs of thalamic axonal boutons (green) and pairs of nearby cortical neurons (red) in layers 1-4 across all imaged subvolumes (n = 12). Only neuron pairs found inside the subvolume imaged for thalamic axons are included. Number of neuron pairs per 60 μm wide bin is between 86 and 3140. Number of bouton pairs per 30 μm wide bin is between 434 and 10626. Error bars are standard error of the mean. (**B**) Mean signal correlation of all neuron and bouton pairs found inside the same cortical subvolumes (n = 12). Thick grey lines indicate medians.

Laminar differences in noise correlations

Noise correlations are a general indicative of shared synaptic input (Cohen and Kohn, 2011). They have been found to be high in sensory cortices, which is thought to be a result of the redundant coding strategies employed by populations of cortical neurons (Harris and Mrsic-Flogel, 2013; Rothschild and Mizrahi, 2015). In order to evaluate the variations in noise correlations of auditory cortical neurons and thalamic axons as a function of cortical depth, I made pairwise comparisons of noise vectors. These vectors were obtained for each neuron or bouton by subtracting its mean response to each stimuli from the corresponding single-trial responses. The noise correlations were the correlation coefficients between the vectors of pairs of boutons or pairs of neurons in the same area. The mean noise correlation between pairs of neurons in the same imaged area was slightly but significantly higher in L2/3 than in L4, both within individual imaged volumes (**Fig. 5.11 B**; L2/3: 0.010; L4: 0.008; $p = 0.013$, $n = 10$, Paired Student's t-test) and in the overall population (**Fig. 5.11 D**; L2/3: 0.016, $n = 3112$ pairs; L4: 0.010, $n = 2385$ pairs; $p < 0.0001$, Wilcoxon rank-sum test). This finding is in agreement with the reports by Winkowski and Kanold (2013) in anaesthetised mice. However, no significant correlation could be found between the depth of the area imaged and the mean noise correlation of neurons in that area (**Fig. 5.11 D**; $R = 0.089$, $P = 0.47918$, Pearson correlation).

To compare the noise correlations between pairs of TC boutons and pairs of cortical neurons, the same pairs were used as for the assessment of signal correlation (**Fig. 5.12 A**). The noise correlation of pairs of boutons was found to be significantly higher than that of pairs of neurons across all but one of the individual imaged volumes (**Fig. 5.12 B**; boutons: 0.054; neurons: 0.020; $p = 0.020$, Wilcoxon signed-rank test). Whilst this could be in part due to the effect of pairs of boutons from the same axon, the analysis of the relationship between noise and signal correlations in chapter 3, revealed that these constitute a very small fraction of all bouton pairs (**Fig. 3.19**). Moreover, the same difference was observed when a most direct measure of noise correlations was used: correlations based on recordings from 60-second long

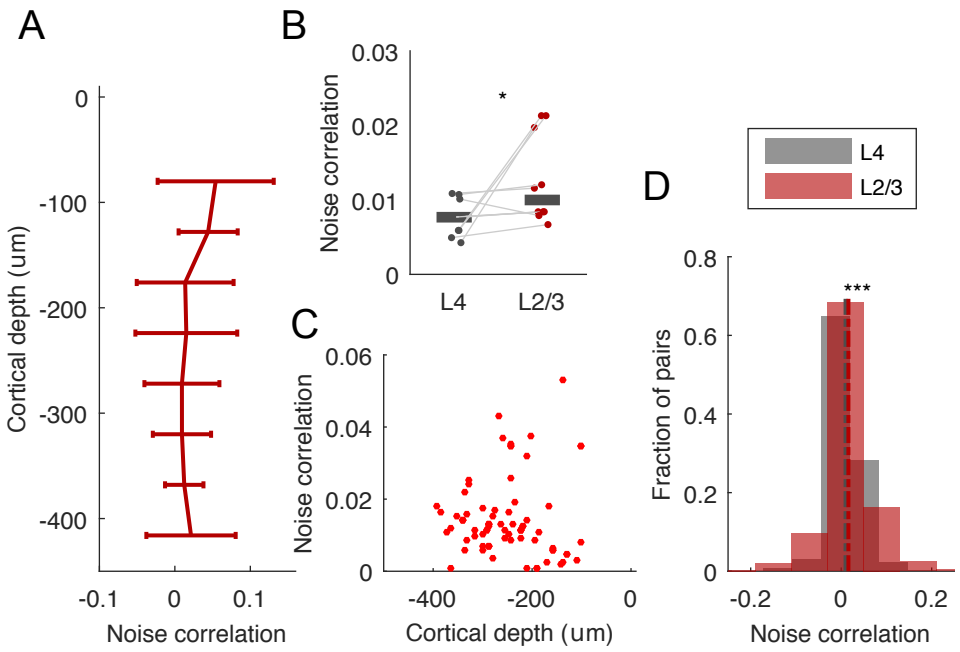

Fig. 5.11: Laminar distribution of neuronal noise correlations. (**A**) Mean noise correlation of pairs of cortical neurons in layers 2-4 across all imaged volumes (n = 12). The mean noise correlation increases from granular to supragranular layers. Noise correlations were calculated between pairs of neurons belonging to the same imaging field. Number of pairs per 50 μm wide bin is between 92 and 1479. Error bars are the standard error of the mean (**B**) Mean noise correlation of all neuron pairs imaged in layer 2/3 (depth $<$ 300 μm) and layer 4 (depth $\geqslant$ 300 μm). Only volumes containing imaging planes in both L2/3 and L4 are included (n = 7). Thick grey lines indicate medians. (**C**) Correlation between imaging depth and noise correlation for all imaged areas (n = 94). (**D**) Distribution of noise correlations from pairs of neurons pooled from all areas imaged in L2/3 (red) and L4 (grey). Dashed lines indicate means.

periods of no stimulus presentation (**Fig. 5.13 A**; boutons: 0.043; neurons: 0.008; p = 0.007, Wilcoxon signed-rank test).

Because of the much smaller size of boutons in comparison to neurons, motion artifacts during imaging can have an stronger effect on the calcium signals recorded from boutons, which could potentially result in artificially high noise correlations. To control for this, I calculated the correlation between the noise vector of each bouton and a vector of motion correction for the bouton's imaged area. The latter is made up of the measurements of deviation of each recorded frame from the registration template of the imaged area. The mean pairwise noise correlation was significantly higher than the correlation of neuronal noise with image motion (**Fig. 5.13 B**) and there was no significant correlation between the two measures (**Fig. 5.13 C**; R = -0.054, P = 0.39715, Pearson correlation).

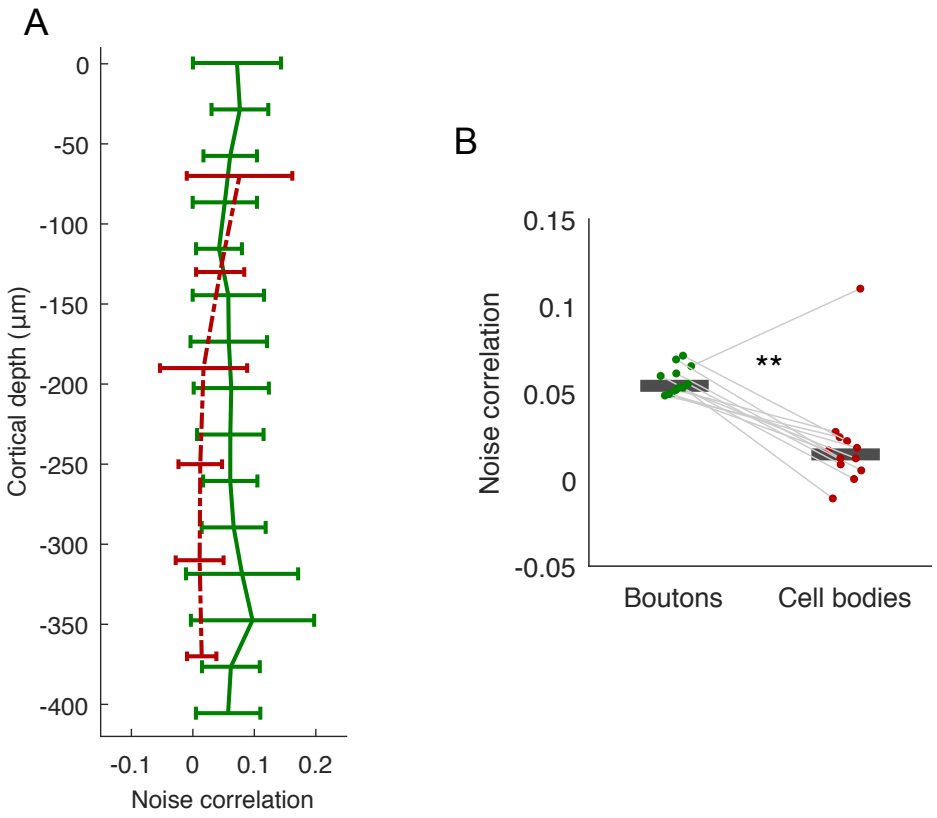

Fig. 5.12: Laminar distribution of neuronal and axonal noise correlations. (**A**) Mean noise correlation of pairs of thalamic axonal boutons (green) and pairs of nearby cortical neurons (red) in layers 1-4 across all imaged subvolumes (n = 12). Only neuron pairs found inside the subvolume imaged for thalamic axons are included. Number of neuron pairs per 60 μm wide bin is between 86 and 3140. Number of bouton pairs per 30 μm wide bin is between 434 and 10626. Error bars are standard error of the mean. (**B**) Mean noise correlation of all neuron and bouton pairs found inside the same cortical subvolumes (n = 12). Thick grey lines indicate medians.

5.5 Thalamocortical functional convergence through the cortical column

If the tonotopic arrangement of thalamic axons in cortex was sharp, one might expect that their contribution to the tuning preference of cortical neurons is greater than their contribution to the rest of their FRAs. However, I have shown in chapters 3 and 4 that tonotopy of thalamic boutons is very weak at the small scale, and this might contribute to spectral broadening in cortical receptive fields. In order to

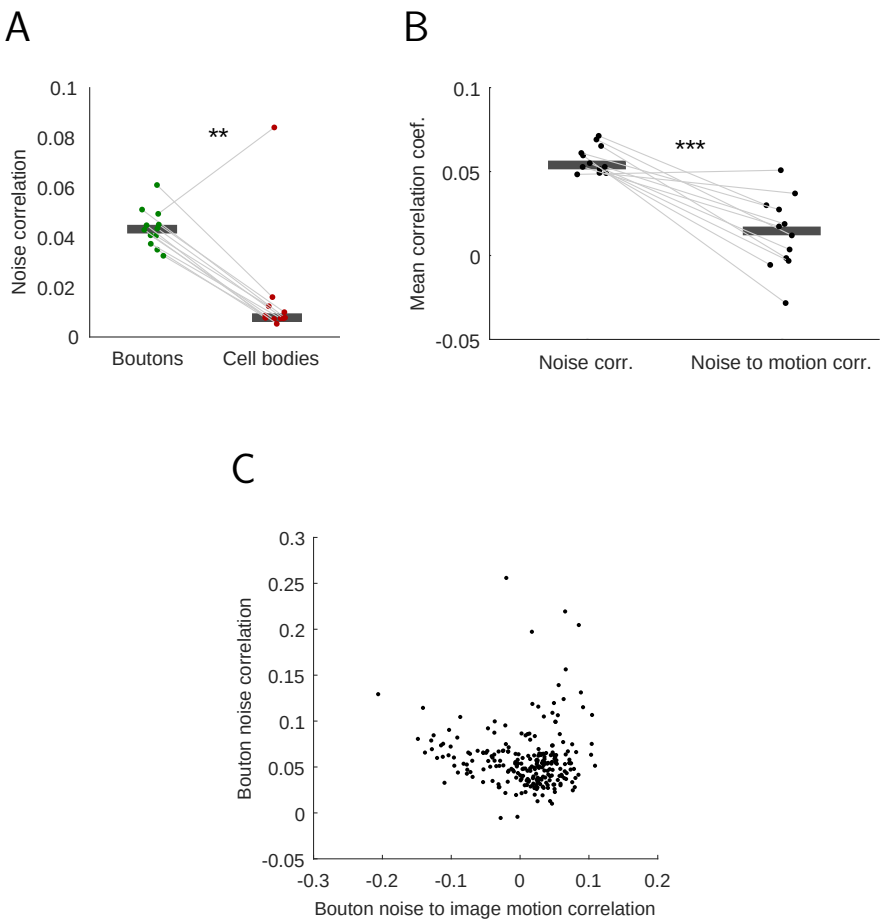

Fig. 5.13: Controls for the observed difference in noise correlations for thalamic boutons and cortical neurons. (**A**) Mean noise correlation of all neuron and bouton pairs found inside the same cortical subvolumes as in Fig. 5.12 (n = 12) but calculated using recordings from periods with no stimulus presentation. Thick grey lines indicate medians. (**B**) In all cortical volumes imaged, the average noise correlation across thalamic boutons within the same imaged area is greater than the average correlation between the noise of each bouton and the corrected motion for its imaged area. (**C**) No significant correlation between the average noise correlation coefficient of all thalamic boutons within an imaged area and the average correlation coefficient of the noise of each bouton and the corrected motion for the same area.

study the contribution of thalamic receptive fields to the receptive fields of cortical neurons, I compared a number of parameters of the FRAs of pairs of cortical neurons and thalamic boutons in the same cortical volume. Because TC terminals can form synapses on apical dendrites which can extend up to layer 1, or on the shorter basal dendrites which in auditory cortex do not normally extend further than 100 μm down from the cell body (Richardson et al., 2009), neurons were only paired to boutons located within these boundaries. Of all cortical volumes imaged, only

those volumes with neuron-bouton pairs throughout the whole span of granular and supragranular layers were included in this analysis (n = 6 volumes). The mean cortical distance across pairs of boutons and L4 neurons was 121 μm $\pm$ 101 (s.d.) and 69 μm $\pm$ 88 (s.d.) for boutons and layer 2/3 neurons.

Differences in best frequency are lowest between L4 neurons and boutons in L3b/4

The difference in best frequency between pairs of axonal boutons and cortical neurons was very similar across layers (**Fig. 5.14**). The overall distributions of BF differences across all bouton-neuron pairs show that the thalamocortical BF difference was very slightly but significantly lower in L4 neurons than in L2/3 (**Fig. 5.14 C**; L4: 0.81 octaves, L2/3: 0.83 octaves; $p < 0.0001$, Wilcoxon rank-sum test). However, this difference was not always consistent when the L2/3 and L4 distributions were compared within each volume (**Fig. 5.14 D**; L4 neurons-all boutons: 0.81 octaves; L2/3 neurons-all boutons: 0.82 octaves; n = 6 volumes; $p = 0.30$, Paired Student's t-test). Closer examination revealed that within L4 neurons, the BF difference with L3b/4 boutons was slightly but significantly lower than with boutons in L1, both in the overall distribution (**Fig. 5.14 E**; L4 neurons-L3b/4 boutons: 0.85 octaves, L4 neurons-L1 boutons: 0.92 octaves; $p < 0.0001$, Wilcoxon rank-sum test) and within each imaged volume (**Fig. 5.14 F**; L4 neurons-L3b/4 boutons: 0.81 octaves, L4 neurons-L1 boutons: 0.85 octaves; n = 6 volumes; $p = 0.046$, Paired Student's t-test). For L2/3 neurons, BF difference with L3b/4 boutons was also slightly but significantly lower than with boutons in L1 in the overall distribution (**Fig. 5.14 G**; L2/3 neurons-L3b/4 boutons: 0.79 octaves, L2/3 neurons-L1 boutons: 0.82 octaves; $p = 0.001$, Wilcoxon rank-sum test), a difference which was often but not always present within each imaged volume (**Fig. 5.14 G**; L2/3 neurons-L3b/4 boutons: 0.72 octaves, L2/3 neurons-L1 boutons: 0.89 octaves; n = 6 volumes; $p = 0.09$, Paired Sign-rank test).

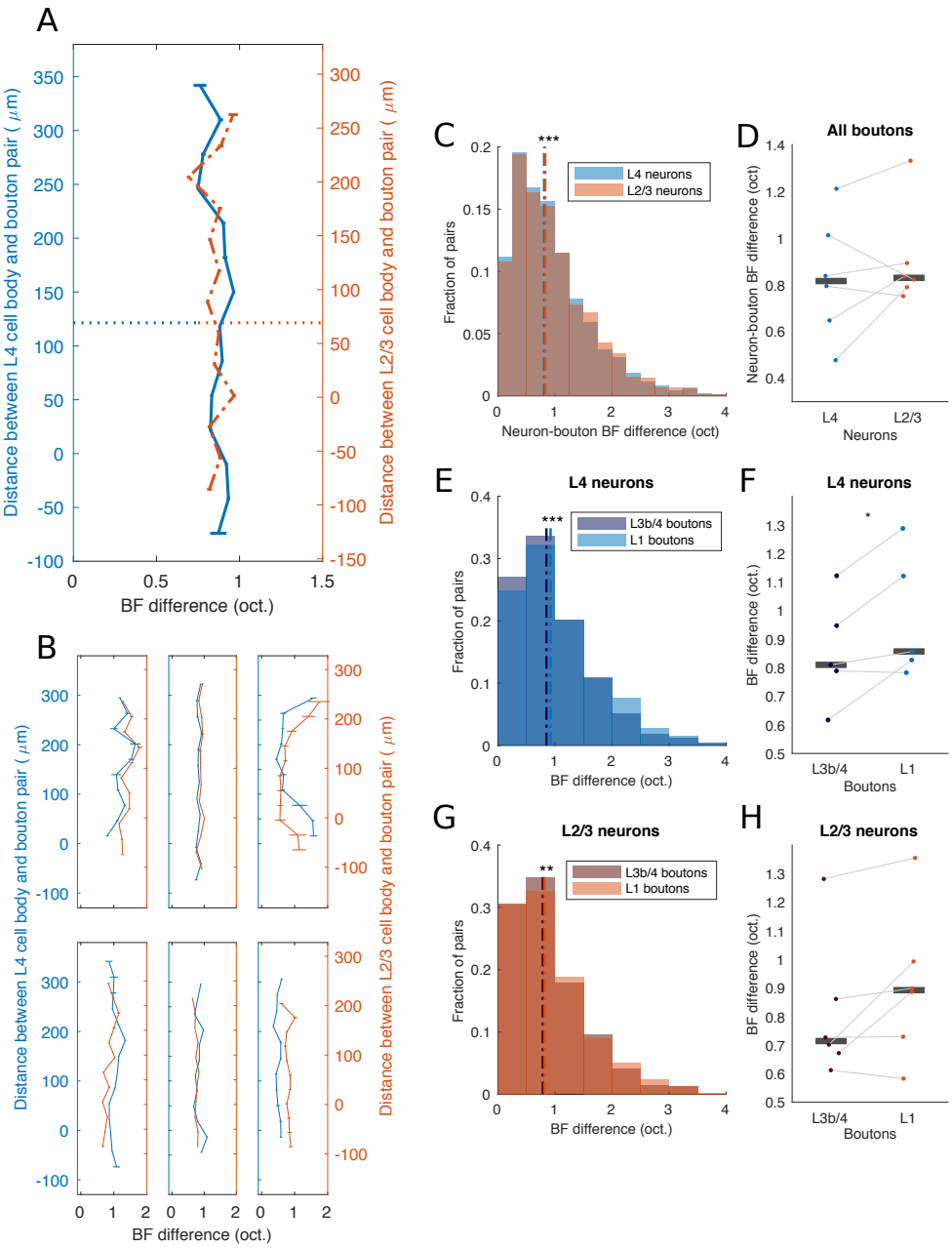
A
Distance between L4 cell body and bouton pair (μm)
Distance between L2/3 cell body and bouton pair (μm)
BF difference (oct.)
B
Distance between L4 cell body and bouton pair (μm)
Distance between L2/3 cell body and bouton pair (μm)
BF difference (oct.)
C
***
L4 neurons
L2/3 neurons
Fraction of pairs
Neuron-bouton BF difference (oct)
D
All boutons
Neuron-bouton BF difference (oct)
L4
L2/3
Neurons
E
L4 neurons
***
L3b/4 boutons
L1 boutons
Fraction of pairs
BF difference (oct.)
F
L4 neurons
*
BF difference (oct.)
L3b/4
L1
Boutons
G
L2/3 neurons
**
L3b/4 boutons
L1 boutons
Fraction of pairs
BF difference (oct.)
H
L2/3 neurons
BF difference (oct.)
L3b/4
L1
Boutons

(previous page)

Fig. 5.14: Laminar distribution of best frequency differences between thalamic boutons and cortical neurons. (**A**-**B**) Differences in best frequency (BF) between pairs of thalamic axonal boutons and cortical neurons in L4 (blue) and L2/3 (red) arranged by the vertical distance of the bouton from the neuronal cell body. Only cortical volumes with a comparable number of neurons and boutons throughout the several cortical layers are included. Number of pairs per 30 μm wide bin is between 174 to 8406 for L4 and 626 to 6400 for L2/3. Error bars are the standard error of the mean. Horizontal lines indicate mean cortical distance across all pairs of boutons and neurons. (**A**) Pooled data. (**B**) Data from individual volumes. (**C**) Distribution of BF differences between all boutons and neurons in L4 (blue) or L2/3 (red). Dashed lines indicate means. (**D**) Mean neuron-bouton BF difference for each included volume (n = 6). Thick grey lines indicate medians. (**E**) Distribution of BF differences between neurons in L4 and boutons in L3b/4 (dark blue) or L1 (light blue). Dashed lines indicate means. (**F**) Mean neuron-bouton BF difference for each included volume (n = 6). Thick grey lines indicate medians. (**G**) Distribution of BF differences between neurons in L2/3 and boutons in L3b/4 (dark red) or L1 (orange). Dashed lines indicate means. (**H**) Mean neuron-bouton BF difference for each included volume (n = 6). Thick grey lines indicate medians.

FRAs are more similar between thalamic boutons and L4 neurons

I next assessed how similar the FRAs of axonal boutons and cortical neurons were across different layers (**Fig. 5.15**). I calculated the FRA correlation coefficients, which are effectively the signal correlations, of pairs of boutons and neurons found within the same cortical column, but not necessarily the same imaged field. I refer to these here as the coefficient of *FRA similarity*, in order to distinguish them from the signal correlation coefficients calculated between pairs of boutons and pairs of neurons within the same imaged field. The overall distributions of FRA similarity coefficients across all bouton-neuron pairs imaged suggests that the thalamic FRAs are slightly but significantly more like those of neurons in L4 than in L2/3 (**Fig. 5.15C**; L4: 0.193, L2/3: 0.185 octaves; $p < 0.0001$, Wilcoxon rank-sum test). However, this difference was not always consistent when the L2/3 and L4 distributions were compared within each volume (**Fig. 5.15D**; L4 neurons-all boutons: 0.163; L2/3 neurons-all boutons: 0.148; n = 6 volumes; p = 0.30, Paired Student's t-test). Closer examination did not reveal any significant difference in FRA correlation between L4 neurons and L3b/4 or L1 boutons, either in the overall distribution (**Fig. 5.15E**; L4 neurons-L3b/4 boutons: 0.162, L4 neurons-L1 boutons: 0.160; p = 0.98, Wilcoxon rank-sum test) or within each imaged volume (**Fig. 5.15 F**; L4 neurons-L3b/4 boutons: 0.078, L4 neurons-L1 boutons: 0.052; n = 6 volumes; p = 0.29, Paired Student's t-test). This was also the case for the FRA similarity

between L2/3 neurons and the two groups of boutons (overall distribution: **Fig. 5.15G**; L2/3 neurons-L3b/4 boutons: 0.186, L2/3 neurons-L1 boutons: 0.185; p = 0.22, Wilcoxon rank-sum test; within volume comparison: **Fig. 5.15H**; L2/3 neurons-L3b/4 boutons: 0.142, L2/3 neurons-L1 boutons: 0.082; n = 6 volumes; p = 0.16, Paired Student's t-test).

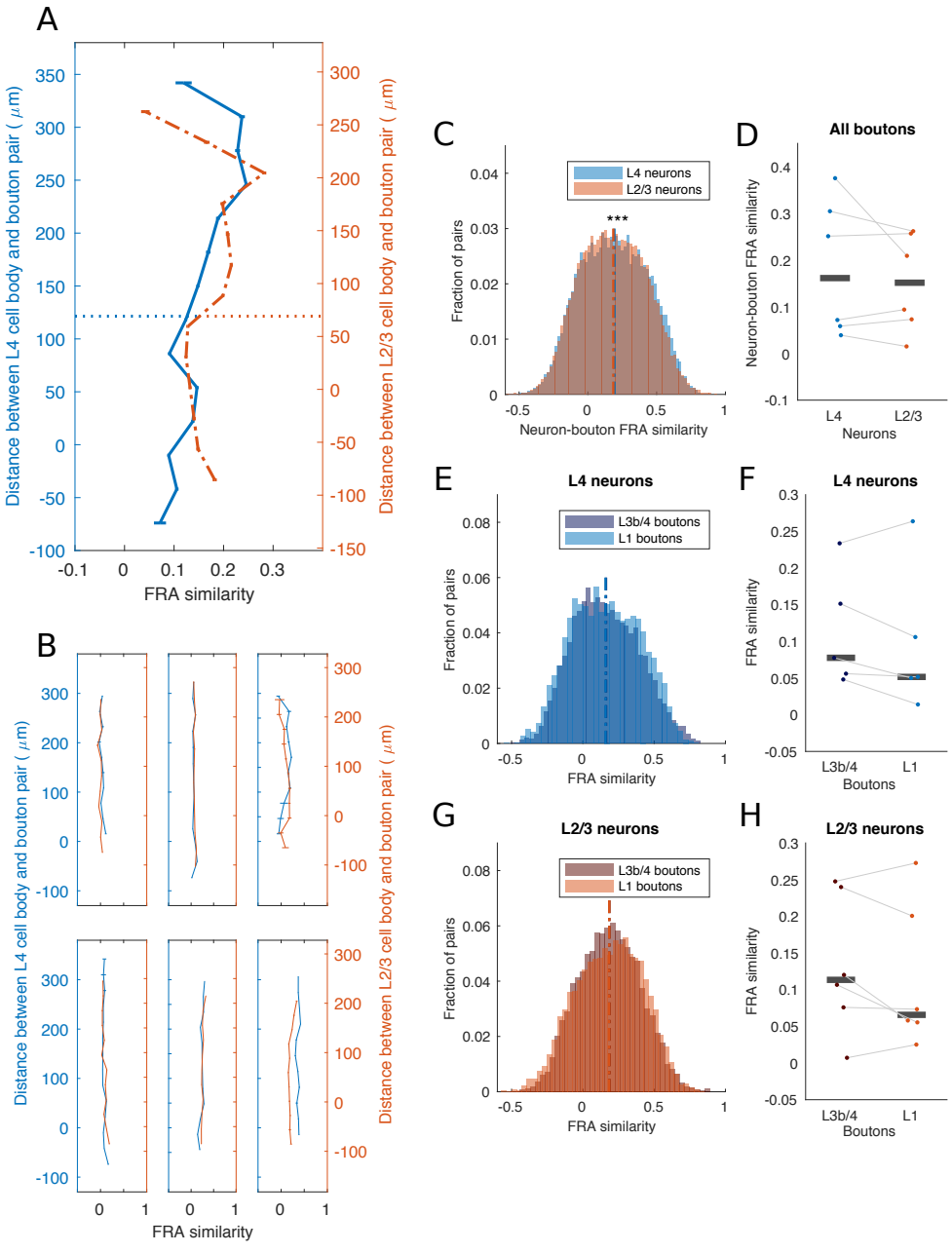

(previous page)

Fig. 5.15: Laminar distribution of FRA similarity between thalamic boutons and cortical neurons. (**A**-**B**) Correlation coefficients of the vectorised frequency response areas (FRA similarity) between pairs of thalamic axonal boutons and cortical neurons in L4 (blue) and L2/3 (red) arranged by the vertical distance of the bouton from the neuronal cell body. Number of pairs per 30 μm wide bin is between 174 to 8406 for L4 and 626 to 6400 for L2/3. Error bars are the standard error of the mean. Horizontal lines indicate mean cortical distance across all pairs of boutons and neurons. (**A**) Pooled data. (**B**) Data from individual volumes. (**C**) Distribution of FRA similarity between all boutons and neurons in L4 (blue) or L2/3 (red). Dashed lines indicate means. (**D**) Mean neuron-bouton FRA similarity for each included volume (n = 6). Thick grey lines indicate medians. (**E**) Distribution of FRA similarity between neurons in L4 and boutons in L3b/4 (dark blue) or L1 (light blue). Dashed lines indicate means. (**F**) Mean neuron-bouton FRA similarity for each included volume (n = 6). Thick grey lines indicate medians. (**G**) Distribution of FRA similarity between neurons in L2/3 and boutons in L3b/4 (dark red) or L1 (orange). Dashed lines indicate means. (**H**) Mean neuron-bouton FRA similarity for each included volume (n = 6). Thick grey lines indicate medians.

Auditory cortex exhibits all forms of functional thalamocortical convergence

In order to assess to what extent the receptive fields of TC inputs to primary auditory cortex converge to generate the receptive fields of nearby neurons, I calculated the coefficients of thalamic overlap and cortical coverage for all bouton-neuron pairs within the same volume of cortex. I took a similar approach to that of Miller et al. (2001), who compared the bandwidth of the main excitatory peak in the level-averaged tuning curves of pairs of auditory cortical and thalamic neurons. Cortical coverage is the proportion of the cortical receptive field peak covered by that of the thalamic input. Thalamic overlap is the proportion of the thalamic receptive field peak overlapping that of the cortical neuron.

If a pair of bouton and neuron show high cortical coverage and high thalamic overlap, it means that their receptive fields are nearly identical and that the neuron might have inherited its tuning from the bouton. If instead one finds low cortical coverage and high thalamic overlap, it means that the receptive field of the bouton is smaller and potentially completely encompassed by the receptive field of the neuron. In this scenario, the bouton might only be contributing a small fraction to the construction of the neuron's receptive field. Finally, if low thalamic overlap with varying degrees of cortical coverage is seen, it means the receptive field of the thalamic input has regions that are not shared by the cortical neuron.

The relationship between thalamic overlap and cortical coverage of all bouton-neuron pairs pooled across all cortical volumes imaged is shown in **Fig. 5.16**. The density in this graph reflects the prevalence of different types of thalamocortical convergence. The striping patterns in some of the panels must be ignored, as they are a mere consequence of the discretisation of sampled frequencies used during the characterisation of the receptive fields. Whilst there appears to be an similar proportion of each of the scenarios described above, there was also a significant fraction of bouton-neuron pairs with low measures of both thalamic overlap and cortical coverage. This effectively means that the thalamic receptive field does not overlap at all with that of the receptive field of the cortical neuron.

Thalamocortical convergence is more prominent between L4 neurons and boutons in L3b/4

The degree of cortical coverage in the receptive fields of pairs of axonal boutons and cortical neurons was compared across layers (**Fig. 5.17**). Neurons in L2/3 and L4 did not show any significant difference in the cortical coverage of their receptive fields by thalamic boutons within each volume (**Fig. 5.17C**; L4 neurons-all boutons: 0.52; L2/3 neurons-all boutons: 0.53; n = 6 volumes; p = 0.46, Paired Student's t-test). However, L4 neurons in each volume did show a significantly higher cortical coverage of their receptive fields by boutons in L3b/4 than by boutons in L1 (**Fig. 5.17D**; L4 neurons-L3b/4 boutons: 0.50, L4 neurons-L1 boutons: 0.40; n = 6 volumes; p = 0.04, Paired Student's t-test). This difference was not observed in L2/3 neurons (**Fig. 5.17E**; L2/3 neurons-L3b/4 boutons: 0.54, L2/3 neurons-L1 boutons: 0.42; n = 6 volumes; p = 0.08, Paired Student's t-test).

The degree of thalamic overlap between the receptive fields of pairs of axonal boutons and cortical neurons was also compared across layers (**Fig. 5.18**). Neurons in L2/3 and L4 did not show any significant difference in the thalamic overlap of their receptive fields with thalamic boutons within each volume (**Fig. 5.18C**; L4 neurons-all boutons: 0.50; L2/3 neurons-all boutons: 0.48; n = 6 volumes; p = 0.19, Paired Student's t-test). However, L4 neurons in each volume did show a significantly

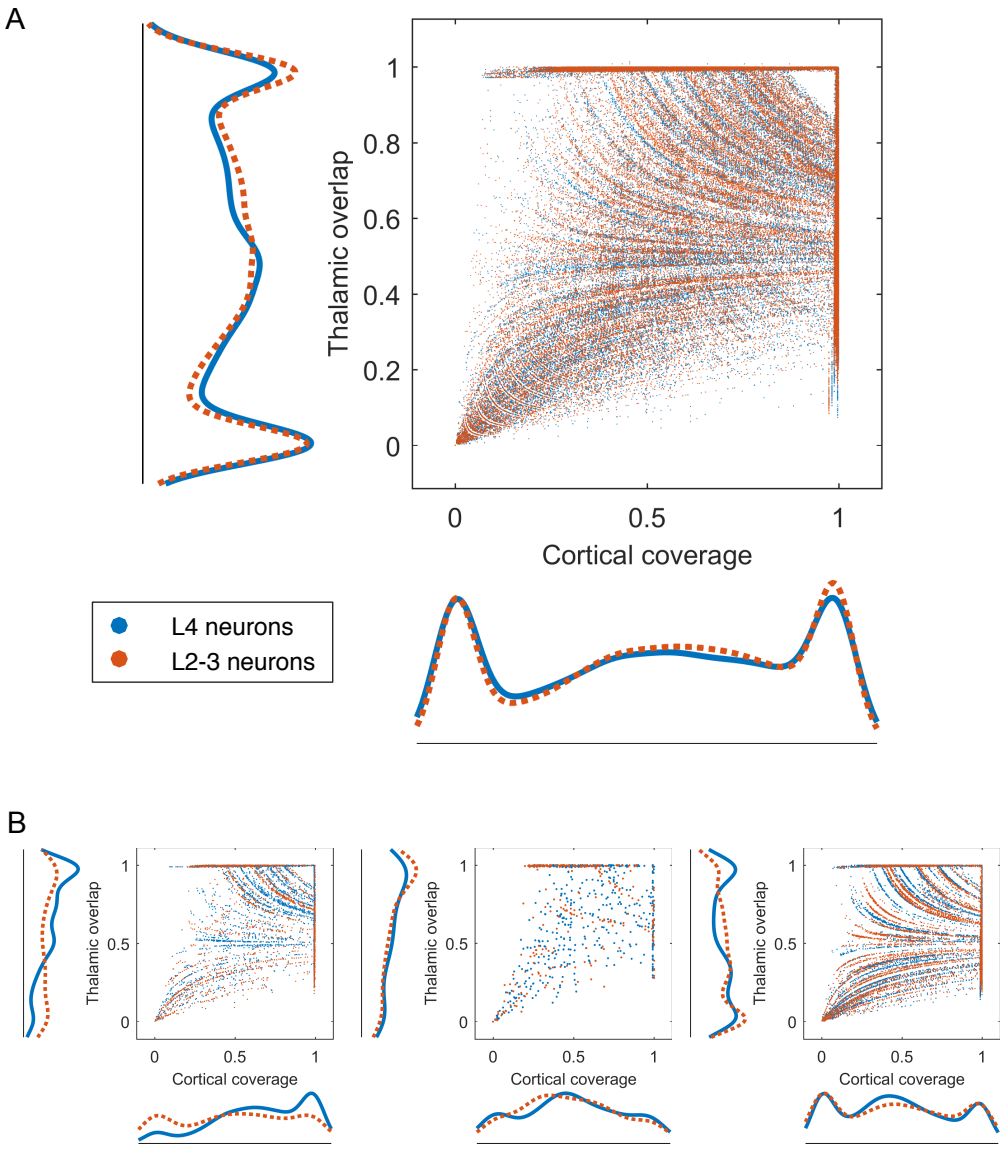

Fig. 5.16: Distribution of thalamocortical convergence measures. Functional convergence of spectral receptive fields of pairs of thalamic boutons and cortical neurons in L4 (blue) or L2/3 (red), assessed by two parameters: cortical coverage and thalamic overlap. Cortical coverage is the proportion of the cortical receptive field peak covered by that of the thalamic input. Thalamic overlap is the proportion of the thalamic receptive field peak overlapping that of the cortical neuron. (**A**) All bouton-neuron pairs from all cortical volumes imaged (n = 6). (**B**) Examples of distributions from single volumes, demonstrating the differences in the distribution shapes.

higher thalamic overlap of their receptive fields with boutons in L3b/4 than with boutons in L1 (**Fig. 5.18D**; L4 neurons-L3b/4 boutons: 0.48, L4 neurons-L1 boutons: 0.46; n = 6 volumes; p = 0.04, Paired Student's t-test). This difference was not observed in L2/3 neurons (**Fig. 5.18E**; L2/3 neurons-L3b/4 boutons: 0.49, L2/3 neurons-L1 boutons: 0.50; n = 6 volumes; p = 0.39, Paired Student's t-test).

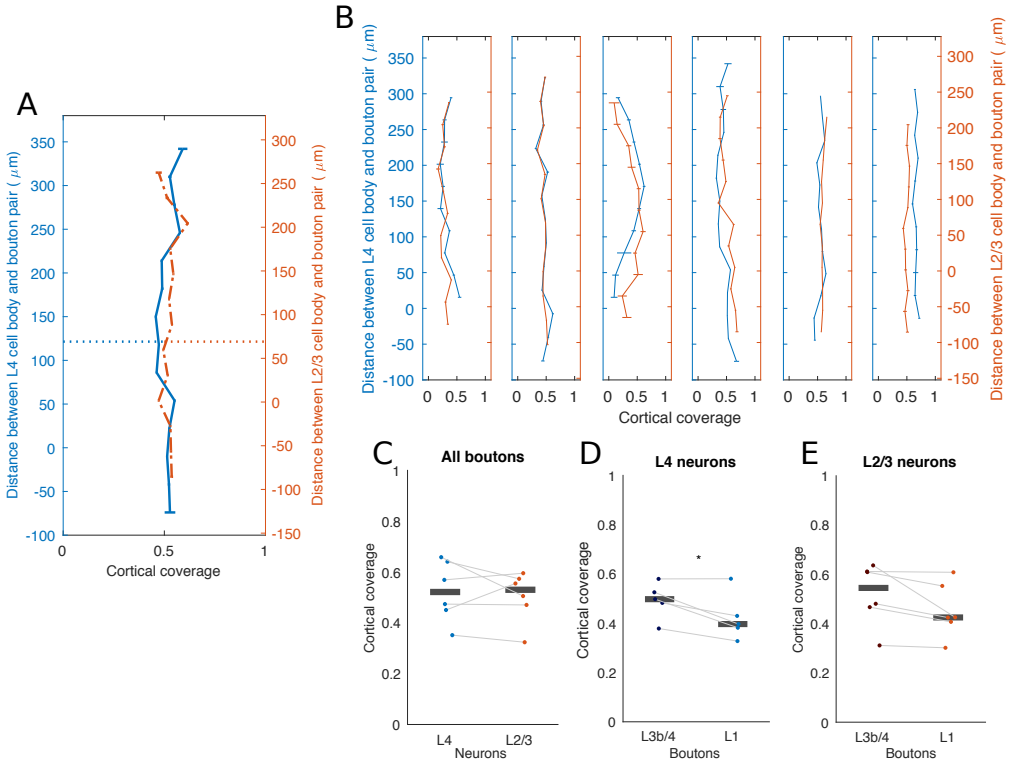

Fig. 5.17: Laminar distribution of cortical receptive field coverage between thalamic boutons and cortical neurons. (**A**-**B**) Coefficients of cortical coverage in the receptive fields of pairs of thalamic axonal boutons and cortical neurons in L4 (blue) and L2/3 (red) arranged by the vertical distance of the bouton from the neuronal cell body. Number of pairs per 30 μm wide bin is between 174 to 8406 for L4 and 626 to 6400 for L2/3. Error bars are the standard error of the mean. Horizontal lines indicate mean cortical distance across all pairs of boutons and neurons. (**A**) Pooled data. (**B**) Data from individual volumes. (**C**) Mean cortical coverage for L4 and L2/3 neurons for each included volume (n = 6). Thick grey lines indicate medians. (**D**) Mean cortical coverage between neurons in L4 and boutons in L3b/4 and L1 within each included volume (n = 6). Thick grey lines indicate medians. (**E**) Mean cortical coverage between neurons in L2/3 and boutons in L3b/4 and L1 within each included volume (n = 6). Thick grey lines indicate medians.

5.6 Discussion

Since its original description by Mountcastle (1997), vertical micro-circuitry has been considered a key element of cortical processing. The physiology, morphology and connectivity patterns of cortical neurons can be remarkably similar within layers, whilst very different across layers (Douglas and Martin, 2004). Yet, discussions about cortical maps often assume that ascending inputs and neurons from all layers in the same location of the cortical sheet are functionally similar with respect to

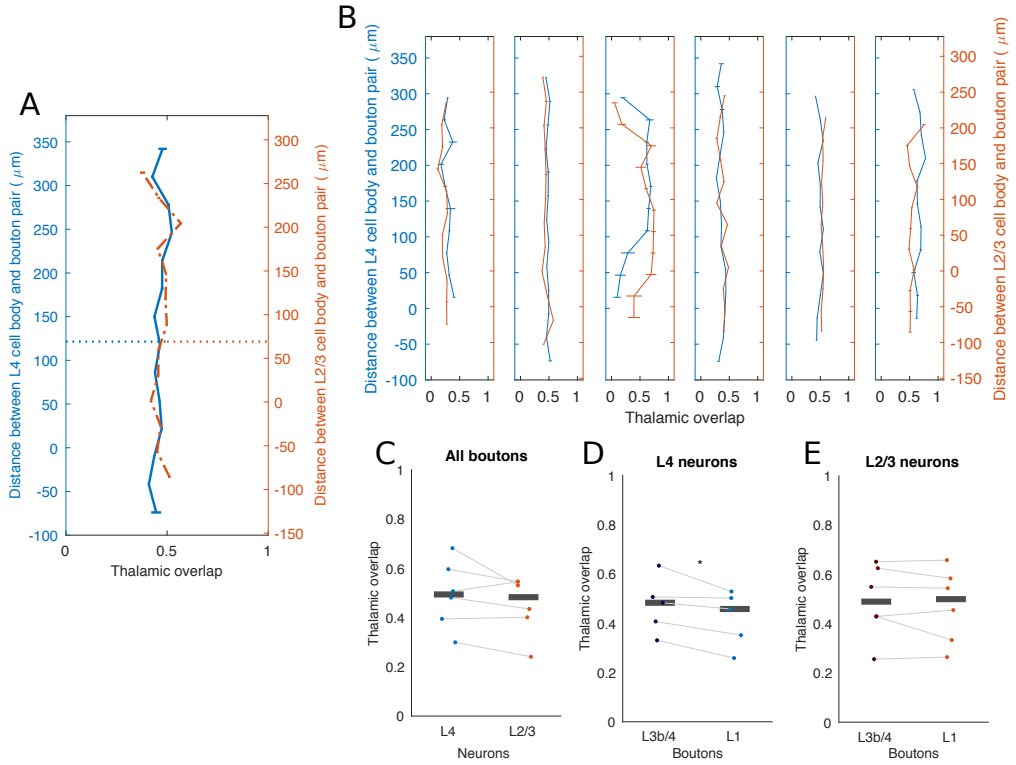

Fig. 5.18: Laminar distribution of thalamic receptive field overlap between thalamic boutons and cortical neurons. (**A**-**B**) Coefficients of thalamic overlap in the receptive fields of pairs of thalamic axonal boutons and cortical neurons in L4 (blue) and L2/3 (red) arranged by the vertical distance of the bouton from the neuronal cell body. Number of pairs per 30 μm wide bin is between 174 to 8406 for L4 and 626 to 6400 for L2/3. Error bars are the standard error of the mean. Horizontal lines indicate mean cortical distance across all pairs of boutons and neurons. (**A**) Pooled data. (**B**) Data from individual volumes. (**C**) Mean thalamic overlap for L4 and L2/3 neurons for each included volume (n = 6). Thick grey lines indicate medians. (**D**) Mean thalamic overlap between neurons in L4 and boutons in L3b/4 and L1 within each included volume (n = 6). Thick grey lines indicate medians. (**E**) Mean thalamic overlap between neurons in L2/3 and boutons in L3b/4 and L1 within each included volume (n = 6). Thick grey lines indicate medians.

the mapped feature. This, however, is not the case, as it has been revealed by electrophysiological (Hubel and Wiesel, 1968; Sakata and Harris, 2009; Kondo and Ohki, 2016; Atencio and Schreiner, 2010b; Atencio and Schreiner, 2010a; Van Hooser et al., 2013; Martinez et al., 2005; Jin et al., 2011) and calcium imaging experiments (Kondo and Ohki, 2016; Winkowski and Kanold, 2013; Roth et al., 2016).

The experiments outlined in this chapter aimed to explore the transformations that take place as acoustic information travelling from the medial geniculate body

arrives to the granular and supragranual layers of auditory cortex, in the awake, passively listening mouse. The focus of analysis has been the spectral receptive field in relation to location within the cortical column. Measures of best frequency, spectral bandwidth, frequency response area and neuronal correlations to signal and noise have been compared across neurons in L2/3, neurons in L4, thalamic inputs to L1 and thalamic inputs to L3b/4. In order to make sense of the findings from such comparisons, I will attempt to synthesise what the experiments tell of the differences and similarities in how neurons from L4 and L2/3 of auditory cortex integrate thalamic inputs.

Consistent with their role as major targets of core-type thalamic input, L4 principal neurons exhibited the strongest functional similarity with thalamic boutons. Neuronal tuning was more prevalent and FRAs were more similar at depths corresponding to L4 than in L2/3. Within each volume of cortex imaged, the mean BF of neurons in L4 correlated well with the mean BF of thalamic inputs through the whole volume, whilst L2/3 neurons did not. Similarly, the pairwise BF differences between L4 neurons and the local thalamic inputs were small, particularly with boutons in L3b/4 which also showed higher thalamic overlap and cortical coverage with L4 neurons. This suggests a higher degree of spectral receptive field inheritance from thalamic inputs in middle layers to L4 neurons. All of this is in accordance with the well known role of L4 neurons as thalamocortical recipients, which can be strongly driven by synchronous thalamic inputs on basal dendrites (Richardson et al., 2009; Bruno and Sakmann, 2006) and which are in general a more functionally homogeneous population (Winkowski and Kanold, 2013). Nevertheless, the mean cortical coverage of L4 neurons by L3b/4 boutons was still only 0.50, and the FRA similarity coefficient only 0.16, suggesting that a significant portion of the receptive fields of L4 neurons might not be inherited from thalamus. In fact, *in vitro* studies have revealed that most of the excitatory synaptic inputs to auditory L4 come from neighbouring cortical cells (Kratz and Manis, 2015; Richardson et al., 2009).

Noise correlations are of significant importance in sensory neuroscience, as they strongly impact the efficiency by which a population of neurons can encode sensory

information (Cohen and Kohn, 2011; Averbeck et al., 2006; Harris and Mrsic-Flogel, 2013). Noise correlations have been found to be significantly high in sensory cortices, which is considered to be the result of redundant coding strategies by populations of cortical neurons (Harris and Mrsic-Flogel, 2013; Rothschild and Mizrahi, 2015). However, there is some dispute about what the origin of these stimulus-independent correlations might be. The prevailing view poses that noise correlations in cortex are the result of recurrent cortical amplification of ongoing activity and neuromodulatory effects (Cohen-Kashi Malina et al., 2016; Reig et al., 2015). An alternative theory suggests that cortical noise correlations, particularly in L4, could be inherited directly from thalamic inputs. This is based on the observation that a large number of synchronous thalamic inputs strongly drive individual L4 cells (Bruno and Sakmann, 2006) and that silencing cortical firing in V1 had a negligible effect on the trial-to-trial variability of L4 responses (Sadagopan and Ferster, 2012). Whilst in reality, both intracortical and thalamocortical connectivity might contribute to the trial-to-trial variability of sensory-evoked cortical responses (Azouz and Gray, 1999), particularly in different layers (Cohen-Kashi Malina et al., 2016), a corollary of the thalamic-origin theory is that thalamic noise correlations might be high in thalamus too.

L2/3 neurons were found to be generally more functionally heterogeneous in their BFs. Whilst their spectral coupling with thalamic boutons was generally weaker than L4, they did show BFs which were, in average, slightly but statistically significantly closer to the BFs of boutons in L3b/4 than to the BFs of boutons in L1. Whilst description of the spatial distributions of synaptic inputs to L2/3 neurons of auditory cortex is lacking, L2/3 neurons in the somatosensory cortex have been shown to receive core-type thalamic inputs on their basal dendrites and matrix-type inputs on their apical dendrites (Petreanu et al., 2009).

The most significant difference between L2/3 and L4 was in noise correlations, an observation that had previously been made in anaesthetised mice (Winkowski and Kanold, 2013). This increase in noise correlations from L4 to L2/3, together with the progressive weakening in co-tuning, could both be the consequence of the

integration in L2/3 of cortico-cortical inputs, including vertical connections from L4 (Thomson, 2007). However, since the tuning quality and bandwidth in L2/3 was not significantly different than in L4, the properties of such synaptic integration by L2/3 neurons might not be fully displayed in their spectral receptive fields. Perhaps L2/3 neurons mediate the emergence of receptive fields with more complex properties, something like what has been described in V1 of the tree shrew, where orientation selectivity in L2/3 emerges as a result of the convergence of ON and OFF inputs derived from L4 neurons (Van Hooser et al., 2013). Whilst this might be an appealing hypothesis and a reason for further enquiry, it is important to point out that what my experiments and those by Winkowski and Kanold (2013) show about L2/3 and L4 of auditory cortex, has yet to be confirmed in other species. For example, the above-mentioned emergence of orientation selectivity in L4 observed in tree shrews does not happen in the V1 of carnivores. Instead their orientation preferences appear already at the level of L4 neurons which integrate inputs from ON and OFF neurons of the lateral geniculate body (LGN). Thus, as with much of what has been described regarding the fine-scale organisation of cortical circuits, there are likely to be some species differences which should not be overlooked (Harris, 2015).

The bouton tuning quality in these experiments, as assessed by Gaussian fitting to the level-averaged tuning curve, was comparable to that from boutons imaged for the awake, axonal imaging experiments in chapter 3 (**Fig. 3.17**), but lower than in anaesthetised animals (**Fig. 4.7**). Lower tuning quality in awake animals could be the result of an increased number of multi-peaked receptive field (Joachimsthaler et al., 2014; Evans and Whitfield, 1964), but also of motion artifacts and noisier FRAs. The imaging stage, mouse head bars and cranial windows used in these experiments, as well as the use of motion correction algorithms during the processing of the imaging data, were aimed to minimise the effects of motion on imaging. This, evidently, is of great importance when imaging small structures like axonal boutons, which would be more susceptible than whole neurons to motion artifacts. Here, the similarity in tuning quality between thalamic axons and neurons imaged in the same

awake, head-fixed animals, suggests that motion artifacts are not strongly affecting the characterisation of receptive fields.

Noise correlations were found to be significantly higher between pairs of thalamic boutons than between pairs of nearby cortical neurons. The simplest explanation would be that this is caused by boutons belonging to the same axons. However, there are several reasons to think this is not the case. First and foremost, pairs of boutons belonging to the same axon would have both very high noise and signal correlations. However, signal correlations between pairs of boutons were not significantly different to those of the cortical neurons. Based on this criteria, I showed in chapter 3 that boutons belonging to the same axon—and thus, exhibiting unusually high signal and noise correlation— constitute a very small fraction of the boutons within an imaged region. Moreover, the weaker co-tuning observed in boutons when compared to neurons also suggests different thalamic origin.

At least one study directly compared thalamic and cortical noise correlations within the somatosensory modality, and found them to be lower in thalamus (Kim et al., 2003). However, a major drawback of this study was that it was performed under anaesthesia, which can significantly affect noise correlations (Ecker et al., 2014). There might also be a degree of species differences, since in the halothane-anesthetised cat, noise correlations were found to be similar in MGB and auditory cortex (Chechik et al., 2006). Yet, effects of behaviour in noise correlations are probably the most significant and yet the least explored. Recently, a study by Guo et al. (2017a) revealed that responses of neurons in the MGBv can be strongly modulated by cortico-cortical projections. In contrast, an earlier study had reported that L4 neurons in mouse A1 exhibit negligible behavioural modulation in comparison to L2/3, although in this case what was considered behaviour was either simple locomotion or spontaneous whisking (Zhou et al., 2014). This is a clear example of the importance of choosing the appropriate behavioural task when exploring neuronal circuits in different brain areas and species (Krakauer et al., 2017).

In conclusion, I find patterns of columnar organisation that agree with what has been previously shown in the anaesthetised mouse (Winkowski and Kanold, 2013) and with what is known about the synaptic organisation of the auditory cortical column (Richardson et al., 2009; Kratz and Manis, 2015; Viaene et al., 2011c). The general observation, however, is that the differences between L2/3 and L4 in terms of their spectral receptive fields and their relationships with thalamic inputs are relatively small. If there are significant transformations taking place in the supragranular layers of auditory cortex, they might not be fully manifest in the tuning of the neurons to pure tone stimuli. Similar conclusions have been drawn in the past by studies attempting to characterise auditory columnar transformations by the insertion of vertical electrode arrays (Wallace and Palmer, 2008; Atencio et al., 2009; Atencio and Schreiner, 2010b; Atencio and Schreiner, 2010a), most of which failed to identify any systematic laminar variation in spectral properties. Thus, advances in our understanding of auditory cortical circuits and their computations might depend on the community embracing the use of new or at least more complex stimulus features than what have been used here (Schreiner and Winer, 2007).

6 Charting the Depths: Fibre-based Imaging of Deep Brain Regions

6.1 Deep-brain microscopy

Current approaches to non-invasive (surface) high-resolution imaging of living systems, such as two-photon microscopy, offer micrometer resolution up to penetration depths of about 1 mm (Ji, 2014; Denk et al., 1990). When imaging the intact mammalian brain, this restricts optical access to dozens of sub-cortical structures including the thalamic local circuits whose function is so inextricably intertwined with that of the cortex (Sherman and Guillery, 2013; Jones, 2007), as well as to the subgranular layers of the neocortex which are some of the least understood components of the cortical circuit[1]. In an attempt to overcome this limitation, a number of approaches have been adopted. Some studies have simply used cortical excavation to obtain optical access to areas like the hippocampus (Mizrahi et al., 2004; Dombeck et al., 2010). Endoscopic approaches have been adopted principally in the form of fibre bundles (Flusberg et al., 2005) or GRIN lens-based endoscopes (Levene et al., 2004; Jung et al., 2004). Sadly, both GRIN lenses and fibre bundles tend to be large—unlike the individual fibres within latter—, and they can cause substantial mechanical damage to overlying brain regions (Bocarsly et al., 2015) precipitating neuropathological gliosis (Xu et al., 2007) and potentially compromising circuit integrity (Moshayedi et al., 2014).

[1] A recent review by Harris (2015) described L6 corticothalamic neurons as the "mysterious creatures of the deep".

Single optical fibres have already been used to monitor the average activity of populations of GCaMP-expressing neurons in the striatum, in a method known as time-correlated single-photon counting (TCSPC) (Cui et al., 2014). What if it was also possible to use an individual fibre, not just as a light guide, but as an image forming device in its own right? Clearly, this would greatly reduce invasiveness and its unwanted effects, as tissue damage is approximately a quadratic function of the outer diameter of the inserted probe (Cui et al., 2014). It would also reduce the duration of the surgeries and improve recovery. Finally, smaller probes mean that it may be possible to implant more of them and image several deep brain areas simultaneously.

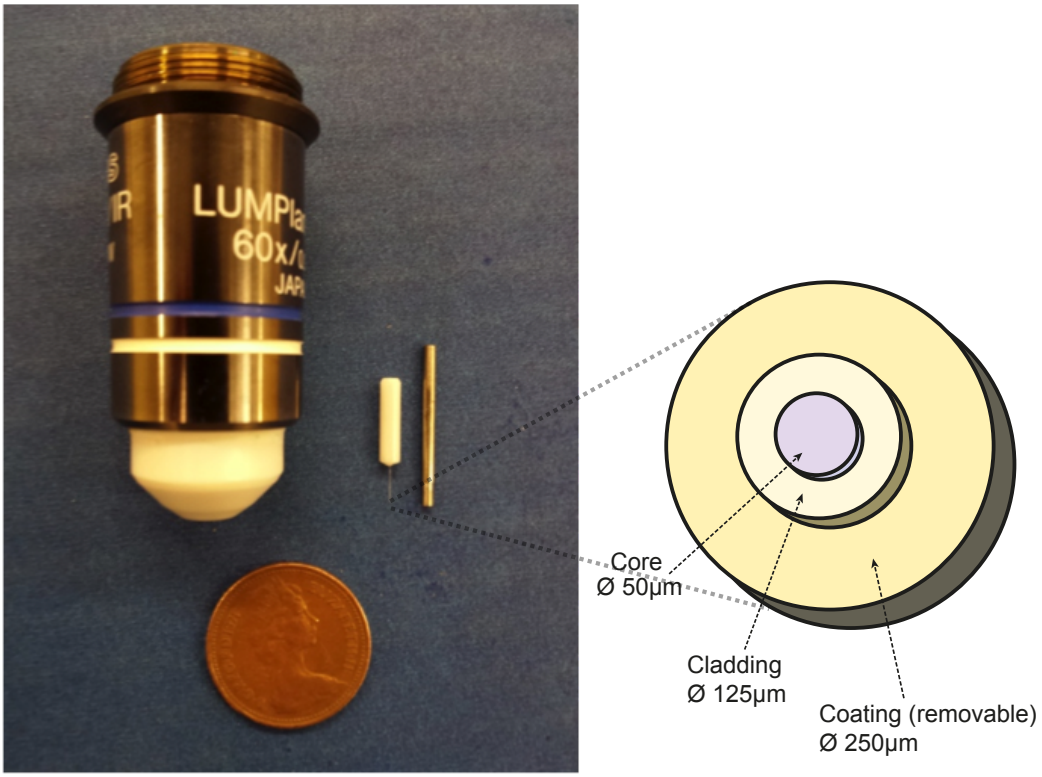

Fig. 6.1: Comparison of the dimensions of the light guides used for *in vivo* imaging. A microscope objective, a GRIN lens and a multi-mode fibre (MMF). Traditional optical lenses (left) can be used to perform scanning two-photon microscopy of the neocortex. GRIN (gradient index) lenses (right) allow endoscopic access to deep brain areas, but with some degree of damage to the overlying cortex. The method implemented here uses a multimode optical fibre (middle) for imaging (shown here attached to a ceramic cannula). Its core diameter is 50 μm, and its total diameter 125 μm, after removal of the external plastic coating.

Holographic methods for imaging through a multi-mode optical fibre

Recently, optical fibre lensless imaging was demonstrated by the group of Tomas Cizmar at Dundee University (Čižmár and Dholakia, 2011; Cižmár and Dholakia, 2012; Plöschner and Čižmár, 2015) (**Fig. 6.2**). Their approach was to regard an optical fibre as a transmission matrix (TM), which completely randomises the light that goes through it, but that can be analysed and thereby reversed. Using a spatial light modulator (SLM) to characterise the transmission matrix, they were able to calculate and apply the inverse transform of the fibre randomising matrix to the propagating light (Čižmár and Dholakia, 2011). This allowed them to perform scanning fluorescence imaging through a standard multimode optical (MMF) fibre of 50 μm core diameter (Cižmár and Dholakia, 2012). As part of my doctorate project, I contributed to the development of a compact and highly optimised imaging system for minimally invasive *in vivo* applications. The system uses holographic control of light propagation to perform scanning fluorescence microscopy through a single $50\,\mu$m-core multimode fibre (**Fig. 6.1**). In this chapter, I present the first applications of this technique for the imaging of living neuronal tissue, first in the form of the characterisation of the system in an *in vitro* context, and then as a demonstration of its *in vivo* capabilities for imaging neurons in deep structures of the mouse brain.

6.2 Assembling the fibre-based imaging system

In the heart of the fibre-based imaging system that I test here, is a computer-controlled dynamic optical element, a spatial light modulator (SLM), which enables manipulation of light propagation through an arbitrary length of MMF (Čižmár and Dholakia, 2011; Cižmár and Dholakia, 2012). Prior to imaging, the SLM is employed in a calibration procedure in which the transmission matrix (TM) of the optical system is determined (Popoff et al., 2010) (**Fig. 6.4**). The availability of the system-specific TM then allows the user to design a set of holographic modulations,

Figure adapted from copyrighted material. Not available in the Online dissemination version of this thesis.

Fig. 6.2: Optical geometry for fibre-based lensless imaging. Diagram of the experimental geometry. Light from a laser source is directed by a series of lenses (L1-4), mirrors and collimators onto a spatial light modulator (SLM). There the light signal is split into two pathways, later recombined on a polarizing beam splitter (PBS) and coupled into the multimode fibre (MF) by a series of lenses (L5-7). A CCD camera and an objective (MO) are used during calibration to image the fibre input facet. During imaging, the fluorescence signal emitted from the sample is collected by the fibre, separated from the excitation pathway using a dichroic mirror and detected by a photomultiplier tube (PMT) (not shown). Re-printed from Plöschner and Čižmár (2015). *L1–L9*, lenses; *PBS*, polarizing beam-splitter; *NPBS*, nonpolarizing beam-splitter; *PMF*, polarization maintaining fibre; *SMF*, single-mode fibre; *MMF*, multimode fibre; *MO*, microscope objective; $\lambda/2$, half-wave plate; *OI*, optical isolator.

which are employed in the consecutive image acquisition procedure. Each of these modulations, when applied at the SLM, will result in the formation of a diffraction-limited focus at a specific location across the fibre output plane. Importantly, the diffraction-limited point may be formed at an arbitrary distance away from the distal fibre facet. Such a feature provides the basis for fibre-based volumetric scanning fluorescence microscopy.

Imaging can be performed immediately after the TM acquisition and, as long as the fibre alignment is not changed, carried out for hours and even days without the need for further calibration. This is in marked contrast with other endoscopic imaging methods that, due to their size and complexity of implantation surgery, typically require several weeks before imaging becomes possible (Bocarsly et al., 2015).

Because MMFs can couple light to several orthogonal modes, their bandwidth can be up to two orders of magnitude greater than a single-mode fibre (or bundle of them) of similar size, albeit with ensuing spatial distortions (Gloge, 1971). The holographic approach I present here allows for the reversion of such distortions, maintain diffraction-limited performance whilst dramatically reducing the probe size, hence reducing tissue damage by several orders of magnitude. This considerably improves the trade-off between resolution and footprint of microendoscopic methods for deep-brain imaging *in vivo*.

Experimental geometry

The optical geometry was optimised to give the functional stability and mobility necessary for use *in vivo* (**Fig. 6.3-A**). First, part of the system distributes light from a laser source into two single-mode polarisation-maintaining optical fibres, one to deliver excitation signal to the SLM, the other to provide reference during calibration. The main optical arm comprising the SLM, MMF probe, relay optics and fluorescence detection unit was designed to be as compact as possible. It is embedded within a robust caged framework and housed on a 3-dimensional micro-positioning stage to facilitate alignment during calibration as well as navigation of the MMF probe inside the brain. Finally, the calibration arm, which is only used during TM acquisition, relays the MMF probe output signal to the CCD camera and combines it with the reference beam. The implementation of a GPU-accelerated toolbox for SLM control (Plöschner and Čižmár, 2015) allows for the acquisition of the full transmission matrix of a $50\,\mu\mathrm{m}$-core MMF in less than 4 minutes.

At the early stages of the project, I assembled a prototype of the fibre-based system, originally built and designed by Plöschner and Čižmár (2015), which was optimised for *in vivo* imaging (**Fig. 6.3-B**). The setup consists of a monochromatic mirror, where linearly polarised light beam ($\lambda = 532/488\,\mathrm{nm}$; CrystaLaser) is split and coupled into two separate optical fibres: a polarisation maintaining (PMF) and a single-mode fibre (SMF). Light exiting the SMF is collimated ($f = 60\,\mathrm{mm}$, achromatic doublet) and its polarisation is aligned with working polarisation of the SLM (Meadowlark

Optics, 512×512 pixels) using a half-wave plate. The light is phase modulated by the SLM in an off-axis regime and Fourier transformed by a plano-convex ($f = 100\,\mathrm{mm}$) lens onto an iris that only transmits the first diffraction order. The transmitted signal is then reflected by a dichroic mirror (Thorlabs MD498) and circularly polarised by a quarter-wave plate to assure minimum coupling between polarisation states. A circularly polarised light then enters a telescope consisting of plano-convex ($f = 50\,\mathrm{mm}$) and aspheric ($f = 8\,\mathrm{mm}$) lenses coupling the light into a multimode fibre (Thorlabs, FG050UGA *NA* = 0.22). The subsequent light path depends on the mode of operation of the optical system. The standard experimental protocol consists of two modes of operation: acquisition of the transmission matrix (system calibration), and image acquisition.

System calibration

The purpose of this mode is to determine the systems' transmission matrix (TM), which is chiefly determined by the piece of multimode fibre (MMF) being used for imaging (**Fig. 6.4-A**). In this mode, the light exiting the MMF is coupled into the calibration unit. Here, the light output is imaged by a microscope objective lens (Olympus 20×, NA = 0.4) and an achromatic doublet ($f = 150\,\mathrm{mm}$) onto a CCD camera (Basler pilot piA640-210gm). In between the lenses, the signal is converted back into the linear polarisation state using a quarter-wave plate and merged with a reference signal using a 50:50 non-polarising beam-splitter.

The TM is a linear relation between bases of input and output modes (Popoff et al., 2010). The input modes are diffraction-limited focal points defined across an orthogonal grid (50×50) at the input facet of the MMF. The 120×120 output modes are analogously defined along the plane of the MMF output facet or any plane axial to the fibre facet (thus allowing for volumetric sectioning). The SLM is used to sequentially generate input modes which propagate through the MMF and leave as a linear combination of output modes. These are analysed by a corresponding number (120×120) of CCD camera pixels, whilst sequential phase offsetting and interference with the reference signal are applied. The result is a vector of the TM.

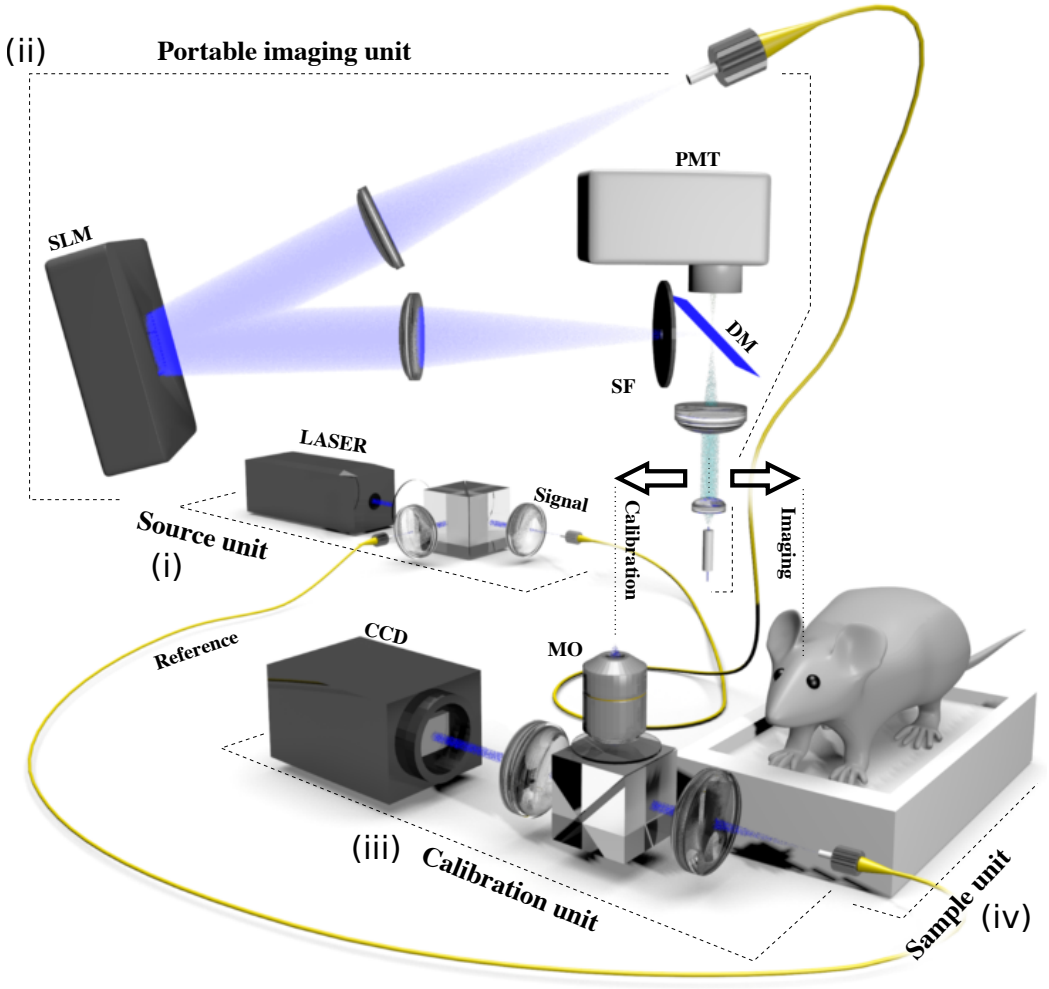

Fig. 6.3: The piloted fibre-based imaging system for deep-brain *in vivo* imaging. (**A**) Schematic diagram of the experimental geometry (i) Laser power distribution unit. (ii) The main portable imaging arm, which by means of phase manipulation of light at individual pixels of the SLM controls the light propagation through the multi-mode fibre (MMF). (iii) The calibration unit for the acquisition of of the transmission matrix. (iv) The sample unit for tissue sections and head fixed animal models. (**B**) The optical setup built for the experiments reported here and based on the geometry in A. Most of the components are attached to a movable stage which can be coupled to a fibre cannula. *DM*, dichroic mirror; *MMF*, multimode fibre; *MO*, microscope objective; *PMF*, polarization maintaining fibre; *PMT*, photo multiplier tube; *SF*, single-mode fibre.

After acquisition of all input modes the TM measurement is completed and can be used to design the input fields (and the necessary SLM gratings) for generation of individual output modes (diffraction limited foci at the MMF output) or any other desired light field leaving the MMF.

Scanning fluorescence imaging

Once calibrated, the microscope objective beneath the MMF is exchanged for the sample unit housing sections of neural tissue or a head-fixed animal model, and the fibre is lowered into the area of interest. The SLM's diffraction grating generates a holographic projection (input field) across the proximal fibre facet (**Fig. 6.4-B**). This linear superposition of focal points, constructively interferes while propagating through the fibre in order to collimate in a single, diffraction limited focal light-point at short distance from the distal fibre end. After this, the principles of imaging are very similar to those of standard scanning fluorescent microscopy. With a maximum SLM refresh rate of 102 Hz, this point can be used to raster-scan a full set of 120×120 output modes or an arbitrary selection of them across the fluorescent sample. The emitted wavelength is then colluded and backtracked through the fibre. The intensity of this transmitted response signal is registered for each raster scan position by a photo-multiplier tube (PMT) and it constitutes the pixel value in the acquired image.

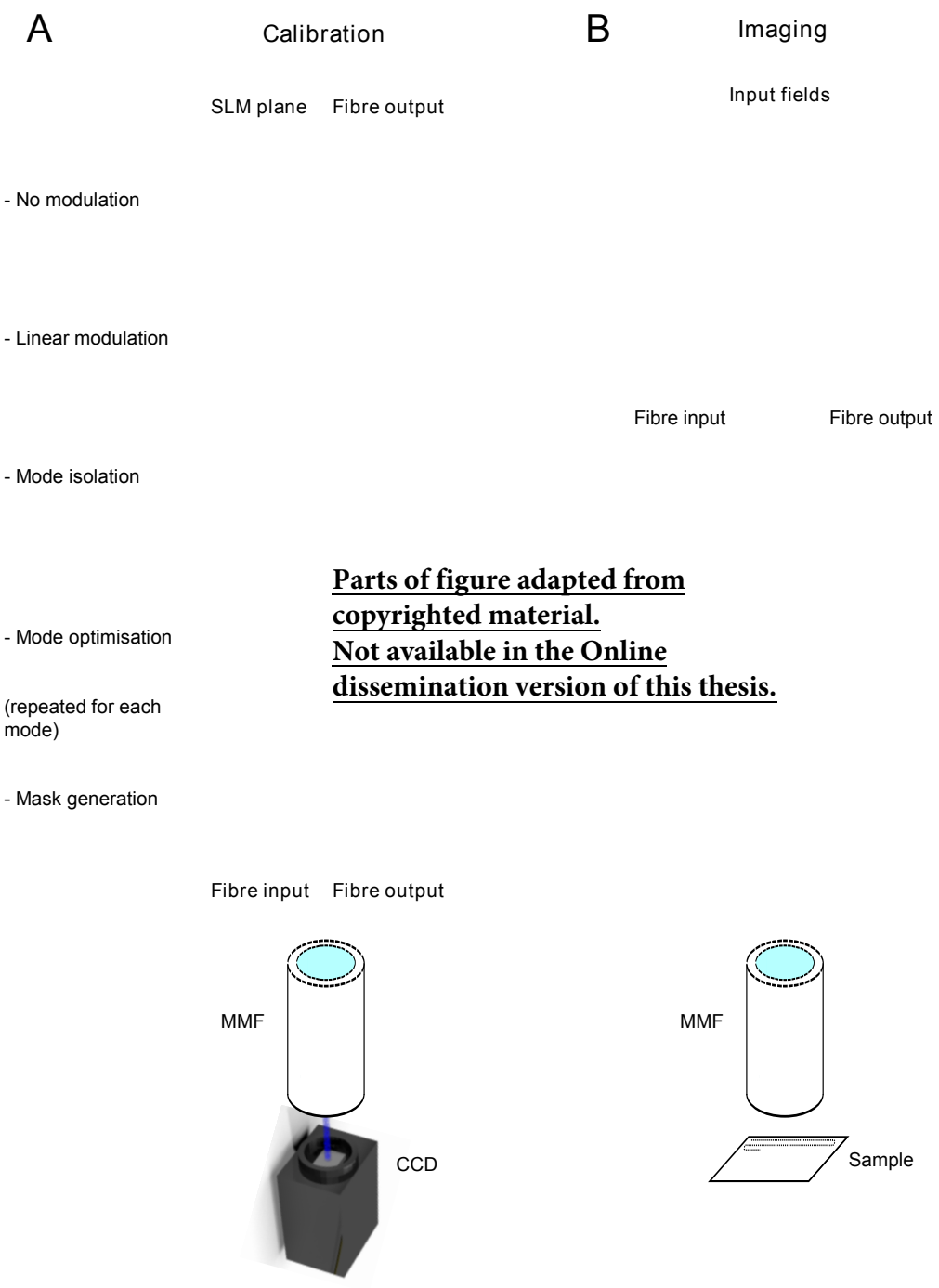

Fig. 6.4: Protocol for fibre-based microscopy *in vivo*. Once a fibre is coupled to the optical geometry a calibration is performed to obtain the transmission matrix (TM). This involves manipulation of the individual modes that make up the laser light wavefront by using an spatial light modulator (SLM). Every mode is isolated and phase-shifted so that it give the highest signal possible. After all modes have been optimised the result is a speckled mask, the fibre input, that generates a focused point of laser light as an output. Different input masks are required to produce focused points at different locations of the image plane. The calibration process is completed in approximately 4 min. The sample is then placed under the optical system for scanning fluorescence imaging by replay of the SLM masks produced during the calibration. Adapted from Čižmár et al. (2010) and Cižmár and Dholakia (2012).

6.3 Resolution measurements and *in vitro* validation

The imaging resolution is unaffected by increasing the sample's light

The spatial resolution of the imaging system was measured with a custom-made USAF-1951 resolution test chart. Fig. 6.5-B shows that at $532\,\mathrm{nm}$ the spatial features can be resolved up to $1.5\,\mu\mathrm{m}$. This agrees well with the Rayleigh criterion for imaging system with corresponding numerical aperture as the one of the fibre used here (0.22). Using the wavelength of $488\,\mathrm{nm}$ enhances the resolution proportionally to $\approx 1.35\,\mu\mathrm{m}$. The fluorescence scanning of this system is free from granulous artefacts, typical of computational approaches (Kim et al., 2017; Mahalati et al., 2013), which can be easily confused with synaptic structures and where high resolution can only be maintained in very sparse samples. As shown in Fig 6.5-A, increasing the content of light emitting structures across the field of view may intensify the magnitude of a uniform background signal, however the resolution is fully maintained and no artefacts are introduced to the imaged structures.

Living neuronal tissue can be imaged through a single multi-mode fibre *in vivo*

First, I tested the capabilities of the fibre-based system using a $532\,\mathrm{nm}$ laser source to image neurons in hippocampal organotypic slices expressing the red fluorescent protein DsRed (**Fig. 6.6**). There are many potential advantages of allowing dual-fluorescent imaging (chapter 5 of this thesis being one example of them), so the system was designed to be compatible with both green ($532\,\mathrm{nm}$) and blue ($488\,\mathrm{nm}$) laser sources. Albeit with the expected lower resolution than when using a $488\,\mathrm{nm}$ source, the acquired images depict fluorescently labelled neurons for which it is possible to differentiate cell bodies and several neuronal processes morphologically similar to dendrites and individual axons.

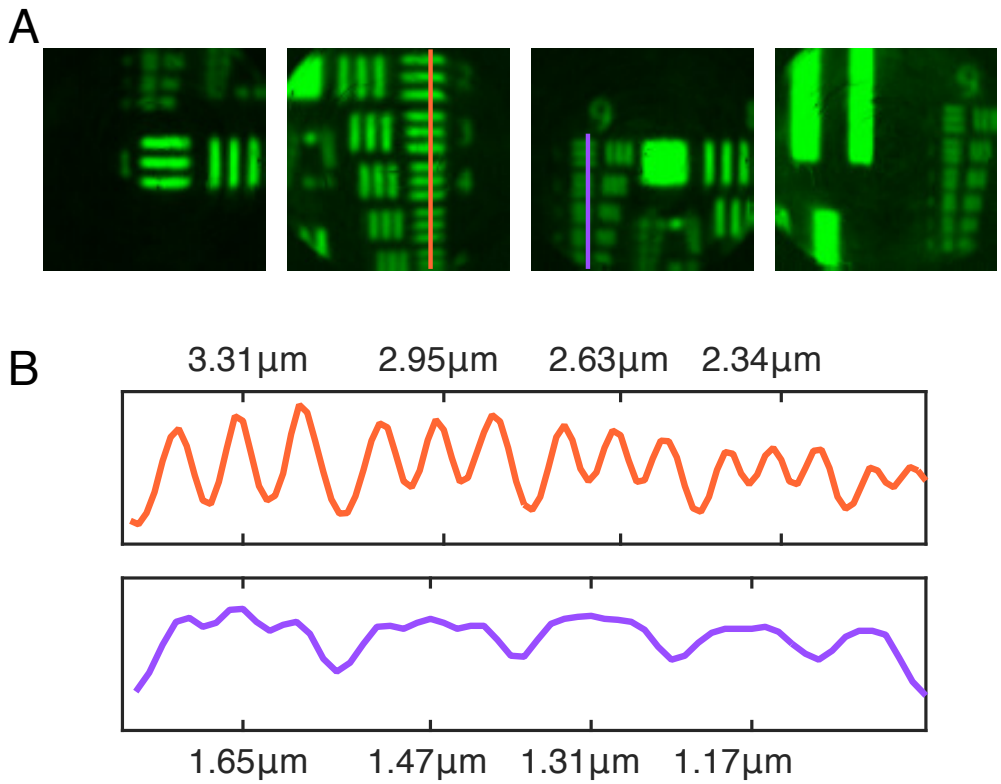

Fig. 6.5: Resolution measurements. (**A**) Resolution measurements were conducted on custom USAF-1951 resolution target. (**B**) The resulting lateral resolution of $\approx 1.5\,\mu\mathrm{m}$ has been confirmed at the wavelength of $532\,\mathrm{nm}$.

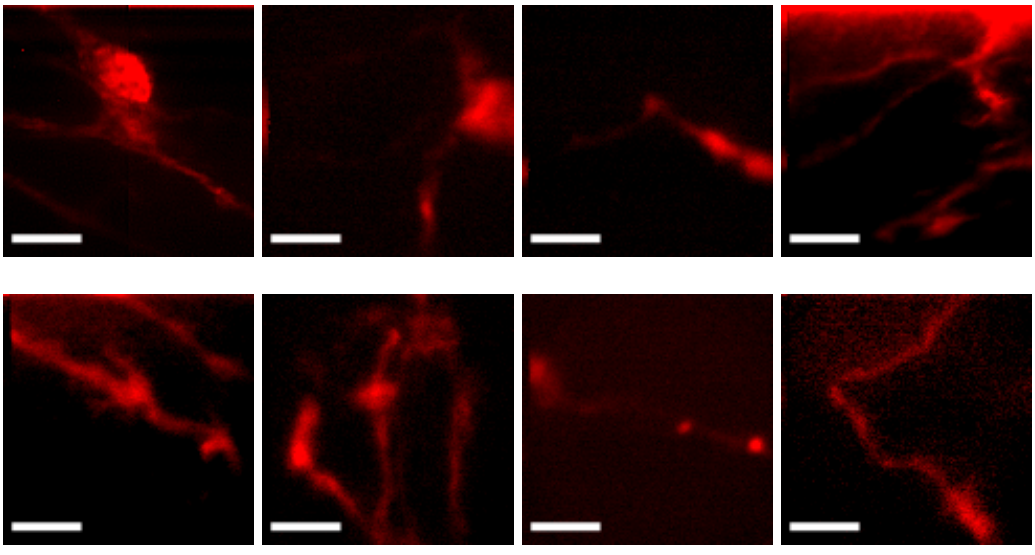

Fig. 6.6: Demonstration of the system adaptability for imaging red fluorescent proteins Hippocampal neurons from *in vitro* slices labelled with the red fluorescent protein *DsRed* and imaged with a version of the fibre-based system with an argon laser source. Scale bars = 20 $\mu\mathrm{m}$.

Fibre-based imaging of dynamic changes in fluorescence *in vitro*

Although the system's scanning rate is currently only 10 ms per pixel (i.e. 2.4 seconds for a 120 x 120 pixels frame), currently available methods (Cižmár and Dholakia, 2012; Conkey et al., 2012; Mitchell et al., 2016) could be readily incorporated to the geometry to increase its scanning speed and make it suitable for functional high-resolution imaging. Nevertheless, my characterisation of the system already provided some indications that this technology is capable of detecting dynamic changes in fluorescence that correlate with neuronal activity both *in vitro* (**Fig. 6.7**) and *in vivo* (**Fig. 6.10**).

6.4 Demonstration of fibre-based imaging *in vivo*

Fibre-based structural imaging of subcortical dendritic spines *in vivo*

Having optimised the system's performance for imaging living neuronal tissue *in vitro*, I set out to demonstrate *in vivo* imaging of neurons from deep regions in the intact mouse brain. I used the Thy1-GFP-M mouse line that expresses GFP sparsely throughout the nervous system and which is routinely used for *in vivo* structural imaging studies (Feng et al., 2000). As the diameter of the fibre is small ($50\,\mu\mathrm{m}$ core inside $125\,\mu\mathrm{m}$ of cladding), I was able to simply lower it into the mouse brain through a small craniotomy and image as I advanced through the tissue. This is a highly significant improvement over existing methods for deep brain imaging which generally require lengthy surgeries, aspiration of overlying brain tissue, and several days until compressed debris clear from the field of view. **Fig. 6.8** shows images of a fluorescent neuron in the dorsal striatum, imaged after lowering a fibre $1.8\,\mathrm{mm}$ into the brain of an anaesthetised mouse. Dendritic spines are clearly identifiable and their three dimensional structure becomes apparent through holographic variations in the focal plane. This represents a further considerable advantage of the MMF

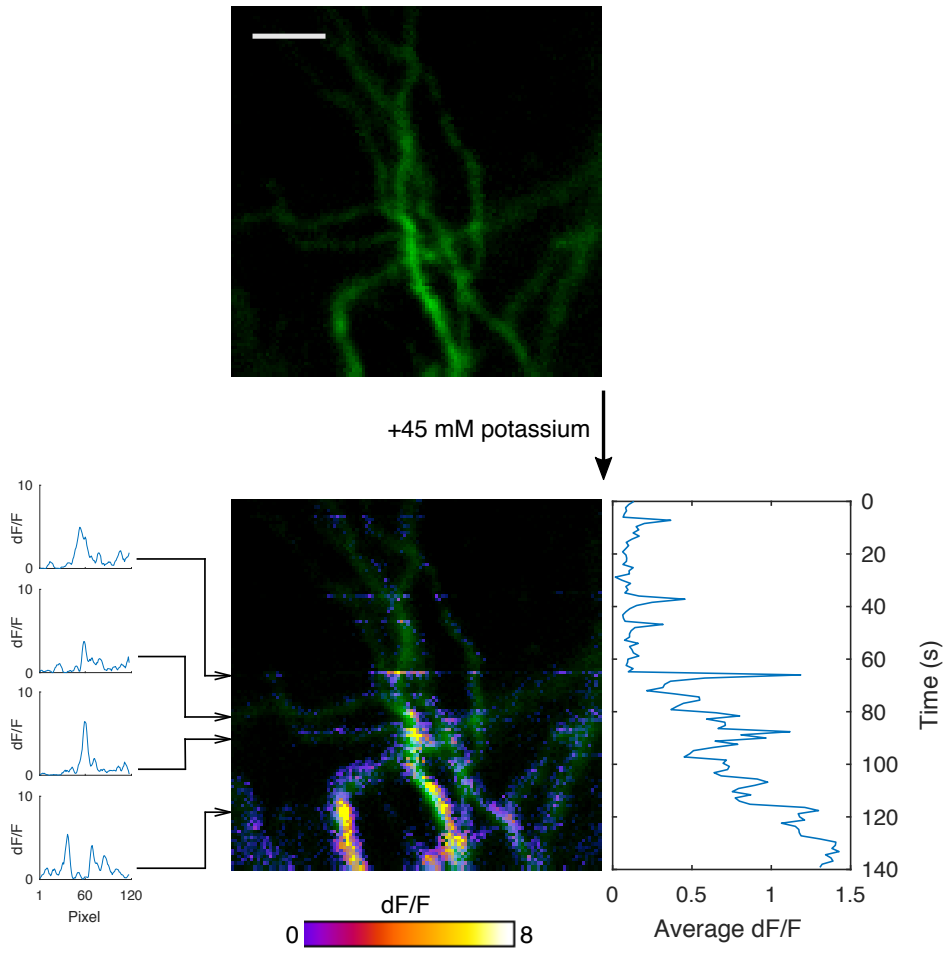

Fig. 6.7: Fibre-based imaging of dynamic changes in calcium signals *in vitro*. Neuron in an organotypic hippocampal slice was filled with the calcium-sensitive dye OGB-1 (top). After a bath application of 45 mM of potassium the gradual increase in intracellular calcium resulting from the depolarisation of the neuron was detected through dynamic changes in fluorescence (bottom). Scale bar = 10 μm.

fibre imaging system, which allow the imaging plane to be changed virtually, with a range from 0 to 100 μm from the fibre facet, without altering the position of the fibre in the sample. Post-mortem histological sectioning revealed a small fibre track in cortex and structurally preserved neurons around its margins (**Fig. 6.9**). Thus, the insertion of the multimode fibre several millimetres into the brain causes minimal mechanical damage to the underlying neuronal tissue.

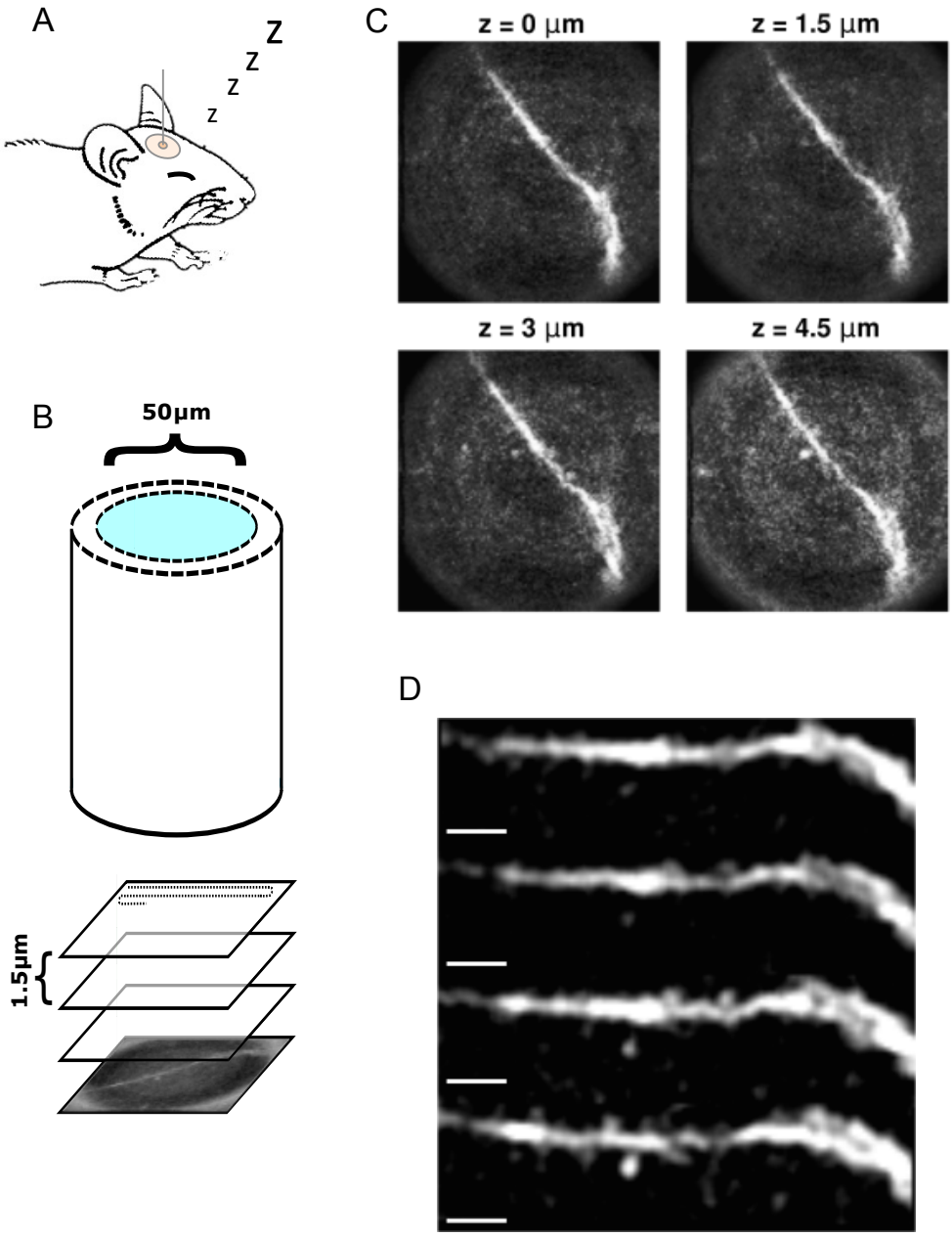

Fig. 6.8: Fibre-based structural imaging of a GFP-labelled dendrite of a neuron in the basal ganglia of an anaesthetised mouse.. (**A**) Imaging was performed by lowering a multi-mode fibre $1.8\,\mathrm{mm}$ into the brain of an anaesthetised mouse. (**B**) Scanning fluorescence imaging can be performed at several distal planes by calibrating the system with to the desired focal distances. (**C-D**) Dendritic spines are clearly identifiable and their three dimensional structure becomes apparent through holographic variations in the focal plane. Scale bars $= 5\ \mu\mathrm{m}$.

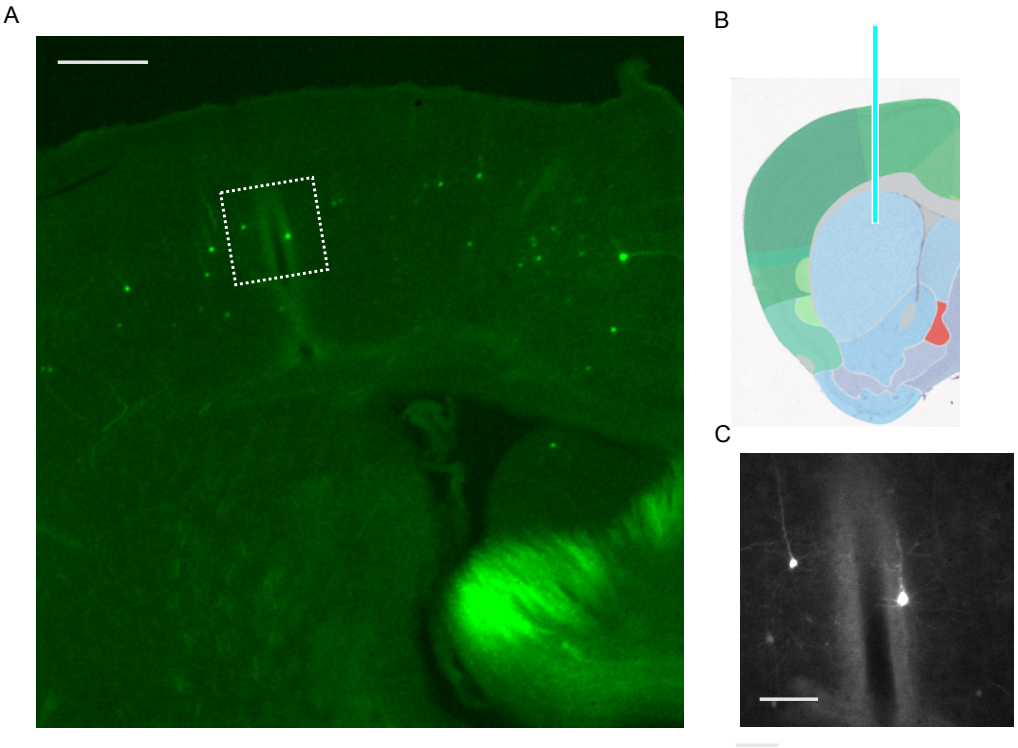

Fig. 6.9: Insertion of a multimode optical fibre causes minimal damage to cortex. (**A**) Histological sectioning of the mouse brain imaged in Fig. 6.8 showing the path of the fibre through cortex. (**B**) Atlas depiction of the region of striatum imaged in Fig. 6.8, adapted from the Allen Mouse Brain Atlas. (**C**) Inset shows the structure of cortical neurons is preserved even around the margins of the fibre track. Scale bars = 200 μm.

Fibre-based functional imaging of stimulus-driven calcium signals in the auditory thalamus *in vivo*

Although the current scanning rate of the system does not allow for full-frame functional imaging (frame rate = 2.4 seconds for a 120 x 120 pixels), it is possible to image single pixels at a 100 Hz rate and up to 3 pixels at 33.3 Hz, which is the full-frame scanning rate of a standard two-photon scanning microscope (for 512 x 512 pixel frames). Thus, to prove the potential of this technology to measure dynamic neuronal signals *in vivo*, I sparsely labelled the MGB of C57BL/6 mice with the calcium indicator GCaMP6m (Chen et al., 2013) and imaged stimulus evoked calcium transients from a neurite of a sound responsive neuron (**Fig. 6.10**). Although these signals come from a single manually selected pixel, they show the potential of implementing existing technologies into the system, such as acousto-

optic deflectors (AOD) (Cižmár and Dholakia, 2012) or digital micromirror devices (Conkey et al., 2012; Mitchell et al., 2016), to increase imaging rate.

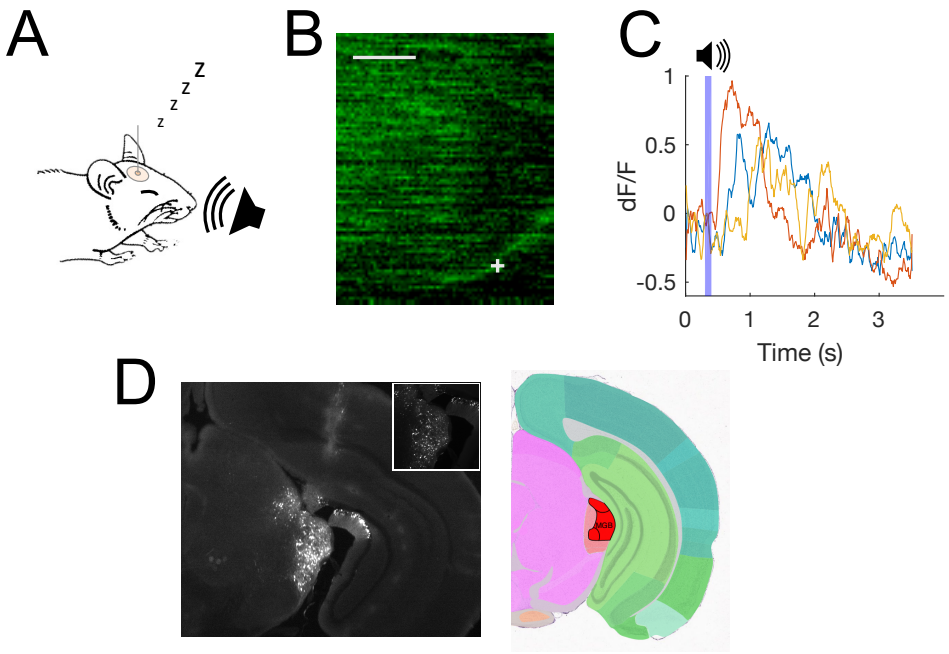

Fig. 6.10: Fibre-based functional imaging of stimulus-evoked calcium responses in auditory thalamus of an anaesthetised mouse. (**A**) A multimode optical fibre was lowered 3 mm down to the medial geniculate body (MGB) of an anaesthetised mouse. (**B**) Image from a single field of view showing neuronal projections fluorescently labelled with GCaMP6m. Scale bar $= 10\ \mu\mathrm{m}$. (**C**) Calcium response recorded at selected region of interest (white cross in B) and elicited by repeated presentation of a 100 ms pure tone of 16 kHz (blue bar). Colour traces show responses from individual trials. (**D**) Left. Post-mortem histological analysis shows sparse expression of the genetically-encoded calcium indicator GCaMP6m in the MGB and fibre track. Inset shows the level of sparse labelling of MGB neurons. Right. Atlas depiction of the MGB adapted from the Allen Mouse Brain Atlas.

6.5 Discussion

By replacing Fourier-based image relay with a holographic approach, the system I have piloted has managed to reduce the volume of tissue damage by more than

100-fold, while preserving diffraction-limited imaging performance. Here, I provide the demonstration of high-resolution fluorescence imaging of dendritic spines and stimulus-evoked calcium signals in deep-brain regions of mice. These results represent a major technological disruption in the hitherto unavoidable compromise between resolution and tissue damage, heralding new possibilities for deep-brain imaging *in vivo*.

In its current configuration, the fibre-based imaging system can operate at a scanning rate of approximately 10 ms per pixel, which is determined by the maximum refresh rate of 102 Hz for the SLM. Faster scan systems based around acousto-optic deflectors (AOD) (Cižmár and Dholakia, 2012) or digital micromirror devices (Conkey et al., 2012; Mitchell et al., 2016) are available and could now be incorporated into the geometry. I have presented some indications that the fibre-based systems is capable of detecting dynamic changes in fluorescence that correlate with neuronal activity, both *in vivo* and *in vitro*. Future developments would allow the scanning speeds necessary for wide-field imaging of neuronal population activity. This would be particularly useful for imaging in freely moving animals using long stretches of fibre. As it has been previously shown (Plöschner et al., 2015), the changes in the transmission matrix caused by fibre bending can be corrected for if fibre shape is accurately monitored. The main challenge for *in vivo* functional imaging comes from the need to avoid contamination of the dynamic signal from epifluorescent sources (Helmchen and Denk, 2005). Some progress has been made on this avenue by implementing a form of holographic confocal microscopy (Loterie et al., 2015) as well as by demonstrating the potential of step-index multimode fibres for achieving fibre-based two-photon microscopy (Morales-Delgado et al., 2015).

This form of *in vivo* fluorescent imaging of neurons within deep-brain structures is likely to be the least invasive, deep-brain, high-resolution approach reported to date. This new method provides a route to achieving high-resolution optical access to deep-brain sub-cellular processes in living and ultimately freely behaving animal models with minimal disruption to associated circuitry. This is also a prominent demonstration of the valuable applications of wavefront-shaping microscopy in

biomedical research (Gigan, 2017) and an overture for future advances in minimally-invasive imaging *in vivo* (Ji, 2014).

7 General Discussion and Conclusions

7.1 Summary of findings

The aims of this thesis were the following:

(1) to characterise the distribution patterns and spectral properties of projection from the various divisions of the medial geniculate body to the primary and secondary auditory cortical subfields in the mouse; (2) to investigate the functional micro-organisation of thalamocortical inputs to primary auditory cortex and its relationship to its large scale tonotopic organisation in the awake and anaesthetised conditions; (3) to evaluate the contribution of thalamocortical inputs to spectral integration in auditory cortex; (4) to explore the transformations in spectral receptive fields taking place between thalamus and cortex and within the granular and supragranular portions of the cortical column, in awake, passively listening animals; (5) to demonstrate the implementation of a novel, minimally invasive method for *in vivo* high-resolution imaging of neuronal circuits in subcortical structures, such as the thalamus.

My key findings are:

(1) Thalamocortical projections from the various subdivisions of MGB in the mouse, show very specific patterns of projection in terms of laminae and cortical area targeted, but they do not appear to be very focal.

(2) Spectral tuning is a functional feature prevalent only in the lemniscal projection from MGBv to primary auditory subfields, but largely absent in higher-order thalamocortical pathways.

(3) Frequency selectivity of individual thalamocortical axons is surprisingly heterogeneous, even in the middle layers (L3b/4) of the primary cortical areas where the thalamic input is dominated by the lemniscal projection.

(4) Thalamic input to layer 1 (L1) of the cortex is largely in register with the main input targeting the middle layers (L3b/4) and exhibits a similarly diffuse tonotopic organization.

(5) In awake, passively listening animals, L4 of auditory cortex exhibits a relatively more homogeneous local distribution of frequency preferences, which might be imparted by thalamic inputs in middle cortical layers. This distribution becomes more heterogeneous when transitioning to L2/3.

(6) By replacing Fourier-based image relay with a holographic approach, it is possible to significantly reduce the size of endoscopic probes, while preserving diffraction-limited imaging performance. This fibre-based probes are suitable for imaging neuronal structures in deep brain regions, such as the thalamus and the striatum.

To finalise this report, I will now discuss some of the broader implications of these findings and the limitations of the experimental approaches used here, as well as some possibilities for future research.

7.2 Auditory thalamocortical maps

Ordered forest, messy trees

A hypothetical explorer, attempting to describe the large masses of forest on our planet, might choose to start her quest through reconnaissance flights. From high up in the air, she would see the dark colours of the European pine forests, and consider them very different from the bright green and dense rain forests of the tropic, or the boreal forests often covered in snow. She could, if she did not know better, also conclude that the forests were all very homogeneous, perhaps each made of single species of tree, and that they smoothly transition from one to another as a function of their latitude. It would take our explorer to actually descend into each of these forests to appreciate the extraordinary dendrological[1] diversity that can be found when looking up close. In neuroscience, much of the research mapping neural circuits has been done by looking at static pictures of large scale anatomical features (Brodmann, 1909; Mountcastle, 1997). Electrode recordings have allowed us to descent into the forest and monitor what happens there, but this is done in the dark, blinded to the fine details and being only aware of the 'loudest' signals (Rothschild and Mizrahi, 2015). More detailed observations often required having to take a sample of the forest and examine it under artificial conditions, as in the case of *in vitro* work (Hackett et al., 2011). The power of high-resolution *in vivo* imaging methods lies on their ability to reveal the fine-scale organisation of the neuronal forest *in situ*.

In recent years, two-photon calcium imaging studies in various cortical areas have revealed a considerable degree of fine-scale functional heterogeneity among neurons embedded within their macroscopic cortical map (Rochefort et al., 2009; Smith and Häusser, 2010; Bandyopadhyay et al., 2010; Rothschild et al., 2010; Bonin

[1] The fact that the word dendrite, first coined in 1889 (Finger, 1994), has a common etymological origin with dendrology, i.e. the study of trees, shows that by no means am I the first one to use the analogy of brains and forests.

et al., 2011; Winkowski and Kanold, 2013; Peron et al., 2015b), even for the features that constitute the map itself. Such maps of the receptor surfaces have been long considered a fundamental feature of sensory system organisation at several ascending stages up until the primary cortices, but are largely absent in non-primary fields (Schreiner and Winer, 2007; Rothschild and Mizrahi, 2015). The results of my experiments add up to the picture of local functional heterogeneity within cortical maps. I have shown that thalamic inputs to small patches of auditory cortex, even in primary fields, show a surprisingly high degree of variation in their receptive fields. Whilst this challenges the view of a highly ordered auditory geniculocortical projection, does it tell us anything else about auditory cortical function and thalamocortical relations in general?

Cortical tonotopy: feature or bug?

The micro-organisation of stimulus features in other thalamocortical modalities suggests that the mouse brain is capable of establishing and maintaining very precise connections between thalamus and cortex (Roth et al., 2016). Thus, the topographically diffuse arrangement of MGB inputs in auditory cortex may be functionally relevant. An important consideration when comparing A1 with other primary cortical areas such as V1 and S1, is that A1 is higher in the processing hierarchy. It has been suggested that only lower stages in the auditory pathway use strict tonotopy as a substrate for local circuit computations, such as feature detection (Nelken et al., 2008). Neurons in cat auditory cortex, for example, show much lower levels of information redundancy when tested with complex sounds than neurons in IC, even if they have the same frequency preference (Chechik et al., 2006). Accordingly, shared frequency tuning is a weak predictor of the response of two cortical neurons to a natural stimulus (Bar-Yosef et al., 2002; Mizrahi et al., 2014).

If neurons if auditory cortex have access to a wider range of spectral inputs, they can integrate them to generate more complex receptive fields. Classical V–shaped frequency tuning in mouse auditory cortex is relatively sparse (Bandyopadhyay

et al., 2010; Rothschild et al., 2010). Even in L4, only about 65% of neurons have single–peaked tuning curves. This is still more pronounced when recording from unanaesthetised animals (Evans and Whitfield, 1964; Guo et al., 2012). The fact that, at the level of mouse MGB, V–shaped is still the most commonly found type of FRA (Anderson and Linden, 2011) suggests that significant spectral integration might occur during thalamocortical convergence. Nonetheless, the considerable difference in the tuning quality of the boutons I imaged (both in the anaesthetised and awake conditions) indicates that some spectral integration might already occur at the level of the thalamus.

Broad spectral integration enables auditory cortical neurons to form representations of behaviorally-relevant sound sources (Bar-Yosef et al., 2002; Las et al., 2005). Furthermore, studies in different species have shown that auditory cortical frequency representations are highly plastic over multiple timescales (Dahmen and King, 2007), and individual neurons can rapidly change their stimulus selectivity with the behavioral context (Fritz et al., 2003). Such dynamic modulation of sound frequency processing can only be possible if cortical neurons have access to spectrally broad inputs (Chen et al., 2011b; Intskirveli et al., 2016; Metherate et al., 2005; Miller et al., 2001; Winer et al., 2005).

It is also worth noting that the observation of large scale tonotopic maps in primary auditory fields might be a consequence of the type of stimuli usually employed by experimenters to characterise neuronal response properties. Whilst perhaps useful for identifying functional subdivisions within the auditory cortex and thalamus, an excessive reliance on tonotopic gradients and the spectral receptive field might be distracting us from exploring different stimulus landscapes that could reveal other forms of organisation in auditory cortical areas (Rothschild and Mizrahi, 2015; Schreiner and Winer, 2007).

Are there as many thalamic subdivisions as there are cortical subfields?

The multiple subdivisions and parallel ascending pathways within each sensory modality can have separate topographic maps, either complete or partial, of the

sensory surface (Schreiner and Winer, 2007), particularly at the level of cortex and thalamus (Sherman and Guillery, 2013). The identification of commonalities and differences in the circuit micro-architecture across different cortical areas can be informative. On one hand, it allows us to determine if a feature can be regarded as a "canonical" rule of organisation that might be part of a common cortical architecture. Alternatively, it might point towards a circuit computation which is specific to a cortical module.

Because every region of cortex receives inputs from one or more thalamic nuclei, many of which exhibit topographic projections (Winer et al., 2005), it is possible that the functional specialisation that is observed in cortex might be re-capitulated in thalamus (Sherman and Guillery, 2013). In the case of the mouse auditory modality, as many MGB subcompartments as there are auditory cortical subfields have been proposed (Tsukano et al., 2017b). Whether these are anything more than segmentations of the ascending inputs and might actually have a specific functional role, it is not known. Functional and anatomical studies of cortico-thalamic projections pathways are likely to shed some light on these matters (Llano and Sherman, 2008).

Awareness of thalamic diversity

The observations from chapter 3 provide evidence of the significant functional and anatomical diversity in auditory thalamocortical projections. Not only did neurons from different MGB nuclei exhibited distinct projection patterns, but they also differed in a number of spectral tuning properties and more prominently still, in the prevalence of frequency tuning. This begs questions such as what information is being conveyed by the vast projection from MGBd to A2, or by the sparse projections from MGBm to all auditory subfields. Given that, in other sensory systems (Roth et al., 2016) input from higher-order thalamic nuclei has been shown to carry more motor and contextual sensory signals than the input from the first order nucleus, these questions will likely only be answered in a behavioural context.

Classification systems for thalamic projection neurons have been proposed based on recent single-axonal imaging studies by Clascá et al. (2016). Based on what was observed in the visual and somatosensory modality, a "specific thalamocortical" class, equivalent to the core-type proposed by Jones (2007), was defined as: focal and terminating in middle layers, but never in L1. As the experiments in chapters 3 and 4 clearly demonstrate, this classification criteria cannot be applied to auditory lemniscal projections from MGBv. Instead, these projections arborise extensively in L4 and send collaterals to L1. Thus, it is likely that thalamic axonal diversity cannot be entirely accounted for by classifications which do not include modality and species-specific differences.

Methodological refinements

Further *in vivo* characterisation studies of the thalamocortical projection system could make use of existing methods to record, not only the firing activity of thalamic projection neurons, but also the dynamics and distribution of thalamocortical synapses. By using synaptically-targeted GCaMP constructs or genetically-encoded glutamate sensors (Marvin et al., 2013), one could monitor the activity not in whole axons, but in individual synapses. Moreover, methods such as GRASP (GFP Reconstitution Across Synaptic Partners) could allow for the identification of thalamocortical synapses between genetically-identified subpopulations of neurons (Feinberg et al., 2008).

Additional refinements in optical methods, such as volumetric imaging (Anselmi et al., 2011; Katona et al., 2012), could provide the possibility to image several optical planes simultaneously and would be of particular value when studying the contribution of inputs in superficial layers to the activity of pyramidal cortical neurons. Moreover, the same methods would provide the means to perform motion correction in the z axis, which would be highly desirable when imaging behaving head-fixed mice as well as larger mammals.

7.3 The auditory cortical column

New or transformed maps across the cortical layers?

The description of cortical maps as two-dimensional patterns of organisation overlooks the laminar complexity of the cortical sheet. The experiments described in chapter 5, together with previous imaging studies (Winkowski and Kanold, 2013), show how in the auditory cortex significant layer differences exist in neuronal correlations and co-tuning. The use spectral tuning measures makes L2/3 appear as more heterogeneous than L4, but this might in fact be the result of spectral integration and the representation of more complex auditory features (Winkowski and Kanold, 2013). The apparent heterogeneous micro-architecture in L2/3 of A1 seems to be far from random (Watkins et al., 2014), and might contain highly specific patterns of local connectivity like those observed in L2/3 of V1 (Ko et al., 2011). What happens in mouse auditory cortex might be similar to what has been reported of the visual cortex of the shrew tree, where L4 inputs converge to generate orientation selectivity in L2/3. Thus, there might be sets of auditory stimuli that capture the response properties of L2/3 neurons better than pure tones of varying frequencies. Whilst this is highly speculative, it is still one more reason to explore stimulus landscapes which would better inform us on the type of computations being carried out across and within cortical areas (Schreiner and Winer, 2007).

Mysterious creatures of the deep

The imaging experiments of chapter 5 were aimed at the exploration of the auditory cortical column, however, because of the optical limits of two-photon microscopy, I could only image from granular and supragranular layers[2]. This, however, leaves unexplored the infragranular layers 5 and 6. Because of these are the main source of feedforward and feedback projections to thalamus, respectively, any exploration

[2] Throughout the chapter, I attempted to use the word volume and not column to refer to the sections of cortex I sampled from.

of thalamocortical relations remains limited without them (Sherman and Guillery, 2013). The shortcoming is not something exclusive to this study. In general, much less is known about the circuit organisation in deep cortical layers than in L4 and L2/3 (Harris, 2015), although there is evidence that suggests the two might be markedly different (Harris et al., 2011; Sakata and Harris, 2009). This, nonetheless, might be starting to change, as demonstrated in a remarkable study by Guo et al. (2017a) which showed that L6 neurons can increase or decrease the gain and tuning precision of neurons from MGBv and from all layers of the cortical column, with behavioural implications in feature detection and discrimination.

Dendritic compartments and inhibitory cells

The viral approach used to label neurons with GCaMP6 for two-photon calcium imaging, only targeted excitatory cells. Whilst this constitutes the entirety of the thalamocortical projection neurons, it leaves out all cortical inhibitory interneurons (**Fig. 7.1**). Thalamic inputs to cortex drive interneurons through all cortical layers, often more strongly than they do principal neurons (Ji et al., 2015). These inputs have been shown to sharpen spike timing and frequency tuning of principal neurons via feed-forward inhibition (Wehr and Zador, 2003; Wu et al., 2008a). Layer 2/3 neurons in auditory and other sensory cortices exhibit very low firing rates (i.e. they fire sparsely), particularly in awake animals (Sakata and Harris, 2009; Harris, 2015; Hromádka et al., 2008), which might be mediated by strong activation of L2/3 inhibitory interneurons by thalamocortical axons (Ji et al., 2015). However, despite their indisputable importance, imaging calcium in interneurons is difficult, due to their different calcium buffer properties and high firing rates (Chen et al., 2013) and the fact that most calcium indicators have been optimised to be used in principal cells.

Another important component of the cortical column which could not be directly evaluated was the dendritic trees of pyramidal neurons (**Fig. 7.1**). They have been shown to act as separate functional compartments to the cell body, that can integrate synaptic inputs a non-linear fashion (London and Häusser, 2005; Branco

and Häusser, 2010; Smith et al., 2013). Imaging dendritic arbours requires the sparse labelling of pyramidal neurons (Xu et al., 2012) and no labelling of supragranular layers. Future experiments could make use of this approach to record the activity of L5 neurons through dendritic calcium signals generated from back-propagating action potentials.

Assessing synaptic connectivity

Whilst dual-colour two-photon calcium imaging can provide high-resolution information about the spatial location of two classes of neuronal structures (e.g. axons and cell bodies), it does not directly assess synaptic connectivity between pairs of them. Moreover, because of having access to only one tunable laser source in my imaging setup, the two fluorescent calcium indicators had to two imaged independently. This prevented the use of neuronal correlations to assess the likelihood of connectivity between the thalamic boutons and the cortical neurons. Thus, one important follow up to this work would be to identify the targets of the thalamic inputs found within a cortical column. Non-invasive optical methods that monitor post-synaptic inputs, such as two-photon calcium imaging of dendritic spines (Chen et al., 2011b), do not provide much information about the pre-synaptic origin of the inputs. Thus, in order to identify actual functional connections, one might make use of trans-synaptic viral methods to selectively label connected neurons (Arenkiel and Ehlers, 2009). The existence of an *in vitro* auditory slice preparation that preservers functional tecto-thalamo-cortical connectivity offers an exceptional opportunity (Cruikshank et al., 2002; Llano et al., 2014). If combined with methods to identify in the slice neurons that have been previously imaged *in vivo* (Ko et al., 2011), one might be able to exploit the whole pallette of both *in vivo* and *in vitro* methods for a more thorough description of these pathways, down to the synaptic level.

The extended column

Decades of studies on thalamocortical connectivity, to which this thesis contributes only a little, have revealed connection patterns between thalamus and cortex with

Figure adapted from copyrighted material. Not available in the Online dissemination version of this thesis.

Fig. 7.1: Open questions on the synaptic targets of thalamocortical projections in auditory cortex Connections on principal neurons in the diagram are derived from the review by Harris (2015) and the findings of chapters 3, 4 and 5 of this thesis. Connections on inhibitory interneurons are derived from work on visual and auditory cortical slices performed by Ji et al. (2015). Questions marks mean possible but unverified synaptic targets. Figures adapted from Harris (2015) and Ji et al. (2015). CT, corticothalamic neuron; L1, layer 1 interneuron; L2 IT, layer 2 intratelencephalic neuron; L3 IT, layer 3 intratelencephalic neuron; L4 IT, layer 4 intratelencephalic neuron; L5A/B IT, layer 5A/5B intratelencephalic neuron; L6 IT, layer 6 intratelencephalic neuron; PT, pyramidal tract neuron; PV, parvalbumin-expressing interneuron; SOM, somatostatin-expressing interneuron; VIP, vasoactive intestinal peptide-expressing interneuron.

degrees of intricacy, specificity and directionality comparable to those of intracortical connections. Our increasing understanding of the canonical principles of thalamocortical circuit organisation is paving the way for exploring the role of thalamocortical interactions in behaviour. Recent studies have demonstrated a thalamocortical mechanism for the modulation of sensory perception during behaviour (Guo et al., 2017a) as well as the gating of sensory cortical plasticity at thalamocortical synapses (Blundon and Zakharenko, 2013). Moreover, thalamic circuits are now being explored beyond the sensory domain, with three recent studies demonstrating the involvement of thalamus in decision-making and working memory (Guo et al., 2017b; Bolkan et al., 2017; Schmitt et al., 2017). All accumulated evidence thus far suggests that what Sherman et al. (2006) said was not exaggeration: thalamus might indeed be considered the 'deepest of cortical layers'.

7.4 Methods pave the way

Light control: a tool for the neuronal explorer

In his *Advice for a Young Investigator*, Santiago Ramon y Cajal declares that "there are times when, on the heels of a chance discovery or the development of an important new technique, magnificent scientific discoveries occur one after another as if by spontaneous generation". We have come a long way in refining our methods to study thalamocortical circuits. From the very earliest studies using retrograde and anterograde axonal degeneration, to the most recent developments in multi-photon and holographic microscopy, each method has contributed to our growing understanding of the organisation and function of this system.

As demonstrated in chapter 6, the combination of holographic methods and micro-endoscopic optical fibres allows for minimally invasive high-resolution microscopy of neuronal structures at virtually any brain depth. The next step in the development of this system is to increase its speed, which would make it suitable for functional imaging. Once this is achieved, the range of opportunity is wide. The technology would allow not only the imaging of circuits, but also their manipulation through optogenetic methods (Scanziani and Häusser, 2009; Miesenböck, 2011). Moreover, the use of long optical fibres would greatly facilitate imaging in freely moving animals, and their small size, the monitoring of a number of brain regions simultaneously.

Not just space but also time

The focus of the above experiments was the study of the spectral receptive field of cortical neurons and thalamic boutons and its relationship to spatial location within the portions of cortex imaged, particularly in relation to cortical laminae. This dense characterisation of receptive fields has only been possible by using two-photon calcium imaging (Vasquez-Lopez et al., 2017; Glickfeld et al., 2013; Roth et al., 2016; Bandyopadhyay et al., 2010; Rothschild et al., 2010; Winkowski and Kanold, 2013; Issa et al., 2014). However, this same method does not allow for the exploration

of other neuronal response properties which are well known to vary across cortical layers, subfields and thalamic subdivisions. Specifically, fine temporal properties, such as first-spike latency (Atencio and Schreiner, 2010b; Atencio and Schreiner, 2010a) and onset–offset responses (Qin et al., 2007), cannot be reliably measured from calcium signals.

A major shortcoming of imaging calcium in neurons is its limited temporal resolution and non-linear relationship with neuronal voltage (Theis et al., 2016; Pnevmatikakis et al., 2016). Calcium concentration changes are slower than voltage signals and are not always present in response to voltage changes (Grienberger and Konnerth, 2012; Gong et al., 2015). Calcium signals might be slowed by the binding kinetics of the indicator used and its expression levels (Hires et al., 2008), making the inference of neuronal spiking from calcium signals difficult (Theis et al., 2016; Pnevmatikakis et al., 2016). Here, recent developments in genetically encoded voltage sensors for use *in vivo* might provide a suitable alternative with better temporal dynamics (Carandini et al., 2015; Gong et al., 2015).

Wanted: Explorers of the subcortical world

If our explorer from the start of this chapter finally decides to go down and venture into the forests that interest her, she would quickly realise that underneath the canopy lies a whole world of complexity that is both unexplored and of fundamental importance for the existence of the forest. We want to be this explorer. As neuroscientists interested in understanding cortical circuits, we ought to be aware and attempt to counteract the "corticocentric bias" (Sherman et al., 2006). Studying cortical function in the context of its interactions with subcortical structures is not only desirable but very likely essential to move the field of systems neuroscience forward (Acsády, 2017). For this, we depend heavily on the development and refinement of experimental tools which would allow us to monitor and manipulate those neuronal circuits which are not at easy reach right underneath the skull (Huang and Zeng, 2013; Tye and Deisseroth, 2012; Luo et al., 2008). Minimally invasive tools, which

would not destroy the whole forest canopy, might be very valuable in this exploration (Gigan, 2017; Ouzounov et al., 2017; Mekhail et al., 2016).

(Circuit) neuroscience needs behaviour

Recent studies (Guo et al., 2017b; Bolkan et al., 2017; Schmitt et al., 2017; Guo et al., 2017a) have demonstrated the importance of studying thalamocortical circuit function in the context of behaviour. Guo et al. (2017a), for example, studied primary auditory pathway function, not by mapping the representation of auditory features, but by varying the requirements of a behavioural task whilst measuring how this affected the encoding of stimuli by neurons in the TC circuit. They showed that, even in primary sensory pathways, the responses of thalamic and L4 neurons can be modulated by behavioural contingencies in ways that had not been predicted by (most) neurophysiological studies. This demonstration did not require the use of particularly complex stimuli (in fact pure tones were used). It was the fact that the stimuli had a behavioural relevance that made all the difference.

This type of work shows us that, besides understanding the importance of research on both cortical and subcortical circuits, we ought to keep one main scientific aim in mind: the neurobiological understanding of behaviour (Krakauer et al., 2017; Guillery, 2017). It might be unusual for a thesis on cortical mapping of spectral features in anaesthetised and passively listening mice to finish by advocating to behavioural studies. However, spending hundreds of hours imaging axons in a dark and silent room, over the course of four years, gives ample opportunity for philosophising about one's scientific views. By the same token, the sheer magnitude of the task provides, on itself, a very strong rectifier for one's reductionist bias.

7.5 In conclusion

My work provides some new insights on the functional micro-organisation of the auditory thalamocortical system, using the mouse as a model organism. The overall message is that auditory cortex exhibits characteristic forms of functional organisation at the small scale (Vasquez-Lopez et al., 2017) which cannot be fully assessed through traditional electrophysiological and anatomical methods or deduced from observations in other cortical areas. Whilst the characterisation of spectral tuning properties has been useful to probe some components of the circuit, such as the lemniscal thalamocortical projection, it falls short when used to investigate higher levels of processing like those taking place through the cortical column and in non-primary auditory pathways.

There is still much mapping to do in the mammalian cortex, and certainly much more underneath it, but we still need to identify what features are more useful to guide our charting. We must also identify and develop the proper experimental tools that would aid our investigations. Only then we will have a real chance of finding our way around the ultimate unexplored forest: the mammalian brain.

Bibliography

Acsády, L. (2017). The thalamic paradox. *Nature Neuroscience* 20.7, pp. 901–902 (cit. on p. 171).

Akerboom, J., Carreras Calderón, N., Tian, L., et al. (2013). Genetically encoded calcium indicators for multi-color neural activity imaging and combination with optogenetics. *Frontiers in molecular neuroscience* 6.March, p. 2 (cit. on p. 111).

Andersen, R. A., Knight, P. L., and Merzenich, M. M. (1980). The thalamocortical and corticothalamic conections of AI, AII, and the anterior auditory field (AFF) in the cat: Evidence for two largely sergregarted systems of connections. *The Journal of Comparative Neurology* 194.3, pp. 663–701 (cit. on pp. 25, 28).

Anderson, L. a., Wallace, M. N., and Palmer, a. R. (2007). Identification of subdivisions in the medial geniculate body of the guinea pig. *Hearing research* 228.1-2, pp. 156–67 (cit. on p. 28).

Anderson, L. a., Christianson, G. B., and Linden, J. F. (2009). Mouse auditory cortex differs from visual and somatosensory cortices in the laminar distribution of cytochrome oxidase and acetylcholinesterase. *Brain Research* 1252, pp. 130–142 (cit. on p. 60).

Anderson, L. a. and Linden, J. F. (2011). Physiological differences between histologically defined subdivisions in the mouse auditory thalamus. *Hearing research* 274.1-2, pp. 48–60 (cit. on pp. 26, 52, 54, 55, 88, 163).

Anselmi, F., Ventalon, C., Bègue, A., Ogden, D., and Emiliani, V. (2011). Three-dimensional imaging and photostimulation by remote-focusing and holographic light patterning. *Proc Natl Acad Sci USA* 108.49, pp. 19504–9 (cit. on p. 165).

Arenkiel, B. R. and Ehlers, M. D. (2009). Molecular genetics and imaging technologies for circuit-based neuroanatomy. *Nature* 461.7266, pp. 900–7 (cit. on p. 168).

Atencio, C. A. and Schreiner, C. E. (2010a). Laminar Diversity of Dynamic Sound Processing in Cat Primary Auditory Cortex. *Journal of Neurophysiology* 103.1, pp. 192–205 (cit. on pp. 135, 140, 171).

Atencio, C. A., Sharpee, T. O., and Schreiner, C. E. (2009). Hierarchical computation in the canonical auditory cortical circuit. *Proceedings of the National Academy of Sciences* 106.51, pp. 21894–21899 (cit. on p. 140).

Atencio, C. A. and Schreiner, C. E. (2010b). Columnar connectivity and laminar processing in cat primary auditory cortex. *PLoS ONE* 5.3 (cit. on pp. 135, 140, 171).

Averbeck, B. B., Latham, P. E., and Pouget, A. (2006). Neural correlations, population coding and computation. *Nature reviews. Neuroscience* 7.5, pp. 358–66 (cit. on pp. 76, 118, 137).

Azouz, R and Gray, C. M. (1999). Cellular mechanisms contributing to response variability of cortical neurons in vivo. *The Journal of neuroscience : the official journal of the Society for Neuroscience* 19.6, pp. 2209–23 (cit. on p. 137).

Bandyopadhyay, S., Shamma, S. a., and Kanold, P. O. (2010). Dichotomy of functional organization in the mouse auditory cortex. *Nature neuroscience* 13.3, pp. 361–8 (cit. on pp. 7, 32, 52, 71, 83, 116, 161, 162, 170).

Banks, M. I. and Smith, P. H. (2011). Thalamocortical Relations. In: *The Auditory Cortex*. Boston, MA: Springer US, pp. 75–97 (cit. on pp. 26, 29).

Bar-Yosef, O, Rotman, Y, and Nelken, I (2002). Responses of neurons in cat primary auditory cortex to bird chirps: Effects of temporal and spectral context. *Journal of Neuroscience* 22.19 (cit. on pp. 107, 162, 163).

Barnstedt, O., Keating, P., Weissenberger, Y., King, A. J., and Dahmen, J. C. (2015). Functional Microarchitecture of the Mouse Dorsal Inferior Colliculus Revealed through In Vivo Two-Photon Calcium Imaging. *Journal of Neuroscience* 35.31, pp. 10927–10939 (cit. on pp. 39, 52, 79, 106).

Barretto, R. P. J., Ko, T. H., Jung, J. C., et al. (2011). Time-lapse imaging of disease progression in deep brain areas using fluorescence microendoscopy. *Nature medicine* 17.2, pp. 223–8 (cit. on p. 35).

Bartlett, E. L. and Smith, P. H. (1999). Anatomic, intrinsic, and synaptic properties of dorsal and ventral division neurons in rat medial geniculate body. *J Neurophysiol* 81.5, pp. 1999–2016 (cit. on p. 55).

Bathellier, B., Ushakova, L., and Rumpel, S. (2012). Discrete neocortical dynamics predict behavioral categorization of sounds. *Neuron* 76.2, pp. 435–49 (cit. on p. 82).

Blundon, J. a. and Zakharenko, S. S. (2013). Presynaptic gating of postsynaptic synaptic plasticity: a plasticity filter in the adult auditory cortex. *The Neuroscientist* 19.5, pp. 465–78 (cit. on p. 169).

Bocarsly, M. E., Jiang, W.-c., Wang, C., et al. (2015). Minimally invasive microendoscopy system for in vivo functional imaging of deep nuclei in the mouse brain. *Biomedical Optics Express* 6.11, p. 4546 (cit. on pp. 35, 141, 144).

Bolkan, S. S., Stujenske, J. M., Parnaudeau, S., et al. (2017). Thalamic projections sustain prefrontal activity during working memory maintenance. *Nat Neurosci* 20.7, pp. 987–996 (cit. on pp. 169, 172).

Bonin, V., Histed, M. H., Yurgenson, S., and Reid, R. C. (2011). Local diversity and fine-scale organization of receptive fields in mouse visual cortex. *The Journal of neuroscience* 31.50, pp. 18506–21 (cit. on pp. 7, 82, 161).

Bordi, F. and LeDoux, J. E. (1994). Response properties of single units in areas of rat auditory thalamus that project to the amygdala - I. Acoustic discharge patterns and frequency receptive fields. *Experimental Brain Research* 98.2, pp. 261–274 (cit. on p. 29).

Braitenberg, V., Schuz, A. A., and Braitenberg, V. (1998). Cortex. Statistics and geometry of neuronal connectivity. Springer, p. 249 (cit. on pp. 32, 110).

Branco, T. and Häusser, M. (2010). The single dendritic branch as a fundamental functional unit in the nervous system. *Current opinion in neurobiology* 20.4, pp. 494–502 (cit. on p. 167).

Brandner, S and Redies, H (1990). The projection from medial geniculate to field AI in cat: organization in the isofrequency dimension. *The Journal of neuroscience* 10.1, pp. 50–61 (cit. on pp. 8, 27, 84).

Brodmann, K. (1909). Vergleichende Lokalisationslehre der Grosshirnrinde in ihren Prinzipien dargestellt auf Grund des Zellenbaues. Barth (cit. on p. 161).

Bruno, R. M. and Sakmann, B. (2006). Cortex is driven by weak but synchronously active thalamocortical synapses. *Science* 312.5780, pp. 1622–7 (cit. on pp. 9, 10, 136, 137).

Budinger, E., Heil, P., and Scheich, H. (2000). Functional organization of auditory cortex in the Mongolian gerbil (Meriones unguiculatus). III. Anatomical subdivisions and corticocortical connections. *European Journal of Neuroscience* 12.7, pp. 2425–2451 (cit. on pp. 26, 27).

Butler, A. B. (1994). The evolution of the dorsal pallium in the telencephalon of amniotes: Cladistic analysis and a new hypothesis. *Brain Research Reviews* 19.1, pp. 66–101 (cit. on pp. 5, 6).

Butler, A. B. (2009). Evolution of the Dorsal Thalamus. In: *Encyclopedia of Neuroscience*. Berlin, Heidelberg: Springer Berlin Heidelberg, pp. 1346–1351 (cit. on pp. 5, 21).

Calford, M. B. (1983). The parcellation of the medial geniculate body of the cat defined by the auditory response properties of single units. *J Neurosci* 3.11, pp. 2350–2364 (cit. on pp. 25, 28).

Carandini, X. M., Shimaoka, D., Rossi, L. F., et al. (2015). Imaging the Awake Visual Cortex with a Genetically Encoded Voltage Indicator. *The Journal of neuroscience* 35.1, pp. 53–63 (cit. on p. 171).

Cetas, J., Venecia, R. de, and McMullen, N. (1999). Thalamocortical afferents of Lorente de Nó: medial geniculate axons that project to primary auditory cortex have collateral branches to layer I. *Brain Research* 830.1, pp. 203–208 (cit. on pp. 81, 84, 94, 104, 106).

Chechik, G., Anderson, M. J., Bar-Yosef, O., et al. (2006). Reduction of Information Redundancy in the Ascending Auditory Pathway. *Neuron* 51.3, pp. 359–368 (cit. on pp. 82, 139, 162).

Chen, B. L., Hall, D. H., and Chklovskii, D. B. (2006). Wiring optimization can relate neuronal structure and function. *Proc Natl Acad Sci USA* 103.12, pp. 4723–8 (cit. on p. 6).

Chen, T.-W., Wardill, T. J., Sun, Y., et al. (2013). Ultrasensitive fluorescent proteins for imaging neuronal activity. *Nature* 499.7458, pp. 295–300 (cit. on pp. 59, 65, 85, 155, 167).

Chen, X., Gabitto, M., Peng, Y., Ryba, N. J. P., and Zuker, C. S. (2011a). A Gustotopic Map of Taste Qualities in the Mammalian Brain. *Science* 333.6047, pp. 1262–1266 (cit. on p. 5).

Chen, X., Leischner, U., Rochefort, N. L., Nelken, I., and Konnerth, A. (2011b). Functional mapping of single spines in cortical neurons in vivo. *Nature* 475.7357, pp. 501–5 (cit. on pp. 7, 107, 163, 168).

Chklovskii, D. B. and Koulakov, A. A. (2004). MAPS IN THE BRAIN: What Can We Learn from Them? *Annual Review of Neuroscience* 27.1, pp. 369–392 (cit. on p. 6).

Chklovskii, D. B., Schikorski, T., and Stevens, C. F. (2002). Wiring optimization in cortical circuits (cit. on p. 6).

Cichon, J. and Gan, W.-B. (2015). Branch-specific dendritic Ca2+ spikes cause persistent synaptic plasticity. *Nature* (cit. on p. 11).

Čižmár, T. and Dholakia, K. (2011). Shaping the light transmission through a multimode optical fibre: complex transformation analysis and applications in biophotonics. *Optics express* 19.20, pp. 18871–84 (cit. on pp. 36, 143).

Cižmár, T. and Dholakia, K. (2012). Exploiting multimode waveguides for pure fibre-based imaging. *Nature communications* 3, p. 1027 (cit. on pp. 36, 143, 149, 152, 156, 157).

Čižmár, T., Mazilu, M., and Dholakia, K. (2010). In situ wavefront correction and its application to micromanipulation. *Nature Photonics* 4.6, pp. 388–394 (cit. on p. 149).

Clascá, F., Rubio-Garrido, P., and Jabaudon, D. (2012). Unveiling the diversity of thalamocortical neuron subtypes. *The European journal of neuroscience* 35.10, pp. 1524–32 (cit. on pp. 16, 19, 55, 56, 81, 106, 108).

Clascá, F., Porrero, C., Galazo, M. J., Rubio-Garrido, P., and Evangelio, M. (2016). Anatomy and Development of Multispecific Thalamocortical Axons. In: *Axons and Brain Architecture*. 1st. Elsevier, pp. 69–92 (cit. on pp. 10, 17, 18, 28, 32, 55, 56, 61, 165).

Clay Reid, R. and Alonso, J.-M. (1995). Specificity of monosynaptic connections from thalamus to visual cortex. *Nature* 378.6554, pp. 281–284 (cit. on p. 105).

Cohen, M. R. and Kohn, A. (2011). Measuring and interpreting neuronal correlations. *Nature neuroscience* 14.7, pp. 811–9 (cit. on pp. 76, 118, 123, 137).

Cohen-Kashi Malina, K., Mohar, B., Rappaport, A. N., and Lampl, I. (2016). Local and thalamic origins of correlated ongoing and sensory-evoked cortical activities. *Nature Communications* 7, p. 12740 (cit. on p. 137).

Conkey, D. B., Caravaca-Aguirre, A. M., and Piestun, R. (2012). High-speed scattering medium characterization with application to focusing light through turbid media. *Optics Express* 20.2, p. 1733 (cit. on pp. 152, 156, 157).

Constantinople, C. M. and Bruno, R. M. (2013). Deep cortical layers are activated directly by thalamus. *Science* 340.6140, pp. 1591–4 (cit. on pp. 30, 110).

Cossell, L., Iacaruso, M. F., Muir, D. R., et al. (2015). Functional organization of excitatory synaptic strength in primary visual cortex. *Nature* 518.7539, pp. 399–403 (cit. on pp. 10, 105).

Cruikshank, S. J., Killackey, H. P., and Metherate, R. (2001). Parvalbumin and calbindin are differentially distributed within primary and secondary subregions of the mouse auditory forebrain. *Neuroscience* 105.3, pp. 553–569 (cit. on pp. 12, 53, 55).

Cruikshank, S. J., Rose, H. J., and Metherate, R. (2002). Auditory thalamocortical synaptic transmission in vitro. *Journal of neurophysiology* 87.1, pp. 361–84 (cit. on p. 168).

Cruikshank, S. J., Lewis, T. J., and Connors, B. W. (2007). Synaptic basis for intense thalamocortical activation of feedforward inhibitory cells in neocortex. *Nature neuroscience* 10.4, pp. 462–8 (cit. on p. 106).

Cui, G., Jun, S. B., Jin, X., et al. (2014). Deep brain optical measurements of cell type-specific neural activity in behaving mice. *Nature protocols* 9.6, pp. 1213–28 (cit. on p. 142).

Dahmen, J. C. and King, A. J. (2007). Learning to hear: plasticity of auditory cortical processing. *Current opinion in neurobiology* 17.4, pp. 456–64 (cit. on pp. 107, 163).

Dalal, N. and Triggs, B (2005). Histograms of Oriented Gradients for Human Detection. In: *2005 IEEE Computer Society Conference on Computer Vision and Pattern Recognition (CVPR'05)*. Vol. 1. IEEE, pp. 886–893 (cit. on p. 44).

Dana, H., Mohar, B., Sun, Y., et al. (2016). Sensitive red protein calcium indicators for imaging neural activity. *eLife* 5.MARCH2016 (cit. on p. 111).

Denk, W., Strickler, J. H, and Webb, W. W (1990). Two-photon laser scanning fluorescence microscopy. *Science* 248.4951, pp. 73–6 (cit. on pp. 65, 84, 141).

Dombeck, D. a., Harvey, C. D., Tian, L., Looger, L. L., and Tank, D. W. (2010). Functional imaging of hippocampal place cells at cellular resolution during virtual navigation. *Nature neuroscience* 13.11, pp. 1433–40 (cit. on pp. 35, 141).

Donishi, T, Kimura, A, Okamoto, K, and Tamai, Y (2006). Ventral area in the rat auditory cortex: a major auditory field connected with the dorsal division of the medial geniculate body. *Neuroscience* 141.3, pp. 1553–67 (cit. on pp. 26, 27).

Douglas, R. J. and Martin, K. A. C. (2004). Neuronal Circuits of the Neocortex. *Annual Review of Neuroscience* 27.1, pp. 419–451 (cit. on pp. 1, 134).

Ecker, A. S., Berens, P., Cotton, R. J., et al. (2014). State dependence of noise correlations in macaque primary visual cortex. *Neuron* 82.1, pp. 235–248 (cit. on p. 139).

Ehret, G. (1979). Quantitative analysis of nerve fibre densities in the cochlea of the house mouse(Mus musculus). *The Journal of Comparative Neurology* 183.1, pp. 73–88 (cit. on p. 88).

Essen, D. C. and Zeki, S. M. (1978). The topographic organization of rhesus monkey prestriate cortex. *The Journal of Physiology* 277.1, pp. 193–226 (cit. on pp. 5, 8).

Evans, E. F. and Whitfield, I. C. (1964). Classifcation of unit responses in the auditory cortex of the unanaesthetized and unrestrained cat. *The Journal of Physiology* 171.3, pp. 476–93 (cit. on pp. 138, 163).

Fay, R. R. (1989). Hearing in Vertebrates: A Psychophysics Databook. Vol. 86. 5. Hill-Fay Associates, p. 2044 (cit. on p. 20).

Feinberg, E. H., Vanhoven, M. K., Bendesky, A., et al. (2008). GFP Reconstitution Across Synaptic Partners (GRASP) defines cell contacts and synapses in living nervous systems. *Neuron* 57.3, pp. 353–63 (cit. on p. 165).

Feng, G, Mellor, R. H., Bernstein, M, et al. (2000). Imaging neuronal subsets in transgenic mice expressing multiple spectral variants of GFP. *Neuron* 28.1, pp. 41–51 (cit. on p. 152).

Ferrier, D. and Turner, W. A. (1894). A Record of Experiments Illustrative of the Symptomatology and Degenerations Following Lesions of the Cerebellum and Its Peduncles and Related Structures in Monkeys. *Philos Trans R Soc Lond B Biol Sci.* 185 (cit. on p. 25).

Finger, S. (1994). Origins of neuroscience: A history of explorations into brain function. New York: Oxford University Press, p. 462 (cit. on p. 161).

Flusberg, B. A., Cocker, E. D., Piyawattanametha, W., et al. (2005). Fiber-optic fluorescence imaging. *Nature methods* 2.12, pp. 941–50 (cit. on p. 141).

Fritz, C. O., Morris, P. E., and Richler, J. J. (2012). Effect size estimates: Current use, calculations, and interpretation. *Journal of Experimental Psychology: General* 141.1, pp. 2–18 (cit. on p. 47).

Fritz, J., Shamma, S., Elhilali, M., and Klein, D. (2003). Rapid task-related plasticity of spectrotemporal receptive fields in primary auditory cortex. *Nature neuroscience* 6.11, pp. 1216–1223 (cit. on pp. 107, 163).

Frost, D. O. and Caviness, V. S. (1980). Radial organization of thalamic projections to the neocortex in the mouse. *The Journal of comparative neurology* 194.2, pp. 369–93 (cit. on pp. 84, 106).

Fuster, J. M. (2005). Cortex and mind: unifying cognition. Oxford University Press, p. 294 (cit. on p. 1).

Gigan, S. (2017). Optical microscopy aims deep. *Nature Photonics* 11.1, pp. 14–16 (cit. on pp. 158, 172).

Glickfeld, L. L., Andermann, M. L., Bonin, V., and Reid, R. C. (2013). Cortico-cortical projections in mouse visual cortex are functionally target specific. *Nature neuroscience* 16.2, pp. 219–26 (cit. on pp. 65, 85, 170).

Gloge, D (1971). Weakly Guiding Fibers. *Applied Optics* 10.10, p. 2252 (cit. on p. 145).

Gong, Y., Huang, C., Li, J. Z., et al. (2015). High-speed recording of neural spikes in awake mice and flies with a fluorescent voltage sensor. *Science* 350.6266, pp. 1361–1366 (cit. on p. 171).

Grienberger, C. and Konnerth, A. (2012). Imaging calcium in neurons. *Neuron* 73.5, pp. 862–85 (cit. on p. 171).

Guillery, R. W. (1995). Anatomical evidence concerning the role of the thalamus in cortico-cortical communication: a brief review. *Journal of anatomy* 187 (Pt 3.Pt 3, pp. 583–92 (cit. on pp. 11, 12).

Guillery, R. W. (2017). Brain as a Tool: A Neuroscientist's Account. Oxford University Press (cit. on pp. 18, 172).

Guizar-Sicairos, M., Thurman, S. T., and Fienup, J. R. (2008). Efficient subpixel image registration algorithms. *Optics Letters* 33.2, p. 156 (cit. on p. 44).

Guo, W., Chambers, A. R., Darrow, K. N., et al. (2012). Robustness of cortical topography across fields, laminae, anesthetic states, and neurophysiological signal types. *The Journal of neuroscience* 32.27, pp. 9159–72 (cit. on pp. 46, 52–54, 66, 70, 73, 80, 82, 83, 86, 104, 163).

Guo, W., Clause, A. R., Barth-Maron, A., and Polley, D. B. (2017a). A Corticothalamic Circuit for Dynamic Switching between Feature Detection and Discrimination. *Neuron* 95.1, pp. 180–194 (cit. on pp. 79, 139, 167, 169, 172).

Guo, Z. V., Hires, S. A., Li, N., et al. (2014). Procedures for behavioral experiments in head-fixed mice. *PLoS ONE* 9.2 (cit. on p. 42).

Guo, Z. V., Inagaki, H. K., Daie, K., et al. (2017b). Maintenance of persistent activity in a frontal thalamocortical loop. *Nature* 545.7653, pp. 181–186 (cit. on pp. 169, 172).

Hackett, T. A., Stepniewska, I, and Kaas, J. H. (1998). Subdivisions of auditory cortex and ipsilateral cortical connections of the parabelt auditory cortex in macaque monkeys. *The Journal of comparative neurology* 394.4, pp. 475–95 (cit. on pp. 26, 51, 80).

Hackett, T. a., Barkat, T. R., O'Brien, B. M. J., Hensch, T. K., and Polley, D. B. (2011). Linking topography to tonotopy in the mouse auditory thalamocortical circuit. *The Journal of neuroscience* 31.8, pp. 2983–95 (cit. on pp. 26, 31, 46, 51, 52, 54–57, 70, 82–85, 91, 104, 107, 161).

Happel, M. F. K., Jeschke, M., and Ohl, F. W. (2010). Spectral Integration in Primary Auditory Cortex Attributable to Temporally Precise Convergence of Thalamocortical and Intracortical Input. *The Journal of neuroscience* 30.33, pp. 11114–11127 (cit. on p. 105).

Harnett, M. T., Makara, J. K., Spruston, N., Kath, W. L., and Magee, J. C. (2012). Synaptic amplification by dendritic spines enhances input cooperativity. *Nature* 491.7425, pp. 599–602 (cit. on p. 81).

Harris, K. D. (2015). Cortical computation in mammals and birds. *Proceedings of the National Academy of Sciences* 112.11, pp. 3184–3185 (cit. on pp. 1, 22, 31, 106, 110, 138, 141, 167, 169).

Harris, K. D. and Mrsic-Flogel, T. D. (2013). Cortical connectivity and sensory coding. *Nature* 503.7474, pp. 51–58 (cit. on pp. 7, 10, 123, 137).

Harris, K. D. and Shepherd, G. M. G. (2015). The neocortical circuit: themes and variations. *Nature Neuroscience* 18.2, pp. 170–181 (cit. on pp. 8, 10, 19).

Harris, K. D., Bartho, P., Chadderton, P., et al. (2011). How do neurons work together? Lessons from auditory cortex. *Hearing research* 271.1-2, pp. 37–53 (cit. on p. 167).

Hashikawa, T., Molinari, M., Rausell, E., and Jones, E. G. (1995). Patchy and laminar terminations of medial geniculate axons in monkey auditory cortex. *Journal of Comparative Neurology* 362.2, pp. 195–208 (cit. on pp. 81, 94, 106).

Helmchen, F. and Denk, W. (2005). Deep tissue two-photon microscopy. *Nature methods* 2.12, pp. 932–40 (cit. on p. 157).

Henry, K. R. and Chole, R. A. (1980). Genotypic differences in behavioral, physiological and anatomical expressions of age-related hearing loss in the laboratory mouse. *Audiology* 19.5, pp. 369–83 (cit. on p. 102).

Hires, S. A., Tian, L., and Looger, L. L. (2008). Reporting neural activity with genetically encoded calcium indicators. *Brain Cell Biol* 36.1-4, pp. 69–86 (cit. on p. 171).

Honma, Y., Tsukano, H., Horie, M., et al. (2013). Auditory Cortical Areas Activated by Slow Frequency-Modulated Sounds in Mice. *PLoS ONE* 8.7 (cit. on p. 53).

Horie, M., Tsukano, H., Hishida, R., Takebayashi, H., and Shibuki, K. (2013). Dual compartments of the ventral division of the medial geniculate body projecting to the core region of the auditory cortex in C57BL/6 mice. *Neuroscience research* 76.4, pp. 207–12 (cit. on pp. 55, 82, 83).

Horstmeyer, R., Ruan, H., and Yang, C. (2015). Guidestar-assisted wavefront-shaping methods for focusing light into biological tissue. *Nat Photon* 9.9, pp. 563–571 (cit. on p. 37).

Horton, J. C. and Adams, D. L. (2005). The cortical column: a structure without a function. *Philosophical Transactions of the Royal Society B: Biological Sciences* 360.1456, pp. 837–862 (cit. on p. 109).

Hromádka, T., Deweese, M. R., Zador, A. M., and Figs, S (2008). Sparse Representation of Sounds in the Unanesthetized Auditory Cortex Figure S7 Neuronal responses are heterogeneous. *PLoS Biology* 6.1. Ed. by D. Plenz, pp. 4–5 (cit. on p. 167).

Huang, C. L. and Winer, J. a. (2000). Auditory thalamocortical projections in the cat: laminar and areal patterns of input. *The Journal of comparative neurology* 427.2, pp. 302–31 (cit. on pp. 28, 29, 84, 106).

Huang, H., Delikanli, S., Zeng, H., Ferkey, D. M., and Pralle, A. (2010). Remote control of ion channels and neurons through magnetic-field heating of nanoparticles. *Nature nanotechnology* 5.8, pp. 602–6 (cit. on p. 51).

Huang, Z. J. and Zeng, H. (2013). Genetic Approaches to Neural Circuits in the Mouse. *Annual review of neuroscience* May (cit. on pp. 52, 171).

Hubel, D. H. and Wiesel, T. N. (1968). Receptive fields and functional architecture of monkey striate cortex. *The Journal of physiology* 195, pp. 215–243 (cit. on p. 135).

Imig, T. J. and Morel, a (1984). Topographic and cytoarchitectonic organization of thalamic neurons related to their targets in low-, middle-, and high-frequency representations in cat auditory cortex. *The Journal of comparative neurology* 227.4, pp. 511–39 (cit. on p. 31).

Imig, T. J. and Morel, A. (1985a). Tonotopic organization in lateral part of posterior group of thalamic nuclei in the cat. *Journal of Neurophysiology* 53.3, pp. 836–851 (cit. on p. 26).

Imig, T. J. and Morel, A. (1985b). Tonotopic organization in ventral nucleus of medial geniculate body in the cat. *Journal of Neurophysiology* 53.1, pp. 309–340 (cit. on p. 28).

Intskirveli, I., Joshi, A., Vizcarra-Chacón, B. J., and Metherate, R. (2016). Spectral breadth and laminar distribution of thalamocortical inputs to A1. *Journal of Neurophysiology*, jn.00887.2015 (cit. on pp. 57, 107, 163).

Ison, J. R., Allen, P. D., and O'Neill, W. E. (2007). Age-related hearing loss in C57BL/6J mice has both frequency-specific and non-frequency-specific components that produce a hyperacusis-like exaggeration of the acoustic startle reflex. *JARO - Journal of the Association for Research in Otolaryngology* 8.4, pp. 539–550 (cit. on p. 102).

Issa, J. B. B., Haeffele, B. D. D., Agarwal, A., et al. (2014). Multiscale Optical Ca2+ Imaging of Tonal Organization in Mouse Auditory Cortex. *Neuron* 83.4, pp. 944–959 (cit. on pp. 43, 52, 66, 71, 80, 83, 170).

Ji, N. (2014). The practical and fundamental limits of optical imaging in mammalian brains. *Neuron* 83.6, pp. 1242–1245 (cit. on pp. 141, 158).

Ji, N. (2017). Adaptive optical fluorescence microscopy. *Nature Methods* 14.4, pp. 374–380 (cit. on p. 36).

Ji, N., Shroff, H., Zhong, H., and Betzig, E. (2008). Advances in the speed and resolution of light microscopy (cit. on p. 33).

Ji, X.-y., Zingg, B., Mesik, L., et al. (2015). Thalamocortical Innervation Pattern in Mouse Auditory and Visual Cortex: Laminar and Cell-Type Specificity. *Cerebral Cortex*, bhv099– (cit. on pp. 10, 30, 31, 57, 84, 106, 110, 167, 169).

Jia, H., Rochefort, N. L., Chen, X., and Konnerth, A. (2010). Dendritic organization of sensory input to cortical neurons in vivo. *Nature* 464.7293, pp. 1307–12 (cit. on p. 7).

Jia, H., Rochefort, N. L., Chen, X., and Konnerth, A. (2011). In vivo two-photon imaging of sensory-evoked dendritic calcium signals in cortical neurons. *Nature protocols* 6.1, pp. 28–35 (cit. on p. 11).

Jin, J., Wang, Y., Swadlow, H. A., and Alonso, J. M. (2011). Population receptive fields of ON and OFF thalamic inputs to an orientation column in visual cortex. *Nature Neuroscience* 14.2, pp. 232–238 (cit. on p. 135).

Joachimsthaler, B., Uhlmann, M., Miller, F., Ehret, G., and Kurt, S. (2014). Quantitative analysis of neuronal response properties in primary and higher-order auditory cortical fields of awake house mice (Mus musculus). *European Journal of Neuroscience* 39.6, pp. 904–918 (cit. on pp. 53, 138).

Jones, E. G. (1998). Viewpoint: the core and matrix of thalamic organization. *Neuroscience* 85.2, pp. 331–45 (cit. on p. 12).

Jones, E. G. and Leavitt, Y (1974). Retrograde axonal transport and the demonstration of non-specific projections to cerebral cortex and striatum from thalamic intralminar nuclei in the rat, cat and monkey. *Journal of Comparative Neurology* 154, pp. 349–378 (cit. on pp. 12, 51).

Jones, E. G. (2001). The thalamic matrix and thalamocortical synchrony. *Trends in Neurosciences* 24.10, pp. 595–601 (cit. on pp. 13, 14, 81, 106).

Jones, E. G. (2007). The thalamus. 1st. Cambridge University Press (cit. on pp. 2, 3, 12, 15, 18, 26, 29, 53, 141, 165).

Jung, J. C., Mehta, A. D., Aksay, E., Stepnoski, R., and Schnitzer, M. J. (2004). In vivo mammalian brain imaging using one- and two-photon fluorescence microendoscopy. *Journal of neurophysiology* 92.5, pp. 3121–33 (cit. on p. 141).

Kaas, J. H. (1995). The evolution of isocortex. *Brain Behav Evol* 46, pp. 187–196 (cit. on pp. 4, 21).

Kaas, J. H. (2009). Evolution of the Somatosensory System in Mammals. In: *Encyclopedia of Neuroscience*. Berlin, Heidelberg: Springer Berlin Heidelberg, pp. 1416–1419 (cit. on p. 21).

Kaas, J. H. (2011). The Evolution of Auditory Cortex: The Core Areas. In: *The Auditory Cortex*. Ed. by J. A. Winer and C. E. Schreiner. Boston, MA: Springer US (cit. on pp. 21, 27, 52, 83).

Kanold, P. O., Nelken, I., and Polley, D. B. (2014). Local versus global scales of organization in auditory cortex. *Trends in neurosciences*, pp. 1–9 (cit. on pp. 21, 83, 84).

Katona, G., Szalay, G., Maák, P., et al. (2012). Fast two-photon in vivo imaging with three-dimensional random-access scanning in large tissue volumes. *Nature methods* 9.2, pp. 201–8 (cit. on p. 165).

Kaur, S, Rose, H. J., Lazar, R, Liang, K, and Metherate, R (2005). Spectral integration in primary auditory cortex: Laminar processing of afferent input, in vivo and in vitro. *Neuroscience* 134.3, pp. 1033–1045 (cit. on pp. 31, 104).

Kim, G., Nagarajan, N., Pastuzyn, E., et al. (2017). Deep-brain imaging via epi-fluorescence Computational Cannula Microscopy. *Scientific Reports* 7, p. 44791 (cit. on p. 150).

Kim, M., Kim, Y., Kang, K.-J., et al. (2003). Neuronal interactions are higher in the cortex than thalamus in the somatosensory pathway. *Neuroscience* 118.1, pp. 205–216 (cit. on p. 139).

Kimura, a, Donishi, T, Sakoda, T, Hazama, M, and Tamai, Y (2003). Auditory thalamic nuclei projections to the temporal cortex in the rat. *Neuroscience* 117.4, pp. 1003–1016 (cit. on pp. 26, 27, 81, 84, 106).

Ko, H., Hofer, S. B., Pichler, B., et al. (2011). Functional specificity of local synaptic connections in neocortical networks. *Nature* 473.7345, pp. 87–91 (cit. on pp. 76, 82, 119, 166, 168).

Kondo, S. and Ohki, K. (2016). Laminar differences in the orientation selectivity of geniculate afferents in mouse primary visual cortex. *Nature neuroscience* 19.2, pp. 316–9 (cit. on pp. 105, 106, 135).

Krakauer, J. W., Ghazanfar, A. A., Gomez-Marin, A., MacIver, M. A., and Poeppel, D. (2017). Neuroscience Needs Behavior: Correcting a Reductionist Bias. *Neuron* 93.3, pp. 480–490 (cit. on pp. 79, 139, 172).

Kratz, M. B. and Manis, P. B. (2015). Spatial organization of excitatory synaptic inputs to layer 4 neurons in mouse primary auditory cortex. *Frontiers in neural circuits* 9.April, p. 17 (cit. on pp. 9, 11, 136, 140).

Krubitzer, L. (2007). The Magnificent Compromise: Cortical Field Evolution in Mammals. *Neuron* 56.2, pp. 201–208 (cit. on pp. 21, 22).

Kuramoto, E., Furuta, T., Nakamura, K. C., et al. (2009). Two types of thalamocortical projections from the motor thalamic nuclei of the rat: A single neuron-tracing study using viral vectors. *Cerebral Cortex* 19.9, pp. 2065–2077 (cit. on pp. 81, 106).

Kuroda, M., Murakami, K., Kishi, K., and Price, J. L. J. (1992). Distribution of the piriform cortical terminals to cells in the central segment of the mediodorsal thalamic nucleus of the rat. *Brain Research* 595.1, pp. 159–163 (cit. on p. 3).

Larkum, M. (2012). A cellular mechanism for cortical associations: an organizing principle for the cerebral cortex. *Trends in neurosciences* 36.3, pp. 141–151 (cit. on p. 11).

Larkum, M. E., Nevian, T., Sandler, M., Polsky, A., and Schiller, J. (2009). Synaptic integration in tuft dendrites of layer 5 pyramidal neurons: a new unifying principle. *Science* 325.5941, pp. 756–60 (cit. on p. 11).

Las, L., Stern, E. A., and Nelken, I. (2005). Representation of tone in fluctuating maskers in the ascending auditory system. *The Journal of neuroscience* 25.6, pp. 1503–13 (cit. on pp. 107, 163).

Le Gros Clark, W. E. (1936). The thalamic connections of the temporal lobe of the brain in the monkey. *Journal of anatomy* 70.Pt 4, p. 447 (cit. on p. 104).

Lee, C. C. (2015). Exploring functions for the non-lemniscal auditory thalamus. *Frontiers in Neural Circuits* 9.November, pp. 1–8 (cit. on p. 13).

Lee, C. C. and Sherman, S. M. (2010). Topography and physiology of ascending streams in the auditory tectothalamic pathway. *Proc Natl Acad Sci USA* 107.1, pp. 372–377 (cit. on pp. 53, 107).

Lee, C. C. and Winer, J. A. (2005). Principles governing auditory cortex connections. *Cerebral Cortex* 15.11, pp. 1804–1814 (cit. on pp. 28, 80).

Levene, M. J., Dombeck, D. a., Kasischke, K. a., Molloy, R. P., and Webb, W. W. (2004). In vivo multiphoton microscopy of deep brain tissue. *Journal of neurophysiology* 91.4, pp. 1908–12 (cit. on p. 141).

Li, H., Fertuzinhos, S., Mohns, E., et al. (2013a). Laminar and Columnar Development of Barrel Cortex Relies on Thalamocortical Neurotransmission. *Neuron* 79.5, pp. 970–986 (cit. on p. 105).

Li, Y.-t., Ibrahim, L. a., Liu, B.-h., Zhang, L. I., and Tao, H. W. (2013b). Linear transformation of thalamocortical input by intracortical excitation. *Nature neuroscience* 16.9, pp. 1324–30 (cit. on p. 10).

Linden, J. F. and Schreiner, C. E. (2003). Columnar transformations in auditory cortex? A comparison to visual and somatosensory cortices. *Cerebral cortex (New York, N.Y. : 1991)* 13.1, pp. 83–89 (cit. on pp. 21, 109).

Linden, J. F., Liu, R. C., Sahani, M., Schreiner, C. E., and Merzenich, M. M. (2003). Spectrotemporal structure of receptive fields in areas AI and AAF of mouse auditory cortex. *Journal of neurophysiology* 90.4, pp. 2660–75 (cit. on p. 53).

Linke, R and Schwegler, H (2000). Convergent and complementary projections of the caudal paralaminar thalamic nuclei to rat temporal and insular cortex. *Cerebral cortex (New York, N.Y. : 1991)* 10.8, pp. 753–71 (cit. on p. 106).

Linke, R. (1999). Organization of projections to temporal cortex originating in the thalamic posterior intralaminar nucleus of the rat. *Experimental Brain Research* 127.3, pp. 314–320 (cit. on p. 106).

Liu, B.-h., Wu, G. K., Arbuckle, R., Tao, H. W., and Zhang, L. I. (2007). Defining cortical frequency tuning with recurrent excitatory circuitry. *Nature neuroscience* 10.12, pp. 1594–600 (cit. on pp. 10, 84, 105).

Llano, D. A. and Sherman, S. M. (2008). Evidence for nonreciprocal organization of the mouse auditory thalamocortical-corticothalamic projection systems. *The Journal of comparative neurology* 507.2, pp. 1209–27 (cit. on pp. 55, 57, 81, 84, 104, 106, 164).

Llano, D. a., Slater, B. J., Lesicko, A. M. H., and Stebbings, K. a. (2014). An auditory colliculothalamocortical brain slice preparation in mouse. *Journal of neurophysiology* 111.1, pp. 197–207 (cit. on p. 168).

London, M. and Häusser, M. (2005). Dendritic computation. *Annual review of neuroscience* 28, pp. 503–32 (cit. on pp. 7, 167).

Loterie, D., Farahi, S., Papadopoulos, I., et al. (2015). Digital confocal microscopy through a multimode fiber. *Optics Express* 23.18, p. 23845 (cit. on p. 157).

Lu, E., Llano, D. a., and Sherman, S. M. (2009). Different distributions of calbindin and calretinin immunostaining across the medial and dorsal divisions of the mouse medial geniculate body. *Hearing Research* 257.1-2, pp. 16–23 (cit. on pp. 55, 58, 59, 80).

Lübke, J, Egger, V., Sakmann, B., and Feldmeyer, D. (2000). Columnar organization of dendrites and axons of single and synaptically coupled excitatory spiny neurons in layer 4 of the rat barrel cortex. *The Journal of neuroscience* 20.14, pp. 5300–11 (cit. on pp. 9, 105).

Luo, L., Callaway, E. E. M., and Svoboda, K. (2008). Genetic dissection of neural circuits. *Neuron* 57.5, pp. 634–60 (cit. on pp. 52, 171).

Mahalati, R. N., Gu, R. Y., and Kahn, J. M. (2013). Resolution limits for imaging through multi-mode fiber. *Optics Express* 21.2, p. 1656 (cit. on p. 150).

Martinez, L. M., Wang, Q., Reid, R. C., et al. (2005). Receptive field structure varies with layer in the primary visual cortex. *Nat Neurosci* 8.3, pp. 372–379 (cit. on p. 135).

Marvin, J. S., Borghuis, B. G., Tian, L., et al. (2013). An optimized fluorescent probe for visualizing glutamate neurotransmission. *Nature methods* 10.2, pp. 162–70 (cit. on p. 165).

McMullen, N. T. and Venecia, R. K. de (1993). Thalamocortical patches in auditory neocortex. *Brain research* 620.2, pp. 317–322 (cit. on p. 81).

Mekhail, S. P., Arbuthnott, G., and Chormaic, S. N. (2016). Advances in Fibre Microendoscopy for Neuronal Imaging. *Optical Data Processing and Storage* 2.1, pp. 30–42 (cit. on p. 172).

Metherate, R., Kaur, S., Kawai, H., et al. (2005). Spectral integration in auditory cortex: Mechanisms and modulation. *Hearing Research* 206.1-2, pp. 146–158 (cit. on pp. 107, 163).

Mianné, J., Chessum, L., Kumar, S., et al. (2016). Correction of the auditory phenotype in C57BL/6N mice via CRISPR/Cas9-mediated homology directed repair. *Genome medicine* 8.1, p. 16 (cit. on pp. 65, 102).

Miesenböck, G. (2011). Optogenetic control of cells and circuits. en. *Annual review of cell and developmental biology* 27, pp. 731–58 (cit. on p. 170).

Miller, L. M., Escabí, M. A., Read, H. L., and Schreiner, C. E. (2001). Functional convergence of response properties in the auditory thalamocortical system. *Neuron* 32.1, pp. 151–160 (cit. on pp. 107, 131, 163).

Mitchell, K. J., Turtaev, S., Padgett, M. J., Čižmár, T., and Phillips, D. B. (2016). High-speed spatial control of the intensity, phase and polarisation of vector beams using a digital micro-mirror device. *Optics Express* 24.25, p. 29269 (cit. on pp. 152, 156, 157).

Mizrahi, A., Crowley, J. C., Shtoyerman, E., and Katz, L. C. (2004). High-resolution in vivo imaging of hippocampal dendrites and spines. *The Journal of neuroscience* 24.13, pp. 3147–51 (cit. on p. 141).

Mizrahi, A., Shalev, A., and Nelken, I. (2014). Single neuron and population coding of natural sounds in auditory cortex. *Current opinion in neurobiology* 24.1, pp. 103–10 (cit. on p. 162).

Mo, C., Petrof, I., Viaene, A. N., and Sherman, S. M. (2017). Synaptic properties of the lemniscal and paralemniscal pathways to the mouse somatosensory thalamus. *Proceedings of the National Academy of Sciences* 114.30, E6212–E6221 (cit. on p. 13).

Moczulska, K. E., Tinter-Thiede, J., Peter, M., et al. (2013). Dynamics of dendritic spines in the mouse auditory cortex during memory formation and memory recall. *Proc Natl Acad Sci USA* 110.45, pp. 18315–20 (cit. on p. 83).

Monakow, C v. (1895). Experimentelle und pathologisch-anatomische Untersuchungen über die Haubenregion, den Sehhügel und die Regio subthalamica, nebst Beiträgen zur Kenntniss früh erworbener Gross-und Kleinhirn-defecte. *European Archives of Psychiatry and Clinical Neuroscience* 27.1, pp. 1–128 (cit. on pp. 25, 51).

Morales-Delgado, E. E., Farahi, S., Papadopoulos, I. N., Psaltis, D., and Moser, C. (2015). Delivery of focused short pulses through a multimode fiber. *Optics Express* 23.7, p. 9109 (cit. on p. 157).

Moshayedi, P., Ng, G., Kwok, J. C., et al. (2014). The relationship between glial cell mechanosensitivity and foreign body reactions in the central nervous system. *Biomaterials* 35.13, pp. 3919–3925 (cit. on pp. 35, 141).

Mothe, L. A. de la, Blumell, S., Kajikawa, Y., and Hackett, T. A. (2006). Thalamic connections of the auditory cortex in marmoset monkeys: core and medial belt regions. *The Journal of comparative neurology* 496.1, pp. 72–96 (cit. on pp. 26, 27, 51).

Mountcastle, V. B. (1997). The columnar organization of the neocortex (cit. on pp. 8, 134, 161).

Nelken, I., Bizley, J. K., Nodal, F. R., et al. (2008). Responses of Auditory Cortex to Complex Stimuli: Functional Organization Revealed Using Intrinsic Optical Signals. *Journal of Neurophysiology* 99.4, pp. 1928–1941 (cit. on p. 162).

Nieuwenhuys, R., Donkelaar, H. J., and Nicholson, C. (1998). The central nervous system of vertebrates. Springer, p. 2219 (cit. on pp. 1, 2).

Nixon, M. and Aguado, A. S. (2012). Feature Extraction & Image Processing for Computer Vision. Academic Press (cit. on p. 45).

No, R. Lorente de (1938). Cerebral cortex: architecture, intracortical connections, motor projections. In: *Physiology of the Nervous System*. Ed. by J. Fulton. Oxford University Press (cit. on p. 12).

O'Brien, J. a. and Lummis, S. C. R. (2006). Biolistic transfection of neuronal cultures using a hand-held gene gun. *Nature protocols* 1.2, pp. 977–81 (cit. on p. 48).

Oda, S., Kishi, K., Yang, J., et al. (2004). Thalamocortical projection from the ventral posteromedial nucleus sends its collaterals to layer I of the primary somatosensory cortex in rat. *Neuroscience Letters* 367.3, pp. 394–398 (cit. on pp. 81, 106).

Ouzounov, D. G., Wang, T., Wang, M., et al. (2017). In vivo three-photon imaging of activity of GCaMP6-labeled neurons deep in intact mouse brain. *Nature Methods* 14.4 (cit. on p. 172).

Pallas, S. L., Roe, A. W., and Sur, M. (1990). Visual projections induced into the auditory pathway of ferrets. I. Novel inputs to primary auditory cortex (AI) from the LP/pulvinar complex and the topography of the MGN-AI projection. *The Journal of Comparative Neurology* 298.1, pp. 50–68 (cit. on pp. 26, 27).

Passingham, R. E. (1982). The human primate. W.H. Freeman, p. 390 (cit. on p. 1).

Passingham, R. E., Stephan, K. E., and Kötter, R. (2002). The anatomical basis of functional localization in the cortex. *Nature reviews. Neuroscience* 3.8, pp. 606–16 (cit. on p. 1).

Paxinos, G. and Franklin, K. B. (2013). The mouse brain in stereotaxic coordinates. Academic Press (cit. on p. 112).

Penfield, W. and Rasmussen, T. (1950). The Cerebral Cortex of Man: Clinical Study of Localization of Function (cit. on pp. 3, 5).

Peron, S., Chen, T.-W., and Svoboda, K. (2015a). Comprehensive imaging of cortical networks. *Current Opinion in Neurobiology* 32, pp. 115–123 (cit. on p. 111).

Peron, S. P., Freeman, J., Iyer, V., Guo, C., and Svoboda, K. (2015b). A Cellular Resolution Map of Barrel Cortex Activity during Tactile Behavior. *Neuron*, pp. 1–17 (cit. on pp. 111, 162).

Petreanu, L., Mao, T., Sternson, S. M., and Svoboda, K. (2009). The subcellular organization of neocortical excitatory connections. *Nature* 457.7233, pp. 1142–5 (cit. on pp. 10, 106, 137).

Petreanu, L., Gutnisky, D. a., Huber, D., et al. (2012). Activity in motor-sensory projections reveals distributed coding in somatosensation. *Nature* 489.7415, pp. 299–303 (cit. on pp. 65, 85).

Pickles, J. O. (2012). An Introduction to the Physiology of Hearing. 4th. Brill, p. 460 (cit. on p. 79).

Plöschner, M. and Čižmár, T. (2015). Compact multimode fiber beam-shaping system based on GPU accelerated digital holography. *Optics Letters* 40.2, p. 197 (cit. on pp. 36, 143–145).

Plöschner, M., Tyc, T., and Čižmár, T. (2015). Seeing through chaos in multimode fibres. *Nature Photonics* 9.8, pp. 529–535 (cit. on p. 157).

Pnevmatikakis, E. A., Soudry, D., Gao, Y., et al. (2016). Simultaneous Denoising, Deconvolution, and Demixing of Calcium Imaging Data. *Neuron* 89.2, p. 299 (cit. on p. 171).

Poliak, S. (1932). The main afferent fiber systems of the cerebral cortex in primates. University of California (cit. on pp. 25, 51).

Popoff, S. M., Lerosey, G., Carminati, R., et al. (2010). Measuring the Transmission Matrix in Optics: An Approach to the Study and Control of Light Propagation in Disordered Media. *Physical Review Letters* 104.10, p. 100601 (cit. on pp. 36, 143, 146).

Portfors, C. V., Mayko, Z. M., Jonson, K, Cha, G. F., and Roberts, P. D. (2011). Spatial organization of receptive fields in the auditory midbrain of awake mouse. *Neuroscience* 193, pp. 429–439 (cit. on p. 107).

Pouchelon, G., Gambino, F., Bellone, C., et al. (2014). Modality-specific thalamocortical inputs instruct the identity of postsynaptic L4 neurons. *Nature* 511.7510, pp. 471–474 (cit. on p. 6).

Qin, L., Chimoto, S., Sakai, M., Wang, J., and Sato, Y. (2007). Comparison Between Offset and Onset Responses of Primary Auditory Cortex ON-OFF Neurons in Awake Cats. *Journal of Neurophysiology* 97.5, pp. 3421–3431 (cit. on p. 171).

Redies, H., Brandner, S., and Creutzfeldt, O. D. (1989). Anatomy of the auditory thalamocortical system of the guinea pig. *Journal of Comparative Neurology* 282.4, pp. 489–511 (cit. on pp. 26, 28).

Reig, R., Zerlaut, Y., Vergara, R., Destexhe, A., and Sanchez-Vives, M. V. (2015). Gain Modulation of Synaptic Inputs by Network State in Auditory Cortex In Vivo. *Journal of Neuroscience* 35.6, pp. 2689–2702 (cit. on p. 137).

Resendez, S. L., Jennings, J. H., Ung, R. L., et al. (2016). Visualization of cortical, subcortical and deep brain neural circuit dynamics during naturalistic mammalian behavior with head-mounted microscopes and chronically implanted lenses. *Nature protocols* 11.3, pp. 566–97 (cit. on p. 35).

Richardson, R. J., Blundon, J. a., Bayazitov, I. T., and Zakharenko, S. S. (2009). Connectivity patterns revealed by mapping of active inputs on dendrites of thalamorecipient neurons in the auditory cortex. *The Journal of neuroscience* 29.20, pp. 6406–17 (cit. on pp. 9, 30, 105, 126, 136, 140).

Rochefort, N. L., Garaschuk, O., Milos, R.-I., et al. (2009). Sparsification of neuronal activity in the visual cortex at eye-opening. *Proceedings of the National Academy of Sciences of the United States of America* 106.35, pp. 15049–54 (cit. on p. 161).

Romanski, L. M. and LeDoux, J. E. (1993). Organization of rodent auditory cortex: anterograde transport of PHA-L from MGv to temporal neocortex. *Cerebral Cortex* 3.6, pp. 499–514 (cit. on p. 81).

Roth, M. M., Dahmen, J. C., Muir, D. R., et al. (2016). Thalamic nuclei convey diverse contextual information to layer 1 of visual cortex. *Nature neuroscience* 19.2, pp. 299–307 (cit. on pp. 43, 47, 65, 79, 80, 85, 106, 107, 135, 162, 164, 170).

Roth, S. (2003). The origin of dorsoventral polarity in Drosophila. *Philos Trans R Soc Lond B Biol Sci.* 358.1436, pp. 1317–29 (cit. on p. 104).

Rothschild, G. and Mizrahi, A. (2015). Global Order and Local Disorder in Brain Maps. *Annual Review of Neuroscience* 38.1, pp. 247–268 (cit. on pp. 9, 52, 83, 85, 123, 137, 161–163).

Rothschild, G., Nelken, I., and Mizrahi, A. (2010). Functional organization and population dynamics in the mouse primary auditory cortex. *Nature neuroscience* 13.3, pp. 353–60 (cit. on pp. 7, 32, 33, 43, 52, 77, 78, 82, 83, 116, 161, 163, 170).

Rubio-Garrido, P., Manzo, F. Pérez-de, Porrero, C., Galazo, M. J., and Clascá, F. (2009). Thalamic input to distal apical dendrites in neocortical layer 1 is massive and highly convergent. *Cerebral cortex (New York, N.Y. : 1991)* 19.10, pp. 2380–95 (cit. on pp. 86, 106).

Ryugo, D. K. and Killackey, H. P. (1974). Differential telencephalic projections of the medial and ventral divisions of the medial geniculate body of the rat. *Brain research* 82.1, pp. 173–177 (cit. on p. 106).

Sadagopan, S. and Ferster, D. (2012). Feedforward Origins of Response Variability Underlying Contrast Invariant Orientation Tuning in Cat Visual Cortex. *Neuron* 74.5, pp. 911–923 (cit. on p. 137).

Sadakane, O., Masamizu, Y., Watakabe, A., et al. (2015). Long-Term Two-Photon Calcium Imaging of Neuronal Populations with Subcellular Resolution in Adult Non-human Primates. *Cell Reports* 13.9, pp. 1989–1999 (cit. on p. 34).

Sakata, S. and Harris, K. D. (2009). Laminar Structure of Spontaneous and Sensory-Evoked Population Activity in Auditory Cortex. *Neuron* 64.3, pp. 404–418 (cit. on pp. 135, 167).

Sawatari, H., Tanaka, Y., Takemoto, M., et al. (2011). Identification and characterization of an insular auditory field in mice. *European Journal of Neuroscience* 34.12, pp. 1944–1952 (cit. on p. 52).

Scanziani, M. and Häusser, M. (2009). Electrophysiology in the age of light. *Nature* 461.7266, pp. 930–9 (cit. on p. 170).

Schmitt, L. I., Wimmer, R. D., Nakajima, M., et al. (2017). Thalamic amplification of cortical connectivity sustains attentional control. *Nature* 545.7653, pp. 219–223 (cit. on pp. 169, 172).

Schneider, G. E. (2014). Brain structure and its origins : function, evolution, development. MIT Press, p. 699 (cit. on pp. 4–6).

Schoonover, C. E., Tapia, J.-C., Schilling, V. C., et al. (2014). Comparative strength and dendritic organization of thalamocortical and corticocortical synapses onto excitatory layer 4 neurons. *The Journal of neuroscience* 34.20, pp. 6746–58 (cit. on p. 9).

Schreiner, C. E. and Winer, J. a. (2007). Auditory cortex mapmaking: principles, projections, and plasticity. *Neuron* 56.2, pp. 356–65 (cit. on pp. 9, 22, 29, 51, 80, 83, 109, 140, 162–164, 166).

Shepherd, G. M. (2004). The synaptic organization of the brain. Oxford University Press, p. 719 (cit. on pp. 8, 9).

Sherman, S. M. and Guillery, R. W. (2013). Functional Connections of Cortical Areas : A New View from the Thalamus. 1st. MIT Press, p. 279 (cit. on pp. 14, 16, 18, 19, 141, 164, 167).

Sherman, S. M., Guillery, R. W., and Sherman, S. M. (2006). Exploring the thalamus and its role in cortical function. MIT Press, p. 484 (cit. on pp. 1, 3, 14, 15, 18, 35, 169, 171).

Smith, P. H. and Populin, L. C. (2001). Fundamental differences between the thalamocortical recipient layers of the cat auditory and visual cortices. *The Journal of comparative neurology* 436.4, pp. 508–19 (cit. on p. 30).

Smith, P. H., Bartlett, E. L., and Kowalkowski, A. (2006). Unique combination of anatomy and physiology in cells of the rat paralaminar thalamic nuclei adjacent to the medial geniculate body. *Journal of Comparative Neurology* 496.3, pp. 314–334 (cit. on p. 55).

Smith, P. H., Uhlrich, D. J., Manning, K. a., and Banks, M. I. (2012). Thalamocortical projections to rat auditory cortex from the ventral and dorsal divisions of the medial geniculate nucleus. *The Journal of comparative neurology* 520.1, pp. 34–51 (cit. on pp. 26–28, 51).

Smith, S. L. and Häusser, M. (2010). Parallel processing of visual space by neighboring neurons in mouse visual cortex. *Nature Neuroscience* 13.9, pp. 1144–1149 (cit. on pp. 106, 161).

Smith, S. L., Smith, I. T., Branco, T., and Häusser, M. (2013). Dendritic spikes enhance stimulus selectivity in cortical neurons in vivo. *Nature* 503.7474, pp. 115–20 (cit. on p. 168).

Stiebler, I, Neulist, R, Fichtel, I, and Ehret, G (1997). The auditory cortex of the house mouse: left-right differences, tonotopic organization and quantitative analysis of frequency representation. *Journal of comparative physiology. A, Sensory, neural, and behavioral physiology* 181.6, pp. 559–71 (cit. on pp. 52–54, 80, 82, 83).

Stiebler, I. and Ehret, G. G. (1985). Inferior colliculus of the house mouse. I. A quantitative study of tonotopic organization, frequency representation, and tone-threshold distribution. *Journal of Comparative Neurology* 238.1, pp. 65–76 (cit. on pp. 88, 107).

Stuart, G., Spruston, N., and Häusser, M. (2017). Dendrites. 3rd. Oxford University Press, p. 616 (cit. on p. 10).

Sun, W., Tan, Z., Mensh, B. D., and Ji, N. (2016). Thalamus provides layer 4 of primary visual cortex with orientation- and direction-tuned inputs. *Nature neuroscience* 19.2, pp. 308–15 (cit. on pp. 30, 105, 106).

Swanson, L. W. (2012). Brain architecture : understanding the basic plan. Oxford University Press, p. 331 (cit. on p. 4).

Szabo, V., Ventalon, C., De Sars, V., Bradley, J., and Emiliani, V. (2014). Spatially Selective Holographic Photoactivation and Functional Fluorescence Imaging in Freely Behaving Mice with a Fiberscope. *Neuron*, pp. 1–13 (cit. on p. 35).

Takemoto, M., Hasegawa, K., Nishimura, M., and Song, W.-J. J. (2014). The insular auditory field receives input from the lemniscal subdivision of the auditory thalamus in mice. *Journal of Comparative Neurology* 522.6, pp. 1373–1389 (cit. on p. 55).

Taniguchi, H., He, M., Wu, P., et al. (2011). A Resource of Cre Driver Lines for Genetic Targeting of GABAergic Neurons in Cerebral Cortex. *Neuron* 71.6, pp. 995–1013 (cit. on pp. 58, 65).

Theis, L., Berens, P., Froudarakis, E., et al. (2016). Benchmarking Spike Rate Inference in Population Calcium Imaging. *Neuron* 90.3, pp. 471–82 (cit. on p. 171).

Thomson, A. M. (2007). Functional maps of neocortical local circuitry. *Frontiers in Neuroscience* 1.1, pp. 19–42 (cit. on p. 138).

Tsukano, H., Horie, M., Bo, T., et al. (2015). Delineation of a frequency-organized region isolated from the mouse primary auditory cortex. *Journal of Neurophysiology* 113.1, pp. 2900–20 (cit. on pp. 52, 53).

Tsukano, H., Horie, M., Hishida, R., and Takahashi, K. (2016). Quantitative map of multiple auditory cortical regions with a stereotaxic fine-scale atlas of the mouse brain. *Nature Publishing Group* October 2015, pp. 1–12 (cit. on pp. 52, 54, 60, 66, 84).

Tsukano, H., Horie, M., Takahashi, K., et al. (2017a). Independent tonotopy and thalamocortical projection patterns in two adjacent parts of the classical primary auditory cortex in mice. *Neuroscience Letters* 637, pp. 26–30 (cit. on pp. 52, 56, 81).

Tsukano, H., Horie, M., Ohga, S., et al. (2017b). Reconsidering Tonotopic Maps in the Auditory Cortex and Lemniscal Auditory Thalamus in Mice. *Frontiers in neural circuits* 11, p. 14 (cit. on pp. 52, 80, 112, 164).

Tye, K. M. and Deisseroth, K. (2012). Optogenetic investigation of neural circuits underlying brain disease in animal models. *Nature Reviews Neuroscience* 13.4, pp. 251–266 (cit. on p. 171).

Van Hooser, S. D., Roy, A., Rhodes, H. J., Culp, J. H., and Fitzpatrick, D. (2013). Transformation of Receptive Field Properties from Lateral Geniculate Nucleus to Superficial V1 in the Tree Shrew. *Journal of Neuroscience* 33.28, pp. 11494–11505 (cit. on pp. 135, 138).

Vasquez-Lopez, S. A., Weissenberger, Y., Lohse, M., et al. (2017). Thalamic input to auditory cortex is locally heterogeneous but globally tonotopic. *eLife* 6, e25141 (cit. on pp. 47, 170, 173, 195).

Velenovsky, D. S., Cetas, J. S., Price, R. O., Sinex, D. G., and McMullen, N. T. (2003). Functional subregions in primary auditory cortex defined by thalamocortical terminal arbors: an electrophysiological and anterograde labeling study. *The Journal of neuroscience* 23.1, pp. 308–16 (cit. on p. 26).

Viaene, A. N., Petrof, I., and Sherman, S. M. (2011a). Properties of the thalamic projection from the posterior medial nucleus to primary and secondary somatosensory cortices in the mouse. *Proc Natl Acad Sci USA* 108.44, pp. 18156–61 (cit. on p. 30).

Viaene, A. N., Petrof, I., and Sherman, S. M. (2011b). Synaptic Properties of Thalamic Input to Layers 2/3 and 4 of Primary Somatosensory and Auditory Cortices. *Journal of Neurophysiology* 105.1, pp. 279–292 (cit. on p. 30).

Viaene, A. N., Petrof, I., and Sherman, S. M. (2011c). Synaptic Properties of Thalamic Input to the Subgranular Layers of Primary Somatosensory and Auditory Cortices in the Mouse. *Journal of Neuroscience* 31.36, pp. 12738–12747 (cit. on pp. 30, 140).

Walker, A. E. (1937). The projection of the medial geniculate body to the cerebral cortex in the macaque monkey. *Journal of anatomy* 71.Pt 3, p. 319 (cit. on pp. 25, 51, 104).

Wallace, M. N. and Palmer, A. R. (2008). Laminar differences in the response properties of cells in the primary auditory cortex. *Experimental Brain Research* 184.2, pp. 179–91 (cit. on p. 140).

Waller, W. H. (1934). Topographical relations of cortical lesions to thalamic nuclei in the albino rat. *Journal of Comparative Neurology* 60.2, pp. 237–269 (cit. on pp. 25, 51).

Watkins, P. V., Kao, J. P. Y., and Kanold, P. O. (2014). Spatial pattern of intra-laminar connectivity in supragranular mouse auditory cortex. *Frontiers in Neural Circuits* 8.March, pp. 1–18 (cit. on p. 166).

Wehr, M. and Zador, A. M. (2003). Balanced inhibition underlies tuning and sharpens spike timing in auditory cortex. *Nature* 426.6965, pp. 442–446 (cit. on p. 167).

Wenstrup, J. J. (2005). The Tectothalamic System. In: *The Inferior Colliculus*. New York: Springer-Verlag, pp. 200–230 (cit. on pp. 29, 53, 107).

Willott, J. (2001). Handbook of Mouse Auditory Research. CRC Press, pp. 137–156 (cit. on pp. 82, 88).

Willott, J. F., Aitkin, L. M., and McFadden, S. L. (1993). Plasticity of auditory cortex associated with sensorineural hearing loss in adult C57BL/6J mice. *Journal of Comparative Neurology* 329.3, pp. 402–411 (cit. on p. 102).

Wilson, D. E., Whitney, D. E., Scholl, B., and Fitzpatrick, D. (2016). Orientation selectivity and the functional clustering of synaptic inputs in primary visual cortex. *Nature neuroscience* 19.8, pp. 1003–9 (cit. on p. 105).

Wilt, B. A., Burns, L. D., Wei Ho, E. T., et al. (2009). Advances in Light Microscopy for Neuroscience. *Annual Review of Neuroscience* 32.1, pp. 435–506 (cit. on p. 33).

Winer, J. A. (1984). Identification and structure of neurons in the medial geniculate body projecting to primary auditory cortex (AI) in the cat. *Neuroscience* 13.2, pp. 395–413 (cit. on p. 29).

Winer, J. A. and Schreiner, C. E. (2010). The Auditory Cortex. Springer US (cit. on pp. 1, 51, 109).

Winer, J. a. and Lee, C. C. (2007). The distributed auditory cortex. *Hearing research* 229.1-2, pp. 3–13 (cit. on pp. 9, 29).

Winer, J. A., Sally, S. L., Larue, D. T., and Kelly, J. B. (1999). Origins of medial geniculate body projections to physiologically defined zones of rat primary auditory cortex. *Hearing Research* 130.1-2, pp. 42–61 (cit. on p. 31).

Winer, J. a., Miller, L. M., Lee, C. C., and Schreiner, C. E. (2005). Auditory thalamocortical transformation: structure and function. *Trends in neurosciences* 28.5, pp. 255–63 (cit. on pp. 28, 107, 163, 164).

Winkowski, D. E. and Kanold, P. O. (2013). Laminar transformation of frequency organization in auditory cortex. *The Journal of neuroscience* 33.4, pp. 1498–508 (cit. on pp. 21, 78, 82, 83, 104, 109, 111, 116, 119, 123, 135–138, 140, 162, 166, 170).

Woolsey, C. N. (1964). Electrophysiological studies on thalamocortical relations in the auditory system. *Unfinished tasks in the behavioral sciences*, pp. 45–57 (cit. on pp. 5, 25).

Woolsey, C. N. and Walzl, E. M. (1942). Topical projection of nerve fibers from local regions of the cochlea to the cerebral cortex of the cat. *Bulletin of the Johns Hopkins Hospital* 71, 315–344 (cit. on pp. 25, 83).

Wu, G. K., Arbuckle, R., Liu, B. h., Tao, H. W., and Zhang, L. I. (2008a). Lateral Sharpening of Cortical Frequency Tuning by Approximately Balanced Inhibition. *Neuron* 58.1, pp. 132–143 (cit. on p. 167).

Wu, X., Tanwar, P. S., and Raftery, L. a. (2008b). Drosophila follicle cells: morphogenesis in an eggshell. *Seminars in cell & developmental biology* 19.3, pp. 271–82 (cit. on p. 10).

Xu, H.-T., Pan, F., Yang, G., and Gan, W.-B. (2007). Choice of cranial window type for in vivo imaging affects dendritic spine turnover in the cortex. *Nature neuroscience* 10.5, pp. 549–51 (cit. on pp. 35, 141).

Xu, N.-l., Harnett, M. T., Williams, S. R., et al. (2012). Nonlinear dendritic integration of sensory and motor input during an active sensing task. *Nature* 492.7428, pp. 247–51 (cit. on p. 168).

Xu, W. and Sudhof, T. C. (2013). A Neural Circuit for Memory Specificity and Generalization. *Science* 339.6125, pp. 1290–1295 (cit. on p. 59).

Zhou, M., Liang, F., Xiong, X. R., et al. (2014). Scaling down of balanced excitation and inhibition by active behavioral states in auditory cortex. *Nature Neuroscience* 17.6, pp. 841–850 (cit. on pp. 10, 139).

Zurita, P., Villa, A. E. P., Ribaupierre, Y. de, Ribaupierre, F. de, and Rouiller, E. M. (1994). Changes of single unit activity in the cat's auditory thalamus and cortex associated to different anesthetic conditions. *Neuroscience Research* 19.3, pp. 303–316 (cit. on p. 103).

Declaration

I hereby declare that the contents of this dissertation are original and have not been submitted in whole or in part for consideration for any other degree or qualification in this or any other university. This dissertation contains less than 50000 words and less than 250 figures. A considerable part of chapters 3 and 4 has been recently published as a research article in a scientific journal for which I am the main contributing author (Vasquez-Lopez et al., 2017).

All the results presented are the product of my own work with the following exceptions:

(1) Michael Lohse acquired the electrophysiological multi-unit recording maps which are part of **Figure 3.11** in Chapter 3.

(2) Vadim Koren and I equally contributed to the acquisition of the fluorescent images of dendritic spines *in vivo* and the subsequent brain histology, which are respectively presented in **Figure 6.8** and **Figure 6.9** of Chapter 6.

(3) The resolution measurements presented in **Figure 6.5** of Chapter 6 were carried out in the laboratory of our collaborator Dr Tomas Cizmar at the University of Dundee.

Oxford, UK, Oct 6th 2017

Sebastian A. Vásquez-López